warwick.ac.uk/lib-publications

Electron paramagnetic resonance studies of point

defects in diamond: quantification,

spin polarisation and preferential orientation.

By

Ben George Breeze

Thesis

Submitted to the University of Warwick

for the degree of

Doctor of Philosophy

Department of Physics

September 2016

Contents

List of Tables

List of Figures

Acknowledgements

Research of this extent is never truly the work of one person in isolation and was only possible due to the support I have received from a host of people. I would like to thank my supervisor Prof. Mark Newton for his supervision, guidance and patience over the course of this PhD and for sharing his infectious enthusiasm for research. I would also like to thank Dr. Gavin Morley for his support and willingness to offer advice whenever it was needed.

I would like to acknowledge Dr. Chris Wedge who has always been very generous with his time and experience. In additional I owe thanks to all the staff of the mechanical and electronic workshops for their excellent work. I would also like to thank Dr. Brad Cann, Dr. David Fisher and Dr. Philip Martineau from De Beers Technologies in Maidenhead who have all offered encouragement and thought provoking conversations during the last four years.

I also have to thank all the member of the Warwick diamond and EPR group students past and present, Ben (1), Chris H, Mika, Matt, Anton, Angelo, Claudio, Sinead, Colin, Phil, Guy and Enrik. You have all at one point over the past four years educated me, provided interesting debate and some good coffee. I would not have made it through without the emotional and practical support that you have all provided and I am eternally grateful to you all.

I would also like to thank my family. Mum and Dad, for their love and belief in me even when I did not believe in myself. Emma and John who have provided beer/tea, an interested ear and welcome distractions in equal measure not to mention the traffic tips. Of course, I must also thank my extended family Sue and J
ohn and the clan across the ocean who have all provided endless support and encouragement. (On a side note an average house brick has a Mohs hardness of approximately three.)

Finally, this thesis is dedicated to my wife Amy. You have consoled me during the dark days and celebrated on the good days. You have provided me with love support and the occasional motivational push, it is true to say I would not have achieved this without you.
I love you always ∞.

Declaration and published work

I declare that the work presented in this thesis is my own except where stated otherwise, and was carried out entirely at the University of Warwick, during the period of October 2012 to September 2016, under the supervision of Prof. Mark Newton and Dr. Gavin Morley. The research reported here has not been submitted, either wholly or in part, in this or any other academic institution for admission to a higher degree. Some parts of the work reported and other work not reported in this thesis have been published, as listed below. It is anticipated that further parts of this work will be submitted for publication in due course.

Published Papers

1. M. A. Tamski, M. W. Dale, B. G. Breeze, J. V. Macpherson, P. R. Unwin, and M. E. Newton, *Electrochemical electron paramagnetic resonance utilizing loop gap resonators and micro- electrochemical cells.* Electrochim. Acta 213, (2016).

Submitted papers

1. B. L. Green, B. G. Breeze, G. J. Rees, J. V. Hanna, J-P. Chou, V. Ivády, A. Gali, and M. E. Newton, All-*optical hyperpolarization of electron and nuclear spins in diamond,* arXiv:1610.03823 (Submitted to Physical review letters. (2017))

2. B. L. Green, B. G. Breeze and M E. Newton, *Electron paramagnetic resonance and photochromism of N_3V^0 in diamond,* arXiv:1702.02959 (Submitted to Journal of condensed matter physics (2017))

Papers in preparation for submission

1. B. G. Breeze, S Liggins, M. W. Dale, Jon Goss and Mark E. Newton, *Uniaxial stress investigation of substitutional nitrogen in diamond,* (2017)

2. M.W. Dale, B. G. Breeze, J. Isoya and Mark E. Newton, *Uniaxial stress and irradiation study of carbon interstitials in diamond,* (2017)

Conference Presentations

1. B. G. Breeze, B. L. Green. G. J. Reese and M. E. Newton, *Optical spin polarisation of the N_3V and Ns^0 defects in diamond,* 67th De Beers Diamond Conference, University of Warwick, Coventry, United Kingdom, oral presentation (2016)

2. B. G. Breeze, M. W. Dale, B. L. Green. and M. E. Newton, *Uniaxial stress of radiation defects in diamond,* 67th De Beers Diamond Conference, University of Warwick, Coventry, United Kingdom, oral presentation (2016)

3. B. G. Breeze, M. W. Dale, B. L. Cann, B. L. Green and M. E. Newton, *Electron paramagnetic resonance on point defects in diamond under uniaxial stress,* International Conference on Diamond and Related Material, Bad Homburg, Germany, poster presentation (2015)

4. B. G. Breeze, M. W. Dale, and M. E. Newton, *In-situ EPR measurements under large uniaxial stress,* IMR-CDT conference, University of Warwick, Coventry, United Kingdom, oral presentation (2015)

5. B. G. Breeze, M. W. Dale, and M. E. Newton, *Electron paramagnetic resonance, diamond and stress,* 66th De Beers Diamond Conference, University of Warwick, Coventry, United Kingdom, oral presentation (2015)

6. B. G. Breeze, M. W. Dale, and M. E. Newton, *Rapid scan electron paramagnetic resonance,* 65th De Beers Diamond Conference, University of Warwick, Coventry, United Kingdom, poster presentation (2014)

7. B. G. Breeze, B. L. Cann, and M. E. Newton, *Rapid passage electron paramagnetic resonance,* The 46th Annual International Meeting of the ESR Spectroscopy Group of the Royal Society of Chemistry, University of Dundee, Dundee, United Kingdom, poster presentation (2014)

8. B. G. Breeze, B. L . Cann, M.W. Dale, B. L. Green, C. B. Hartland and M. E. Newton, *Improving the sensitivity of quantitative electron paramagnetic resonance,* 64th De Beers Diamond Conference, University of Warwick, Coventry, United Kingdom, poster presentation (2013)

9. B. G. Breeze, B. L . Cann, M.W. Dale, B. L. Green, C. B. Hartland and M. E. Newton, *Improving the accuracy of quantitative electron paramagnetic resonance,* The 45th Annual International Meeting of the ESR Spectroscopy Group of the Royal Society of Chemistry, University of Warwick, Coventry, United Kingdom, oral presentation (2013)

Ben Breeze
September 2016

Abstract

This thesis reports research on point defects in synthetic single crystal diamond. The principal technique used for investigation is electron paramagnetic resonance, EPR. Nuclear magnetic resonance, NMR, and optical absorption spectroscopy have also been employed. Uniaxial stress has been used to investigate the properties and migration of defects under an applied perturbation.

The use of field modulated rapid passage EPR, RP-ERP$^{(FM)}$, for quantitative measurements of neutral single substitutional nitrogen, N_S^0, in diamond has been investigated. Optimisation of field sweep rate and experiment temperature have been shown to provide a factor of 5.6 improvent in signal to noise; a $\times 25$ speed up on previous conditions. The repeatability of RP-EPR$^{(FM)}$ has been investigated by repeated measurements of the same sample (containing N_S^0). These results indicate a random error of $\pm 2.5\%$; a 50% reduction compared with slow passage EPR, SP-EPR. Careful cavity characterisation has been utilised to enable reliable quantitative measurements of diamond samples that are large compared to an EPR cavity.

An EPR probe has been developed to deliver in situ large (>1 GPa) uniaxial stress whilst simultaneously performing measurements. This probe was used to investigate the effect of uniaxial applied stress on the paramagnetic relaxation of N_S^0 in diamond. N_S^0 is found to reorientate its principle <111> axis away from applied stress with an activation of 17(1) meV/GPa for a [111] applied stress. Unexpectedly the spin lattice relaxation, T_1, was found to be invariant with a pressure up to 1 GPa: this is inconsistent with the prevailing model for T_1 relaxation of the defect in the literature which relies on the relies on the reorientation of the defect. The phase memory time T_m of N_S^0 was found to be tuneable using uniaxial stress. This is modelled in terms of a reduction of spin diffusion and has potential to be used as a tuneable relaxation mechanism in future experiments in other defects which can be preferentially orientated with uniaxial stress.

Uniaxial stress was also used to investigate the migration of the ⟨001⟩ split-interstitial defect, R2, which is understood to migrate through the lattice by consecutive reorientation of the defect. The sample was annealed under [001] uniaxial stress to create an initially preferentially orientated population and the reorientation back to equilibrium was monitored by EPR during a second in situ anneal. An activation energy, 2.0(1) eV and an attempt frequency 3×10^{13} Hz for the migration of the defect was measured.

The electron and nuclear spin polarisation of $^{15}N_S^0$ and $^{15}N_3V^0$ has been explored by use of optically pumped EPR. The polarisation is found to be present for temperature up to 150 K and for optical excitation energies > 1.9 eV. Long lived nuclear polarisation of the nitrogen is found to continue after the optical excitation has ended. The decay of this polarisation allows measurement of a nuclear T_1 of 40(3) minutes through EPR. Optically pumped NMR showed that the spin polarisation spread to the bulk ^{13}C matrix of the diamond. Polarisation factors of -180(20) at room temperature and -480(30) at 240 K are reported. Given diamond's biocompatibility this potentially provides a route to microwave free hyperpolarisation of biological samples for NMR

Abbreviations

A & B	Prefactors for relaxation rates
B	Magnetic field
B_0	Static magnetic field
B_1	Microwave field
B_{mod}	Modulation field
β	inhomogeneity parameter
χ	Magnetic susceptibly
CVD	Chemical vapour deposition
CW-EPR	Continuous wave electron paramagnetic resonance
DNP	Dynamic nuclear polarisation
E_A	Activation energy
ELDOR	Electron electron double resonance
ENDOR	Electron nuclear double resonance
EPR	Electron paramagnetic resonance
ε	Polarisation factor
η	Filling factor
FID	Free induction decay
FT-EPR	Fourier transform electron paramagnetic resonance
FT-IT	Fourier transform infra-red
g	g-factor
γ_i	Gyromagnetic ratio of i
HPHT	High pressure high temperature
I	Quantum number for the nuclear spin
k_B	Boltzmann constant
LGR	Loop gap resonator
$\boldsymbol{\mu}_B$	Bohr magneton
MP-CVD	Microwave plasma chemical vapour deposition
NMR	Nuclear magnetic resonance
ω_{ij}	Transition between energy levels i and j
ω_B	Larmor frequency
PCD	Polycrystalline diamond
ppb	Parts per billion
ppm	parts per million
Q	Resonator Quality factor
RP-EPR	Rapid passage EPR
RP-EPR$^{(\mathrm{FM})}$	Field modulated rapid passage EPR
RP-EPR$^{(\mathrm{DD})}$	Direct detected rapid passage EPR
S	Quantum number for the electron spin
SNR	Signal to noise ration

SP-EPR	Slow passage EPR
T_1	Electron spin lattice relaxation
T_{1n}	Nuclear spin lattice relaxation
T_2	Electron spin spin relaxation
T_m	Electron phase memory
UV-Vis	Ultraviolet - visible
ZPL	Zero phonon line
$[hkl]$	Crystallographic direction
$<hkl>$	Set of equivalent crystallographic directions
(hkl)	Crystallographic plane
$\{hkl\}$	Set of equivalent crystallographic planes

Chapter 1

"They don't make diamonds the size of bricks."

-traditional[1]

1 Introduction

For much of history diamond has been of interest as a decorative item. Diamond's clarity and sparkle along with their scarcity have led them to become associated with wealth and power. The largest natural diamonds have become part of the crown jewels of royalty. The world's largest gem quality example, the 3106 ct Cullinan diamond, is part of the British crown jewels and the largest pink diamond, the 182 ct Daria-i-Noor, is part of the Iranian crown jewels. Alongside this there is an industry built around exploiting diamond for its mechanical properties, and growing industries surrounding its electrical and optical properties.

1.1 Structure and applications of diamond

Diamond, like graphite and graphene, is an allotrope of carbon [1]. All of these allotropes have very different properties, to understand the atomic and electron structure must be considered. The ground state of a carbon atom is the $1s^2 2s^2 2p^2$ electronic configuration. In graphite and graphene, the 2s and 2p orbitals form sp^2 hybridised orbitals, creating strong covalent bonds between neighbouring carbon in a hexagonal pattern. In the case of graphene these sheets exist as a 2D layer but in graphite, weak van der Waals forces attract layers together. For diamond the carbon orbitals are sp^3 hybridised orbitals and form bonds with four nearest neighbours in a tetrahedral geometry. The electron promotion in this process is energetically expensive, but the resultant electron sharing gives a completed electron shell making the final product energetically favourable [2].

---

[1] Author attributes it to W. Clulow.
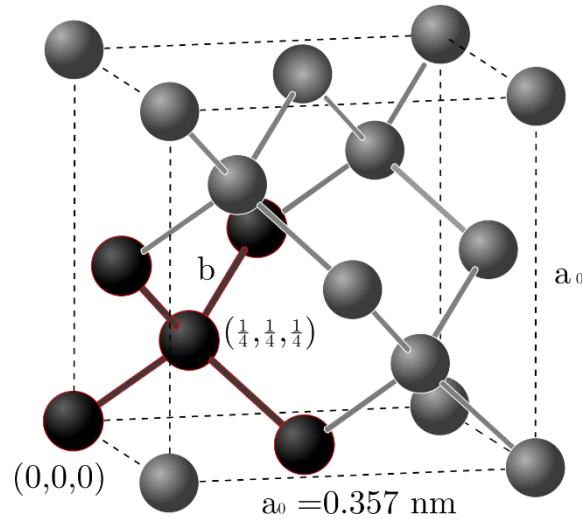
Figure 1-1 Diagram of the unit cell of diamond with side length of a_0 = 0.357 nm. The tetrahedral lattice structure is highlighted by the darker atoms with red outline. Adapted from [3].

The resulting crystal structure, shown in Figure 1-1, is described as two face centred cubic cells with one lattice displaced by $a_0/4$. The cubic unit cell constant, a_0, is 0.357 nm and the average C-C bond length is b=0.154 nm. This close packing creates an atomic density of 1.76×10^{23} cm^{-3} the highest of any solid. It follows that an impurity with concentration 1.76×10^{17} cm^{-3} has a concentration a 1 part per million (ppm).

The structure of diamond gives it unique properties, some of which are outlined in Table 1-1; it is these properties that make diamond a suitable material for many applications. The first industrial application of diamond was as an abrasive where it was bonded to grinding wheels at the start of World War Two [4] and abrasive applications remain the main market for synthetic diamond. Intrinsic diamond is an electronic insulator but a good thermal conductor making it an ideal material for a heat spreader in high power electronic devices [5].

Diamond is transparent over a wide range of frequencies and as such is often employed for optical windows [5]. There is also growing interest in the use of diamond in Raman lasers [6,7]. The potential for biocompatibility has led to research into the use of diamond as a scaffold for the reconstruction of bones [8,9]. Research into biological applications of diamond is at an early stage but diamond scalpels have been used for eye surgery for many years.

Properties of diamond		Ref
Semiconductor		
Bandgap	5.47 eV	[10]
Breakdown field	20 MV cm^{-1}	[10]
Electron mobility	4500 cm^2 V^{-1} s^{-1}	[10]
Hole mobility	3800 cm^2 V^{-1} s^{-1}	[10]
Good insulator	$>10^{13}$ Ω cm	[11]
High thermal conductivity	22.3 W cm^{-1} K^{-1} (natural) 33.2 W cm^{-1} K^{-1} (^{13}C enriched)	[12]
Low thermal expansion	0.8(1) x 10^6 K	[11]
Highest Young's modulus	1223 GPa	[13]
Bulk modulus	443 GPa	[14]
Extremely hard Mohs hardness	Mohs 10	[15]
Low coefficient of friction	0.1	[11]
Chemically inert & biologically compatible		[9]

Table 1-1 List of some properties of diamond.

The electronic properties of diamond have come under increased interest in recent years, boron doping is used to increase the conductivity of diamond opening up many applications. High breakdown voltage and hole mobility may be employed to create efficient high power active electronics [16,17]. Diamond's radiation hardness makes devices capable of working for long periods, under heavy doses of radiation without degradation in performance and this has been harnessed to create radiation detectors [18]. Its chemically stable nature offers potential in becoming a reliable sensor in extreme environments for temperature, pH and in electrochemistry [19–21]. The potentially low spin density in the diamond lattice provides long paramagnetic relaxation times [22–24], and can be used as a host material for point defects that can be used as quantum qubits or in high resolution magnetometry [25,26].

1.1.1   Classification of diamonds

The perfect diamond lattice consists only of carbon atoms arranged in a crystal structure, anything deviating from this is considered a defect. Defects fall broadly into two categories: point defects and extended defects [27]. For the purposes of this thesis a point defect will be considered to be any defect which does not significantly exceed the unit cell; structures such as a vacancy site, substitutional impurity or cluster of impurities are considered point defects. An extended defect is one that is significantly larger than the unit cell; large voids, dislocations

Diamond Type			Description
Type I			contain nitrogen concentration measurable by IR ($> \sim 1$ ppm)
	Ia		Nitrogen forms aggregate clusters
		IaA	Contains nitrogen as A-centres
		IaB	Contains nitrogen as B-centres
	Ib		Contains single substitution of nitrogen.
Type II			contain nitrogen concentration not measurable by IR ($<\sim 1$ ppm)
	IIa		No detectable boron
	IIb		Contain boron impurities

Table 1-2 The classification of diamond adapted from [29].

and grain boundaries are part of this category. This thesis is concerned with the properties of point defects.

It is a truth universally acknowledged that not all diamonds are created equal. In the early part of the 20th century it was noticed that a set of absorption lines in the IR spectra of diamonds was not always present. Robertson *et al* proposed that diamond could be classified according to this property; referring to diamonds with these IR features as Type I, and the smaller set which did not, Type II [28]. These features were later identified as being caused by the presence of nitrogen.

This system was later refined by Sutherland to include the aggregated state of the nitrogen and later to include the presence of boron in the lattice [29]. Diamonds could now be classified into five categories depending on the nature of the impurities they contain as outlined in Table 1-2. The first sub division, Type I, splits into samples with aggregates of nitrogen, Type Ia, and Type Ib containing substitutional nitrogen or C-centres, (N_s). Type Ia is further refined by the nature of the aggregates present: Type IaA has next neighbours pairs (A-centres) [30] and Type IaB where the nitrogen forms B-centres (four nitrogen atoms about a vacancy) [31]. Samples containing significant concentrations of A- and B-centres are referred to as Type IaAB diamonds. The purer Type II samples can be subdivided into two categories depending on the detectable presence of boron in the sample. If substitutional boron is detected the sample is classified as a Type IIb. When neither nitrogen or boron are detectable the sample is a Type IIa.

1.2 Motivation for study

The primary impurity in synthetic diamond is nitrogen. Measurement of the incorporation of impurities aids the understanding of nitrogen's effect on the properties of the final material [32] and furthermore offers insight into growth conditions [33,34]. The recent improvements in the production of highly pure synthetic diamonds have challenged the detection limits of classical techniques [35]. Material with nitrogen concentrations below 100 ppb are impossible to reliably measure with non-destructive optical techniques and even destructive techniques such as SIMS and combustion are unable to provide accurate results [36–41]. Optically detected magnetic resonance is capable of single detection of some defects [42,43] but these are an exciting exception rather than the rule.

Electron paramagnetic resonance, EPR, offers an attractive solution to detection at these low concentration limits. In Type IIa samples nitrogen is predominately substitutional and in the neutral charge state, due to the lack of electron acceptors, therefore paramagnetic. EPR is non-destructive and offers potential detection of sub ppb concentrations. In practice the stiff, spin diffuse lattice of diamond creates long relaxation times, therefore saturation effects limit the measureable concentrations well above 1 ppb. The work presented here will build on the use of field modulated rapid passage EPR, RP-EPR$^{\text{(FM)}}$, previously shown to be quantitative [44,45], as a technique to negate saturation effects and assess low concentrations.

The drive towards using diamond for quantum devices has centred around a number of functional defects that show optically effected spin polarisation states [46,47]. Long relaxation times that are a problem for EPR measurement are excellent potential sources of coherent memory in quantum applications. As such, the understanding of relaxation mechanisms is important to enable the tailoring of defect properties. In this work, uniaxial stress is used as a perturbation to investigate the relaxation mechanisms of N_S^0 and the migration of R2. The possibilities offered by coupled systems, either as a gate in quantum devices or as a method for reading out spin states of a separate defector, are of interest [48]. Optically pumped magnetic resonance will also be used to investigate the properties of two potentially coupled systems $^{15}N_S^0$ and $^{15}N_3V^0$.

1.3 Thesis outline

The remainder of this thesis contains three background chapters and four chapters of results:

- In addition to the background information in this chapter, Chapter 2 provides a synopsis of relevant previous work. It covers the production of diamond and the history of pertinent defects.

- Chapter 3 provides the theoretical basis for experiments performed and outlines the theory underpinning magnetic resonance and optical techniques used in the results chapters. A brief history of EPR is also presented.

- The final background chapter, Chapter 4, provides information regarding the experimental aspects of EPR and other techniques used. The spectrometers and equipment used in this work are detailed and key points regarding experimental procedures are outlined.

- Chapter 5 explores the quantification of nitrogen in diamond using EPR. The use of RP-EPR$^{\text{(FM)}}$ to lower detection limits is presented. Some of the challenges posed by large or high concentration samples are also investigated.

- The use of high pressure EPR to investigate N_S^0 is presented in Chapter 6. The work focuses on the rotation of the defect within the lattice and its impact on relaxation times.

- Chapter 7 covers the optically induced spin polarisation of the $^{15}N_S^0$ and $^{15}N_3V^0$ defects. This work not only investigates the conditions required for optimal electron spin polarisation but also demonstrates that this spin polarisation is transferred to the bulk ^{13}C matrix of the sample by use of NMR.

- The final experimental chapter discusses the migration of the R2 defect in diamond. Chapter 8 covers the use of annealing under uniaxial stress to create a preferentially oriented population which can then be used to measure the energy associated with reorientation and migration.

- In closing, Chapter 9 offers a summary of the presented work.

1.4 References

[1]   A. Hirsch, Nat. Mater. 9, 868 (2010).

[2]   G. Davies and T. Evans, Proc. R. Soc. London 328, 413 (1972).

[3]   A. M. Edmonds, Magnetic Resonance Studies of Point Defects in Single Crystal Diamond - PhD Thesis, University of Warwick, 2008.

[4]   K. Anderson, MRS Bull. September, 66 (1994).

[5]   R. S. Balmer, J. R. Brandon, S. L. Clewes, H. K. Dhillon, J. M. Dodson, I. Friel, P. N. Inglis, T. D. Madgwick, M. L. Markham, T. P. Mollart, N. Perkins, G. Scarsbrook, D. J. Twitchen, A. J. Whitehead, J. J. Wilman, and S. M. Woollard, J. Phys. Condens. Matter 21, (2009).

[6]   A. Sabella, J. Piper, and R. P. Mildren, Opt. Lett. 35, 3874 (2010).

[7]   H. Liu, S. Reilly, J. Herrnsdorf, E. Xie, V. G. Savitski, A. J. Kemp, E. Gu, and M. D. Dawson, Diam. Relat. Mater. 65, 37 (2016).

[8]   K. Fox, J. Palamara, R. Judge, and A. D. Greentree, J. Mater. Sci. Mater. Med. 24, 849 (2013).

[9]   R. J. Narayan, R. D. Boehm, and A. V. Sumant, Mater. Today 14, 154 (2011).

[10] S. Hadlington, IEE Rev. 51, 30 (2005).

[11] J. E. Field, *The Properties of Natural and Synthetic Diamond* (Academic Press, London, 1992).

[12] T. R. Anthony, W. F. Banholzer, J. F. Fleischer, L. Wei, P. K. Kuo, R. L. Thomas, and R. W. Pryor, Phys. Rev. B 42, 1104 (1990).

[13] S. F. Wang, Y. F. Hsu, J. C. Pu, J. C. Sung, and L. G. Hwa, Mater. Chem. Phys. 85, 432 (2004).

[14] H. J. McSkimin, J. Appl. Phys. 24, 988 (1953).

[15] S. Mukherjee, *Applied Mineralogy: Application in Industry and Enviroment* (Springer Science & Business Media, 2012).

[16] S. Shikata, Diam. Relat. Mater. 65, 168 (2016).

[17] O. A. Williams, R. B. Jackman, C. Nebel, and J. S. Foord, Diam. Relat. Mater. 11, 396 (2002).

[18] M. Franklin, A. Fry, K. K. Gan, S. Han, H. Kagan, S. Kanda, D. Kania, R. Kass, S. K. Kim, R. Malchow, F. Morrow, S. Olsen, W. F. Palmer, L. S. Pan, F. Sannes, S. Schnetzer, R. Stone, Y. Sugimoto, G. B. Thomson, C. White, and S. Zhao, Nucl. Inst. Methods Phys. Res. A 315, 39 (1992).

[19] P. Neumann, I. Jakobi, F. Dolde, C. Burk, R. Reuter, G. Waldherr, J. Honert, T. Wolf, A. Brunner, J. H. Shim, D. Suter, H. Sumiya, J. Isoya, and J. Wrachtrup, Nano Lett. 13, 2738 (2013).

[20] Z. J. Ayres, A. J. Borrill, J. C. Newland, M. E. Newton, and J. V. Macpherson, Anal. Chem. 88, 974 (2016).

[21] J. Svítková, T. Ignat, Ľ. Švorc, J. Labuda, and J. Barek, Crit. Rev. Anal. Chem. 46, 248 (2016).

[22] B. Grotz, M. Hauf, M. Dankerl, B. Naydenov, S. Pezzagna, J. Meijer, F. Jelezko, J. Wrachtrup, M. Stutzmann, F. Reinhard, and J. A. Garrido, Nat. Commun. 3, 729 (2012).

[23] K. D. Jahnke, B. Naydenov, T. Teraji, S. Koizumi, T. Umeda, J. Isoya, and F. Jelezko, Appl. Phys. Lett. 101, (2012).

[24] L. J. Rogers, K. D. Jahnke, M. H. Metsch, J. M. Binder, T. Teraji, H. Sumiya, J. Isoya, M. D. Lukin, P. Hemmer, and F. Jelezko, Phys. Rev. Lett. 113, 1 (2014).

[25] H. Clevenson, M. E. Trusheim, T. Schroder, C. Teale, D. Braje, and D. Englund, Nat. Phys. 11, 393 (2015).

[26] J. R. Maze, P. L. Stanwix, J. S. Hodges, S. Hong, J. M. Taylor, P. Cappellaro, L. Jiang, M. V. G. Dutt, E. Togan, A. S. Zibrov, A. Yacoby, R. L. Walsworth, and M. D. Lukin, Nature 455, 644 (2008).

[27] M. Lannoo and J. Bourgoin, *Point Defects in Semiconductors I: Theoretical Aspects*, 1st ed. (Springer, 1981).

[28] R. Robertson, J. J. Fox, and A. E. Martin, Philos. Trans. R. Soc. London 23253, 463 (1934).

[29] G. B. B. M. Sutherland, D. E. Blackwell, and W. G. Sinmeral, Nature 174, 901 (1954).

[30] G. Davies, Whitehall Pap. 3, 35 (1976).

[31] R. M. Chrenko, R. E. Tuft, and H. M. Strong, Nature 270, 141 (1977).

[32] H. Godfried, WO 2004.0464271 (2004).

[33] Y. V. Babich, B. N. Feigelson, D. Fisher, A. P. Yelisseyev, V. A. Nadolinny, and J. M. Baker, Diam. Relat. Mater. 9, 893 (2000).

[34] Z. Yiming, F. Larsson, and K. Larsson, Theor. Chem. Acc. 133, 1 (2014).

[35] A. Tallaire, A. T. Collins, D. Charles, J. Achard, R. Sussmann, A. Gicquel, M. E. Newton, A. M. Edmonds, and R. J. Cruddace, Diam. Relat. Mater. 15, 1700 (2006).

[36] A. T. Collins, Phys. B Condens. Matter 185, 284 (1993).

[37] F. De Weerdt and A. T. Collins, Diam. Relat. Mater. 17, 171 (2008).

[38] N. Fujiyama, A. Karen, D. B. Sams, R. S. Hockett, K. Shingu, and N. Inoue, Appl. Surf. Sci. 203–204, 457 (2003).

[39] J. E. Butler, Diam. Conf. (2015).

[40] S. R. Boyd, A. Rejou-michel, and M. Javoy, 6, 297 (1995).

[41] K. Ohno, F. Joseph Heremans, L. C. Bassett, B. A. Myers, D. M. Toyli, A. C. Bleszynski Jayich, C. J. Palmstrom, and D. D. Awschalom, Appl. Phys. Lett. 101, (2012).

[42] E. Neu, D. Steinmetz, J. Riedrich-Muller, S. Gsell, M. Fischer, M. Schreck, and C. Becher, New J. Phys. 13, (2011).

[43] F. Jelezko and J. Wrachtrup, J. Phys. Condens. Matter 16, R1089 (2004).

[44] D. G. Mitchell, M. Tseitlin, R. W. Quine, V. Meyer, M. E. Newton, A. Schnegg, B. George, S. S. Eaton, and G. R. Eaton, Mol. Phys. 111, 2664 (2013).

[45] B. L. Cann, Magnetic Resonance Studies of Point Defects in Diamond - PhD Thesis, University of Warwick, 2005.

[46] C. Wang, C. Kurtsiefer, H. Weinfurter, and B. Burchard, J. Phys. B At. Mol. Opt. Phys. 39, 37 (2006).

[47] M. W. Doherty, V. V. Struzhkin, D. A. Simpson, L. P. McGuinness, Y. Meng, A. Stacey, T. J. Karle, R. J. Hemley, N. B. Manson, L. C. L. Hollenberg, and S. Prawer, Phys. Rev. Lett. 112, 47601 (2014).

[48] H. Wang, C. S. Shin, Seltzer, C. E. Avalos, A. Pines, and V. S. Bajaj, Nat. Commun. (2014).

Chapter 2

2 Introduction

purpose of this chapter is to offer a brief historical perspective on diamond research and the field of electron paramagnetic resonance, EPR. An exhaustive review is beyond the scope of this thesis but this chapter aims to cover the background necessary to understand later results and put them into context. An overview of synthetic diamond production is followed by a more in-depth look at the defects that are studied in this thesis. Finally, a brief history of EPR and its key techniques is presented.

2.1 Diamond synthesis

Under atmospheric conditions the lowest energy state of carbon is graphite (Figure 2-1 The pressure temperature phase diagram of carbon showing the relevant area for diamond growth adapted from [4]. The pressure of CVD growth has been exaggerated for clarity adapted from [2].). Therefore, for diamonds to be grown either the pressure and temperature need to be altered so that the diamond structure becomes thermodynamically stable, or chemical kinetics must be altered to allow diamond to be produced in the graphite stable region. The first approach is used in high pressure high temperature, HPHT, and the latter is employed in chemical vapour deposition, CVD, synthesis. Diamonds may also be produced through detonation and impact (HPHT for a short time) but these approaches will not be discussed here [1]. This work considers only growth of single crystal diamond; reviews of polycrystalline diamond and nanocrystalline diamond are available [2].

2.1.1 HPHT

The first reliable report of laboratory grown diamond was created using the HPHT method in 1955 [3]. All HPHT diamond growth reproduces the thermodynamic conditions at which natural diamonds are grown in the lithosphere. The conditions for stable diamond growth can
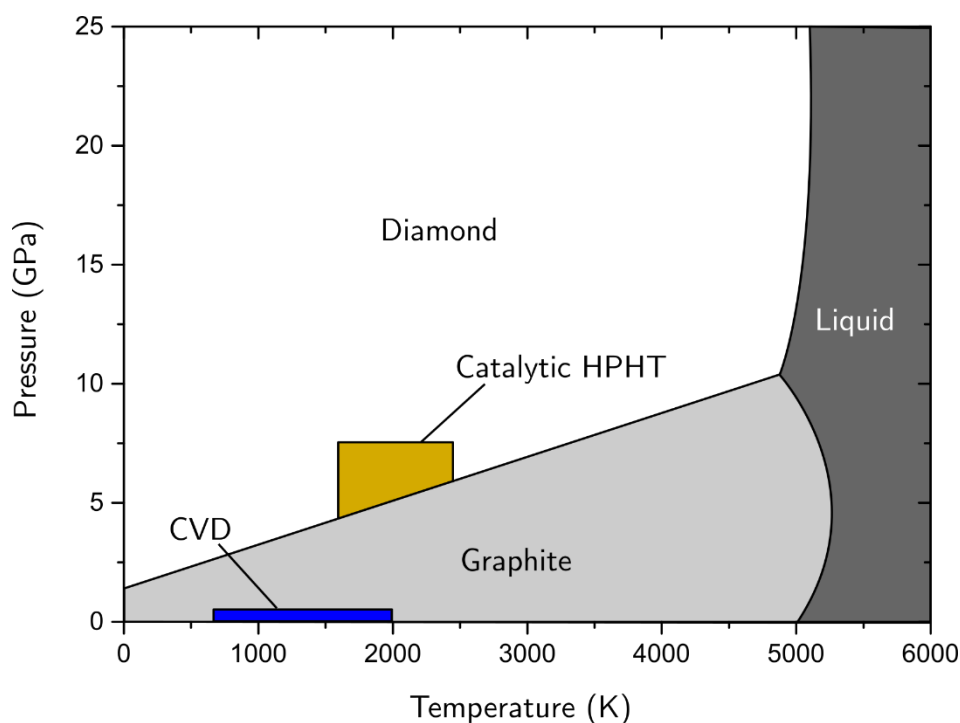
Figure 2-1 The pressure temperature phase diagram of carbon showing the relevant area for diamond growth adapted from [4]. The pressure of CVD growth has been exaggerated for clarity adapted from [2].

be seen in Figure 2-1 The pressure temperature phase diagram of carbon showing the relevant area for diamond growth adapted from [4]. The pressure of CVD growth has been exaggerated for clarity adapted from [2].; the conditions of growth typically used in the commercial growth of HPHT diamonds using metal solvent are highlighted.

During synthetic diamond growth temperatures in the range of 1200-1700 °C and pressures of 5-6 GPa are typically used [5,6], but higher temperatures and pressures can be employed [7]. For single crystal HPHT growth, seeds are placed inside a capsule containing a metal solvent along with a source of high purity carbon. Either a temperature or a solubility gradient is used to transfer the high purity carbon to the seed. The advantage of the metal solvent is that it allows a lower temperature to be used in diamond growth than could be achieved through non-catalytic growth [4]. The solvents used are typically transition metals; iron, nickel, cobalt or alloys of these metals [4,8].

To achieve the high pressures required a number of different types of apparatus are available, including belt presses, split sphere presses and cubic presses. It is beyond the scope of this review to fully cover HPHT growth and in depth reviews are available [8].

Diamonds grown by the HPHT method are prone to the incorporation of nitrogen during growth. Nitrogen is incorporated into the growth chemistry from a number of sources; impurities in the growth media (graphite, metal solvent), from atmospheric gases or from adsorbates on the capsule [6]. Unless efforts are made to control nitrogen content, concentrations of 100-300 ppm are typical, although concentrations up to 3000 ppm have been reported [9]. Nitrogen is predominantly incorporated substitutionally in the diamond lattice as N_S. When the growth temperature is high enough aggregation into nitrogen pairs, A-centres, occurs [10].

The growth morphology of the diamond is determined not only by the growth chemistry but by temperature and pressure [11]. Morphology is important when considering impurities, as incorporation rates alter between growth sectors; for example, under normal growth conditions highest nitrogen incorporation is found in {111} growth sectors followed by the {001}, {113} and {110} growth sectors [12]. Thus incorporation of nitrogen has a temperature dependence with higher temperatures increasing uptake in the {111} and {001} growth sectors [13]. The uptake of nitrogen was investigated through growth zoning experiments, where the conditions of growth were modified during the growth process. These experiments linked growth rate with uptake of nitrogen samples showed increased nitrogen levels in the faster growing sectors [14]. The amount of nitrogen in the final lattice can be controlled by the addition of a nitrogen "*getter*" into the capsule, typically Ti or Al which have a strong affinity to nitrogen [15]. This reduces the uptake of nitrogen at the cost of potential inclusion of the "*getter*" into the end product [16]. This approach has been used to create 10 ct synthetic colourless gemstones [17].

It is also possible to control incorporation impurities by evacuation and outgassing the sealed growth capsule before growth begins [6]. This process can be used to reduce the nitrogen uptake in diamonds and may also be exploited for intentional doping of the material. An example of this doping would be the creation of isotopically enriched samples by using isotopically enriched material in the growth capsule. Diamonds with ≥95% ^{15}N enrichment

have been grown and samples with altered ratios of carbon isotopes have been demonstrated [18,19].

2.2.1 CVD

Where HPHT attempts to mimic the natural process of diamond creation, CVD operates in conditions far outside the thermodynamically stable region for diamond growth (Figure 2-1). To achieve growth CVD utilises chemical kinetics which favour sp^3 growth over sp^2. This process was first demonstrated in 1962 [20]. During CVD growth source gases containing carbon and hydrogen are disassociated to form radicals. Typical gases are H_2 and CH_4 with a much higher percentage of H_2 [21]. The carbon radicals are laid down epitaxially onto a seed material forming both sp^3 and sp^2 material. The hydrogen radicals help growth, stabilising the sp^3 growth by terminating the surface. The growth surface is then reactivated by hydrogen mediated abstraction of a surface hydrogen, exposing a carbon which may then bond to an incoming carbon radical or another hydrogen radical [22].

There are a number of methods for dissociating the source gases including direct heating with a hot filament and microwave plasma heating, MP-CVD. Hot filament is the simplest method of CVD growth. A filament, classically tungsten, is heated to 2000 °C and the source gases, typically methane and hydrogen, flow over it and are dissociated before deposition of diamond on a cooler plate below. There are problems associated with this growth method: growth rates are reduced if the tungsten reacts with the methane, inhibiting the disassociation of source gases and slowing growth rates, and samples are susceptible to incorporation of the filament material [23].

MP-CVD of diamond is the focus of much modern research and has produced the highest purity material [24]. MP-CVD operates in a wide parameter space with source gasses, temperature, pressure, plasma shape, power density, dopant gasses and substrate material all influencing growth [25]. A typical growth uses microwaves of frequency 2.45 GHz, using H_2 and CH_4 as source gases at temperatures between 750–1500 °C [26]. The growth rates for CVD

growth are typically between 1-150 µm/h with the high growth rates producing lower quality material. Reviews of the current state of MP-CVD of diamond are available [25,27].

Single crystal diamond is normally grown on a diamond substrate, homoepitaxial growth. This approach gives high quality crystal but limits the size of samples grown due to the availability of large single crystal diamond substrate; typically, the maximum size of a sample is 1 cm across. An alternative approach is to grow onto layered non-diamond material, heteroepitaxial growth. These materials need to have a close match to the diamond lattice parameter and must not melt during CVD growth, for example an iridium layer on silicon Si [28]. This process allows much larger wafers, 100 mm diameter [29], to be produced but the material is highly strained [30]. A further approach to creating larger substrates is to clone a sample and create a mosaic of samples with the equivalent crystalline states which have a homoepitaxial layer grown on top. This has produced samples 25 mm across with reduced mechanical strain compared to heteroepitaxial grown samples but the substrate boundaries cause dislocations into the material [31].

The material used for the substrate has a large effect on the grown material. Any surface defects on the substrate propagate through the grown material creating a high density of dislocations [32]. The strain of these dislocations causes birefringence greatly affecting the optical properties of the material [33]. Plasma etching the material prior to growth can greatly reduce the density of dislocations, as can growth of low strain HPHT substrates [34]. The highest quality optical grade material is currently grown {001} HPHT material and with a small amount of nitrogen in the growth chemistry. These conditions reduce the dislocation density and therefore reduces the lattice strain [35].

As with HPHT, nitrogen remains the main impurity incorporated during CVD growth despite a low incorporation probability, $\sim$0.01-0.001% [36]. Although, in theory, it is possible to control all the gases used in CVD growth, it is a great challenge to exclude all nitrogen from the growth chamber and source gases. The purest reported samples have a $<$0.2 ppb concentration of N_S^0 [24]. A small amount of nitrogen can alter the morphology of the sample and increase the growth rate by a factor of 2.5 [24]; but samples grown at fast rates often have a brownish

colour which can be reduced by heat treating at 1600 °C [37]. High concentrations of nitrogen used during growth have been shown to have an unfavourable effect on the material grown [38].

2.2 Defects in diamond

Any structure or impurity that deviates from the perfect diamond lattice is a defect. These defects can be large structures such as dislocations, inclusions or twinning or may be point defects such as impurities, vacancies and interstitials. This work is focused on point defects in diamond. There is a myriad of such defects and this section will cover the background for defects that are relevant to later work.

2.3.1 Radiation damage

When the diamond lattice is irradiated with particles of sufficiently high energy, carbon atoms can be displaced from the lattice site. The exact nature of the damage caused by the irradiation depends on the conditions of irradiation and the starting material but in general vacancy interstitial pairs are created in the lattice. The study of the defects created in this manner has been conducted with many spectroscopic techniques and a large number of defects have been identified.

2.2.1.1 Vacancies

The neutral vacancy, V^0, has a zero phonon line, ZPL, that is observed as a doublet at 1.673 eV (741.1 nm) and 1.665 eV (744.6 nm) which are collectively labelled GR1 along with the vibronic side band [39]. There is also a series of features between 2.880-3.010 eV labelled GR2-8 that have been assigned to electronic transition of the neutral vacancy [40,41]. Uniaxial stress measurements of GR1 in combination with theoretical analysis determined the defect had T_d symmetry and the doublet corresponded to transitions between a ^1E ground state and a $^1T_2$ excited state [42,43].

The ND1 optical absorption feature at 3.150 eV (393.6 nm) was determined to also have T_d symmetry by uniaxial stress [44]. Davies went on to argue that ND1 was the negative charge

state of the vacancy, V^-, by comparison to GR1 in nitrogen rich diamonds [45]. V^- has a $^4A_2$ ground state that is S=3/2 and is EPR active [46]. The ground state of V^0 is S=0 [47] and as such is EPR silent. With optical illumination of energy greater than 3.1 eV the $^5A_2$ excited state of the defect that is S=2 has been observed in EPR [48].

The migration energy of both V^- and V^0 has been determined as 2.3(3) eV through isothermal anneals [49,50]. The anneals revealed an intermediate step at 1.7(2) eV that corresponded to a 15% drop in GR1; this was interpreted as the recombination of vacancies with local interstitials [50,51]. Once the vacancy becomes mobile it can aggregate with other impurities and with itself forming divacancies, in high purity low strain material. The divacancy has been identified as the source of the EPR spectrum called R4/W6 and has been correlated to the TH5 optical absorption band [52,53].

2.2.1.2 $\langle 001 \rangle$-split interstitial

There is potentially a family of self-interstitial related defects that could occur in diamond but theory suggested that the $\langle 001 \rangle$-split interstitial, $I^0_{\langle 001 \rangle}$, is the configuration with the lowest energy [54].

The R2 EPR spectrum was initially reported as the c system, in electron irradiated Type IIa diamonds by Faulkner in 1962 [55]. The spectrum has broad EPR lines and is axially symmetric around $\langle 111 \rangle$ unlike many irradiation related defects. An S = 1 defect, the EPR signal has an unusually large zero field splitting, D/h = ±4173(3) MHz. The spectrum arises from an excited triplet state 50 meV above the ground singlet state [56].

R2 also has very large line widths, up to ~8 mT, but a narrow line width on the $M_s = 2$ transition means the broadening is unlikely to be relaxation related and such a wide line cannot be accounted for by dipolar interactions. This broadening varies the orientation and is considered to be the result of a distribution of D values for the defect [56]. If this was the mechanism, a temperature dependence to the broadening would be expected, such as that seen

in N_S^0, but no evidence of this has been witnessed between 77 K and 650 K. Temperature measurements are impossible below this range due to the depopulation of the excited state that gives rise to R2, and above this range the defect is destroyed.
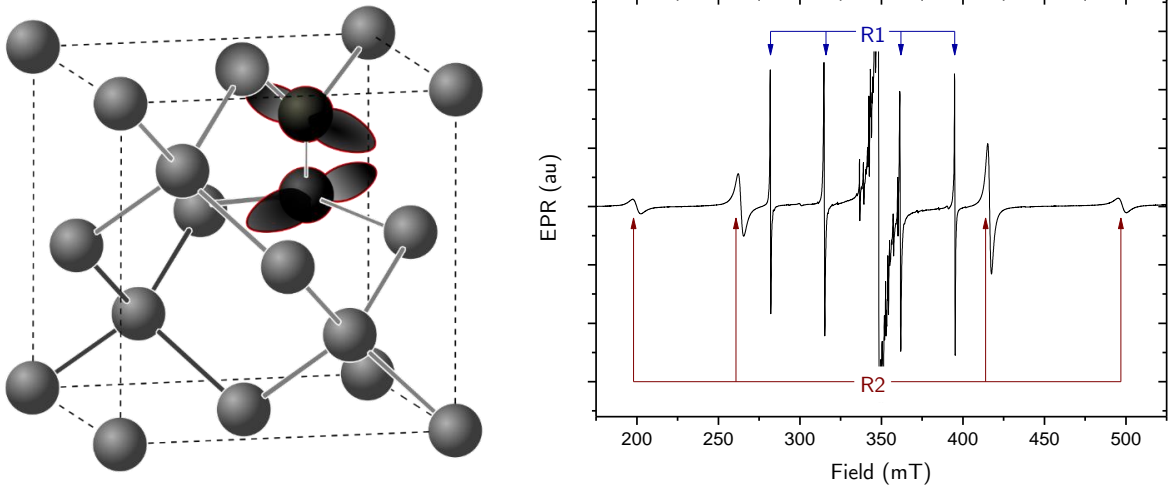
Figure 2-2   Left, the structure of ⟨001⟩-split interstitial, R2, defect, the interstitial atoms are darker and highlighted in red. Right. An EPR spectrum of an irradiated diamond with the R1 and R2 spectra highlighted.

The geometric structure of the defect that gave rise to the R2 spectrum remained a subject of debate for 40 years with two proposed models: the compressed vacancy [54] and $I_{\langle 001 \rangle}^0$ [57]. The $I_{\langle 001 \rangle}^0$ was supported by *ab initio* calculations using local-density-functional pseudopotential theory predictions that it was the only stable structure for the interstitial [58]. The $I_{\langle 001 \rangle}^0$ configuration was eventually confirmed experimentally by Hunt using the angular dependence of the EPR spectrum [56]. The $I_{\langle 001 \rangle}^0$ can be seen in Figure 2-2 and is a D_{2d} defect that consists of two central carbon atoms sharing a site. These two carbons have a sp^2 bond between them and non-bonding π orbitals normal to the plane of the sp^2 bond. In addition to the R2 EPR spectrum, $I_{\langle 001 \rangle}^0$ also has two associated optical absorption features at 1.685 eV (735.8 nm) and 1.859 eV (666.9 nm) [56,59,60].

2.2.1.3 Other interstitial defects

The di-⟨001⟩-split interstitial can be created through the aggregation of mobile interstitials during irradiation [61]. R1 was first observed in EPR in electron irradiated type II diamonds [55] but has also been seen in type I material but at a lower production rate [62].

R1 was assigned as the nearest neighbour di-⟨001⟩-split interstitial by study of the ^{13}C EPR spectrum. The R1 defect has C_{1h} symmetry and is S=1. It has electrons in parallel non-bonding orbitals perpendicular to the {110} plane of the defect.

R1 is formed even if irradiation is carried out at temperatures below 100 K [63] indicating that interstitials are mobile during irradiation even at low temperatures. To explain this a hypothetical highly mobile interstitial, I^*, was assumed to be present during the anneal [50].

As well as the nearest neighbour di-⟨001⟩-split interstitial there is also the Humble or next nearest neighbour configuration of the di-⟨001⟩-split interstitial. DFT calculations predict that the Humble interstitial is a lower energy configuration than R1 by 0.7 eV [64]. The Humble interstitial is $S = 0$ but has been correlated with the optical absorption spectrum, 3H, which has a ZPL at 2.465 eV (503.4 nm) [64]. 3H is created by electron irradiation and its production increases linearly with concentration of A-centres and linearly decreases with concentration of B-centres [65]. There is increased production of 3H with irradiation at 80 K compared to room temperaturee irradiation [66].

2.4.1 Nitrogen in diamond

2.2.1.4 Single substitutional nitrogen

Single substitutional nitrogen in the neutral charge state, N_S^0, is possibly the most common impurity in synthetic diamond. Nitrogen enters the lattice substitutionally during growth, having been present during the growth process. Nitrogen is either intentionally used in growth chemistry to increase growth rates [38,67,68] or is incorporated from impurities in the growth gases.

The geometric structure of N_S^0 is simple with the nitrogen replacing carbon on a lattice site and bonding with the four nearest neighbours (Figure 2-3). In the neutral charge state, the nitrogen has one unpaired electron which is accommodated in an anti-bonding orbital with one of the neighbours, the unique carbon. The bond between the nitrogen and unique carbon
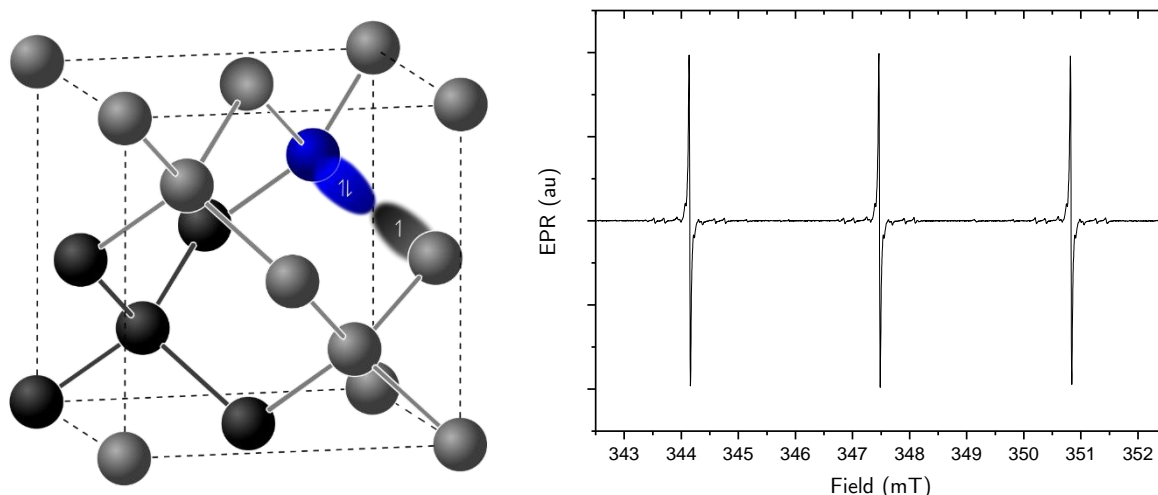
Figure 2-3 Left, the structure of the N_s^0. Nitrogen atom is represented in blue. Right, An experimental spectrum of a diamond containing 1 ppm of N_s^0 with B_0 aligned along the [001] crystalline direction.

is elongated by approximately 25-28% and the remaining C-N bonds shrink by ~3% [69–71]. The consequent reduction of symmetry from T_d to C_{3v} was confirmed by EPR [72,73]. The unpaired electron is accommodated into any one of the four possible C-N bond anti bonding orbitals and can relax into any of the ⟨111⟩ directions. In the absence of local lattice strain, the energy of each orientation of the defect will be equivalent, therefore an equal population in all orientations is found. It is possible for the elongated C-N bond to reorient between sites either by hopping at high temperatures or tunnelling at moderate/low temperatures between sites [74–76].

Initial EPR reports of N_S^0, commonly known as P1[2], were from work using natural diamonds in 1959 by Smith *et al.* [73]. The EPR signals of both the ^{13}C structure and "*forbidden*" transitions were later identified in EPR by Loubser [77]. Subsequently 8 different ^{13}C sites have been identified experimentally showing good agreement to predictions from *ab initio* calculations [72,78,79].

Substitutional nitrogen can also be found in the positive charge state, N_S^+. N_S^0 creates a deep lying donor state and can donate an electron to nearby defects. N_S^+ is a S=0 defect and as such cannot be assessed with EPR, however, it does give rise to an absorption line at 1332 cm^{-1}, and is associated with two additional features at 905 cm^{-1} and 1046 cm^{-1} [80]. There is also

---

[2] Poughkeepsie one/Paramagnetic one

some evidence of the existence of N_S^- but it remains unclear if this a stable charge state for the defect [81].

2.2.1.5 Nitrogen related aggregates

Annealing of the diamond above 1950 K for extended periods creates A-centres; a complex of two neighbouring nitrogen atoms [10]. The A-centre has features between 1050-1330 cm^{-1} with a prominent peak at 1282 cm^{-1}. The rate of aggregation of nitrogen is increased by the presence of vacancies in the lattice allowing the formation of A-centres at lower temperatures [82].

There is a family of vacancy nitrogen complexes ($N_m V_n$) in diamond. One of the more common is the B-centre which is found after further heat treatment of samples containing A-centres. The B-centre consists of four nitrogen atoms surrounding a vacancy, $N_4 V$, and has a prominent feature at 1332 m^{-1} [70]. The NVN^0 defect has been observed in EPR [48] as well as the H3 optical absorption feature, and the H2 optical has been confirmed as arising from NVN^- [83].

2.2.1.6 Nitrogen vacancy

The most well-known nitrogen related point defect in diamond is probably the nitrogen vacancy centre, NV (Figure 2-4). Du Preez observed that an absorption band around 1.945 eV (637 nm) appeared in samples that had been irradiated and annealed to 900 K [84]. Uniaxial stress measurements determined that the defect had C_{3v} symmetry and ZPL at 1.945 eV originated from a transition between an A ground state and excited E state [85]. The absorption was suggested as originating from a vacancy next to a substitutional nitrogen.

EPR of diamonds that had received similar treatment to that used by du Preez, found a new EPR centre. This centre was S=1, I=1 with a zero field splitting of 2.88 GHz. A C_{3v} symmetry was determined for the defect by assignment of three equivalent carbon atom positions from the ^{13}C hyperfine structure [86]. From these results the centre was thought to originate from
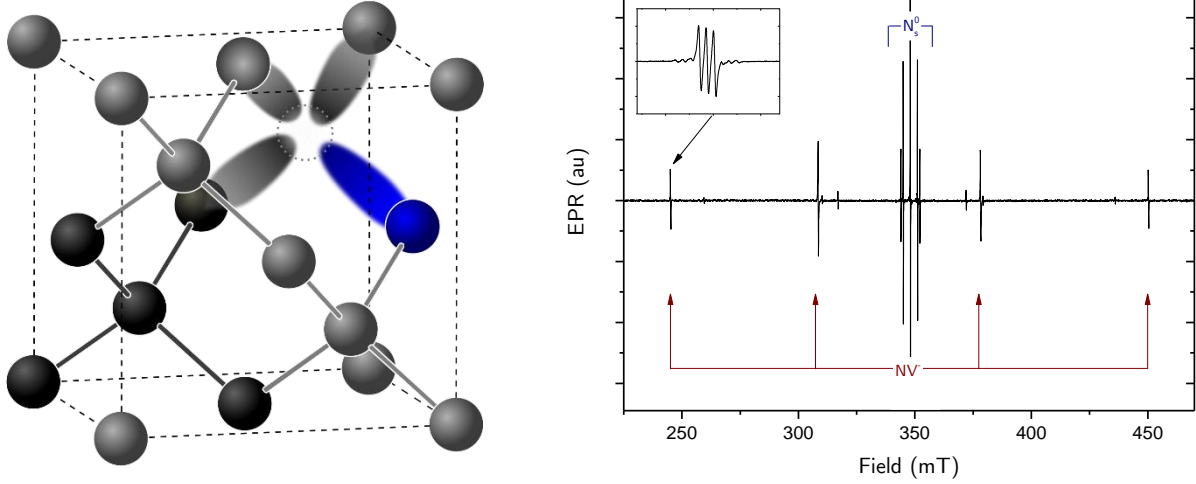
Figure 2-4 Left, the structure of NV. Nitrogen atoms are shown in blue and the dotted feature represents a vacancy. Right, an experimental EPR spectrum of NV^- with B^0 aligned along [111] crystallogrpahic direction. Inset shows a zoom- in of the lone site and shows the nitrogen hyperfine splitting.

the NV defect. This assumption was confirmed by two laser hole burning experiments which found antiholes at ±2.88 GHz of the EPR signal with the 1.945 eV line [87].

A further absorption band at 2.156 eV (575 nm) was observed in type Ib diamond that had undergone similar irradiation and anneal treatments [88]. Uniaxial stress measurement of the 2.156 eV ZPL determined it was from a transition between an E to A state of a C_{3v} symmetry defect [89]. A correlation was established between the 1.945 eV and 2.156 eV features and it was reported that an increase in radiation led to a sudden increase in the 2.156 eV [90]. The 1.945 eV and 2.156 eV features were assigned to NV^- and NV^0 respectively. The argument behind this was that at low irradiation doses after the combination of V^0 and N_S^0 into NV^0 centres there was still a population of N_S^0 present which could donate an electron such that:

$$(1.1) \quad N_S^0 + NV^0 \rightarrow N_S^+ + NV^-$$

Eventually with increased radiation a critical point would be reached where there was no longer an excess of N_S^0, allowing NV^0 to be produced. Although the ground state of NV^0 has not been observed in EPR, an excited state has been reported [91]. Both charge states of the defect have been reported as grown CVD material indicating that it grows in as a unit, and has been shown to be grown in with preferentially oriented populations [92,93].
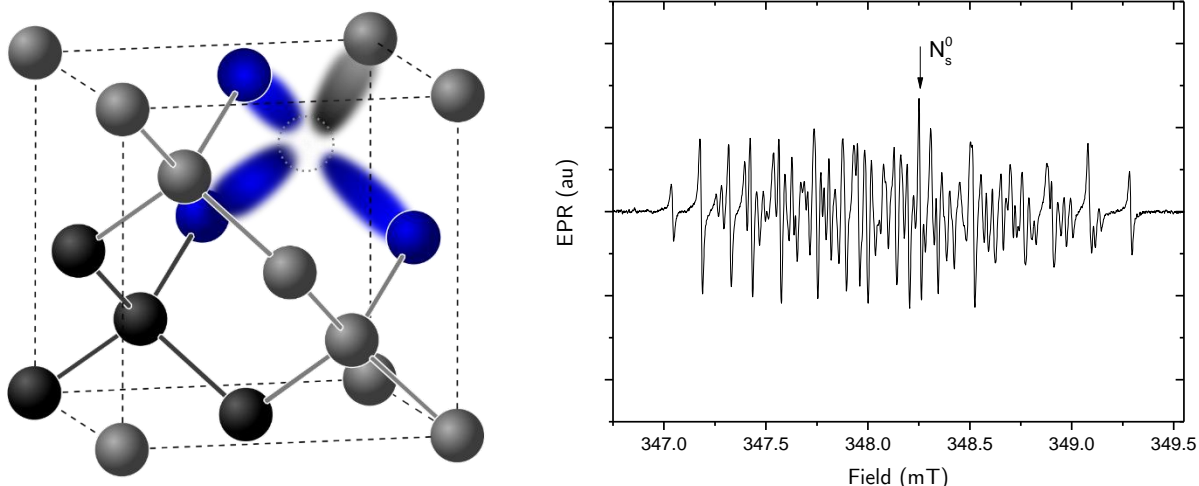
Figure 2-5 Left, the structure of N_3V^0 defect. Nitrogen atoms are represented in blue and The dotted feature depicts the vacancy. Right, an experimental EPR spectrum of N_3V^0 with B^0 aligned along the [001] crystallographic direction.

2.2.1.7 N_3V^0

N_3V^0 was amongst the first defects observed optically in diamond with a ZPL at 415 nm reported by Walter in 1891 [94]. The defect consists of three nitrogen atoms adjacent to a vacancy (Figure 2-5). This feature, later named N3 (naturally occurring 3), was found to be very common in natural yellow diamonds and consists of a ZPL at 2.985 eV (415.2 nm) and a large vibronic structure. Studies involving irradiation and annealing of samples showed that additional broad features at 2.596 eV (477.6 nm) and 3.603 eV (344.2 nm), N2 and N4 respectively, were also associated with the defect [39]. The nature of the association is still a subject of research; with the thermochromic behaviour of N2 being inconsistent with that of N3 and N4 [95].

N_3V^0 was first reported in EPR in 1959 [73] as P2, but the spectrum was incorrectly assigned to substitutional aluminium, which was thought to be a good candidate for substitutional inclusion and had previously been reported [96], also incorrectly. Poor fits to the data prompted further investigation and ENDOR revealed that the P2 spectrum was indeed the result of three equivalent nitrogen atoms [97]. Later the unique ^{13}C interaction was observed using ENDOR by van Wyk [98] who later used advances in techniques to improve the parameters of the defect [99]. Correlation between N3 and P2 has been demonstrated over a range of concentrations and substantiated by similar behaviour under photo excitation [100]. The extremely complicated EPR spectrum meant a poor fit was still seen away from the [001]

direction until work by Green using isotopically enriched samples offered improved g factor and hyperfine parameters [101].

2.5.1 Further impurities

During CVD growth of diamonds, the major element in the growth plasma by number density is hydrogen which is also incorporated into the diamond lattice. It is currently unclear exactly how much hydrogen is incorporated into the single crystal CVD material, but up to 1 ppm of hydrogen has been reported in polycrystalline and natural samples [102]. A number of hydrogen related defects have been identified by bulk EPR, VH, NVH^-, N_2VH^0 and OVH [103–105]. IR optical absorption measurements have identified hydrogen in the grain boundaries [102] of polycrystalline diamond. Isotropic substitution has helped identified several IR features related to the stretch and bend mode of the C-H bond [106,107].

Silicon is also incorporated during MP-CVD growth after being either deliberately introduced or etched off reactor components such as windows [108]. There are a number of silicon related defects that have been identified including SiV, $SiV{:}H$ [109,110]. Substitutional silicon is predicted as being invisible to both electronic-optical and magnetic resonance spectroscopy [111]. Vibrational modes at $1333\,\mathrm{cm^{-1}}$ and $1338\,\mathrm{cm^{-1}}$ have been suggested as originating from substitutional silicon [111,112].

2.3 History of EPR

Early experiments regarding magnetic resonance were conducted by Rabi in 1938 working on molecular beams [113] and electron paramagnetic resonance was reported by Zavoisky in 1945 [114]. The advances in radar technologies during World War Two allowed Bloch and Purcell to lay the foundations for modern magnetic resonance expanding the technique to include liquid and solid state measurements in 1946 [115,116]. In the same journal the theoretical basis for magnetic resonance was laid out by Bloch [117].

Although starting from the same point EPR[3] as a technique began to fall behind the more widely used nuclear magnetic resonance, NMR, a gap that was significantly extended by the introduction of pulsed Fourier transform NMR by Ersnt in 1965 [118]. These faster, pulsed techniques had been demonstrated by Blume previously in EPR [119] but the technological challenges posed limited development of the technique to a small number of groups. Although research continued to produce results using continuous wave EPR, CW-EPR, the introduction of the first commercial pulsed EPR spectrometer in 1985 [120] led to a renewed interest in the technique. The requirement for an unpaired electron may seem to limit the applications where EPR can be used, but EPR matured into an important tool in the study of biomolecular systems [121–124], catalysts [125] and in the identification of defects in semiconductors [57]. Indeed the fields in which EPR has been applied are broad; food stability [126], atmospheric pollution [127] and archaeological dating [128] have all been addressed. A good introduction to the wide uses of EPR has been given by Eaton and Eaton [129].

All magnetic interactions discussed in §3.1.5 affect the CW-EPR spectrum but not all of the interactions are large enough to be resolved. Electron nuclear double resonance, ENDOR, uses radio waves to drive nuclear transitions whilst simultaneously reading out the electron spin state with microwave on the electron transition giving great insight into the structure of defects [130]. ENDOR can be read out with a saturation contiguous microwave [131] or with pulsed microwaves [132,133]. Hyperfine and nuclear quadrupole interaction can also be studied by electron spin echo envelope modulation, ESEEM. Rowan et al. reported in 1965 that in some samples the spin echo was modulated by a combination of nuclear frequencies [134], with the theory being refined later by Mims [135]. The simplified experimental equipment has led to ESEEM being a popular technique and reviews of its modern application are available [136] [137]. Possibly the largest growth in recent years has been electron-electron double resonance, ELDOR[4] . In these experiments two microwave frequencies are employed to measure the dipolar coupling between two unpaired electrons. Early developments used continuous microwaves [138] but in recent years work has focused on pulsed ELDOR [139].

---

[3] Also commonly referred to as ESR, and less commonly ESS, EMR etc...

[4] DEER in some works.

Since the strength of dipolar coupling is related to distance, ELDOR offers insight about the distance between spins and potentially the angle between them [121].

Rapid Passage EPR, RP-EPR has been a relatively under exploited branch of EPR. RP-EPR employs field sweeps that do not give the spin system time to fully come into equilibrium and may be performed at much higher powers than SP-EPR on samples with long relaxation times. The effect was first experimentally reported by Portis working on LiF in 1955 [140] who observed that a rapidly changed static field coupled with a small modulation field created a response that was 90° out of phase with the modulation and resembled an absorption lineshape; this result was later confirmed by Hyde [141]. The first report of RP-EPR on diamond came from Mailer in 1973 [142]. RP-EPR's prime advantage is that it allows operation at higher microwave powers for systems that easily saturate such as SiO_2 and diamond [143,144].

The rapidly moving static field does not allow the spins to be modelling by their equilibrium states meaning there are no analytical solutions to the Bloch equations. Portis interpreted his results by numerical analysis of the Bloch Equation [140] and a complete numerical evaluation for many passage conditions was presented by Weger in 1960 [145]. Advances in computing power allowed Harbridge to numericaly solve the Bloch equations for a single spin and then the process could be repeated thousands of times to build up a whole spectrum [143]. The results showed a good match for the experimental spectrum but were very time consuming and could not always be applied due to the required knowledge of the starting condition of each spin packet in the spectrum.

The majority of modern improvements in RP-EPR have been conducted by the Eaton group who have exploited the increased signal to remove the field modulation and have used direct detection instead, RP-EPR[DD]. The group have used RP-EPR[DD] as a quantitative technique [146] and for *in-vivo* imaging using 250 MHz excitation [147]. Custom built spectrometers have been designed to give very rapid field sweeps with sweep rates of 80 T/s being [148]. These faster sweep rates give much larger signal to noise and allow direct detection of the resonance signal removing the need for field modulation and the associated distortions [149,150]. These undistorted spectra have been exploited to measure the distances

between spin labels in helical peptide [150,151], and in EPR imaging [147,152,153]. The signal can be further increased by using the Kramers-Kronig relationship to combine both the real and imaginary parts of the recoded signal [154].

The nature of the signal used to sweep the static field can create distortions and procedures have been presented to correct for the distortions from both sine waves and triangular waves allowing the undistorted spectra to be recorded for both [155,156]. The effect of a rapidly changing field on the resonator has also been considered where it was found that the sweeping static field induced inhomogeneous fields in split ring and dielectric resonators [157]. These fields were found to lead to a reduction in sensitivity when using 35 GHz excitation by filtering the high frequency response.

2.4 References

[1]   V. N. Mochalin, O. Shenderova, D. Ho, and Y. Gogotsi, Nat. Nanotechnol. 7, 11 (2012).

[2]   R. S. Balmer, J. R. Brandon, S. L. Clewes, H. K. Dhillon, J. M. Dodson, I. Friel, P. N. Inglis, T. D. Madgwick, M. L. Markham, T. P. Mollart, N. Perkins, G. Scarsbrook, D. J. Twitchen, A. J. Whitehead, J. J. Wilman, and S. M. Woollard, J. Phys. Condens. Matter 21, (2009).

[3]   F. Bundy, H. Hall, and H. Strong, Nature 176, (1955).

[4]   F. P. Bundy, W. A. Bassett, M. S. Weathers, R. J. Hemley, H. K. Mao, and A. F. Goncharov, Carbon N. Y. 34, 141 (1996).

[5]   R. A. Spits and C. N. Dodge, (2010).

[6]   C. Stromann, WO 2006/061672 A1 (2006).

[7]   Y. N. Palyanov, Y. M. Borzdov, I. N. Kupriyanov, Y. V. Bataleva, A. F. Khokhryakov, and A. G. Sokol, Cryst. Growth Des. 15, 2539 (2015).

[8]   J. E. Field, *The Properties of Natural and Synthetic Diamond* (Academic Press, London, 1992).

[9]   Y. Borzdov, Y. Pal'yanov, I. Kupriyanov, V. Gusev, A. Khokhryakov, A. Sokol, and A. Efremov, Diam. Relat. Mater. 11, 1863 (2002).

[10] R. M. Chrenko, R. E. Tuft, and H. M. Strong, Nature 270, 141 (1977).

[11] A. T. Collins and S. C. Lawson, Philos. Mag. Lett. 60, 117 (1989).

[12] H. Kanda and T. Sekine, in *Prop. Growth Appl. Diam.*, edited by A. J. Neves and M. H. Nazare (IEE - Inspec, 1994), pp. 247–255.

[13] R. C. Burns, V. Cvetkovic, and C. N. Dodge, 104, (2000).

[14] Y. V. Babich, B. N. Feigelson, D. Fisher, A. P. Yelisseyev, V. A. Nadolinny, and J. M. Baker, Diam. Relat. Mater. 9, 893 (2000).

[15] H. M. Strong and R. M. Chrenko, J. Phys. Chem. 75, 1838 (1971).

[16] H. Sumiya, US006030595A (2000).

[17] U. F. S. D'Haenens-Johansson, A. Katrusha, K. Soe moe, P. Johnson, and W. Wang, GEMS Gemol. Fall, 260 (2015).

[18] B. L. Green, M. W. Dale, M. E. Newton, and D. Fisher, Phys. Rev. B 92, 165204 (2015).

[19] E. Shabanova, K. Schaumburg, and J. P. F. Sellschop, J. Magn. Reson. 130, 8 (1998).

[20] W. G. Eversole, (1962).

[21] A. J. S. Fernandes, Q. H. Fan, F. Silva, and F. M. Costa, in *Prop. , Growth Appl. Diam.*, edited by A. J. Neves and M. H. Nazare (IEE - Inspec, London, 2001), pp. 290–296.

[22] M. Frenklach and K. E. Spear, J. Mater. Res. 3, 133 (1988).

[23] J. Angus, C. Kovach, and A. Argoitia, *In Handbook of Industrial Diamonds and Diamond Films,* (1977).

[24] A. Tallaire, A. T. Collins, D. Charles, J. Achard, R. Sussmann, A. Gicquel, M. E. Newton, A. M. Edmonds, and R. J. Cruddace, Diam. Relat. Mater. 15, 1700 (2006).

[25] A. Tallaire, J. Achard, F. Silva, O. Brinza, and A. Gicquel, Comptes Rendus Phys. 14, 169 (2013).

[26] J. Achard, F. Silva, A. Tallaire, X. Bonnin, G. Lombardi, K. Hassouni, and A. Gicquel, J. Phys. D. Appl. Phys. 40, 6175 (2007).

[27] J. E. Butler, Y. A. Mankelevich, A. Cheesman, J. Ma, and M. N. R. Ashfold, J. Phys. Condens. Matter 21, 1 (2009).

[28] M. Schreck, J. Asmussen, S. Shikata, J.-C. Arnault, and N. Fujimori, MRS Bull. 39, 504 (2014).

[29] M. Fischer, S. Gsell, M. Schreck, R. Brescia, and B. Stritzker, Diam. Relat. Mater. 17, 1035 (2008).

[30] B. Ramsay, F. Schoofs, R. Bodkin, and A. P. Jardine, in *Diam. Conf.* (Warwick, 2015).

[31] H. Yamada, A. Chayahara, Y. Mokuno, H. Umezawa, S. I. Shikata, and N. Fujimori, Appl. Phys. Express 3, (2010).

[32] P. M. Martineau, M. P. Gaukroger, K. B. Guy, S. C. Lawson, D. J. Twitchen, I. Friel, J. O. Hansen, G. C. Summerton, T. P. G. Addison, and R. Burns, J. Phys. Condens. Matter 21, 364205 (2009).

[33] H. Pinto and R. Jones, J. Phys. Condens. Matter 21, 364220 (2009).

[34] D. J. Twitchen, P. M. Martineau, G. A. Scarsbrook, B. S. C. Dorn, and A. M. Cooper, WO03052177A1 (2003).

[35] H. Godfried, WO 2004.0464271 (2004).

[36] R. Samlenski, C. Haug, R. Brenn, C. Wild, R. Locher, and P. Koidl, Appl. Phys. Lett. 67, 2798 (1995).

[37] R. U. A. Khan, B. L. Cann, P. M. Martineau, J. Samartseva, J. J. P. Freeth, S. J. Sibley, C. B. Hartland, M. E. Newton, H. K. Dhillon, and D. J. Twitchen, J. Phys. Condens. Matter 25, 275801 (2013).

[38] Z. Yiming, F. Larsson, and K. Larsson, Theor. Chem. Acc. 133, 1 (2014).

[39] C. D. Clark, R. W. Ditchburn, and H. B. Dyer, Proc. R. Soc. A Math. Phys. Eng. Sci. 234, 363 (1956).

[40] G. Davies and C. Foy, J. Phys. C Solid State Phys. 13, 2203 (1980).

[41] J. Walker and L. A. Vermerlen, Proc. R. Soc. London 341, 235 (1974).

[42] C. D. Clark and J. Walker, Proc. R. Soc. London 334, 241 (1973).

[43] C. A. Coulson and M. J. Kearsley, Proc. R. Soc. Lond. A. Math. Phys. Sci. 241, 433 (1975).

[44] G. Davies and E. C. Lightowlers, J. Phys. C Solid State Phys. 3, 638 (1970).

[45] G. Davies, Nature 269, 498 (1977).

[46] J. Isoya, H. Kanda, Y. Uchida, S. C. Lawson, S. Yamasaki, H. Itoh, and Y. Morita, Phys. Rev. B 45, 1436 (1992).

[47] I. N. Douglas and W. A. Runciman, J. Phys. C Solid State Phys. 10, 2253 (1977).

[48] J. van Wyk and G. S. Woods, J. Phys. Condens. Matter 7, 5901 (1995).

[49] G. Davies, S. C. Lawson, A. T. Collins, A. Mainwood, and S. J. Sharp, Phys. Rev. B 46, 13157 (1992).

[50] M. E. Newton, B. A. Campbell, D. J. Twitchen, J. M. Baker, and T. R. Anthony, Diam. Relat. Mater. 11, 618 (2002).

[51] L. Allers, A. T. Collins, and J. Hiscock, Diam. Relat. Mater. 7, 228 (1998).

[52] D. Twitchen, M. Newton, J. Baker, T. Anthony, and W. Banholzer, Phys. Rev. B 59, 12900 (1999).

[53] M. A. Lea-Wilson, J. N. Lomer, and J. A. van Wyk, Philos. Mag. Part B 72, 81 (1995).

[54] A. Mainwoodt, J. E. Lowther, and J. A. van Wyk, J. Phys. Condens. Matter 5, 7929

(1993).

[55]   E. A. Faulkner and J. N. Lomer, Philos. Mag. 7, 1995 (1962).

[56]   D. C. Hunt, D. J. Twitchen, M. E. Newton, J. M. Baker, T. R. Anthony, W. F. Banholzer, and S. S. Vagarali, Phys. Rev. B 61, 3863 (2000).

[57]   F. Larkins and A. Stoneham, 112 (1970).

[58]   S. J. Breuer and P. R. Briddon, Phys. Rev. B 51, 6984 (1995).

[59]   G. Davies, H. Smith, and H. Kanda, Phys. Rev. B 62, 1528 (2000).

[60]   H. Smith, G. Davies, M. Newton, and H. Kanda, Phys. Rev. B 69, 45203 (2004).

[61]   D. J. Twitchen, M. E. Newton, J. M. Baker, O. D. Tucker, T. R. Anthony, and W. F. Banholzer, Phys. Rev. B 54, (1996).

[62]   G. A. Watt, M. E. Newton, and J. M. Baker, Diam. Relat. Mater. 10, 1681 (2001).

[63]   D. C. Hunt, A Study of Defect in Diamond - PhD Thesis, University of Oxford, 1999.

[64]   J. P. Goss, B. J. Coomer, R. Jones, T. D. Shaw, P. R. Briddon, M. Rayson, and S. Öberg, Phys. Rev. B 63, 195208 (2001).

[65]   I. Kiflawi, A. T. Collins, K. Iakoubovskii, and D. Fisher, J. Phys. Condens. Matter 19, 46216 (2007).

[66]   J. Walker, J. Phys. C Solid State Phys. 10, 3031 (1977).

[67]   D. Raabe and T. Liu, Appl. Phys. Lett. 94, 5 (2009).

[68]   W. Müller-Sebert, E. Wörner, F. Fuchs, C. Wild, and P. Koidl, Appl. Phys. Lett. 759, 759 (1995).

[69]   P. R. Briddon and R. Jones, Phys. B Phys. Condens. Matter 185, 179 (1993).

[70]   A. Mainwood, 49, 7934 (1994).

[71]   E. B. Lombardi, A. Mainwood, K. Osuch, and E. C. Reynhardt, J. Phys. Condens. Matter 15, 3135 (2003).

[72]   A. Cox, M. E. Newton, and J. M. Baker, J. Phys. Condens. Matter 6, 551 (1994).

[73]   W. V. Smith, P. P. Sorokin, I. L. Gelles, and G. J. Lasher, Phys. Rev. 115, (1959).

[74]   C. Ammerlaan and E. Burgemeister, Phys. Rev. Lett. 47, 954 (1981).

[75]   J. H. N. Loubser and W. P. Van Ryneveld, Br. J. Appl. Phys. 18, 1029 (1967).

[76]   J. H. N. Loubser and J. A. van Wyk, Reports Prog. Phys. 41, 1201 (1978).

[77]   J. H. N. Loubser and L. Du Preez, Br. J. Appl. Phys. 16, 457 (1964).

[78]   C. Peaker, M. K. Atumi, J. P. Goss, P. R. Briddon, M. J, and Rayson1, 1 (2015).

[79]   R. C. Barklie and J. Guven, J. Phys. C Solid State Phys. 14, 3621 (1981).

[80]   S. C. Lawson, D. Fisher, D. C. Hunt, and M. E. Newton, J. Phys. Condens. Matter 10, 6171 (1998).

[81]   R. Ulbricht, S. T. Van Der Post, J. P. Goss, P. R. Briddon, R. Jones, R. U. A. Khan, and M. Bonn, Phys. Rev. B - Condens. Matter Mater. Phys. 84, 1 (2011).

[82]   A. T. Collins, J. Phys. C Solid State Phys. 13, 2641 (1980).

[83]   Y. Mita, Y. Ohno, Y. Adachi, H. Kanehara, Y. Nisida, and T. Nakashima, Diam. Relat. Mater. 2, 768 (1993).

[84]   H. B. Dyer, F. A. Raal, L. Du Preez, and J. H. N. Loubser, Philos. Mag. 11, 763 (1965).

[85]   G. Davies and M. F. Hamer, J. Chem. Inf. Model. 348, 285 (1976).

[86]   J. H. N. Loubser and J. A. van Wyk, Diam. Relat Mater 11, (1977).

[87]   N. R. S. Reddy, N. B. Manson, and E. R. Krausz, J. Lumin. 38, 46 (1987).

[88]   G. Davies, J. Phys. C Solid State Phys. 12, 2551 (1979).

[89]   A. T. Collins and S. C. Lawson, J. Phys. Condens. Mat. 1, 6929 (1989).

[90]   Y. Mita, Phys. Rev. B 53, 11360 (1996).

[91]   S. Felton, A. M. Edmonds, M. E. Newton, P. M. Martineau, D. Fisher, and D. J. Twitchen, Phys. Rev. B - Condens. Matter Mater. Phys. 77, 1 (2008).

[92]   A. M. Edmonds, U. F. S. D'Haenens-Johansson, R. J. Cruddace, M. E. Newton, K.-M. C. Fu, C. Santori, R. G. Beausoleil, D. J. Twitchen, and M. L. Markham, Phys. Rev. B 86, 35201 (2012).

[93]   T. A. Kennedy, J. S. Colton, J. E. Butler, R. C. Linares, and P. J. Doering, Appl. Phys. Lett. 83, 4190 (2003).

[94]   A. M. Zaitsev, *Optical Properties of Diamond - A Data Handbook* (SPRINGER VERLAG, Berlin, 2001).

[95]   D. Fisher and A. Fitch, in *Diam. Conf.* (Waiwick, 2015).

[96]   F. a. Raal, Am. Mineral. 42, 354 (1957).

[97]   J. H. N. Loubser and A. C. J. Wright, Diam. Res. 16, (1973).

[98]   J. Van Wyk, J. Phys. C Solid State Phys. 15, L981 (1982).

[99]   J. A. van Wyk, J. H. N. Loubser, J. a Van Wyk, and J. H. N. Loubser, J Phys Condens Matter 5, 3019 (1993).

[100] G. Davies, C. M. Welbourn, and J. H. N. Loubser, Diam. Res. 23 (1978).

[101] B. Green, Optical and Magnetic Resonance Studies of Point Defects in Single Crystal Diamond - PhD Thesis, Unviersity of Warwcik, 2013.

[102] B. Dischler, C. Wild, W. Muller-Sebert, and P. Koidl, Phys. B Phys. Condens. Matter 185, 217 (1993).

[103] C. Glover, M. Newton, P. Martineau, D. Twitchen, and J. Baker, Phys. Rev. Lett. 90, 185507 (2003).

[104] C. B. Hartland, A Study of Point Defects in CVD Diamond Using Electron Paramagnetic Resonance and Optical Spectroscopy - Phd. Thesis, 2014.

[105] N. Mizuochi, H. Watanabe, H. Okushi, S. Yamasaki, J. Niitsuma, and T. Sekiguchi, Appl. Phys. Lett. 88, 9 (2006).

[106] S. Liggens, Identification of Point Defects in Treated Single Crystal Diamond by Department of Physics, University of Warwick, 2010.

[107] R. J. Cruddace, Magnetic Resonance and Optical Defects in Studies of Point Single CVD Crystal Diamond - PhD Thesis, University of Warwck, 2007.

[108] J. Barjon, E. Rzepka, F. Jomard, J. M. Laroche, D. Ballutaud, T. Kociniewski, and J. Chevallier, Phys. Status Solidi Appl. Mater. Sci. 202, 2177 (2005).

[109] U. F. S. D'Haenens-Johansson, A. M. Edmonds, B. L. Green, M. E. Newton, G. Davies, P. M. Martineau, R. U. A. Khan, and D. J. Twitchen, Phys. Rev. B 84, 245208 (2011).

[110] A. M. Edmonds, M. E. Newton, P. M. Martineau, D. J. Twitchen, and S. D. Williams, Phys. Rev. B - Condens. Matter Mater. Phys. 77, 1 (2008).

[111] J. P. Goss, P. R. Briddon, and M. J. Shaw, Phys. Rev. B 76, 75204 (2007).

[112] A. M. Edmonds, Magnetic Resonance Studies of Point Defects in Single Crystal Diamond - PhD Thesis, University of Warwick, 2008.

[113] I. Rabi, J. Zacharias, S. Millman, and P. Kusch, Phys. Rev. 53, 318 (1938).

[114] E. Zavoisky, J. Phys. USSR 9, (1945).

[115] F. Bloch, W. Hansen, and M. Packard, Phys. Rev. 70, 474 (1946).

[116] E. Purcell, H. Torrey, and R. Pound, Phys. Rev. 69, 37 (1946).

[117] F. Bloch, Phys. Rev. 70, 460 (1946).

[118] R. R. Ernst and W. A. Anderson, Rev. Sci. Instrum. 37, 93 (1966).

[119] R. J. Blume, Phys. Rev. 109, 1867 (1958).

[120] D. Schmalbein, in *Found. Maodern EPR*, edited by S. S. Eaton and G. R. Eaton (World Scientific, 1998).

[121] M. A. Stevens, J. E. McKay, J. L. S. Robinson, H. EL Mkami, D. G. Norman, and G. M. Smith, Phys. Chem. Chem. Phys. 18, 5799 (2016).

[122] L. Song, Z. Liu, P. Kaur, J. M. Esquiaqui, R. I. Hunter, S. Hill, G. M. Smith, and G. E. Fanucci, J. Magn. Reson. 265, 188 (2016).

[123] K. Halbmair, J. Seikowski, I. Tkach, C. Höbartner, D. Sezer, and M. Bennati, Chem. Sci. 17, 3172 (2016).

[124] W. R. Hagen, *Biomolecular EPR Spectroscopy*, 1st ed. (CRC Press, 2008).

[125] S. Van Doorslaer and D. M. Murphy, in *EPR Spectrosc. Appl. Chem. Biol.*, edited by M. Drescher and G. Jeschke (Springer Berlin Heidelberg, Berlin, Heidelberg, 2012), pp. 1–39.

[126] J. Polak, M. Bartoszek, and I. Stanimirova, Food Chem. 141, 3042 (2013).

[127] F. Ledoux, E. Zhilinskaya, S. Bouhsina, L. Courcot, M. L. Bertho, A. Aboukaïs, and E. Puskaric, Atmos. Environ. 36, 939 (2002).

[128] N. F. Cano, C. S. Munita, S. Watanabe, R. F. Barbosa, J. F. D. Chubaci, S. H. Tatumi, and E. G. Neves, Quat. Int. 352, 176 (2014).

[129] S. S. Eaton and G. R. Eaton, J. Magn. Reson. 223, 151 (2012).

[130] G. Feher, Phys. Rev. 103, 834 (1956).

[131] A. Cox, M. E. Newton, and J. M. Baker, J. Phys. Condens. Matter 4, 8119 (1992).

[132] M. Nechtschein and J. Hyde, Phys. Rev. Lett. 24, 672 (1970).

[133] W. Mims, Proc. R. Soc. (1965).

[134] L. Rowan, E. Hahn, and W. Mims, Phys. Rev. 137, A61 (1965).

[135] W. Mims, Phys. Rev. B 5, 2409 (1972).

[136] T. Prisner, M. Rohrer, and F. MacMillan, Annu. Rev. Phys. Chem. 52, 279 (2001).

[137] G. E. Cutsail, J. Telser, and B. M. Hoffman, Biochim. Biophys. Acta - Mol. Cell Res. 1853, 1370 (2015).

[138] P. P. Sorokin, G. J. Lasher, and I. L. Gelles, 1546, (1959).

[139] M. Pannier, S. Veit, A. Godt, G. Jeschke, and H. W. Spiess, J. Magn. Reson. 77, 371 (1999).

[140] A. M. Portis, Phys. Rev. 100, 1219 (1955).

[141] J. S. Hyde, Phys. Rev. 119, 1483 (1960).

[142] C. Mailer and C. P. Taylor, Biochim. Biophys. Acta 322, 195 (1973).

[143] J. R. Harbridge, G. A. Rinard, R. W. Quine, S. S. Eaton, and G. R. Eaton, J. Magn. Reson. 156, 41 (2002).

[144] D. G. Mitchell, R. W. Quine, M. Tseitlin, V. Meyer, S. S. Eaton, and G. R. Eaton, Radiat. Meas. 46, 993 (2011).

[145] M. Weger, Bell Syst. Tech. J. 39, 1013 (1960).

[146] R. W. Quine, G. A. Rinard, S. S. Eaton, and G. R. Eaton, J. Magn. Reson. 205, 23 (2010).

[147] J. R. Biller, M. Tseitlin, R. W. Quine, G. a Rinard, H. a Weismiller, H. Elajaili, G. M. Rosen, J. P. Y. Kao, S. S. Eaton, and G. R. Eaton, J. Magn. Reson. 242, 162 (2014).

[148] R. W. Quine, G. A. Rinard, S. S. Eaton, and G. R. Eaton, (2002).

[149] J. W. Stoner, D. Szymanski, S. S. Eaton, R. W. Quine, G. A. Rinard, and G. R. Eaton, J. Magn. Reson. 170, 127 (2004).

[150] A. W. Kittell, E. J. Hustedt, and J. S. Hyde, J. Magn. Reson. 221, 51 (2012).

[151] A. W. Kittell, T. G. Camenisch, J. J. Ratke, J. W. Sidabras, and J. S. Hyde, J. Magn. Reson. 211, 228 (2011).

[152] S. V Sundramoorthy, B. Epel, and H. J. Halpern, J. Magn. Reson. 240, 45 (2014).

[153] T. Czechowski, W. Chlewicki, M. Baranowski, K. Jurga, P. Szczepanik, P. Szulc, P. Kedzia, M. Szostak, P. Malinowski, S. Wosinski, W. Prukala, and J. Jurga, J. Magn. Reson. 243, 1 (2014).

[154] M. Tseitlin, R. W. Quine, G. a Rinard, S. S. Eaton, and G. R. Eaton, J. Magn. Reson. 203, 305 (2010).

[155] J. P. Joshi, J. R. Ballard, G. A. Rinard, R. W. Quine, S. S. Eaton, and G. R. Eaton, J. Magn. Reson. 175, 44 (2005).

[156] M. Tseitlin, D. G. Mitchell, S. S. Eaton, and G. R. Eaton, J. Magn. Reson. 223, 80 (2012).

[157] J. P. Joshi, G. R. Eaton, and S. S. Eaton, Appl. Magn. Reson. 28, 239 (2005).

Chapter 3

3 Theory

This chapter presents the background theory of techniques used in the investigations described in later chapters. It is not intended to be a comprehensive background on all the areas covered, as such a work would be beyond the scope of a single volume, but instead will provide sufficient information to aid an understanding of the results presented. A background for magnetic resonance is presented along with details of optical absorption measurements. A review of the use of chemical kinetics to model the annealing of defects in diamond follows and the chapter concludes with a brief introduction to the symmetry of point defects.

3.1 Magnetic resonance

Paramagnetic resonance is a spectroscopic technique that monitors the absorption or emission of electromagnetic waves by either the electron or nucleus: electron paramagnetic resonance, EPPR, and nuclear magnetic resonance respectively, NMR. In most cases this requires the application of an external magnetic field and allows non-destructive, non-invasive investigation of the geometric and electron structures of materials. NMR can be performed on any nuclear species that does not have an even number of protons and an even number of neutrons and therefore nuclear spin $I \neq 0$. EPR can be performed on systems with unpaired electrons therefore a net electron spin $S \neq 0$. There are fewer systems that satisfy this condition resulting in EPR being less widely used than NMR. The lack of EPR active systems is in fact an advantage when dealing with complex materials reducing unwanted background signals. The results in later chapters of this work are concerned with EPR and as such the explanations of resonance will be concerned with the electron.

3.1.1 Magnetisation

Paramagnetic resonance experiments are generally performed on bulk spin ensembles. Therefore, it is the macroscopic bulk magnetisation, $\mathbf{M}$, of the ensemble that is detected experimentally. Considering a set of electrons in free space, in an allied magnetic field, at equilibrium each spin will be in one of two states, $m_S = +\frac{1}{2}$ or $m_S = -\frac{1}{2}$, representing the magnetic moment being either parallel of antiparallel to B_0. The relative population of these states is given by the Boltzmann distribution:

$$(3.1) \qquad \frac{N_{+\frac{1}{2}}}{N_{-\frac{1}{2}}} = \exp\left(-\frac{\Delta E}{k_B T}\right) = \exp\left(-\frac{g_e \mu_B B_0}{k_B T}\right)$$

where $N_{m_s = \pm\frac{1}{2}}$ represents number of spins, in the $m_S = \pm 1/2$ state. For temperatures where $\frac{g_e \mu_B B_o}{k_B T} \ll 1$, the population difference can be approximated as $\frac{g_e \mu_B B}{k_B T}$. From this the magnetism can be expressed in terms of the total number of spin, N, which for the free electron is:

$$(3.2) \qquad \mathbf{M}_0 = N \frac{g_e^2 \mu_B^2 B_0}{4 k_B T} = N \frac{\hbar^2 \gamma_e^2 B_0}{4 k_B T} \ .$$

From (3.2) it is clear that in the absence of any additional disruption to the system, such as microwave power saturation, the signal response will be proportional to the number of spins allowing magnetic resonance to be a quantitative technique.

3.1.2 The resonance condition

Spin angular momentum $\mathbf{S}$ is equivalent to the classical orbital angular momentum $\mathbf{L}$, and gives rise to a magnetic moment $\boldsymbol{\mu}$ given by:

$$(3.3) \qquad \boldsymbol{\mu} = -\hbar \gamma_e \mathbf{S} = -g \mu_B \mathbf{S} \ .$$
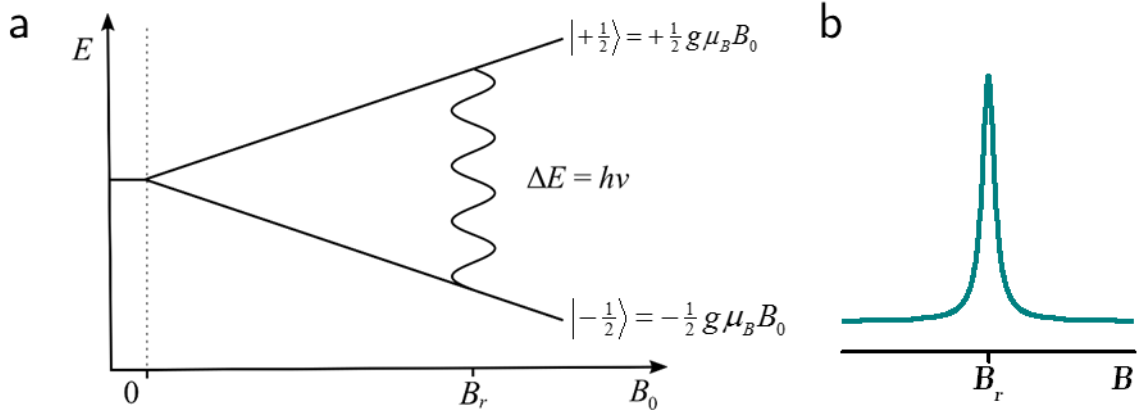
Figure 3-1 a, The electronic Zeeman effect for an S=1/2 system subjected to an increasing B_0.
b, The Lorentzian absorption line shape observed on resonance.

In (3.3) the constants are the gyromagnetic ratio $\gamma_e = \frac{eg_e}{2m_e}$, the Bohr magneton $\mu_B = \frac{e\hbar}{2m_e}$ and finally g or "g-factor", an intrinsic parameter of the particle and for a free-electron $g = g_e = 2.0023193043617(15)$. It is one of the most accurately known fundamental constants both theoretically and experimentally [1]. When an external magnetic field, B_0, is applied such that it is along the z-axis, $\mathbf{B}^T = (0, 0, B_0)$, to an electron its energy is given by:

(3.4)
$$\hat{H} = -\mathbf{B}^T \cdot \boldsymbol{\mu} = g\mu_B \mathbf{B}^T \cdot \mathbf{S} = g\mu_B B_o \hat{S}_z$$

The spin states (m_s) are no longer degenerate and for an electron (S=1/2) the energy difference between the two states is given by:

(3.5)
$$\Delta E = \pm \frac{1}{2} g_e \mu_B B_0.$$

Magnetic dipole transitions may be driven between these two energy levels by application of a high energy photon with frequency such that its energy ΔE matches the transition energy:

(3.6)
$$\Delta E = h\nu = g_e \mu_B B_o$$

this is the resonance condition (Figure 3-1). It is possible to see from (3.6) there are two ways to conduct a magnetic resonance experiment: either applying a fixed magnetic field and

changing the photon frequency or conversely by sweeping the magnetic field with a fixed photon frequency. In typical SP-EPR and RP-EPR experiments the field is swept bringing transitions into resonance. Pulsed EPR and NMR experiments are conducted at a fixed field and frequency.

3.1.3 Bloch equations

In the presence of an external magnetic field, $\mathbf{B}$, the magnitude of $\mathbf{M}$ is in a dynamic equilibrium but it is not fixed in space and moves according to:

$$(3.7) \qquad \frac{d\mathbf{M}}{dt} = \gamma_e \mathbf{M} \times \mathbf{B} \; .$$

If $\mathbf{B} = (0, 0, B_0)$ and in the absence of any relaxation (3.7) becomes:

$$(3.8) \qquad \begin{aligned} \frac{dM_x}{dt} &= \gamma_e B_0 M_x \\ \frac{dM_y}{dt} &= -\gamma_e B_0 M_y \\ \frac{dM_z}{dt} &= 0 \end{aligned}$$

with solutions:

$$(3.9) \qquad \begin{aligned} M_x &= M_\perp{}^0 \cos(\omega_B t) \\ M_y &= M_\perp{}^0 \sin(\omega_B t) \; . \\ M_z &= M_z{}^0 \end{aligned}$$

The solutions demonstrate that the magnetisation precesses about the applied magnetic field at a frequency $\omega_B = -\gamma_e B$ known as the Larmor frequency (Figure 3-2a). This is a very simplistic model and does not accurately describe experimental conditions. To do that a second oscillating applied field needs to be included along with the relaxation of the magnetisation to equilibrium values.
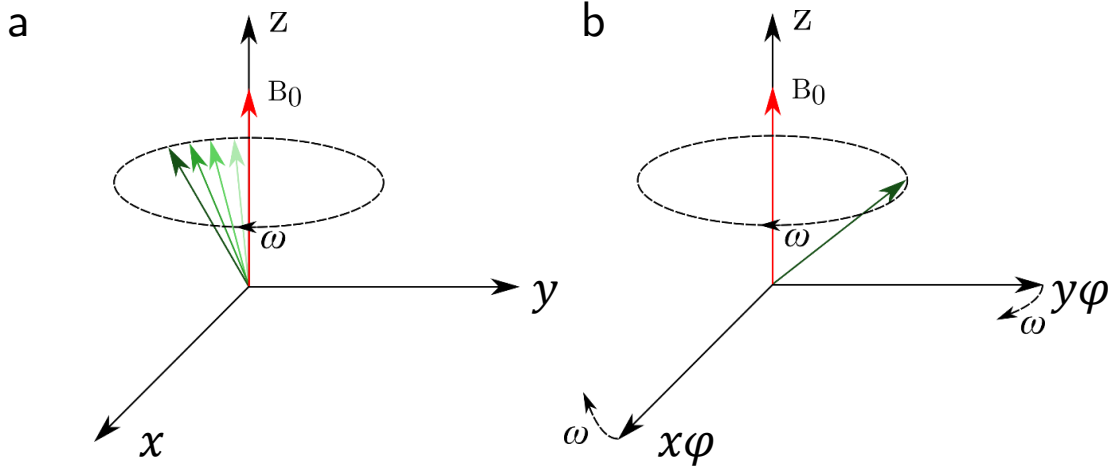
Figure 3-2 Free precession of the magnetisation, green arrow, in different frames of reference
a, The lab frame of reference (x,y,z), magnetisation rotates around z with a frequency ω.
b, The rotating frame magnetisation remains along yφ as the frame rotates about z with frequency ω.

Considering first relaxation: that is characterised by two empirical terms, T_1 and T_2. These are the time constants representing the time it takes the system to recover equilibrium populations after a sudden change: T_1 represents the longitudinal relaxation. If the magnetic field was suddenly turned off the net magnetisation would return to the equilibrium value $\mathbf{M} = 0$, equation (3.2). The return to equilibrium population would be an exponential in the M_z component of the magnetisation with a time constant T_1. T_2, the transverse relaxation, represents the loss of coherence in the M_x M_y plane due to spin-spin interactions. Adding relaxation to (3.8) yields:

(3.10)
$$\frac{dM_x}{dt} = \gamma_e B_0 M_y - \frac{M_x}{T_2}$$
$$\frac{dM_y}{dt} = -\gamma_e B_0 M_x - \frac{M_y}{T_2} \ .$$
$$\frac{dM_z}{dt} = -\frac{M_z^{\,0} - M_z}{T_1}$$

Finally, we consider the application of an oscillating field, $\mathbf{B}_1$ such that:

$$(3.11) \qquad \mathbf{B} = \begin{pmatrix} 0 \\ 0 \\ B_0 \end{pmatrix} + \begin{pmatrix} B_1 \cos(\omega t) \\ B_1 \sin(\omega t) \\ 0 \end{pmatrix} = \begin{pmatrix} B_1 \cos(\omega t) \\ B_1 \sin(\omega t) \\ B_0 \end{pmatrix}$$

taking ω as positive in (3.11) and combining with (3.10) leads to:

$$(3.12) \qquad \begin{aligned} \frac{dM_x}{dt} &= \gamma_e \left(B_o M_y - B_1 \sin(\omega t) M_z \right) - \frac{M_x}{T_2} \\ \frac{dM_y}{dt} &= \gamma_e \left(B_1 \cos(\omega t) M_z - B_o M_x \right) - \frac{M_y}{T_2} \\ \frac{dM_z}{dt} &= \gamma_e \left(B_1 \sin(\omega t) M_x - B_1 \cos(\omega t) M_y \right) - \frac{M_z{}^0 - M_z}{T_1} \end{aligned} \qquad .$$

This set of equations completely describe the motion of the magnetisation and were first laid out by Bloch in 1946 [2].

3.1.4 Line shape

It is convenient when discussing line shape to redefine the coordinates to a system that is rotating around the z axis at the same frequency of the applied oscillating field $\left((x, y, z) \rightarrow (x\varphi, y\varphi, z) \right)$ see Figure 3-2b. In this coordinate frame (3.12) becomes:

$$(3.13) \qquad \begin{aligned} \frac{dM_{x\varphi}}{dt} &= -\left(\omega_B - \omega \right) M_{y\varphi} - \frac{M_{x\varphi}}{T_2} \\ \frac{dM_{y\varphi}}{dt} &= \left(\omega_B - \omega \right) M_{x\varphi} - \frac{M_{y\varphi}}{T_2} \\ \frac{dM_z}{dt} &= \gamma_e B_1 M_{y\varphi} - \frac{M_z{}^0 - M_z}{T_1} \end{aligned}$$

and has the steady state solutions:

$$M_{x\varphi} = -M_z^0 \frac{\gamma_e B_1 (\omega_B - \omega) T_2^2}{1 + (\omega_B - \omega)^2 T_2^2 + \gamma_e^2 B_1^2 T_1 T_2}$$

(3.14)
$$M_{y\varphi} = +M_z^0 \frac{\gamma_e B_1 T_2}{1 + (\omega_B - \omega)^2 T_2^2 + \gamma_e^2 B_1^2 T_1 T_2} \quad .$$

$$M_z = +M_z^0 \frac{1 + (\omega_B - \omega)^2 T_2^2}{1 + (\omega_B - \omega)^2 T_2^2 + \gamma_e^2 B_1^2 T_1 T_2}$$

(3.14) assumes **B** to be invariant during the course of the experiment and that magnetisation has reached an equilibrium condition such that $\frac{dM_{x\varphi}}{dt} = \frac{dM_{y\varphi}}{dt} = \frac{dM_z}{dt} = 0$.

Under conventional operation EPR spectrometers detect magnetic susceptibility, $\chi = \frac{M}{H}$, in the $x\varphi y\varphi$-plane $\chi = \chi' + i\chi''$. $M_{x\varphi}$ represents the dispersion component of the signal, χ', and the $M_{y\varphi}$ represents the absorption of the component of the signal, χ''. and it is this that is normally detected. The signal response Y as a function of field can be expressed as:

(3.15)
$$Y(B) \propto \chi'' \frac{\gamma_e B_1 T_2}{1 + (B - B_r)^2 \gamma_e^2 T_2^2 + \gamma_e^2 B_1^2 T_1 T_2}$$

where B_r is the resonance field. When B_1 is small such that $\gamma_e^2 B_1^2 T_1 T_2 \ll 1$ the signal will be proportional to B_1. However, when this is not the case the system is said to be microwave power saturated and the spin populations will no longer be in the Boltzmann equilibrium state. This causes a potential reduction in signal and means measurements are no longer quantitative. In the absence of microwave power saturation (3.15) has the same form as a Lorentzian function:

(3.16)
$$Y = Y_{max} \frac{\Gamma^2}{\Gamma^2 + (x - x_0)^2}$$

with $\Gamma = (\gamma_e T_2)^{-1}$. The EPR line shape is seldom actually recorded as a true Lorentzian line shape as perturbations create a broadening of the line.

3.1.5 EPR interactions

Beyond the simple case of a lone electron spin we must consider a general description of the energy levels for a system. The spin Hamiltonian is the most complete way of describing the interactions that are present in EPR spectrum. The basic spin Hamiltonian for a system of total electron spin, S, and with a single or multiple nucleus, i, with nuclear spin $I > 0$, shown in (3.17); for clarity higher order terms have been omitted [3].

$$(3.17) \qquad \hat{H} = \underbrace{\mu_B \mathbf{B}^{\mathrm{T}} \cdot \mathbf{g} \cdot \hat{\mathbf{S}}}_{\text{electron Zeeman}} + \underbrace{\hat{\mathbf{S}}^{\mathrm{T}} \cdot \mathbf{D} \cdot \hat{\mathbf{S}}}_{\text{zero field}} + \sum_i^n \{ \underbrace{-\mu_N g_{ni} \mathbf{B}^{\mathrm{T}} \cdot \hat{\mathbf{I}}_i}_{\text{nuclear Zeeman}} + \underbrace{\hat{\mathbf{S}}^{\mathrm{T}} \cdot \mathbf{A}_i \cdot \hat{\mathbf{I}}_i}_{\text{nuclear hyperfine}} + \underbrace{\hat{\mathbf{I}}_i^{\mathrm{T}} \cdot \mathbf{P}_i \cdot \hat{\mathbf{I}}_i}_{\text{quadrapole}} \} + terms$$

3.1.5.1   Electron Zeeman

The electron Zeeman term expresses the lifting of the degeneracy of energy levels for the electron spin in an external magnetic field and is usually the dominant term for a S=1/2 system at typical fields used for EPR. The definition of the magnetic moment, $\boldsymbol{\mu}$, equation (3.3) only took into account the spin $\hat{\mathbf{S}}$ of the free electron but it may also have a component from the orbital angular momentum, and therefore is fully defined as:

$$(3.18) \qquad \boldsymbol{\mu} = -\mu_B (\hat{\mathbf{L}} + g_e \hat{\mathbf{S}})$$

Spin orbital coupling may also be represented by a Hamiltonian operator, $\hat{H}_{so}$, with λ_{SO} the spin orbit coupling constant recording the strength of coupling:

$$(3.19) \qquad \hat{H}_{so} = \lambda_{SO} \hat{\mathbf{L}}^T \cdot \hat{\mathbf{S}}$$

in the simple case of isotropic spin orbit coupling. The energy arising from spin and orbital angular moment is now:

$$(3.20) \qquad \hat{H}_{ez} + \hat{H}_{so} = \mu_B \mathbf{B}^{\mathrm{T}} \cdot (\hat{\mathbf{L}} + g_e \hat{\mathbf{S}}) + \lambda_{SO} \hat{\mathbf{L}}^T \cdot \hat{\mathbf{S}} \, .$$

Considering a ground state, $\left|\psi_g, m_S\right\rangle$, it is possible to view the effect of spin orbit coupling on the g tensor. It can be shown to the first order since S_x and S_y terms vanish if B is defined along the z axis [4], applying this to (3.20) gives:

$$(3.21) \qquad E = \left\langle \psi_g, m_S \left| g_e \mu_B B_z \hat{S}_z \right| \psi_g, m_S \right\rangle + \left\langle \psi_g, m_S \left| \left(B_z \mu_B + \lambda_{SO} \hat{S}_z \right) L_z \right| \psi_g, m_S \right\rangle$$

The first term in (3.21) is the spin only interactions and the second term is more conveniently written:

$$(3.22) \qquad \left\langle m_s \left| B_z \mu_B + \lambda_{SO} \hat{S}_z \right| m_s \right\rangle \left\langle \psi_g \left| \hat{L}_z \right| \psi_g \right\rangle$$

It can be shown that the expectation value of L is zero and therefore, $\left\langle \psi_g \left| \hat{L}_z \right| \psi_g \right\rangle = 0$. Using (3.22) and second order perturbation theory leads to the following correction term summed over all states [4]:

$$(3.23) \qquad \hat{H} = -\sum_{n \neq g} \frac{\left| \left\langle \psi_g, m_s \left| (\mu_B \hat{\mathbf{B}} + \lambda_{SO} \hat{\mathbf{S}})^{\mathrm{T}} \cdot \hat{\mathbf{L}} + g_e \mu_B \mathbf{B}^{\mathrm{T}} \cdot \hat{\mathbf{S}} \right| \psi_n, m_s' \right\rangle \right|^2}{\left(E_n - E_g \right)}$$

Since $\left\langle \psi_g | \psi_n \right\rangle = 0$ the $g_e \mu_B \mathbf{B}^{\mathrm{T}} \cdot \hat{\mathbf{S}}$ term in the numerator will disappear and the remainder can be simplified to:

$$(3.24) \qquad \hat{H} = \left\langle m_s' \left| \mu_B{}^2 \hat{\mathbf{B}} \cdot \Lambda \cdot \hat{\mathbf{B}} + 2\lambda \mu_B \hat{\mathbf{B}}^{\mathrm{T}} \hat{\mathbf{S}} \cdot \Lambda \cdot \hat{\mathbf{S}} + \lambda^2 \hat{\mathbf{S}}^{\mathrm{T}} \cdot \Lambda \cdot \hat{\mathbf{S}} \right| m_s' \right\rangle$$

where the first term is a representation of the constant contribution of temperature independent magnetism and causes no change in the observable spectrum and is therefore ignored and Λ defined as:

$$(3.25) \qquad \Lambda_{ij} = -\sum_{n \neq g} \frac{\left\langle \psi_n \left| \hat{\mathbf{L}}_i \right| \psi_g \right\rangle \left\langle \psi_n \left| \hat{\mathbf{L}}_j \right| \psi_g \right\rangle}{\left(E_n - E_g \right)} \ .$$

This corrected Hamiltonian can now be combined with (3.20) to yield the 'spin Hamiltonian':

(3.26)
$$\hat{H} = \mu_B{}^2 \mathbf{B}^T \cdot \left(g_e \mathbf{I}_3 + 2\lambda_{SO}\Lambda \right) \cdot \hat{\mathbf{S}} + \lambda_{SO}^2 \hat{\mathbf{S}}^T \cdot \Lambda \hat{\mathbf{S}}$$
$$= \mu_B \mathbf{B}^T \cdot \mathbf{g} \cdot \hat{\mathbf{S}} + \hat{\mathbf{S}}^T \cdot \mathbf{D} \cdot \hat{\mathbf{S}}$$

where $\mathbf{I}_3$ is a 3x3 identity matrix. For a free electron we would expect g to be isotropic with a value of g_e but (3.26) makes it clear that any deviation away from this is as a result of a non-zero Λ term. The second term is the Zero Field splitting term from (3.17) and will be discussed in §3.1.5.5.

3.1.5.2   Nuclear Zeeman

The nuclear Zeeman interaction arises from coupling between the nuclear spin and an applied magnetic field and is equivalent to the electron Zeeman interaction with the nuclear magneton, μ_N, and the g factor, g_n, of the nucleus in question replacing their electron counterparts. This interaction is given by:

(3.27)
$$\hat{H}_{nz} = -\mu_N g_{ni} \mathbf{B}^T \cdot \hat{\mathbf{I}}_i \; ,$$

which will need to be summed for all nuclei coupled to the electron. Nuclear Zeeman interactions are typically isotropic and since $\mu_N \ll \mu_e$ normally have negligible impact on the EPR spectrum.

3.1.5.3   Electron nuclear hyperfine interaction

Electron nuclear hyperfine interaction, often referred to as hyperfine, is the interaction between the electron and nuclear spins and is described by:

(3.28)
$$\hat{H}_{nh} = \sum_i \hat{\mathbf{S}}^T \cdot \mathbf{A}_i \cdot \hat{\mathbf{I}}_i \; .$$

Nucleus	Natural Abundance (%)	m_I	$\gamma \ \left(\text{rad s}^{-1}\text{T}^{-1}\right)$
^1H	99.984426(5)	$\frac{1}{2}$	267.522×10^6
^{13}C	1.1078(28)	$\frac{1}{2}$	67.283×10^6
^{14}N	99.6337(4)	1	19.338×10^6
^{15}N	0.3663(4)	$\frac{1}{2}$	-27.126×10^6
^{29}Si	4.68316(32)	$\frac{1}{2}$	-53.190×10^6
electron		m_S	
e	-	$\frac{1}{2}$	1.760×10^{11}

Table 3-1   The most common nucleus with I<0 found in diamond. Natural abundancies from [5], gyromagnetic ratios from [3,6].

The hyperfine interaction is perhaps the most important interaction for EPR as it allows the study of the chemical composition of the local environment of the electron. By analysing the abundance of different isotopes along with their relative I values, it is possible to assign a signal to a specific nucleus; a list of the most common isotopes with $I>0$ found in diamond can be seen in Table 3-1.

There are two contributing factors to the hyperfine interaction: the isotropic, Fermi contact interaction, and the dipole-dipole coupling between the electron and nucleus. The isotropic interaction is given by:

(3.29)
$$H_{iso} = a_{iso}\hat{\mathbf{S}}^{\text{T}}\bullet\hat{\mathbf{I}},$$

where the isotropic hyperfine couple constant, a_{iso}, is given by:

(3.30)
$$a_{iso} = \frac{2}{3}\frac{\mu_0}{\hbar}g_e g_N \mu_B \mu_N \left|\psi_0\left(0\right)\right|^2$$

where $\left|\psi_0\left(0\right)\right|^2$ is the electron wave function density at the nucleus. The isotropic part of the hyperfine interaction is concerned with non-zero electron probability density of the electron at the nucleus. When the electron wavefunction is centred on the nucleus in question only

electrons in s orbitals are considered since the probability density function of higher p, d, and f orbitals being localised on the nucleus is zero.

The dipolar coupling component of the hyperfine interaction is a change of energy levels due to mutually interacting magnetic fields of the electron and nuclei. This interaction is anisotropic and as such offers insight into the configuration of local nuclear spins and hence the structure of the defect. The dipolar coupling is defined as:

$$(3.31) \qquad \hat{H}_{dip} = \frac{\mu_0}{4\pi\hbar} g_e g_N \mu_B \mu_N \left[\frac{\left(3\hat{\mathbf{S}}\cdot\mathbf{r}\right)\left(\mathbf{r}^{\mathrm{T}}\cdot\hat{\mathbf{I}}\right)}{r^5} - \frac{\hat{\mathbf{S}}^{\mathrm{T}}\cdot\hat{\mathbf{I}}}{r^3} \right]$$

where $\mathbf{r}$ is a vector between the electron and nuclear dipoles. By integrating over electron probability density it possible to simplify this to:

$$(3.32) \qquad \hat{H}_{dip} = \hat{\mathbf{S}}^{\mathrm{T}}\cdot\mathbf{T}\cdot\hat{\mathbf{I}},$$

where T is the dipolar coupling tensor given by:

$$(3.33) \qquad T_{ij} = \frac{\mu_0}{4\pi\hbar} g_e g_N \mu_B \mu_N \left\langle \phi_o \left| \frac{3r_i r_j - \partial_{ijr^2}}{r^5} \right| \phi_o \right\rangle.$$

In systems where the $\mathbf{g}$ is either isotropic or the anisotropy is very small the dipolar interaction can be described by the diagonal tensor:

$$(3.34) \qquad \mathbf{T} = \frac{\mu_0}{4\pi\hbar} g_e g_N \mu_B \mu_N \begin{pmatrix} -b & & \\ & -b & \\ & & 2b \end{pmatrix}$$

where $b = \dfrac{3r_i r_j - \partial_{ijr^2}}{r^5}$. It is now possible to express the full hyperfine tensor as:

$$(3.35) \qquad \mathbf{A} = a_{iso}\mathbf{1} + \mathbf{T}.$$

3.1.5.4   Nuclear quadrupole

For nuclear species with spin $I \geq 1$, the distribution of charges within the nucleus is non-spherical and is described by the quadrupole moment, Q. Such a distribution of charges will interact with a magnetic field gradient, typically from nearby nuclei or electrons, in a manner described by:

$$(3.36) \qquad \hat{H}_{quad} = \hat{\mathbf{I}}^{T} \mathbf{P} \hat{\mathbf{I}}$$

where $\mathbf{P}$ is the quadrupole tensor that is made traceless by subtraction of constants, which do not alter the difference between energy levels and therefore, the recorded EPR spectrum. In the same axis frame used in (3.21) $\hat{H}_{quad}$ becomes:

$$(3.37) \qquad \hat{H}_{quad} = \frac{e^{2}qQ}{4I(2I-1)\hbar} \left[\left(3I_{z}^{2} - I\left(I+1 \right)^{2} \right) + \rho \left(I_{x}^{2} - I_{y}^{2} \right) \right]$$

with $\rho = \dfrac{\left(P_{x} - P_{y} \right)}{P_{z}}$. The nuclear quadrupole interaction effect on the spectrum is second order and as such normally small, shifting the positions of allowed transitions, quadruple also increases the probability of forbidden transitions [3].

3.1.5.5   Zero-field splitting

Zero-field splitting can originate from spin orbit coupling §3.1.5.1 or if two or more unpaired electrons are present in a system, $S \geq 1$. The dipole-dipole interaction between the multiple electron spins can lift the $\left(2S+1 \right)$ degeneracy of the ground state if symmetry allowed. This interaction is expressed by (3.38). Since this interaction is field independent and is observed at $B = 0$ this splitting is called *zero-field splitting*.

$$(3.38) \qquad \hat{H}_{zf} = \hat{\mathbf{S}}^{T} \cdot \mathbf{D} \cdot \hat{\mathbf{S}}$$

where $\mathbf{D}$ is the *zero-field* tensor and contains contributions from both spin orbit and dipole-dipole interactions and is by convention traceless (analogous to nuclear quadrupole term). The

tensor $\mathbf{D}$ is often rewritten in terms of $D = {}^{3D_z}\!/_{2}$ and $E = {}^{\left(D_x - D_y\right)}\!/_{2}$, where E is a measure of the rhombicity of the interaction and in the lab axis frame is expressed as:

$$(3.39) \qquad \hat{H}_{zf} = D\left[S_z^2 - \frac{1}{3}S(S+1)\right] + E\left(S_x^2 - S_y^2\right).$$

For systems with cubic symmetry $D=E=0$, $D \neq 0$ for a system with axial symmetry or lower, and for lower than axial symmetry $E \neq 0$ as well. The dipole-dipole interactions are often very strong and can dominate magnetic interactions in conventional EPR.

3.1.6 The (S=1/2, I=1/2) model system

An arbitrary spin system of electron spin S and nuclear spin I has an energy matrix that can be constructed from the elements of $\left\langle m'_s, m'_I \middle| \hat{H}_{B_1} \middle| m_s, m_I \right\rangle$ where the Hamiltonian describing the perturbation from microwave field $\hat{H}_{B_1} = \mu_B \mathbf{B_1^T} \cdot g \cdot \hat{\mathbf{S}}$; the eigenvalues of the energy matrix will be energy levels of the system. A model system consisting of one electron spin $S=1/2$ and one nuclear spin $I=1/2$ will have four energy levels. The probability of transition between any two levels is proportional to $\left| \left\langle m'_s, m'_I \middle| \hat{H}_{B_1} \middle| m_s, m_I \right\rangle \right|^2$. Such a system is depicted in Figure 3-3; in this example $\mathbf{A} > g_n \mu_N B$ and the energy levels are labelled 1 to 4.

Transitions w_{14} and w_{23} are the allowed EPR transitions $\left(\Delta I = 0 \, ; \Delta S = \pm\frac{1}{2}\right)$; w_{12} and w_{34} are *"forbidden"* in an EPR experiment but are allowed NMR transitions $\left(\Delta I = \pm\frac{1}{2} \, ; \Delta S = 0\right)$ and are the basis for an NMR experiment. The transitions w_{13} and w_{24} are double spin flips $\left(\Delta I = \pm\frac{1}{2} \, ; \Delta S = \pm\frac{1}{2}\right)$ and are *"forbidden"* in both NMR and EPR, but can be weakly allowed due to state mixing.

3.1.6.1 Polarisation

The intensity of a transition is proportional to the probability of transition but is also proportional to the relative population of the two energy levels involved, assuming they are
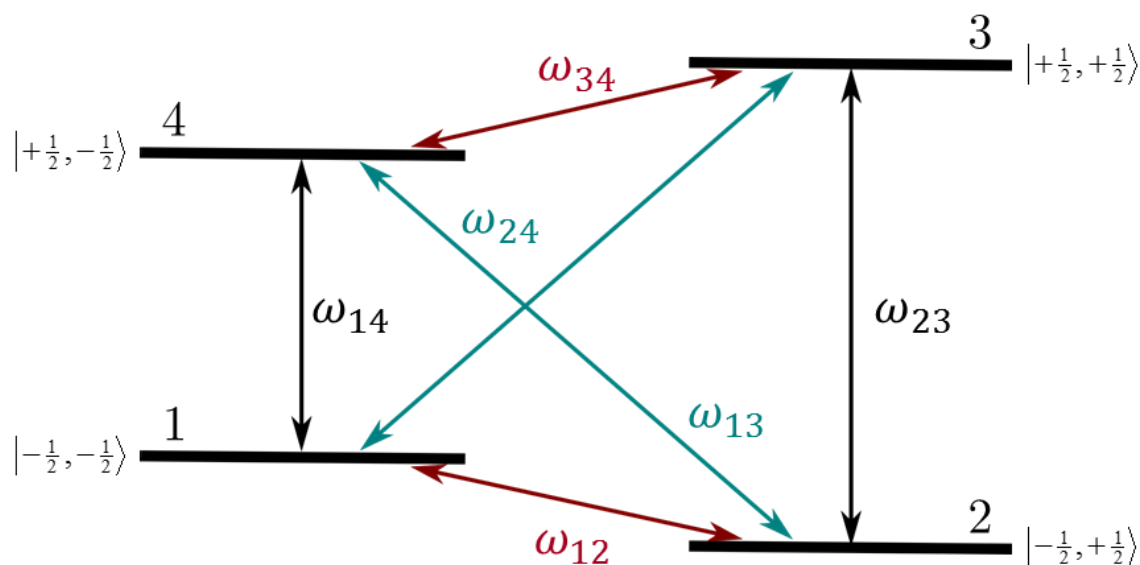
Figure 3-3 The energy level diagram for a system with S=1/2 and I = 1/2. All possible transitions are labelled: black arrows indicate EPR transitions, red arrows NMR transitions and cyan arrows the "forbidden" transitions.

not degenerate. At thermal equilibrium this is given by (3.1) for a one spin system but can be more generally described between two energy levels i and j by:

$$(3.40) \qquad \Delta N_{ij} = \frac{\exp(\frac{-E_i}{k_B T}) - \exp(\frac{-E_j}{k_B T})}{\sum_n \exp\left(\frac{-E_n}{k_B T}\right)} \ .$$

Energy level populations may be altered away from thermal equilibrium by processes such as optical polarisation or microwave power saturation. This is often desirable to achieve greater signal intensity for a paramagnetic transition and the enhancement to signal, ε, is defined as:

$$(3.41) \qquad \varepsilon = \frac{I_{pol} - I_0}{I_0}$$

where I_{pol} and I_0 are the intensity of the polarised and the thermal populations respectively.

3.1.7 Dynamic nuclear polarisation

As was discussed in §3.1.1 the polarisation of a spin 1/2 nucleus is limited by the Boltzmann distribution which is dependent on the gyromagnetic ratio of the nucleus as well as the field

and temperature at which the experiment is conducted (equation (3.2)). NMR experiments are normally measured at high fields to improve the polarisation and low temperature may also be employed. There is an alternative approach to increasing polarisation offered by the much greater gyromagnetic ratio of the electron; at the same field and temperature the amount of polarisation achieved of an electron is ∼660 times greater than for the proton. The transfer of this greater polarisation from the electron to the nucleus is the subject of dynamic nuclear polarisation, DNP.

The possibility that the electron spin polarisation could be transferred to the nuclear spin bath was first proposed by Overhauser in 1953 [5], DNP was demonstrated experimentally later that year by Slichter *et al* [6]. The process in these early experiments, known as the Overhauser effect, is not achieved by direct transfer of polarisation but rather by cross-relaxation through the *"forbidden"* transitions w_{13} and w_{24} Figure 3-3. The rate of these double spin flip transitions is governed by time dependent dipolar couplings between the electron and the nucleus. In experiments high powered saturating microwaves are applied to an *"allowed"* EPR transition $\left(w_{14} \text{ or } w_{23} \right)$ to build up non thermal population [7]. The efficiency of the Overhauser effect becomes less efficient as field increases [8] since $\omega_S \tau_c < 1$ must be true, where τ_c is the rotation correlation time of the spin system. The Larmor frequency of the electron increases with field, greatly attenuating the polarisation achieved [9]. There are several microwave driven mechanisms for DNP in solids; the solid effect, the cross effect, and optically driven polarisation processes such as chemically induced polarisation but these are much rarer.

The solid effect also uses the *"forbidden"* transitions w_{13} and w_{24} that become weakly allowed through state mixing. Rather than transferring the polarisation through relaxation, as in the Overhauser effect, the solid effect is achieved by directly exciting the *"forbidden"* transitions. If the *"forbidden"* transition w_{13} and w_{24} are excited simultaneously then both positive and negative nuclear polarisation occurs leading to no net polarisation. As such the solid effect is most efficient when the linewidth of the EPR spectrum and the total width of the spectrum are much smaller than the nuclear Larmor frequency, allowing an individual forbidden

transition to be selected for excitation [10]. The efficiency of the solid effect also drops off with increased field since the mixing of states reduces at higher fields.

The cross effect requires a three spin system with two electrons with Larmor frequencies, ω_{S1} and ω_{S2} that are separated by a nuclear Larmor frequency, ω_I, such that $\omega_{S1} - \omega_{S2} = \omega_I$ [9]. The cross effect produces the largest polarisation in insulating solids that have inhomogeneously broadened lineshapes such that the line is broad compared to the nuclear Larmor frequency, ω_n [11]. Saturating microwaves are applied to one of the EPR *"allowed"* transitions burning a hole in the EPR spectrum, creating conditions where the *"forbidden"* combined nuclear and electron flip transitions are more likely. The polarisation then disperses through the sample via spin diffusion allowing continued application to polarise the whole sample.

These chemically induced polarisation processes are referred to as CiDNP and CiDEP for nuclear and electron polarisation respectively [12]. Radical pairs are normally created by the disassociation of an optically excited molecule or by the electron transfer between an optically excited molecule and a neighbour in the ground state. A spin-correlated radical pair can create spin polarisation through the three spin mixing process, TSM. Initially two singlet spatially adjacent systems are in equilibrium. Electron transfer between the two systems occurs creating a radical pair. This transfer happens either during or shortly after photoexcitation of one of the systems from the singlet ground state to an excited singlet state. The conversion between the radical pair spin triplet (anti phase) and spin singlet (in phase) configurations is governed by small differences in the local spin environments during the spin evolution. If the evolution rates matched the electron nuclear hyperfine interaction and the nuclear Larmor frequency, polarisation can be transferred from the electron to the nucleus. As such it requires anisotropic interactions to create the off diagonal terms in the hyperfine interaction, and is strongest when the double matching parameter is met [13]:

$$(3.42) \qquad\qquad 2\left|\Delta\omega_S\right| = 2\left|\omega_I\right| = \left|A\right|.$$

3.1.8 Time evolution of spin

During a continuous wave experiment, as outlined in §3.1.3 & 3.1.4, the spin is considered to be in a steady state, as such it is difficult to directly measure precise information about relaxation times. To do this a pulse of microwaves can be used to dramatically perturb the system and allow the temporal evolution of the spin to be observed. A comprehensive guide to time resolved EPR is given by Scweiger and Jeschke [14] and for NMR by Levitt [15].

3.1.8.1   Vector notation

The most intuitive notation for pulsed experiments is the classical model which describes the effect of the oscillating magnetic pulse on the bulk magnetisation, M. This can be expressed as a vector and is easily viewed pictorially, the rotating frame of reference introduced in §3.1.4 is once again employed $\left((x, y, z) \rightarrow (x\varphi, y\varphi, z) \right)$. To perform a pulsed experiment, the magnetic field is not swept as in a CW-EPR experiment, but is fixed at the resonance field $\left(B_0 = B_{res} \right)$ and a high powered microwave pulse is applied to create a large $\mathbf{B_1}$ for a period t_p. The length of the pulse needs to be short compared to the relaxation time of the paramagnetic system so that no relaxation occurs during the pulse. This pulse rotates M about the $x\varphi$ axis; the amount of rotation is given by $\Omega_{tp} = \left| \gamma_e \right| B_1 t_p$ and is known as the tip angle [3]. After the pulse has ended, M will return to its equilibrium value through longitudinal and transverse relaxation, T_1 and T_2^*.

The two basic pulses that are used as the building blocks for most pulse experiments are the π-pulse and the π/2-pulse, labelled for their tipping angle. The π-pulse completely inverts the magnetisation (e.g. $z \rightarrow -z$) rotating M by 180° whilst maintaining its magnitude. The π/2-pulse rotates M by 90°. From equilibrium a π/2-pulse would move M from being aligned with z to being in the $x\varphi y\varphi$-plane. Most spectrometers detect presence of magnetisation in the $x\varphi y\varphi$-plane and as such the π/2-pulse offers the simplest pulsed magnetic resonance experiment, the return to equilibrium of the magnetisation after a pulse or free induction decay, FID. The decay of M is considered free because it is no longer influenced by $\mathbf{B_1}$.

Although simple the single pulse FID experiment can be used to collect an entire resonance spectrum. In this chapter it has already been shown that a system may have more than one resonance, therefore it will not be possible to exactly meet the resonance conditions for the entire spectrum simultaneously. After a $\pi/2$-pulse the magnetisation for the on-resonance transition and off-resonance transition will tip into the $x\varphi y\varphi$-plane. Considering first the on-resonance transition, after being tipped it will precess at its Larmor frequency that is equal to the microwave rotation frequency $\left(\omega = \omega_B\right)$ so that it remains parallel to the $y\varphi$ axis. The net magnetisation will not remain parallel to the $y\varphi$ axis indefinitely, spin-spin relaxation will gradually alter the precession rate and the response will decay with an envelope of T_2^*.

For an off-resonance transition flipped into the $x\varphi y\varphi$-plane it will initially be parallel to the $y\varphi$ axis but will precess at a different frequency $\left(\omega \neq \omega_B\right)$. Now the magnetisation will appear to rotate in the rotation frame at a rate $\delta\omega = (\omega_B - \omega)$ even in the absence of spin-spin relaxation. The on- and off-resonance frequencies will now mix together causing an oscillating FID; these oscillations contain the information about all resonances effected by the pulse. Performing a Fourier transform, converting from the time to frequency (and therefore field) domain will return a full spectrum assuming the bandwidth of the resonator and excitation is larger than the spectrum.

The spectral width that can be excited by a single pulse is limited by minimum length of t_p and the bandwidth of the resonator used. Fourier transform EPR, FT-EPR, is limited by these factors but the technique is common in NMR where the length of RF pulses required are not as technically challenging and the resonator bandwidths are much larger. FT-EPR is further limited by the dead time of the spectrometer: the period after the pulse when the detector is shielded from the residual ringing of the microwave pulse in the resonator. For systems with short T_2^* the portion of the recorded magnetisation where the FID is most intense will be lost.
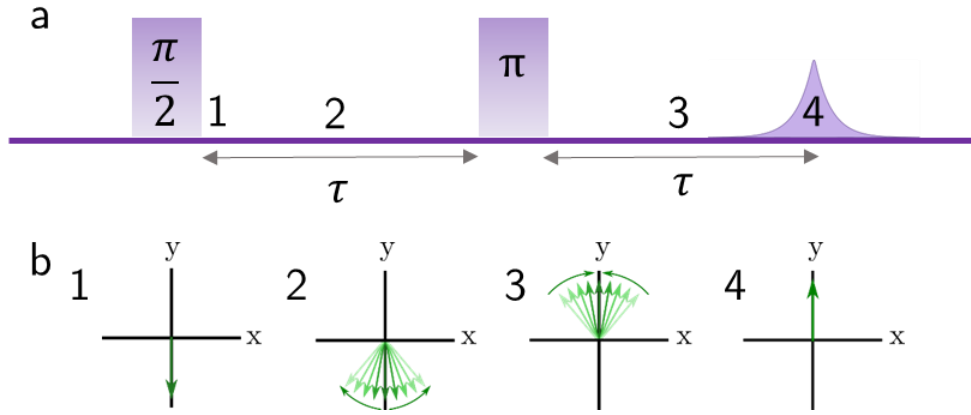
Figure 3-4   Schematics of the primary echo, a, the formation pulse sequence. b, pictorial illustration of evolution of the magnetisation during the sequence. Adapted from [14].

3.1.8.2   Echo decay

A method for circumventing dead time experienced whilst the detector is protected from thin ringing of the microwave pulse is the Spin Echo detection sequence $\left(\frac{\pi}{2} - \tau - \pi\right)$ (Figure 3-4), sometimes referred to as a *Hahn Echo* [16]. A group of spins with the identical resonance condition can be thought of as a spin packet, local inhomogeneity in fields means that each resonance line is built up of a number of these spin packets. A spin echo is created by first applying a π/2-pulse, a period of time τ is left to allow the magnetisation to evolve, individual packets fanning out due to local inhomogeneity causing some spins at higher fields to rotate quicker and spins at lower fields to rotate slower. A π-pulse is applied to flip the spins 180°; the magnetisation evolves again but this time the slower spins are caught up by the faster ones and after a period τ all the spins will be focused again and this is detected.

The *echo decay* sequence $\left(\frac{\pi}{2} - \tau + \delta\tau - \pi\right)$ is a simple way of measuring spin-spin relaxation. For a period between pulses, $\tau + \varphi\tau$, all the spins will remain coherent and will all refocus after the π pulse giving the maximum intensity of echo. As τ is increased some of the spins will be affected by external factors and no longer refocus after the π pulse causing a drop of intensity. The drop in echo intensity will follow an exponential decay with a time constant T_m or the phase memory of the system. T_m is related to T_2 by [17,18]:

(3.43)
$$\frac{1}{T_m} = \frac{1}{T_2} + \frac{1}{T_{SD}} + \frac{1}{T_{ID}}$$

where T_{SD} and T_{ID} are time constants associated with spectral and instantaneous diffusion.

3.1.9 Multiple pulse T1 measurements

Spin lattice relaxation, T_1, governs the relaxation in a longitudinal direction, M_z, (aligned along B_0). However, by the detection of pulsed spectrometers being conducted perpendicular to B_o and thus a $\frac{dM_z}{dt}$ cannot be directly measured using a simple single π-pulse sequence. Therefore, multiple pulse sequences need to be constructed. This chapter section will only deal with two: inversion and saturation recovery, and both will be described with echo detection: FID detection is analogous.

The first sequence is the *echo detected inversion recovery sequence*, $\left(\pi - \tau + \delta\tau - \frac{\pi}{2} - t - \pi \right)$ that uses three pulses to measure T_1 (Figure 3-5). The path that the magnetisation follows during the sequence is this: the first π-pulse inverts the magnetisation $\left(M_z \rightarrow -M_z \right)$, the magnetisation then relaxes for a time τ ($\delta\tau$ is initially =0), the π/2-pulse then moves magnetization into the $x\varphi y\varphi$-plane and the final π-pulse is used to create the echo which is detected. For short values of $\delta\tau$ the magnetisation has not relaxed and therefore the echo will be proportional to the initial magnetisation, M_z. This sequence is then repeated for increasing values of $\delta\tau$. During the time between the initial pulse and the final pulse the magnetisation evolves according to (3.13) and decays exponentially with a time constant T_1.

The *echo detected inversion recovery sequence* has an inversion pulse that is short relative to other spectral processes, and as such does not necessarily saturate all spin levels. This allows off-resonance spins to aid the relaxation through spectral diffusion and reduce the measured relaxation time. To combat this a very long saturating pulse $\left(t_p \gg T_1 \right)$ is used to saturate all
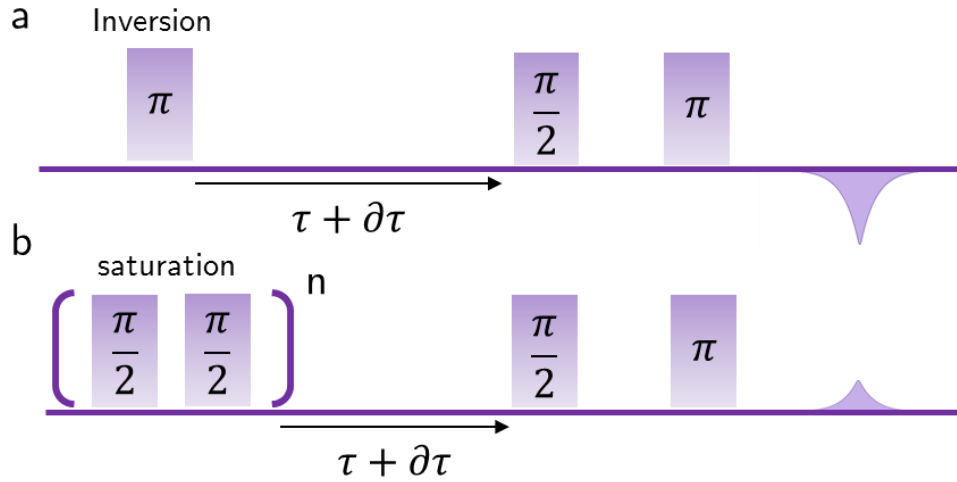
Figure 3-5 Sequences used for measurement of T_1
a, The inversion recovery sequence.
b, Saturation recovery sequence where the space between the saturating pulses t_s is $T_2 < t_s < T_1$ and n is sufficient to completely saturate all nearby spins.

the spin levels that can be accessed through spectral diffusion, thus removing their contribution for the relaxation times. The saturated spins can then be detected by either CW-EPR or via echo detection.

The very long pulses required for saturation recovery are often limited by the duty cycle of microwave amplifiers and therefore *picket fence saturation recovery* is employed (Figure 3-5). In this sequence the single inverting/saturating pulse is replaced with a string of π/2 pulses (the picket fence); the length of these pulses is sufficient to saturate the magnetisation of all local spins scrambling the net magnetisation $\mathbf{M} = 0$. By swapping the picket fence sequence for the inversion pulse in the *inversion recovery sequence* it is possible to measure T_1 free from spectral diffusion effects.

3.1.10 Rapid passage EPR

Rapid passage electron paramagnetic resonance, RP-EPR, is defined as an experiment where the rate of change of the magnetic field $\mathbf{B}$ is greater than the relaxation rate of an electron spin packet such that [19]:
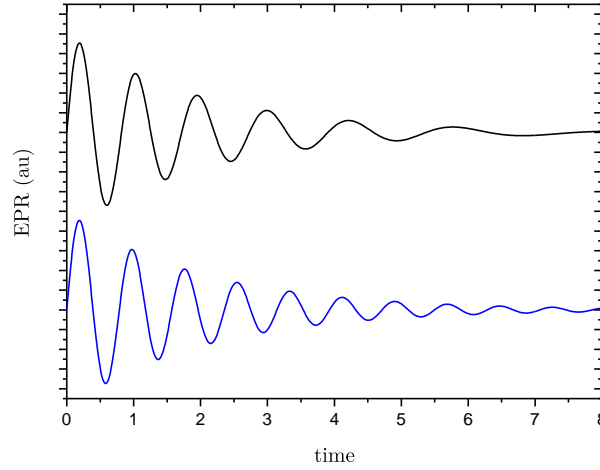
Figure 3-6 Simulation of a characteristic stretched FID-like response seen in direct detected RP-EPR experiments (top in black). Also shown is a simulation of an FID response for comparison (bottom in blue).

(3.44)
$$\frac{\Delta \mathbf{B}}{d\mathbf{B}\big/dt} \ll \sqrt{T_1 T_2} \ .$$

The conditions under which RP-EPR is performed do not allow analytical solutions to the Bloch equations. The magnetisation is not in a steady state as with a CW-EPR experiment; the effect on magnetisation of the changing field is closer to a pulsed EPR experiment. Experimentally the RP-EPR signal is found at higher powers than a steady state resonance and is also found to lag the field modulation phase by 90° when it is used. The most comprehensive attempt to classify different passage conditions was performed by Weger working with the Bloch equations to predict line shapes [19]. The most relevant model for this work is *"Rapid non-adiabatic passage with a short time between field modulation cycles and rapid field sweep".*

RP-EPR can be explained by discussion of the magnetisation of a single spin packet. Like the steady state conditions (§3.1.4) at equilibrium the magnetisation is aligned along B_0 $\left(\mathbf{M} = M_z \right)$. The spin packet is then suddenly brought into resonance and as suddenly brought off resonance. Viewing this from the rotating frame of reference the effect of this process on the magnetisation is similar to a $\pi/2$ pulse, although the tipping angle is likely to be smaller. Whilst on resonance the magnetisation will precess at a Larmor frequency and remain parallel

to the $y\varphi$ axis, however, as the field sweep continues the precession frequency of the spin packet will slow down as it moves off resonance, creating characteristic stretched FID-like response (Figure 3-6).

Experimentally, there is rarely a single spin packet in a resoance line and numerical evaluation of the Bloch equations for individual spin packets by using fourth order Runge-Kutta numerical integration allows investigation of the source of the response [20,21]. All spins in the modulation window produce the stretched FID response when brought into resonance, but over time it is the spin packets towards the edge of the modulation field that give the strongest response [20].

3.2 Symmetry

When looking at ensembles of defects we must consider the possible orientation of a defect and point group symmetry of the defect within the diamond lattice; an introduction to symmetry is given by Atkins [22]. This is of particular interest to EPR which is sensitive to any anisotropic interactions between the field and the defect, and can be explicitly seen for the hyperfine interaction in equation (3.31). The symmetry of the diamond lattice is T_d, and as such the maximum number of orientations for a point defect in the lattice is 24. As the distortions to the lattice increase the number of symmetry related defect orientations is lowered; Table 3-2 outlines some of the pertinent symmetry groups in diamond. The recorded EPR spectrum is a sum of all possible defect orientations and the pattern of line intensities and angular dependence provides information about the symmetry. The expected number of EPR lines for an S=1/2 I=0 system and their intensities when measured with B aligned along principal directions is shown in Table 3-2 and assumes no accidental degeneracy.
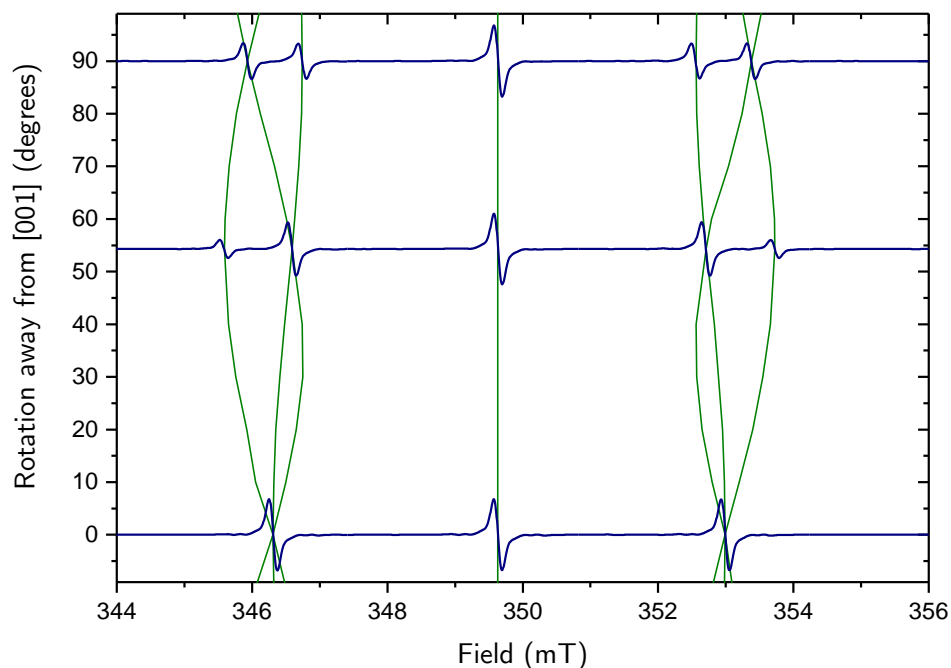
Figure 3-7 Simulated road map and spectra of the principal directions for N_S^0 as it is rotated in a $(1\bar{1}0)$ plane. Simulations obtained at 9.8 GHz

It is possible to visualise the effects of this symmetry by considering N_s^0, a C_{3v} symmetry defect, with a stretched N-C bond in the $\langle 111 \rangle$ crystalline direction. Therefore, the defect can exist along each of the $\langle 111 \rangle$ directions, this leads to four unique defect orientations, since [111] and $[\bar{1}\bar{1}\bar{1}]$ are indistinguishable in EPR. N_s^0 is a $S = 1/2$ and ^{14}N (99.6% natural abundance) has $I = 1$, we would therefore expect a three resonance spectrum for each orientation. The g tensor is isotropic along $\langle 111 \rangle$ and therefore has no angular dependence. However, the magnitude of the hyperfine splitting depends on the relative orientations of the applied field B_0 and the hyperfine tensor, A (§3.1.5.3). This angular dependence can be built up into a road map (Figure 3-7), allowing the symmetry of the defect to be confirmed.

Symmetry $\begin{pmatrix} \text{Schoenflies} \\ \text{notations} \end{pmatrix}$	Distortion	Symmetry related orientations	Line intensities		
			$\langle 100 \rangle$	$\langle 111 \rangle$	$\langle 110 \rangle$
T_d	No Distortion	1	1	1	1
D_{2d}	[110] axial distortion	3	2,1	3	2,1
C_{3v}	[111] axial distortion without inversion symmetry	4	4	1,3	2,2
C_{1h}	[111] non-axial distortion, not along [110] Or [110] non-axial distortion, not along [001]	12	8,4	6,3,3	4,2,4,2

Table 3-2 Common symmetries for point group distortions in diamond, relative intensities are for a S=1/2 defect with no hyperfine interaction and no accidental degeneracies. Based on original by Cox [23] .

3.3 Chemical kinetics

The movement of a defect within the lattice and the potential creation and destruction of defects can be modelled with chemical kinetics: first order and second order processes are introduced here, but a full description of higher order processes is available [24].

3.3.1 First order kinetics

A two species process where one species has an effectively infinite population can be modelled as a first order process. An example of this would be the loss of a vacancy by migration to a void or dislocation. Consider a vacancy [V] that must overcome an energy barrier, E_A, to exchange position with its neighbour; this energy is known as the activation energy. This vacancy can be thought of as being at the low point in a potential well, vibrating with a frequency, v_o. The probability, p_A, that any one of these vibrations has enough energy to overcome the potential barrier and allow the defect to hop sites is classically given by:

(3.45)
$$p_A = \exp\left(\frac{-E_A}{k_B T}\right).$$

The rate at which the change of concentration of V can now be thought of in terms of the average number of "hops", n, before change in state (arrival at the surface). The rate, k, is given by [24]:

$$(3.46) \qquad k = \frac{v_o}{n} \exp\left(\frac{-E_A}{k_B T}\right).$$

This rate allows us to model the changing population of V as a function of time, t:

$$(3.47) \qquad \frac{d[V]}{dt} = -k[V] \; ;$$

which has the solution for a known starting concentration $[V_0]$:

$$(3.48) \qquad \left[V_{(t)}\right] = [V_o] \exp(-kt).$$

3.3.2 Second order kinetics

When one of the reactants has a finite population second order kinetics must be employed. Consider two vacancies merging to form a di-vacancy, $[V] + [V] \rightarrow [2V]$. Strictly for a second order process to be applied, the starting concentration must be equal. An example of this in diamond is the creation of A-centres since both populations are N_s. In this case the change in concentration is described by [24]:

$$(3.49) \qquad \frac{d[V]}{dt} = -k[V]^2 \; ,$$

with the solution

$$(3.50) \qquad [V(t)]^{-1} = [V_0]^{-1} + kt \; .$$

3.4 Optical absorption

Optical absorption concerns electrical dipole transitions. An electromagnetic wave passing through the crystal lattice will interact with defects in the lattice as well as the lattice itself. Such interactions can provide useful information about the composition and symmetry of defects. In diamond, scattering effects are negligible at the typical energies of such experiments and therefore these optical interactions are typically through absorption mechanisms and are fundamentally quantitative. Absorption spectroscopy is customarily classified by the energy of light used, ultraviolet UV, visible Vis, and infra-red IR. Whilst luminescence is a more sensitive technique, allowing probing of a single defect in the correct circumstance; it is not a quantitative technique as it can be affected by non-radiative processes. Only a brief outline of theory required for understanding the work presented is given, more full treatment is given by [25,26].

3.4.1 Absorption coefficient

The intensity of light absorbed whilst propagating through a material is characterised by the fraction of the light absorbed in the length, t, of the material, designated the absorption coefficient, α. To a first approximation the transmitted intensity of light, I_T, at an energy, E, can be described as

$$(3.51) \qquad I_T(E) = I_0(E)\exp(-\alpha(E)t)$$

with I_0 the initial light intensity and

$$(3.52) \qquad \alpha(E) = \left(\frac{1}{t}\right)\ln\left(\frac{I_0(E)}{I_T(E)}\right)$$

This expression is only strictly true for gases and in the absence of any reflections from surfaces, it is important to take this into account where absorption is small. In Figure 3-8b we can see that it is possible for light to undergo multiple reflections at each surface resulting in the detected light being a sum of multiple paths with different lengths and phases, the Etalon
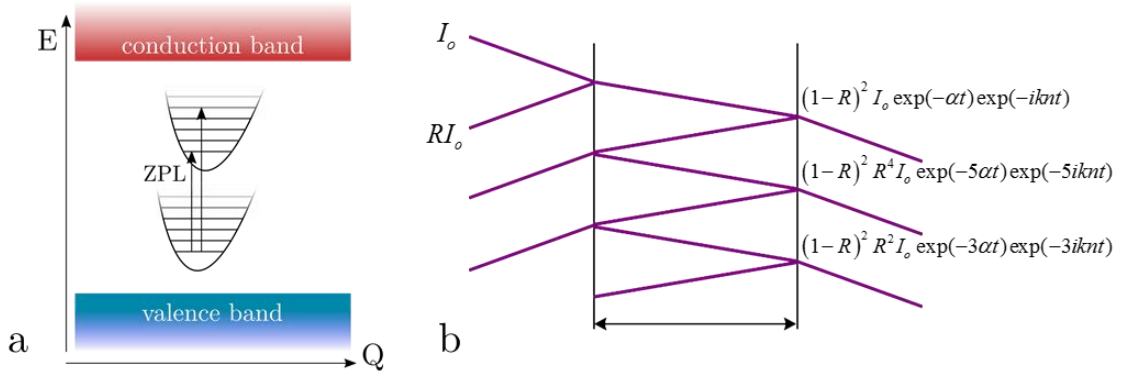
Figure 3-8   a, The zero phonon and phono aided transitions in absorption spectroscopy shown against configuration coordinates Q and energy E.
b, Schematic of the multiple reflection undergone by light passing through a diamond of thickness t (Etalon effect).

effect. For a material with refractive index, n, the total transmission of light with wavenumber, k, is given by [26]

$$I_T = \frac{I_0(1-R)^2 \exp(-\alpha t)}{\left[1 + R^2 \exp(-2\alpha t) - 2R\exp(-\alpha t)\cos(2knt)\right]}.$$

(3.53)

The final term in the denominator is often seen experimentally as a periodic beating in the recorded spectrum when IR energies are used to measure samples <1 mm thick. The impact of this interference on the recorded spectrum can be reduced either experimentally, by polishing a slight wedge onto the sample, or in data processing where its periodic nature allows it to be effectively removed with a band block FFT filter.

3.4.2 Sources of absorption

Intrinsic diamond is essentially transparent to light with wavelengths longer than 225 nm, diamond has a band gap of 5.4 eV [27], apart from a region between 2.5 µm and 6.6 µm where there is absorption from multi-phonon processes [28]. The symmetry of the tetrahedrally-bonded lattice of pure diamond does not allow absorption of light in the one phonon region. The maximum frequency of a single phonon propagating through the diamond lattice is 1332 cm⁻1. This frequency is achieved at the Brillouin centre and hence is also the

Raman frequency of diamond [29]. The addition of impurities or imperfections in the diamond lattice break the local symmetry and can give rise to new absorption features which can be used to identify defects.

Defects in the crystal may induce in-gap energy states and transitions can be driven from or into such states. When these transitions involve either the conduction or valence bands the observed spectrum is very broad but if the transition is between two in-gap states that are sufficiently localised a sharp zero phonon line, ZPL, is observed. As well as ZPLs there are also vibrionic structures that originate from interactions between the electronic excitation and phonons in the lattice; these phonon interactions often couple to specific frequencies giving a distinct pattern allowing defect identification. The ratio of ZPL and sideband alters with temperature as the number of phonons in the lattice reduces and experiments are typically conducted at 80 K to maximise the ZPL, since the ZPL is the lowest phonon energy state. A schematic of such transitions is seen in Figure 3-8a.

3.5 References

[1]   B. Odom, D. Hanneke, B. D'urso, and G. Gabrielse, Phys. Rev. Lett. 97, 6 (2006).

[2]   F. Bloch, Phys. Rev. 70, 460 (1946).

[3]   Weil and J. R. Bolton, *Electron Paramagnetic Resonance*, 2nd ed. (Wiley & Sons Inc, New York, 2007).

[4]   P. Mohn, *Magnetism in the Solid State: An Introduction* (Springer, 2003).

[5]   A. W. Overhauser, Phys. Rev. 92, 411 (1953).

[6]   T. R. Carver and C. P. Slichter, Phys. Rev. 92, 212 (1953).

[7]   E. Ravera, C. Luchinat, and G. Parigi, J. Magn. Reson. 264, 78 (2016).

[8]   K. H. Hausser and D. Stehlik, Adv. Magn. Opt. Reson. 3, 79 (1968).

[9]   M. L. Mak-Jurkauskas and R. G. Griffin, in *Solid-State NMR Stud. Biopolym.*, edited by A. E. McDermott and T. Polenova, First (John Wiley & Sons, Chichester, West Sussex, 2010), pp. 159–174.

[10]   Y. Hovav, A. Feintuch, and S. Vega, J. Magn. Reson. 207, 176 (2010).

[11]   R. A. Wind, M. J. Duijvestijn, C. van der Lugt, A. Manenschijn, and J. Vriend, *Applications of Dynamic Nuclear Polarization in 13C NMR in Solids,* (1985).

[12]   H. Van Willigen, P. R. Levstein, and M. H. Ebersoies, Chem Rev 93, 173 (1993).

[13]   G. Jeschke, J. Am. Chem. Soc. 120, 4425 (1998).

[14]   A. Schweiger and G. Jeschke, *Principles of Pulse Electron Paramagnetic Resonance* (Oxford University Press, New York :, 2001).

[15]   M. H. Levitt, *Spin Dynamics* (John Wiley & sons Ltd, 2001).

[16]   E. Hahn, Phys. Rev. 80, 580 (1950).

[17]   S. S. Eaton and G. R. Eaton, J. Magn. Reson. Ser. A 102, 354 (1993).

[18]   K. M. Salikohov and Y. D. Tsvetkov, in *Time Domain Spin Reson.*, edited by L. Kevan, R. N. Schwartz, and . (John Wiley & Sons Ltd, 1980), p. 414.

[19]   M. Weger, Bell Syst. Tech. J. 39, 1013 (1960).

[20]   J. R. Harbridge, G. A. Rinard, R. W. Quine, S. S. Eaton, and G. R. Eaton, J. Magn. Reson. 156, 41 (2002).

[21]   A. S. Stefan Stoll, J. Magn. Reson. 178, 42 (2006).

[22]   R Atkins and P Friedman, *Molecular Quantum Mechanics* (Oxford University Press, 2011).

[23]   A. Cox, PhD Thesis, University of Oxford, 1993.

[24]   B. Capellos and C. Capellos, *Kinetic Systems* (Krieger Publishing Company, 1980).

[25]   M. Fox, *Optical Properties of Solids* (2010).

[26]   G. Davies, Semicond. Semimetals 51, 1 (1999).

[27]   C. D. Clark, P. J. Dean, and P. V. Harris, Proc. R. Soc. A Math. Phys. Eng. Sci. 277, 312 (1964).

[28]   M. Lax and E. Burstein, Phys. Rev. 97, 39 (1955).

[29]   D. Krishnamurti, Proceeding Indian Acad. Sci. - A 40, 211 (1954).

Chapter 4

4 Experimental

This chapter will outline the main techniques used to produce the results in this work. The important aspects of continuous wave and pulsed EPR experiments will be covered as well as EPR experiments performed at variable temperature and under uniaxial stress. Relevant optical absorption experiments are also covered.

4.1 Quantitative EPR

The recorded SP-EPR signal is proportional not only to the number of spins present but also to the filling factor, quality factor, microwave power and magnetic susceptibility [1]:

$$I \propto \chi'' \eta Q \sqrt{P_{\mu w}} \ . \tag{4.1}$$

Equation (4.1) demonstrates that EPR is a quantitative technique; intensity of the signal is dependent on the imaginary part of the magnetic susceptibility of the paramagnetic system χ''. The intensity is also the product of the quality and filling factors, Q and η respectively, so maximising this product is the prime concern of resonator design and selection. Signal intensity depends on a number of other factors and experimental conditions for these are outlined in (4.2). The numbers that are recorded in EPR are therefore compared to a reference for quantification or made in a calibrated spectrometer. For a sample, S, the defect concentration, $[S]$, may be found by comparison to a reference sample of known concentration, $[ref]$, by the following relationship when working in the linear power regime (non-saturating microwave powers) [1]:

$$[S] = [ref] \frac{I_s}{I_{ref}} \frac{\eta_{ref}}{\eta_S} \frac{Q_{ref}}{Q_S} \frac{\sqrt{P_{\mu w_{ref}}}}{\sqrt{P_{\mu w_S}}} \frac{B_{m_{ref}}}{B_{m_S}} \frac{G_{ref}}{G_S} \frac{T_{ref}}{T_S} \frac{g_{ref}^2}{g_S^2} \frac{S(S+1)_{ref}}{S(S+1)_S} \frac{t_{aq_{ref}}}{t_{aq_S}} \frac{N_{ref}}{N_S} \tag{4.2}$$

Where the subscripts denote which scan, the other terms are:

- I - the double integrated intensity of the EPR spectrum.

- η - the filling factor discussed in §4.1.2.

- Q - the loaded quality factor of the cavity see §4.1.1.

- $P_{\mu w}$ - the incident microwave power (note $B_1 \propto \sqrt{P_{\mu w}}$) §4.1.3.

- B_m - the modulation amplitude.

- G - the receiver gain.

- T - temperature.

- g - the g factor of the defect being measured.

- S - the electron spin of the measured defect.

- t_{aq} - the acquisition or dwell time at each point of the spectrum.

- N - the number of scans taken.

For quantitative measurement on diamond, a highly characterised type IB single sector HPHT synthetic diamond, Syn93-04. This sample has a concentration of $270(20)$ ppm of N_S^0 determined from FT-IR measurements. The sample has mass 2.68(1) mg and has approximate dimensions of 2.5 mm cube and can be considered a point sample in a cavity resonator. To reduce errors on quantitative measurements is it critical that the sample is positioned reproducibly in the resonator.

4.1.1 Resonator quality factor

The loaded quality factor, Q_L, of a resonator is an important parameter since the recorded signal is directly proportion to Q_L. When performing quantitative EPR it is vital that Q_L is either constant between the reference and sample under inspection or the difference is accounted for. When a resonator is on resonance it stores some of the applied microwave energy. A resonator that is "critically coupled" to the transmission line will have no reflected microwaves at its resonant frequency. In real resonators most of the incident microwave power is not stored by the resonator but dissipated by ohmic losses from the resonator wall resistance. The efficiency of this process is characterised by Q_L as shown in (4.3). Experimentally Q_L can

be measured by the resonant frequency, v_{res}, divided by the half width of the cavity dip, Δv

:

$$(4.3) \qquad Q = \frac{2\pi \times energy\ stored}{energy\ dissipated\ per\ cycle} = \frac{v_{res}}{\Delta v} \quad .$$

There are a number of contributions to Q_L. For a small, non-conducting sample the dominant contributions are from: the unloaded Q, Q_U, which takes into account the losses in the wall of the resonator, the effect of dielectric loss on Q, Q_ε, and the power lost through radiation, Q_r. For a critically coupled resonator Q_r equals the effects of all the other effects on Q and allows Q_L which can be defined as [2]:

$$(4.4) \qquad \frac{1}{2Q_L} = \frac{1}{Q_U} + \frac{1}{Q_\varepsilon}$$

Bruker EMX spectrometers offer an estimation of the Q_L of a resonator using the bandwidth of the tuning dip and the resonant frequency. This estimation is very convenient and, although inaccurate at low values of Q_L or if the baseline is distorted off resonance, for the high Q values normally associated with diamond provides a reliable way of comparing samples [2]. As such all values of Q_L quoted in this work are for a critically coupled cavity with the sample mounted in the cavity.

4.1.2 Filling factor

The filling factor, η, is the extent that a sample intercepts the applied microwave field and as such, the filling factor for a sample can be accurately expressed by the ratio:

$$(4.5) \qquad \eta = \frac{\displaystyle\int_{sample} B_1^2 dV_{sample}}{\displaystyle\int_{resonator} B_1^2 dV_{resonator}} \quad .$$

The recorded signal intensity is proportional to η. For a sample small enough to act as point, peak signal can be found by placing the sample at the position in the cavity with the highest B_1 field. Calculating filling factors requires full knowledge of the B_1 field within the cavity once the sample is present. The dielectric properties of the sample and holder may affect the distribution of B_1 and lead to a change in η [3]. Practically, the filling can be estimated by simulation or from model values; wherever possible a reference sample should be used that closely matches the sample under observation [2,4]. Cavity resonators typically have very low filling factors due to their large volume and there is always interest in creating resonators with smaller sample spaces such as loop gap resonators [5–7].

4.1.3 Saturation

The intensity of the recorded EPR spectrum is proportional when $\gamma_e^2 B_1^2 T_1 T_2 \ll 1$ (equation (3.14)). If this condition is not met the paramagnetic system is said to be microwave power saturated and the signal intensity will be less than expected for a given power. In practice, it is the power of the microwaves that are controlled and B_1 is proportional to $\sqrt{P_{\mu w}}$, the efficiency of the conversion of microwave power to B_1 varies between resonators and is defined by the conversion efficiency, C_e (Table 4-3 in §4.2.4). To establish if the spectrum is taken in the linear regime, the microwave power dependence of the intensity must be established by plotting signal intensity against power (Figure 4-1). The dependence can be fitted to [8]:
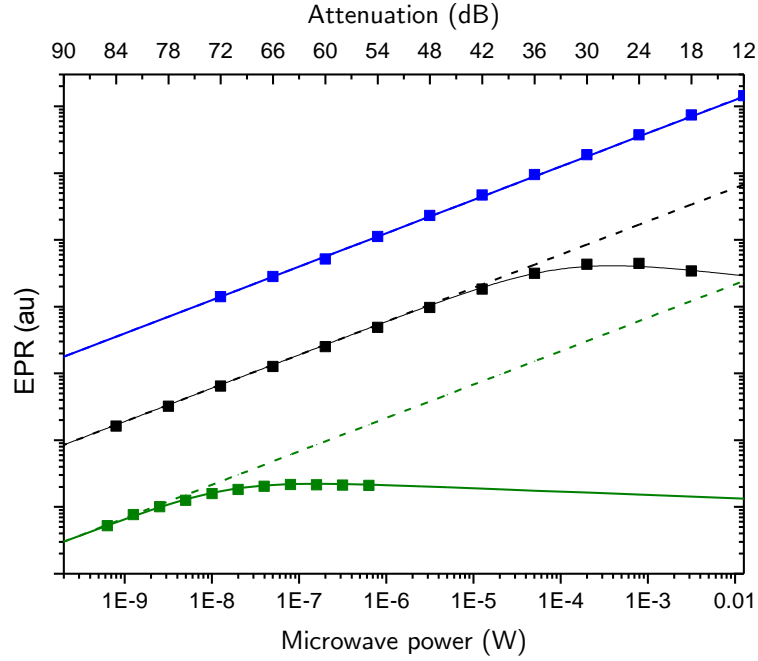
Figure 4-1 Microwave power saturation curves recorded at room temperature in the ER 4122SHQ. Top (blue) DPPH, Middle (black) HPHT Type Ib diamond containing 270(20) ppm N_S^0 and bottom (green) CVD Type IIa Diamond containing 40(4) ppb N_S^0. Fits (solid lines) are from equation (4.6), dashed lines represent expected intensity in absence of power saturation. Data is offset for clarity.

$$(4.6) \qquad\qquad I = \frac{\alpha \sqrt{P_{\mu w}}}{\left(1 + \dfrac{P_{\mu w}}{P_{1/2}}\right)^{\frac{\beta}{2}}}$$

where $P_{1/2}$ is the half power point of the system, α and β are constants where β can take on values between 1 and 2; typically, between 1.1-1.5. The inhomogeneity factor β is an imperial parameter required to fit systems that are not homogenous. For a completely homogenous system $\beta = 1$, when saturating powers are used the signal intensity will remain constant with increasing power. However, many systems are inhomogeneous; this could be through inhomogeneous B_1, non-uniform field or irregular distribution of defects in the sample. In these cases, the signal intensity will decrease with increased power after the saturation point has been passed. When $\beta = 2$, the very inhomogeneous case, the signal intensity drops as $1/\sqrt{P_{\mu w}}$ with power above $P_{1/2}$.

4.1.4 Simulation and fitting

The first harmonic spectrum typically recorded in SP-EPR must be double integrated to find the signal intensity. Performing a double integration on the recorded spectrum has a number of difficulties. There is an error associated with any noise on the spectrum which will be summed at every data point. If the spectrum has any background signal (cavity background, other defects) these will be included in the intensity. Finally, if there are two defects with overlapping spectra, these cannot be deconvolved. These problems can be overcome by fitting the spectrum and finding the intensity directly from the fit.

Simulation and fitting were performed using in house fitting software based on EasySpin [9] called EPRSimulator [10]. EasySpin is used to simulate the fields of resonances from provided Hamiltonian parameters for the defect to be fitted. Once the resonances have been calculated, EPRSimulator uses least squared fitting to fit a pseudo modulated Voigt line shape to the recorded EPR spectrum. The software allows the orientation of the simulation to the recorded spectrum, giving an accurate fitting of many defects at an arbitrary alignment. It is also possible with this method to fit each defect simultaneously and extract the intensities of both defects.
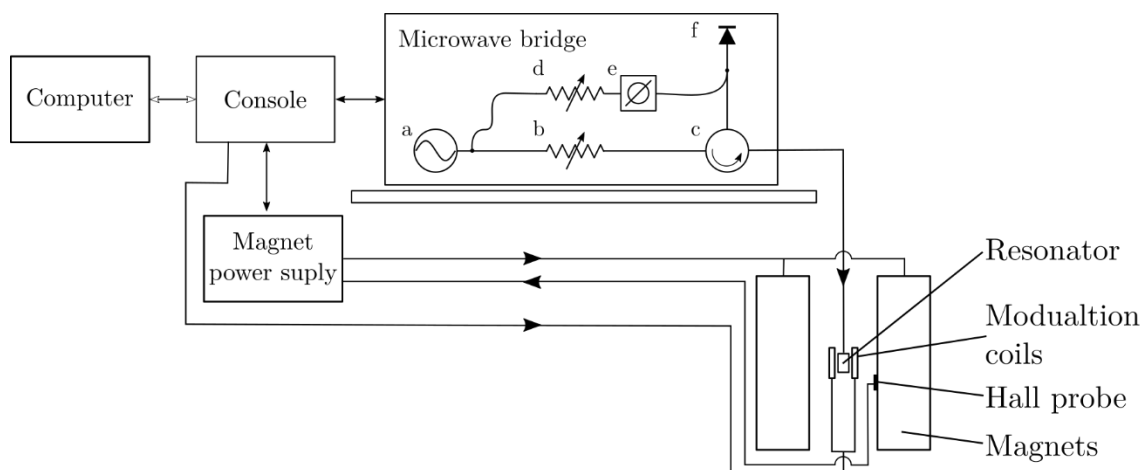
Figure 4-2 Schematic representation of the key components for an EPR spectrometer. In the microwave bridge the high path is the reference arm and the low path the sample arm and a, Gunn diode, b, attenuator, c, circulator, d, attenuator e, phase shifter, f, diode, adapted in part from [2].

4.2 The EPR spectrometer

The EPR spectrometer consists of three systems: the magnet (electromagnets, PSU and field controller), the microwave (bridge and the resonator), and the control and data acquisition units. These are shown schematically in Figure 4-2 and will be discussed in further detail in this chapter. Experiments presented in this work were conducted on Bruker EMX and EMX-E spectrometers coupled to ER041X (60 dB attenuation) or ER041XG (90 dB attenuation) X-Band microwave bridges. A Bruker Elexsys E580 spectrometer equipped with an FT-EPR X-band and a SuperQ-FT Q-band bridge was also used. The standard experimental parameters used in this work for slow passage, SP, and rapid passage, RP, continuous wave EPR measurements, can be seen in Table 4-1.

	Centre field (mT)	Sweep (mT)	Sweep rate (mT/s)	Power (µW)	Modulation Amplitude (mT)	Phase (°)
SP-EPR	348	20	0.012	<0.2 (60 dB)	0.01-0.1	0
RP-EPR$^{(FM)}$	348	20	1.91	252 (29 dB)	0.002	90

Table 4-1 Typical spectrometer configuration for RP- and SP-EPR experiments on N_S^0 at X-band in part adapted from [11].

4.2.1 The static magnetic field

The main field for EPR experiments at X- and Q-band is created by a large, sweepable, iron core electromagnet; at higher fields >2 T superconducting magnets are used; typical operating fields are shown in Table 4-2. The iron core magnet is designed to provide a uniform field over the sample volume. All magnets used have a working area of approximately 50 mm diameter and 10 mm height with a field homogeneity of $\pm 3 \times 10^{-5}$ mT at 350 mT [12]. Given that the typical size of a diamond sample is 2 mm^3 this is a very homogenous field.

Band	Typical Frequency (GHz)	Resonant field for g_e (mT)
L	1.5	55
S	3	110
X	9.8	350
Q	35	1249
W	94	3354
G or mm	250	8921

Table 4-2 Conventional frequencies at which EPR is conducted. X-Band and Q-Band are of interest to this work and highlighted. Bands labelled according to the IEEE standard [3].

The magnets are controlled by a variable power supply, however, the field produced from the magnet is fundamentally non-linearly dependant on the current and affected by hysteresis. To ensure reproducibility of field a Hall probe is mounted inside the magnet and calibrated against a proton NMR measurement to know absolute field. Field control is achieved through a feedback loop which corrects the current to ensure the requested field is produced. The Hall probe is temperature stabilised by being mounted onto the outer case of the water cooled magnets and in this way a stable field can be maintained for long periods. For conventional SP-EPR, very slow field sweep rates are employed (<0.01 mT s-1), for RP-EPR$^{(FM)}$ faster sweep rates are employed to the maximum achievable rate 2 mT s-1 given the hysteresis of the magnetic system.
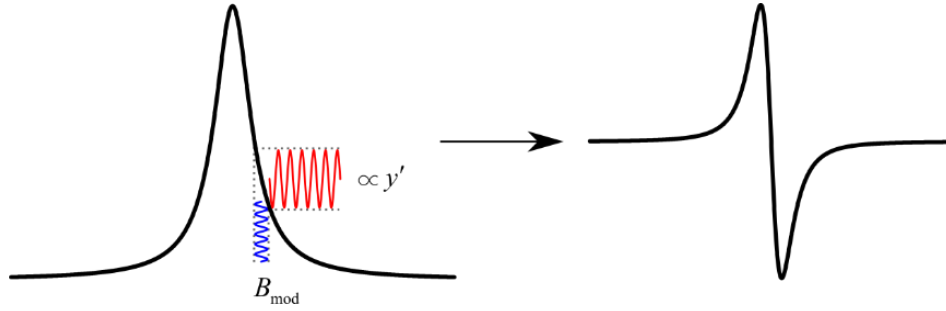
Figure 4-3 The effect of modulated detection, the absorption lineshape left and the first harmonic of y that is detected after lock in detection.

4.2.2 Modulation

Low magnetic susceptibly and dilute paramagnetic systems, coupled with the low powers for B_1, mean the microwave absorption measured by the bridge is small. Therefore, lock in detection is utilised and a sinusoidally oscillating field of amplitude B_m and frequency v_m is applied parallel to B_0. Typically, v_m of 100 kHz; the detector noise has been reduced below other noise sources at these frequencies [13]. B_m should be a tenth of the natural EPR linewidth to avoid distortion [2], greater amplitudes are often used sacrificing precise lineshape in favour of the increased signal offered by larger modulation amplitudes.

The key to lock in detection is a mixer which multiplies the detected EPR signal with a reference signal at the same v_m. The output of the mixer can be decomposed into two components: one with the sum of the input frequencies and a second with the difference. By applying a low pass filter to remove the high frequencies, a DC signal proportional to the EPR signal is created. The signal is also proportional to the cosine of the phase difference between the modulated EPR signal and reference signal. The demodulated DC signal output is proportional to the gradient of the resonance lineshape, hence EPR is recorded as the first harmonic of the absorption line (Figure 4-3). For SP-EPR the maximum signal is found when the phase difference is zero but for RP-EPR$^{(FM)}$ the maximum is found with a phase difference of 90°.

4.2.3 The microwave bridge

The source of the microwaves for modern EPR spectrometers is a Gunn diode. Microwave frequencies are classified into bands with names derived from their military use, the most common are shown in Table 4-2 with the resonant field for a g_e defect. Only X and Q are used in this thesis but multi-frequency EPR is a key tool in the identification of paramagnetic centres. Since $g\mu_B B_0$ is dependent on field but hyperfine splitting is not, multi frequency work provides a way of distinguishing them. The field dependence of the Zeeman splitting can also be used to separate defects with different g at high fields which may overlap at low fields. Paramagnetic relaxation mechanisms often have a field dependence and multi frequency measurements can help identify which is the dominant relaxation mechanism for a defect.

The output from the Gunn diode is initially split into two paths: the sample arm and reference arm. The desired power in the sample arm is set by an attenuator; the diode produces 200 mW but typically experiments on diamond are conducted at <1 µW. After attenuation the microwaves go through a circulator and are passed to the resonator. The microwaves that are reflected from the resonator are directed by the circulator to the detector diode. To keep the detector in the linear regime ~1 mW of microwaves in the reference arm is used to bias the diode [1]. The reference arm microwaves are passed through an attenuator and a phase shifter. Typically, in SP-EPR the reflected microwaves are mixed with the reference arm and the phase shifter is set so both arms are in phase, allowing detection of the absorption (imaginary) component of the EPR signal.

4.2.4 Resonators

To increase the sensitivity of EPR experiments the sample is placed inside a resonator which amplifies the signal by increasing the energy density at the sample. There are many types of resonator and cavity, dielectric and loop gap resonators have been used in this work (Table 4-3). All resonators need to be impedance matched to the microwave wave guides or coaxial lines. Coupling to an X-band cavity resonator is performed using a plastic screw with a metal tip situated at the interface of the cavity and the microwave wave guide. For systems that

have coaxial lines coupling is achieved through fine tuning the position of the resonator relative to the microwave aerial. Critical coupling of the resonator and line is crucial for EPR as it is much easier to detect the small changes in reflected power on a zero baseline.

Resonator	Description	Mode	Q_L	η	C (mT/$\sqrt{W}$)	Frequency
ER 4122SHQ	Spherical super high Q	TE011	7500	0.02	20	X-band
ER 4122SHQ-E	Cylindrical super high Q	TE011	7000	0.01		X-band
ER 4109HS	Cylindrical	TE011	5000	0.01		X-band
ER 4102ST	Standard rectangular	TE102	2500	0.01	14	X-band
ER 4118 MD5	Dielectric resonator	TE011	4000	0.06	42	X-band
			100		10	(overcoupled)
5L4G	Custom LGR	-	1000	0.50		X-band
EN 5107D2	Dielectric ENDOR		1000			Q-band
		TE011	1000			(overcoupled)
			2000			

Table 4-3 List of resonators used in this research. All resonators detailed are manufactured by Bruker expect for the LGR, adapted in part from [13]. Filling factors are for 10 mm of non-lossy sample in a 4 mm od EPR tube [7].

A cavity resonator is fundamentally a metallic chamber with dimensions that are comparable to the wavelength of the applied microwaves, that concentrates the microwave B_1 onto the sample position and keeps the associated electric field at a minimum at the sample. Cavities are classified by the modes which they support, these modes may be either transverse electric, TE, or transverse magnetic, TM. Superscripts are used to denote the number of half waves supported in each dimension. An example of the TE_{011} is shown in (Figure 4-4). For the cavity resonators used in the work the samples were mounted in dual axis goniometers which allow rotation about both the x and z axis. These sample holders enable precise alignment of the crystal and ensure repeatable positioning of the sample at the optimum position for the resonator.

Dielectric resonators consist of a ring of dielectric material that is non-lossy and has a high dielectric constant; often sapphire. Dielectric resonators tend to radiate microwaves and are therefore placed inside a radiation shield. The ability to overcouple dielectric resonators and
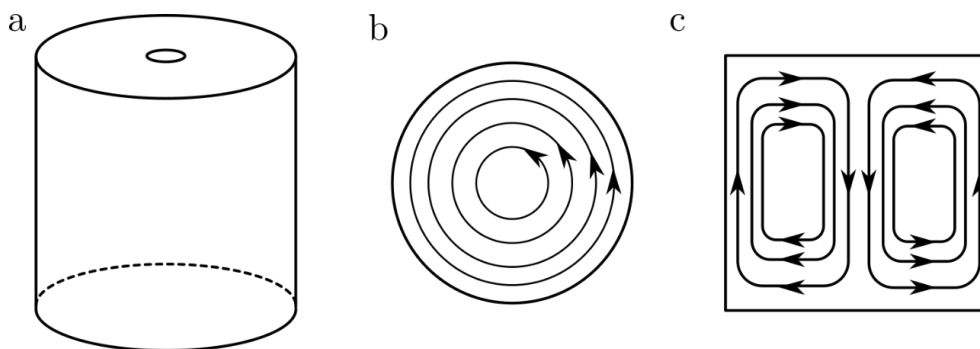
Figure 4-4 a, Basic geometry of a TE₀₁₁ cavity such as the Bruker ER 4109HS.
b, Top view of the cavity showing the electric field lines, note at the centre the value if zero.
c, side view of cavity showing the microwave magnetic field contours, the maximum B₁ is found at the centre
of the cavity. Adapted from [13]

deliberately reduce the Q to ~50 from at typical Q of 5000 when coupled, coupled with the increased filling factor (Table 4-3) make them ideal for pulsed EPR experiments. The electric field is essentially contained within the dielectric material making this style of resonator suitable for experiments requiring rotation of the sample. The sample is mounted on the bottom of polished EPR silent natural fused quartz rods or on Rexolite™ rods with ledges machined, which allow accurate height positions, held with a single axis goniometer to align the sample.

4.2.4.1   Loop gap resonators

Loop gap resonators, LGR, like dielectric resonators, take a different approach to cavity resonators and can be considered a lumped circuit. The idea of loop gaps was original developed by magnetron design [14] and later adapted for NMR [15] before finally being applied to EPR by Hyde and Froncisz [16]. The most basic design requires only a single loop and a gap to act as an inductor and capacitor respectively, and therefore they are modelled as LCR circuits. The resonance frequency of a LGR with n gaps capacitance, C, is given by [16]:

(4.7)
$$v_{res} = \frac{1}{2\pi\sqrt{LC}}$$

(4.8)
$$L = \frac{\mu_o \pi r^2}{Z} \quad \text{and} \quad C = \epsilon_r \epsilon_0 \frac{Zw}{nt}$$
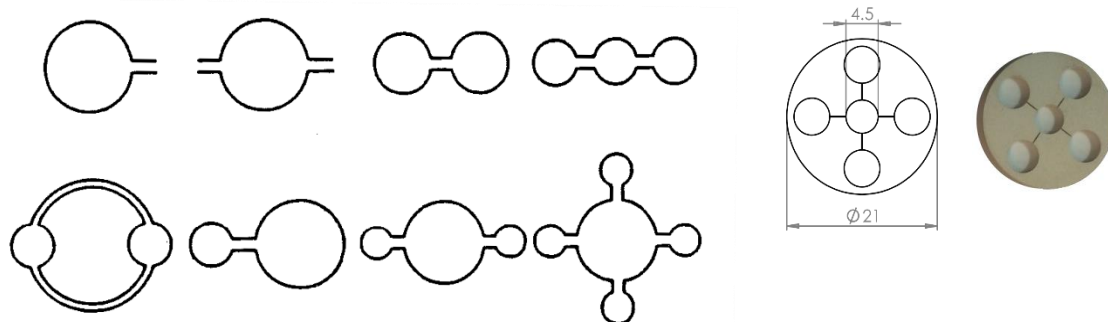
Figure 4-5 The cross section of a number of loop gap resonator designs (adapted from [27]) and the dimensions and photograph of the LGR used in this work.

where $\in_r$ is the dielectric constant between the gaps, Z the height of the LGR, w the gap width and t the gap thickness, r the radius and L the inductance of a single loop [16]. This relationship demonstrates that the thickness of the structure does not affect the resonance frequency. This is true in the absence of fringing effects and more accurate models including these effects have been described [7]. It is possible to tailor a loop gap to gain the maximum filling factor whilst maintaining a high resonance frequency. This can be achieved by reducing the size of the sample loop; this, however, will lower L requiring a proportionate increase in C commonly achieved by the addition of more gaps. Designs from the simple single-loop single-gap up to the multi-loop multi-gap *"rising sun"* have been reported [7]. Some common designs are seen in Figure 4-5.

The main advantages of LGRs are the increased filling factor compared to a cavity resonator, resulting in large signal from small samples, and efficient separation of electric and magnetic fields, with the electric field being confined to the gaps [7]. Along with these advantages LGRs have been produced to operate at frequencies from <1 GHz to 35 GHz [17,18]. They have been used in ELDOR experiments [19], Electrochemical EPR [20,21] and have been modified to allow optical access to the sample [22]. However, LGRs have lower Q_L than cavity resonators, advantageous in pulsed EPR but a drawback for SP-EPR experiments. LGRs can be experimentally difficult to use; a small working area requires careful sample positioning.

The LGRs used in this work are five-loop four-gap *"rising sun"* resonators (kindly produced by Tadaeusz Oles) with a resonance frequency of ~9.6 GHz. Figure 4-5 shows a LGR used in this work; it was machined from glass ceramic (Macor®) then electroplated with a layer of

silver sufficiently thin to allow the 100 kHz modulation to penetrate. LGRs like dielectric resonators have a tendency to radiate the microwaves away therefore require a microwave shield to maintain a reasonable Q_L. To combat this a foil 10 µm aluminium radiation shield is placed around the resonator. In these configurations Q_L ranging from $900 - 1200$ were measured with the sample in place. Despite the lower Q the increased η meant SNR was not compromised compared to a cavity resonator and the LGRs had a clearer background signal.

4.3 Pulsed electron paramagnetic resonance

The Bruker Elxysis E580 spectrometer was used for all pulsed experiments and its configuration for these experiments is shown schematically in Figure 4-6. Field control is the same as for CW-EPR operation but is set to the resonant frequency rather than swept.

The PatternJet II contains a number of SPFU (standard pulse former units) that are able to generate pulses. The SPFU produces low powered pulses with a 1 ns resolution by the rapid switching of PIN diodes. Multiple SPFU channels allow the generation of pulses that rotate the magnetisation around multiple axes and in different senses; this is required for phase cycling. At X-band the pulse sequence is passed to the bridge and the low powered pulses are amplified by a traveling wave tube amplifier, TWT, to a maximum power of 1 kW (Applied Systems Engineering, Inc. Fort Worth, Texas.). The absolute power of the pulse that is sent to the resonator is determined by an attenuator allowing control of the turning angle of the pulse. For Q-Band this second amplification stage is not employed. The pulses pass down a semi rigid coaxial cable to which the resonator is coupled. Due to the high power of the pulses the detector is protected during the pulse with a defence switch which attenuates the reflected power. The high power pulses can also cause ringing which may be powerful enough to damage the low noise amplifier and detector; it is therefore common for the defence circuit to be employed for a period of time after the pulse (detection *dead time")*.

The mixer is capable of quadrature detection of both the real and imaginary components in the rotating frame simultaneously. Both components are combined to produce the FID or echo response. The signal is digitised by a SpecJet II fast digitiser which has a 1 ns resolution. Data

points can be averaged on board or after transfer to the computer. When averaging it is important that the shot repetition time, SRT, is sufficiently long enough to allow the system to return to thermal magnetisation; a minimum SRT of 5 T_1 is required.

Figure 4-6   Schematic representation of the key components for a pulsed EPR spectrometer, adapted from [26].

4.3.1 Turning angle

The optimisation of the turning angle for a pulse length or power used in measurements is performed with the "*nutation sequence*". This three pulse sequence consists of an inversion pulse, followed by an echo detection sequence (*inv*-τ-π/2-τ-π). The inversion pulse is initially set to a very low turning angle, t_p =2 ns, the length of the pulse is then incrementally increased, creating larger turning angles. As the turning angle increases, the echo intensity follows a sinusoidal pattern, and the point of maximum inversion gives the optimum length for a π pulse at that power.

4.3.2 Phase cycling

Experiments with three or more microwave pulses can create unwanted echoes in addition to the primary echo. To combat this, phase cycling is employed. Phase cycling also has the benefit of removing any artefacts created by imbalances in the quadrature detection. Taking advantage of the different pathways to all the unwanted pulses, it is possible to use pulses in difference phases and then add or subtract the results to maximise the primary echo whilst

suppressing unwanted spectral features. In this work a 4-step and 16-step phase cycling programme was used to suppress unwanted echo refocuses.

4.4 Low temperature

In this work low temperature measurements between 4 and 300 K have been conducted on both the Bruker E580 and EMX spectrometer. The magnetic susceptibility of paramagnetic defects follows the Curie Law and therefore in the absence of microwave power saturation EPR signal intensity will increase proportionally to 1/T, and for a S=1/2 defect this means that the relative population of the high energy and low energy states is governed by the Boltzman population:

$$(4.9) \qquad \frac{N_\uparrow}{N_\downarrow} = \exp\left(-\frac{g\mu_B B}{k_B T}\right).$$

At X-band frequencies, this population difference is very small and can be simplified to $g\beta B \big/ 2k_B T$ and the magnetic moment can be approximated as:

$$(4.10) \qquad M = N\frac{g^2 \mu_B^2 B}{4k_B T}$$

Measurements were made with two different cryostats depending on the resonator being used: an Oxford Instruments ERS900 cryostat was used in conjunction with the cavity resonators and an Oxford Instruments CF935-O cryostat when using the dielectric or loop gap resonators (Figure 4-7). The presence of the quartz insert that is part of the ESR900 can considerably alter the B_1 and therefore results for saturation power and filling factor will not be directly comparable to measurements made without the cryostat in place [23].
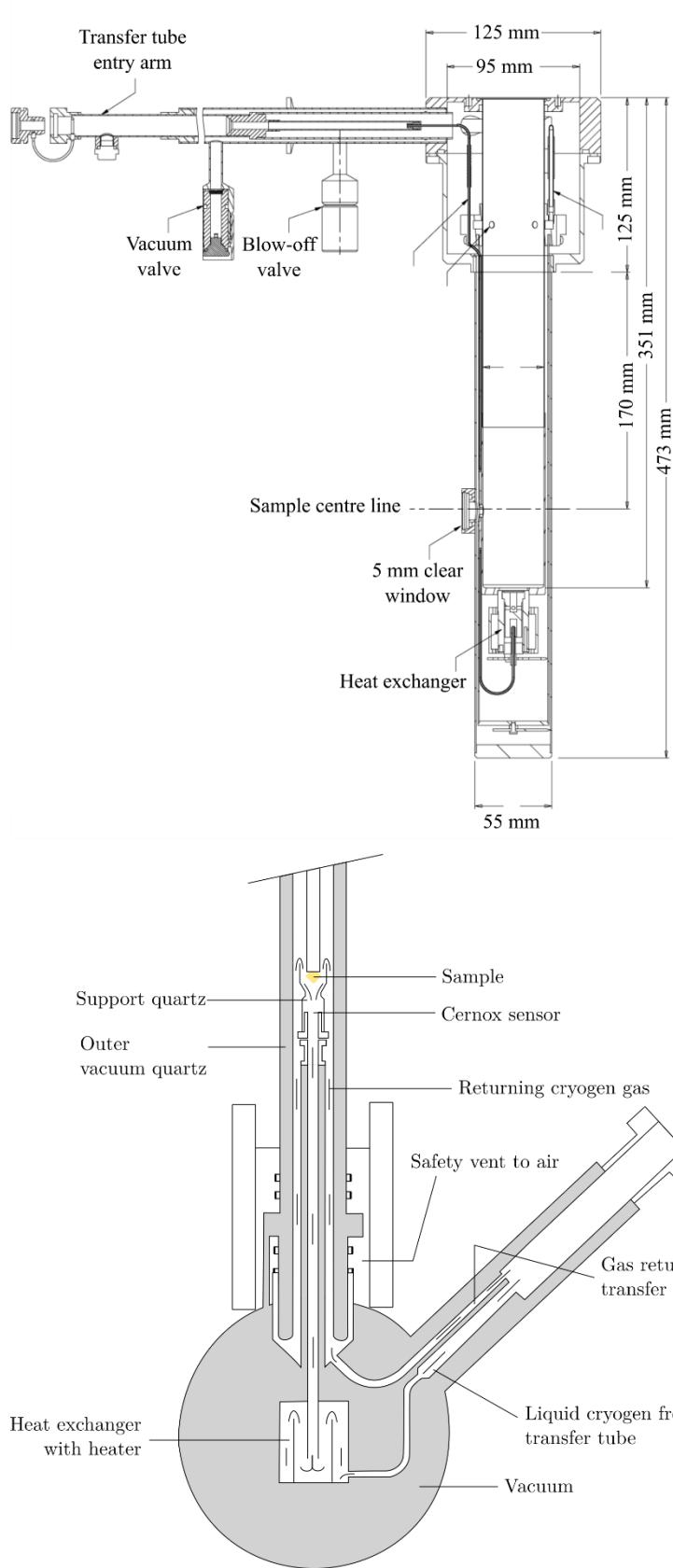
Figure 4-7 Schematic of cryostats used in this work.
top: Oxford Instruments CF935-O cryostat with optical access used with dielectric and LGR resonators.
Bottom: Oxford Instruments ESR900 continuous cryostat used for low temperature measurements with cavity resonators. Both figures adapted from those in the Oxford Instruments product guide [27]

Both Oxford Instruments ESR900 and CF9350-O use a reservoir of liquid cryogen; in this work liquid nitrogen for temperature >80 K and helium <80 K. Evaporated cryogen gas is drawn through an evacuated Oxford Instruments GFS300 transfer line into the cryostat where it passes through a heat exchanger then passes through a capillary and is sprayed directly onto the sample. The sample is mounted on a quartz rod and sits inside the quartz insert and is supported by a quartz egg cup shaped mount. After being sprayed onto the sample the low temperature gas is drawn back to the transfer line by a small pump (for the ESR900 the gas passes around the quartz insert).

For coarse control the sample temperature is achieved by altering the flow of the cryogen using an Oxford Instruments VC30 controller. An accurate temperature measurement is made using a Cernox™ sensor mounted just below the sample. An Oxford Instruments ITC503 uses the signal from this sensor to control the current passing to a heater in the heat exchanger thus ensuring stable fine control of the temperature at the sample.

4.5 EPR with in situ uniaxial stress

A new probe has been designed to allow the application of uniaxial stress *in-situ* during EPR measurements (Figure 4-8). The probe has been the work of previous group members and final construction was carried out for the results presented in this thesis; including modification to optimise performance. The probe is designed to be compatible with commercial spectrometers and cryostats and in principle can be operated at 4 K.

The generation of stress is the same as for previously documented optical probes [24] and uses compressed gas (nitrogen or compressed air) as the initial source of pressure. A Brokenhurst EL-Press 602CV mass flow controller connected to a computer with custom software[*] was used to regulate the pressure of the gas. The controlled gas is used to fill a pressure chamber containing a 3800(100) mm^2 piston. The pressure on the sample is proportional to the ratio of the area of the piston and the area of the sample and is given by:

---

[*] Written by group member B. Green.
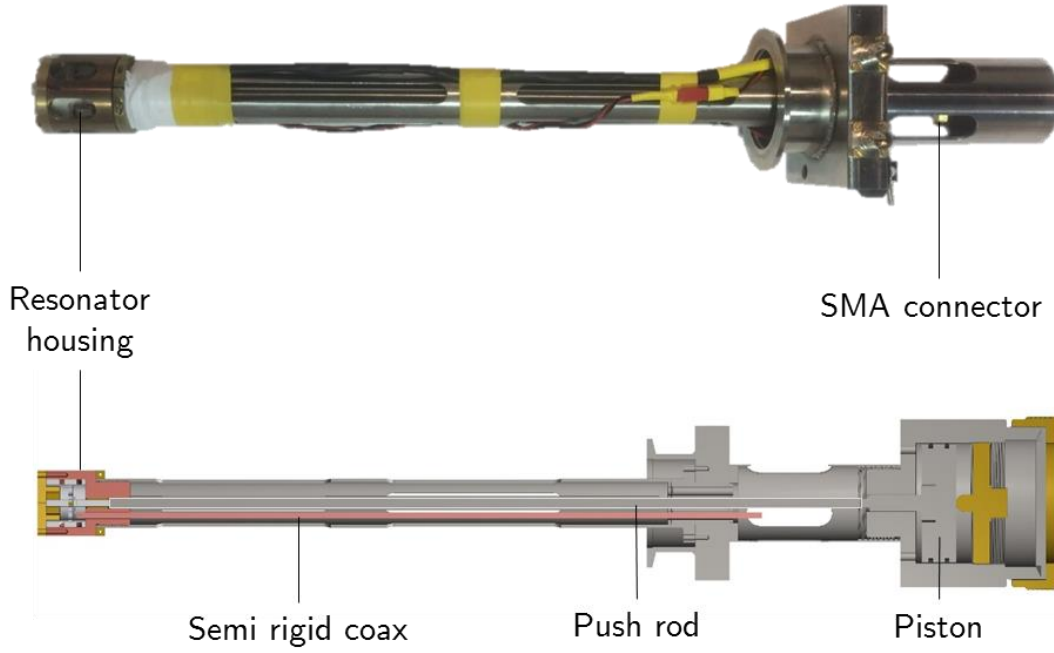
Figure 4-8 *The uniaxial stress probe with key components labelled. Top: photograph of the probe (note pressure vessel is removed). Bottom: cross section diagram.*

(4.11)
$$P_{sample} = P_{gas} \frac{A_{piston}}{A_{sample}}$$

The main difficulty in performing uniaxial stressed EPR is the limitation imposed by the use of non-magnetic materials, because of the large magnetic fields under which the experiments will be conducted. For this reason, the majority of the probe was built from 316 stainless steel and the resonator housing was machined from beryllium copper to minimise interactions with the magnetic fields. Transferring the pressure from the piston to the sample presents further problems since only non-conducting material can be used inside and close to the resonator. In previous work on silicon, PTFE was used for the final delivery of pressure [25] but large bulk modulus of diamond further limits the available materials to those with high compressive strength.

The push rod assembly used consisted of a 316 stainless steel rod from the piston to the outside of the resonance chamber and then short pieces of fused quartz rod inside the chamber (Figure 4-9). At the final interface between the push rod assembly and the sample was either a diamond anvil or PCD spreaders. At each interface of the push rod assembly the surfaces were polished
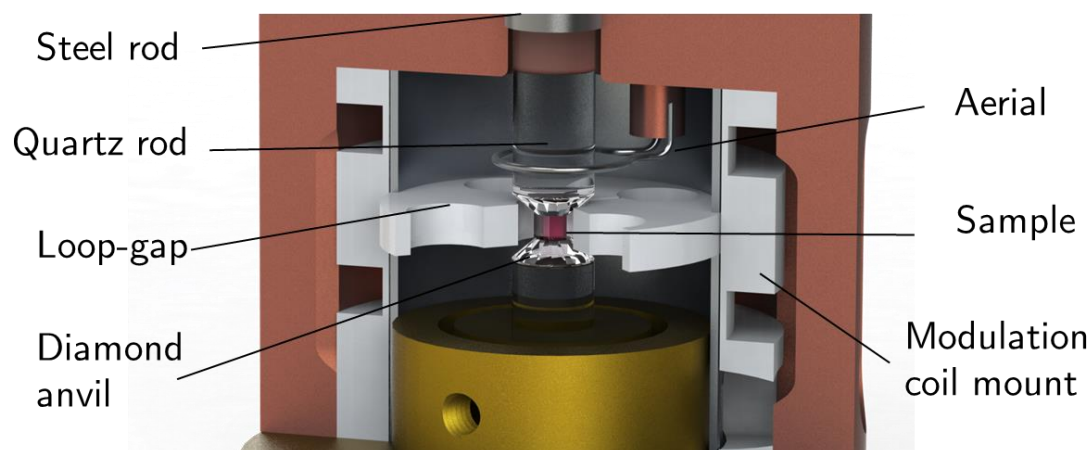
Figure 4-9   Cutaway diagram of the resonator housing with key components labelled.

to a mirror/optical finish and a Kapton® gasket was used to smooth any imperfections in the surface. The quartz rods are the weak link in this assembly and limit the maximum achievable pressure to 6 GPa for a 1 mm² sample (although a maximum of 3 GPa has so far been achieved). Sapphire has also been tested due to its higher compressive strength but was deemed unsuitable partly due to the high cost compared to quartz but also due to a tendency to fail catastrophically under high pressure.

A 5 loop 4 gap LGR was used, as described in §4.2.4.1. The height of these resonators is 2.5 mm therefore the sample nearly filled the central loop giving a high filling factor and therefore high SNR. This allowed the anvils to be kept away from the working area limiting any background signal; no signal from the polycrystalline diamond spacers or anvils was reported in any experiment conducted. The LGR was held in place with two Rexolite® spacers which were coated in 10 µm of aluminium foil and acted as a radiation shield. These spacers were held inside a Rexolite® spacer which housed a pair of saddle coils that served as modulation coils. This assembly was then positioned inside the beryllium copper housing and held tightly in place by the cap which was secured by 6 brass screws.

To ensure that the samples were subject to a uniform uniaxial stress, samples were carefully prepared with paired parallel faces of the same area. The samples were polished so that they were free from cracks under a x10 optical examination. Samples were thoroughly cleaned before each experiment since small dust particles can be a source of a fracture or cleavage. Kapton or PTFE gaskets were used on each diamond pushrod interface. Samples were prepared to

approximately 1.4 mm x 1.4 mm x 2 mm as this provided a compromise between the small geometry required for high pressure and making the sample too small from a spectroscopic view point.

4.6 Infra-red absorption spectroscopy

The optical absorption measurements presented in this work were conducted using a Perkin Elmer Spectrum GX FT-IR spectrometer. This spectrometer has an energy range of 0.04-0.96 eV (300-7800 cm^{-1}) and uses a glow bar light source and a triglycine sulphate detector. The sample compartment was fully purged during measurements with a flow of dry N_2 gas to minimise absorption from atmospheric water and CO_2. All measurements were conducted using a beam condenser that reduced the beam from a 6 mm to a 2 mm spot and also had the advantage of allowing horizontal mounting of samples. Samples were placed on an aperture of appropriate size to maximise sample cross sectional area.

Spectra were fitted using in-house software SpectrumManipulator [10]. Intrinsic diamond gives a characteristic absorption spectrum which has an absorption coefficient of 12.3 cm^{-1} at 2000 cm^{-1}. This spectrum can therefore be used as an internal calibration for converting absorbance to absorption coefficient for quantitative measurements.

4.7 References

[1]   Weil and J. R. Bolton, *Electron Paramagnetic Resonance*, 2nd ed. (Wiley & Sons Inc, New York, 2007).

[2]   G. R. Eaton, S. S. Eaton, D. P. Barr, and R. T. Weber, *Quantitative EPR*, 1st ed. (Springer, New York, 2010).

[3]   V. Nagy, Appl. Magn. Reson. 6, 259 (1994).

[4]   S. Y. Elnaggar, R. Tervo, and S. M. Mattar, J. Magn. Reson. 242, 57 (2014).

[5]   W. L. Hubbell, W. Froncisz, and J. S. Hyde, Rev. Sci. Instrum. 58, 1879 (1987).

[6]   S. V Sundramoorthy, B. Epel, and H. J. Halpern, J. Magn. Reson. 240, 45 (2014).

[7]   G. A. Rinard and G. R. Eaton, in *Biomed. EPR, Part B Methodol. Instrumentation, Dyn.*, edited by S. S. Eaton, G. R. Eaton, and L. J. Berliner (Springer, 1999), pp. 19–52.

[8]   C. Glover, A Study of Defects in Single Crystal Diamond - PhD Thesis, University of Warwick, 2003.

[9]   A. S. Stefan Stoll, J. Magn. Reson. 178, 42 (2006).

[10]   M. W. Dale, Colour Centres on Demand in Diamond - PhD Thesis, University of Warwick, 2015.

[11]   B. L. Cann, Magnetic Resonance Studies of Point Defects in Diamond - PhD Thesis, University of Warwick, 2005.

[12]   Bruker BioSPin, in *52nd Rocky Mt. Conf. Magn. Resoance* (2010).

[13]   C. Poole, *Electron Spin Resonance: A Comprehensive Treatise on Experimental Techniques*, 3rd ed. (Courier Dover Publications, 1983).

[14]   N. Kroll, *Microwave Magnetrons* (McGraw-Hill, New York, 1948).

[15]   W. N. Hardy and L. A. Whitehead, Rev. Sci. Instrum. 52, 213 (1981).

[16]   J. S. Hyde, W. Froncisz, and A. Kusumi, Rev. Sci. Instrum. 53, 1934 (1982).

[17]   W. Froncisz, T. Oles, and J. S. Hyde, J. Magn. Reson. 82, 109 (1989).

[18]   W. Froncisz, T. Oles, and J. S. Hyde, Rev. Sci. Instrum. 57, 1095 (1986).

[19]   J. S. Hyde, J. J. Yin, W. Froncisz, and J. B. Feix, J. Magn. Reson. 63, 142 (1985).

[20]   M. A. Tamski, J. V Macpherson, P. R. Unwin, and M. E. Newton, Phys. Chem. Chem. Phys. 17, 23438 (2015).

[21]   R. D. Allendoerfer, W. Froncisz, C. C. Felix, and J. S. Hyde, J. Magn. Reson. 76, 100 (1988).

[22]   M. Dutka, O. Tadeusz, M. Mossakowski, and W. Froncisz, J. Magn. Reson. 210, 44 (2011).

[23]   N. D. Yordanov and P. Slavov, Appl. Magn. Reson. 10, 351 (1996).

[24]   S. Liggins, Identification of Point Defects in Treated Single Crystal Diamond by Department of Physics - PhD Thesis, University of Warwick, 2010.

[25]   G. D. Watkins and J. W. Corbett, Phys. Rev. 121, 1001 (1961).

[26]   Bruker, *Elexsys E500 User's Manual* (Bruker Instruments, Inc., 2001).

[27]   Oxford Instruments, *ESR 900 , ESR 910 and CF 935 Cryostats - DF OI64802104* (Oxford Instruments Superconductivity Limited, Oxford, 2004).

Chapter 5

5 Quantification of nitrogen in diamond

5.1 Introduction

Nitrogen is the dominant impurity incorporated during growth of synthetic diamond in the absence of intentional doping. The form in which it incorporates will depend on the growth and treatment history of the sample. Nitrogen may be found as a substitutional defect, N_S, or as the basis for other complexes such as, A-centres, B-centres, NV, N_2V, NVH. This chapter focuses on improving the quantification of nitrogen in diamond, specifically the paramagnetic N_S^0.

The amount of nitrogen used in the source gases during CVD growth has been shown to affect not only the growth rate but also the morphology of the diamonds produced [1–3]. There is growing demand for highly pure diamonds for use in optical devices, electronic devices and sensors, but the requirements for these devices are not the same. Electronic grade material has a concentration of N_S^0 <1 ppb creating a near spin free material ideal for quantum applications. The low levels of nitrogen in the growth chemistry lead to low growth rates and create highly strained material with large birefringence. However, increasing the nitrogen in the source gases to a few ppm alters the morphology of growth and reduces dislocations. The subsequent reduction in the birefringence comes at the cost of a small increase in absorption, but the material is ideal for optical applications.

Nitrogen affects the properties of the diamond. The most obvious is the colour; high concentration of nitrogen creates yellow or brown diamonds. This increased absorption reduces the use of diamonds for optical applications. The thermal conductivity is found to be greatest in Type IIa diamonds (2000 W m^{-1}K^{-1}) [4] and lower in Type Ia diamonds, where Martinez found a reduction in thermal conductivity proportional to nitrogen concentration [5]. The hardness of diamond is affected by the concentration of nitrogen. Increasing the concentration

of nitrogen leads to a reduction in the damage sustained by a diamond undergoing solid particle erosion [6].

Depending on the form of the nitrogen, and information about it required, there are a number of methods of detection. SIMS can provide the total concentration of nitrogen in a sample and has a lower limit of detection ~100 ppb for nitrogen in diamond [7]. SIMS provides no information about the form of nitrogen and also causes undesired damage to the sample.

Optical absorption techniques have long been key tools in the quantification of nitrogen. IR spectroscopy is routinely used for quantification of A- and B-centres as well as N_S^+ and N_S^0. UV-Vis spectroscopy can also be used for detection for N_S^0 and many other nitrogen related defects including NV^-, NV^0 and N_3V. These techniques require special preparation of the sample to provide parallel polished faces. Overlapping spectra from other impurities can lead to misidentification of a defect; over-estimation of concentrations is also a potential problem. The lower limits for N_S^0 detection are 0.5 ppm in IR [8] and in UV-Vis [9] it is possible to detect 0.3 ppm using the 400 nm absorption.

Electron paramagnetic resonance, EPR, is a powerful tool for the study of paramagnetic centres in diamond since the signal not only provides information about the structure of the defect but also on the number of spins present. The practical lower limits for N_S^0 detection with SP-EPR is ~20 ppb and RP-EPR$^{(FM)}$ can extend this to ~1 ppb [10]. Due to the electronic properties of the NV^- defect it is possible to detect a single centre using optically detected magnetic resonance [11]. However, the potential range of defect concentrations that can be found in diamond can cause issues when quantifying samples; for example even with commercial products the incorporation of nitrogen can range from <1 ppb for an electronic grade CVD plate [12] to >500 ppm in a Type Ib HPHT plate [13]. Substitutional nitrogen is only paramagnetic when in the neutral charge state. This can cause a problem for EPR if there is a population of electron acceptors in the sample. Charge transfer between nitrogen and, for example, vacancies can lead to underestimation of nitrogen concentration. This is not a

problem in high purity samples where limited acceptor population leads to nearly 100% N_S^0 charge balance.

There are also problems associated with the range of sizes that synthetic diamonds are now presented for quantification. In the past it has often been assumed that the diamond under investigation is effectively a point sample but this assumption does not always hold true because of increased interest in quantification of diamond grit and powders [14], and improved growth mechanisms leading to very large synthetic samples [15].

In this chapter, field modulated rapid passage EPR, RP-EPR[(FM)], will be investigated with a view to lowering the detection limits of diamond or reducing the time to acquire spectra of high purity samples. The effect of sample size and shape on the resonator will be investigated with a view to providing a better understanding of potential errors on quantitative measurements. Finally, a suite of high concentration samples is investigated to ensure that upper bounds of detection have not been met.

5.1.1 EPR detection limits

Hyde is reported to have said that "of all the measurements one can make with EPR equipment, the determination of absolute spin concentration is the most difficult" [16], a view shared by eminent members of the field nearly fifty years later [17]. To establish the minimum possible spin sensitivity, a number of factors which affect not only the signal intensity but also the noise of the spectrometry must be considered. For a spectrum recorded at unsaturated microwave power the minimum number of spins measurable, $N_{\min}$ in a 1 Hz bandwidth is approximated by [18]:

$$N_{\min} = \frac{12\pi V_c k_B T_s \Gamma}{\mu_0 g^2 \mu_B^{\ 2} S(S+1) B_r Q} \left(\frac{F k_B T_d}{P_{\mu w}} \right)^{1/2}$$

(5.1)

Where V_c is the volume of the cavity, T_s and T_d are the temperature of the sample and detector respectively, Γ is the HWHM linewidth, B_r is the resonance field, F is a noise factor

attributed to thermal noise of the detector and all other symbols have their normal meaning. This equation predicts that for a SNR of 1 $N_{\mathrm{min}} \approx 10^{10}$ spins/mT; assuming $F = 100$ and $P_{\mu w} = 100$ mW.

Commercial EPR spectrometers have a quoted spin sensitivity of 1.7×10^{11} spins/mT for a one second acquisition time [19,20]. In the most commonly used sensitivity test, the sample used is weak pitch with approximately 10^{13} spins/cm of length [19]. The sample is typically 2 cm long, roughly twice the length of the high sensitivity part of a HS cavity, giving a filling factor of around 1.6% [17]. The weak pitch is measured at a slightly saturated microwave power (2 mW), to give peak signal.

A diamond sample with 1 ppb of N_S^0 will contain 2×10^{14} spins/cm^3; for a typical diamond of size 5×10^{-3} cm^3 this gives 10^{12} spins. The spectrum for N_S^0 has 1.6×10^{13} spins/mT; once the hyperfine splitting from the ^{14}N (I=1) which reduces the intensity in each line by a third and a typical EPR line width of 0.02 mT are taken into account. Such a spectrum should be well within detectable limits for SP-EPR but despite this it is found in our lab that for an acquisition time of 68 hours, the practical limit for quantification for SP-EPR is closer to 20 ppb.

To understand why the stated detection limits are not achieved it is important to consider the difference between the potential ideal test measurement and a typical measurement made of a diamond. Changes in any of the parameters outlined in §4.1 may reduce the sensitivity; the key parameters are sample size and microwave power.

When measuring diamonds, it is normally the concentration sensitivity that is important rather than absolute sensitivity, as such smaller samples that reduce filling factor will have a lower EPR response and therefore sensitivity. For a typical diamond 5×10^{-3} cm^3 the filling factor will be reduced by a factor of 13 compared to the standard weak pitch sample.

The dominant reduction in sensitivity comes from microwave power. High purity CVD diamonds have relatively long relaxation times; a sample with N_S^0 40 ppb will have a $T_1 \sim 1.5$ ms and a $T_2 \sim 2$ μs at room temperature. This requires that very low microwave powers are used to avoid the problems associated with power saturation. Typically, the spectra of a high purity diamond sample must be acquired with powers of 2 nW or lower whilst a spectra of a reference sample for sensitivity are typically acquired at 2 mW. Signal response is linear to the square root of microwave power; when unsaturated, this represents a factor of 10^3 decrease in sensitivity.

It is potentially possible to gain improvements in concentration sensitivity by increasing the measurement time. In our lab the maximum reasonable acquisition time for a sample is 68 hours (ie a weekend run) or ~ 1500 scans. As SNR increases proportionally to $\sqrt{N}$ when noise is random, this generates a 40-fold increase in SNR compared to a single scan. To acquire over a longer time brings with it issues of spectrometer stability and puts large pressure on spectrometer availability in a busy lab.

5.2 RP-EPR

Comparison of the signal to noise achievable with different EPR techniques offers potential for reductions in detection limits. Direct detected RP-EPR[DD] has been shown to offer a factor of 25 greater SNR in the same acquisition time in N@C_{60} when compared to SP-EPR and a factor of 3 in a shorter acquisition time compared to FT-EPR [21]. The majority of recent work on RP-EPR has focused on direct detection, without modulation of the static field, which is possible due to the increased signal [22,23]. The absence of field modulation allows the collection of undistorted line shapes which has enabled the measurement of inter spin distances [23,24]. The absorption line shape recorded in direct detected RP-EPR imaging has advantages for imaging; the absorption line decreases linearly with increasing field gradient instead of quadratically as found with the first derivative. Direct detected RP-EPR imaging has been conducted at X-Band (nominally 9.8 GHz) as well as at 250 MHz, opening up the possibility for *in vivo* applications [25,26].
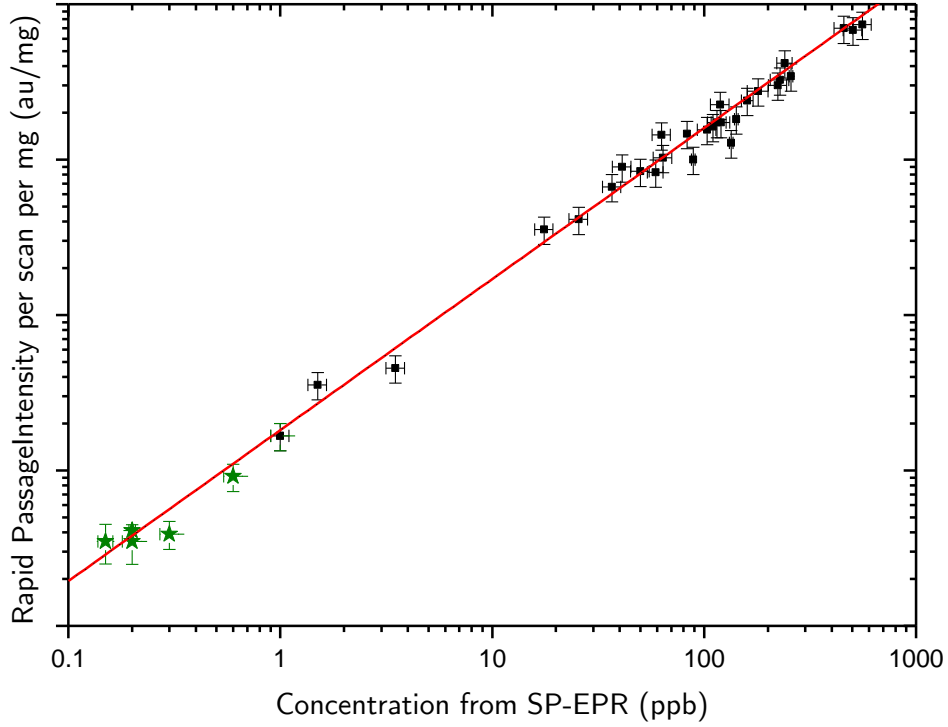
Figure 5-1   The RP-EPR$^{(FM)}$ integrated intensity of the N_S^0 signal plotted against the concentration determined by SP-EPR, both measurements at X-Band. The green stars represent data where only determination of an upper limit on concentration was possible from SP-EPR and are omitted from the fit. Red line is a linear fit to the data. Adapted from [10] with additional data from this report.

	RP-EPR	Fourier transform EPR	Field swept echo detected EPR	SP-EPR
SNR	3800	-	-	25
Acquisition time (hours)	3	-	-	3
SNR (SNR/s)	116	260	64	<1
Acquisition time (s)	15	240	30	20

Table 5-1 Table of SNR for different EPR techniques. Upper values are from this laboratory on a sample containing 20 ppb N_S^0 using field modulated RP-EPR$^{(FM)}$. Bottom results are of a sample containing 40 ppb N_S^0 and using direct detected RP-EPR from [21].

Direct detected and field modulated RP-EPR have been shown to offer increased SNR for N_S^0 (Table 5-1). RP-EPR$^{(FM)}$ performed quantitatively on commercial spectrometers has been found to be sensitive to a lower limit of 1 ppb N_S^0 in CVD diamonds [10], see Figure 5-1. Quantification using RP-EPR$^{(FM)}$ does have limitations, overlap of resonances for two different defects allowing cross relaxation will cause an underestimation. T_2 is dependent on the concentration of other paramagnetic centres and this means there is an upper limit to the application of RP-EPR$^{(FM)}$ of approximately 1 ppm [10]. Below 1 ppm the population of N_S^0

is dilute in the lattice and further reduction in concentration does not significantly alter T_2 [27]. This means that the same sweep rate can be used for many concentrations and there is no lower limit to quantification imposed by the RP-EPR conditions, but the current RP-EPR$^{(FM)}$ protocols have a lower detection limit for quantitative measurements of 0.5 ppb for a 50 mg sample with a 68 hours acquisition time.

5.2.1 Repeatability

Field modulated RP-EPR can be employed to increase sensitivity when examining samples with long relaxation times. Diamonds typically have long T_1 relaxation times and high purity samples also have increasingly long T_2 relaxation times. With an increasing interest in high purity samples for quantum technology applications [28], it is important to understand the errors associated with this technique and potential methods for reducing detection limits or increasing lab throughput.

5.2.1.1   Method for repeatability measurements

An investigation was conducted into the repeatability of RP-EPR$^{(FM)}$ to establish the magnitude of associated errors for quantitative measurement. A large number (85) of separate scans of the 0577207-C(ii) were taken over a period of three weeks. Both the Bruker E580 spectrometer fitted with the SHQ-E resonator and Bruker EMX-E spectrometer fitted with the SHQ resonator were used. To minimise errors from position the sample was mounted in a dual axis goniometer and held in place using a polystyrene insert; great care was taken to align along a [001] crystallographic direction. Between each measurement the sample was removed from the resonator and sample mounting, and was then remounted and repositioned before alignment and tuning procedures were repeated before the next measurement. A second set of measurements (60 scans) was made under the same conditions but with the diamond in a random orientation. Concentrations were found from the fitted spectra using the methodology outlined in §4.1.4.

5.2.1.2 Results and analysis of experiments into the repeatability of RP-EPR$^{(FM)}$

A histogram of the results of both studies can be found in Figure 5-2 illustrating the deviation in concentrations associated with random errors. The mean value of the distributions was set to 41 ppb, the known concentration of N_S^0 for this sample, previously established from rigorous CW-EPR measurements. The SNR for each spectrum was 360(20); therefore, this was not a significant source of error. For the aligned measurements the standard deviation, σ, was found to be 0.9 ppb (2.5%) and all outlying data points were found to be within 7% of the mean value. When the sample was misaligned a σ of 2.1 ppb was found with all outliers falling within 13% of the mean value. This results in a random error of 2% and 4% for aligned and un-aligned quantitative measurements of the N_S^0 centre respectively.

These results compare favourably with similar studies of SP-EPR conducted on a high nitrogen sample, Syn93-04, where a σ of 5% were reported [29]. The previous study was conducted in this lab on the same spectrometers but with a different fitting package, EPRng [29]. as such it was important to ensure that the improvement was not because of the change in software. To this end SP-EPR spectra of N_S^0 were simulated in EasySpin [30] and noise added (white, Gaussian and uniform noise functions from EasySpin) to give a signal to noise ratio, SNR, of 50:1, which is a typical value for a reference scan. The two fitting packages, EPRng and EPRSimulator were found, not surprisingly, to perform far better when fitting simulated data than when fitting experimental data, with a standard deviation of σ = 0.4% and σ = 0.3% respectively. This indicates that the dominating source of deviation is experimental error not fitting and that the different fitting does not account for the increased repeatability.

With EPRsimulator it is possible to *"align the simulation to the spectrum"* [31] and for N_s^0 this provides a consistent fit to the spectrum at any orientation when using SP-EPR. However, for RP-EPR$^{(FM)}$ there is an issue with fitting the N_S^0 when B_0 is not aligned along [001]. At other alignments the hyperfine lines of the spectrum do not have a uniform intensity (Figure
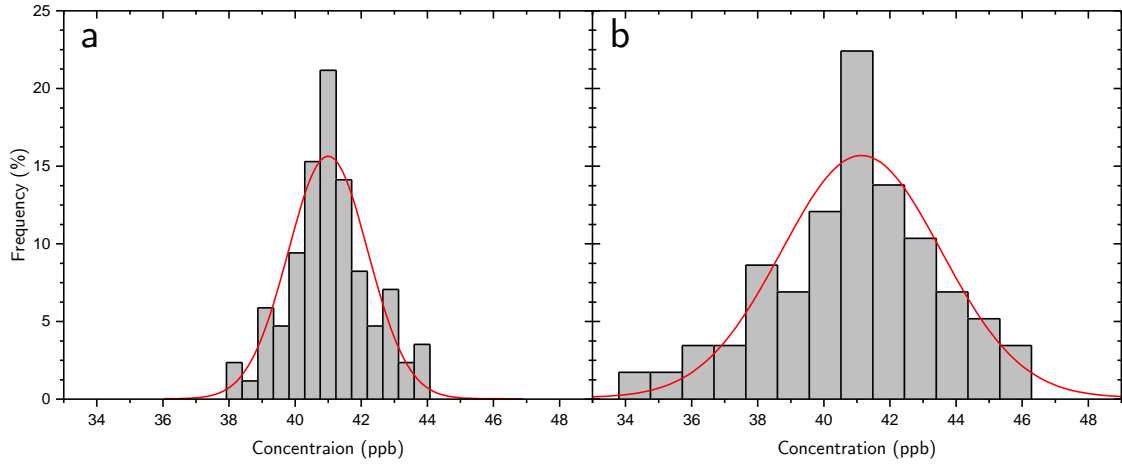
Figure 5-2 Histograms showing the reproducibility of quantitative measurements for RP-EPR$^{(FM)}$. The grey bins are set to half standard deviation (σ) and the red line shows a Gaussian fit to each data set.
a, RP-EPR$^{(FM)}$ on 0577207-C(ii) with the B_0 parallel to the [001] crystallographic direction, σ=0.9 ppb.
b, RP-EPR$^{(FM)}$ on 0577207-C(ii) with the B_0 aligned in arbitrary crystallographic direction, σ=2.1 ppb

5-3). To investigate this each spectrum was fitted to nine independent Voight lineshapes; four each for all the orientations of the $m_I = +1$ & $m_I = -1$ hyperfine lines and the final one for the $m_I = 0$ transition. This *"allowed"* the different intensities for each line to be measured and each set of orientations of hyperfine lines ($m_I = +1$ & $m_I = -1$) was found to have the same total intensity of the $m_I = 0$ line within 2%. The hyperfine lines were found to have a reduced line width typically 0.015(3) mT compared to 0.020(1) mT for the $m_I = 0$ EPR transition.

There are two factors that created the reduction in random error associated with RP-EPR$^{(FM)}$ compared to SP-EPR for a sample aligned with B_0 along the [001] crystallographic direction. Firstly, the increased SNR for RP-EPR$^{(FM)}$ compared to the SP-EPR; a typical scan of 0577207-C(ii) in RP-EPR$^{(FM)}$ has SNR of <300, whereas a SP-EPR scan of Syn93-04 has a SNR ~50:1. Secondly, the narrower linewidths for RP-EPR$^{(FM)}$ lead to a smaller uncertainty of the orientation of the diamond when slightly misaligned away from the principal axis. This greater certainty translates to an improved fit for the simulation to the experimental spectrum.

The explanation for the difference in hyperfine intensities between defect orientations seen when B_0 is aligned other than parallel to the [001] crystallographic direction, could be that there is insufficient time between resonances to allow the resonance to be at equilibrium, due to cross relaxation between sites. N_S^0 has been previously shown to cross relax between
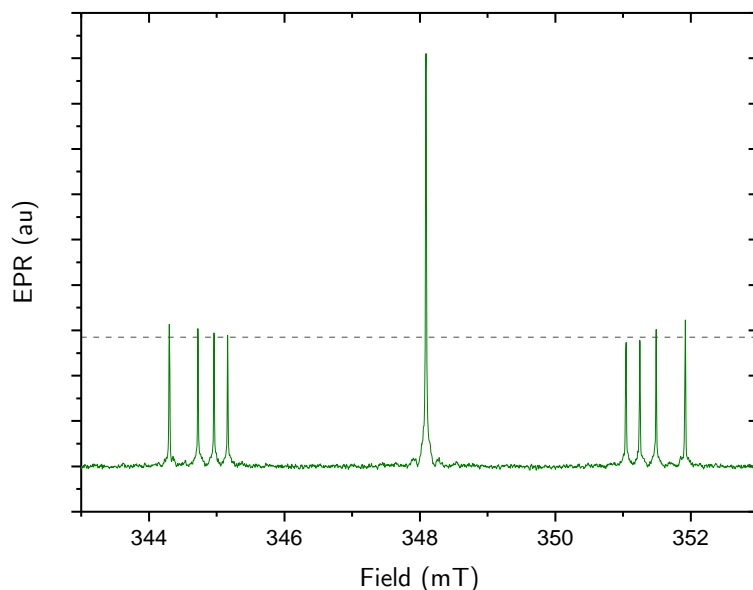
Figure 5-3   Typical spectrum of 0577207-C(ii) not aligned along the principal direction ($\theta=103°$, $\varphi=67°$) showing the unequal hyperfine transition intensities. Dotted line indicates the expected intensity of hyperfine lines.

different orientations [32] and is known to rotate between orientations at room temperature [33]. It is therefore possible that the first resonance reached alters the population of the remaining orientations for that transition. Since it is invariably the orientation with the largest splitting that has the largest signal for both the $m_I = +1$ and the $m_I = -1$ hyperfine lines this seems unlikely as the orientations are brought into resonance in the opposite order. Another explanation is that the four orientations now have different relaxation times leading to a different response; RP-EPR$^{(FM)}$ has a relaxation related response.

5.2.2 Temperature

An option that may offer increased signal response from the same number of spins, and therefore reduce detection limits further, is to lower the temperature at which the experiment is conducted. In the absence of microwave power saturation EPR signal intensity is inversely proportional to temperature. For an S=1/2 defect the intensity of the EPR signal should increase relative to the ratio of the temperatures offering a potential 3.5 times improvement in signal at 77 K compared to room temperature measurements.

Such gains are often not realised when performing low temperature SP-EPR on diamond. Relaxation times increase at lower temperatures [34] exacerbating problems of microwave

power saturation; therefore, microwave power must be reduced to reach the linear regime, offsetting any gains. For high purity samples, it may not be possible to reduce microwave power enough to access the linear regime. RP-EPR$^{(FM)}$ is performed at much higher powers and therefore may potentially be less affected by the problems associated with low temperature SP-EPR measurements.

5.2.2.1 *Experimental: temperature dependence*

To investigate the possible gains from cryogenic temperatures 0577207-C(ii), (N_s^0 = 41 ppb) was scanned for the same acquisition time at varying temperatures with B_0 aligned along the [001] crystal direction. Measurements were taken on the X-band Bruker E580 Spectrometer equipped with a MD-5 Flexline resonator and cooling was achieved using an Oxford Instruments CF935. Sweep rate, modulation amplitude and acquisition time were kept constant for each temperature but a microwave power sweep was conducted at each temperature to ensure that the spectra were recorded at maximum SNR (Table 5-2). Q was also recorded at each temperature to account for changes induced by the altered resistance of the metal used in the MD-5 resonator at cryogenic temperatures [35].

Temperature (K)	Sweep (mT)	Sweep Rate (mT/s)	Conversion time (ms)	Time Constant (ms)	No. scans	Power (µW)	Modulation Amplitude (mT)	Phase (°)
300 − 77	20	1.91	2.56	2.56	200	Optimised	0.002	90

Table 5-2 List of experimental parameters used to investigate the effect of temperature on RP-EPR$^{(FM)}$

The noise associated with each spectrum was determined by finding the root mean square of the first 350 data points in the spectrum. The first 350 points were chosen which occur before any spectral feature and are essentially flat, since cavity background often associated with EPR is not seen in RP-EPR$^{(FM)}$. The measured noise was invariant with temperature across the range measured. Signal intensity was found from fits to the data using EPRSimulator and the peak integrated intensity was recorded.
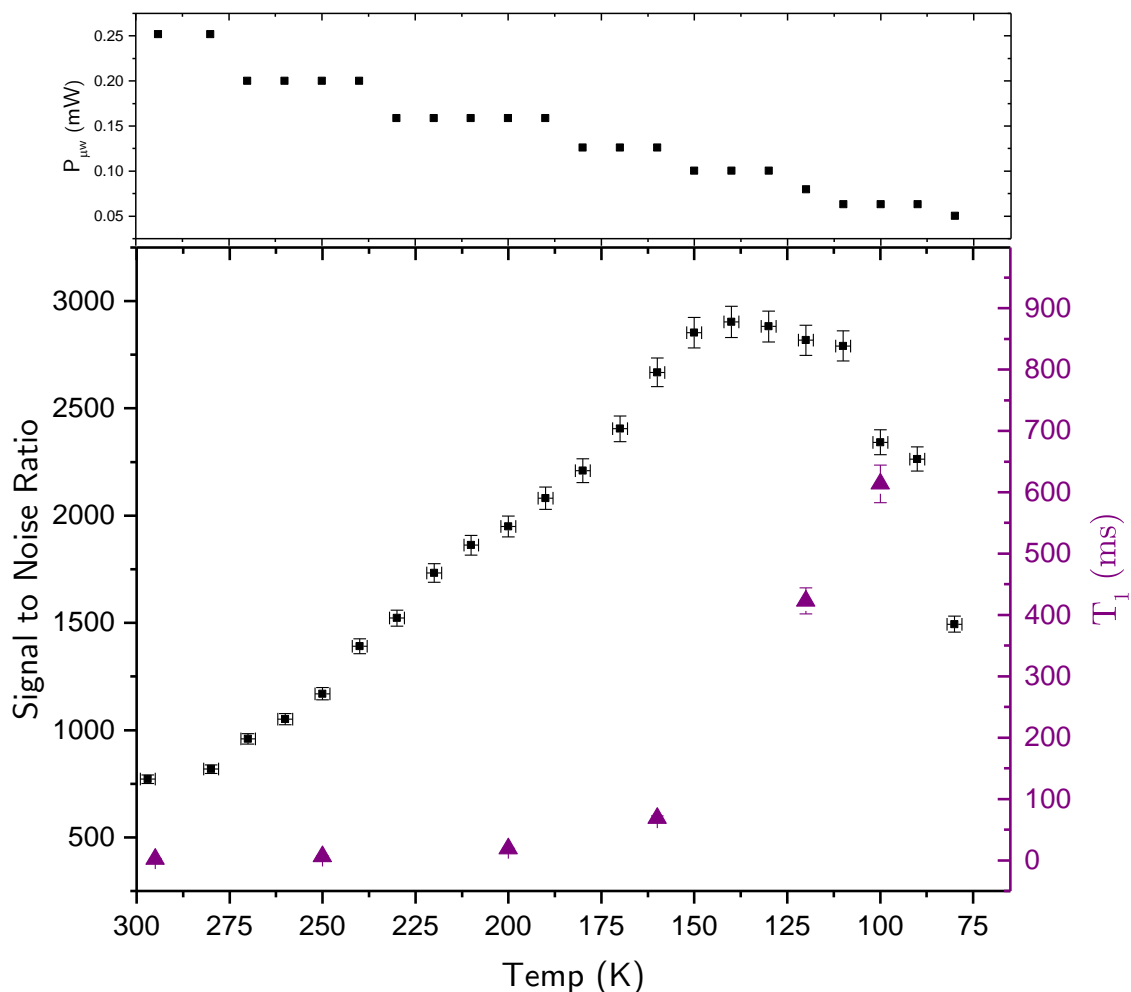
Figure 5-4 The SNR ratio for RP-EPR$^{(FM)}$ against temperature. All measurements were made for the same acquisition time (200 scans). The data shown is for the $m_I=0$ transition of N_S^0. The right axis and Purple data points show the change in T_1 for N_S^0 with temperature. The upper graph shows the optimised $P_{\mu W}$ used at each temperature.

5.2.2.2 Results for temperature dependence

The result for the $m_I = 0$ hyperfine line can be seen in Figure 5-4. The EPR line width of the spectrum did not change and was 0.02 mT at all temperatures. The cavity Q_l however, increased from 9200 to 12500 as the temperature was lowered from 290 K to 80 K. The microwave power at which peak signal was also found to decrease with temperature from 0.25 mW at room temperature to 0.05 mW at 80 K.

The behaviour of the signal intensity can be split into two regions, the first between 297 K and 150 K and a second region below 150 K. In the 297 K to 150 K region the SNR rapidly increases linearly as the temperature drops; this increase is far faster than would be expected from the Curie Law. The maximum signal intensity is found at 150 K and is 3.7 times that

found at room temperature, nearly twice that expected. In the region below 150 K, reduction in temperature does not lead to further increases in SNR and for temperatures below 120 K the SNR reduces.

Temperature (K)	T_1 (ms)	Time between Resonances (T_1)
295	2.40(5)	740
250	19.0(5)	90
200	69.0(5)	25
120	420(5)	4
100	610(5)	2

Table 5-3 T_1 times for 0577207-C(ii), indicating the time between "allowed" transitions in units of T_1.

In the room temperature to 150 K regime it is possible to account for some of this increase by the improvement in Q for the resonator but even after correcting for this, an increase of a factor 3.2 compared to room temperature is found. This additional improvement is attributed to the increased T_1 relaxation times as the temperature is reduced (Table 5-3). The source of this is discussed in §5.2.4.

The intensity of the three N_S^0 hyperfine lines were not equal (Figure 5-5a) at temperatures below 150 K. The distortion in the spectrum at 100 K was found to reduce if the sweep rate was reduced. The intensity of the peak heights was found to return to equal values for the three *"allowed"* transitions if a 60 second sweep time was used; equivalent to 20 T_1 between resonances, Figure 5-6. If the distortion was caused by interactions between the *"allowed"* transitions the return to equilibrium would be expected once the time between resonance was greater than 5 T_1 but peak intensities were not the same until >14 T_1 between resonances. As well as the EPR *"allowed"* transitions there are also the double spin flip *"forbidden"* transitions which are resonant at fields between the *"allowed"* transitions for N_S^0 aligned with B_0 parallel to the [001] crystal direction (Table 5-4 & Figure 5-5b). And although *"forbidden"* transitions have reduced transition probabilities compared to the *"allowed"* transitions they may be the source of the spectral distortions.
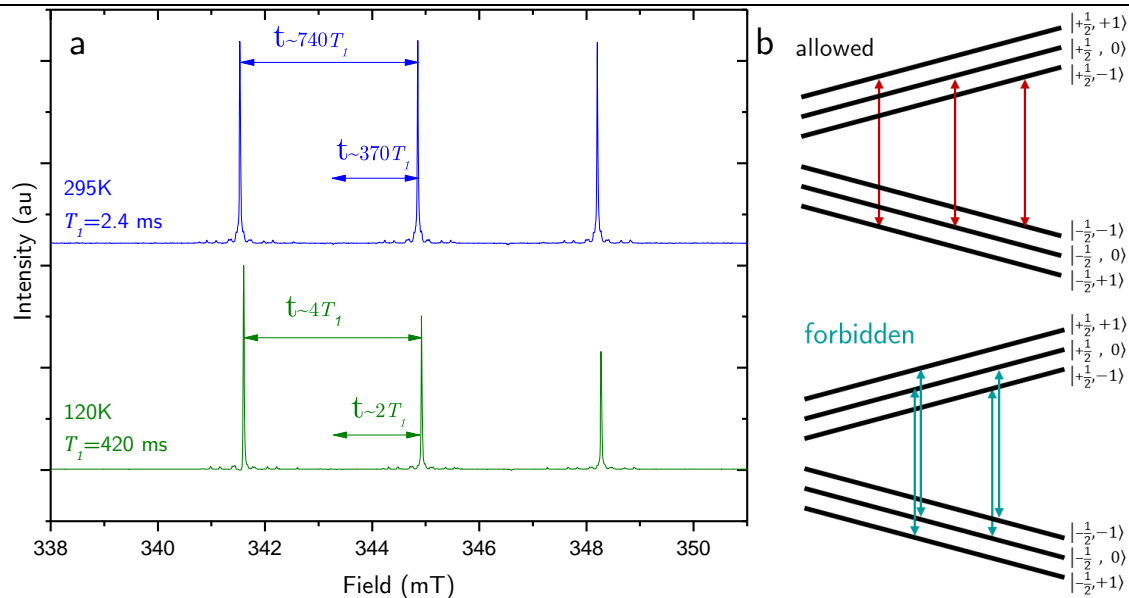
Figure 5-5 a, Comparison of the RP-EPR$^{(FM)}$ spectrum of 0572207-C(ii) recorded at 295 K (top blue) and at 120 K showing the distorted intensities (bottom green). Number of T_1 times between "allowed" and "forbidden" transitions are indicated.

b. Energy level diagram as a function of magnetic field showing the "allowed" and "forbidden" EPR transitions for N_S^0. Double nuclear spin flips are omitted due to low probability.
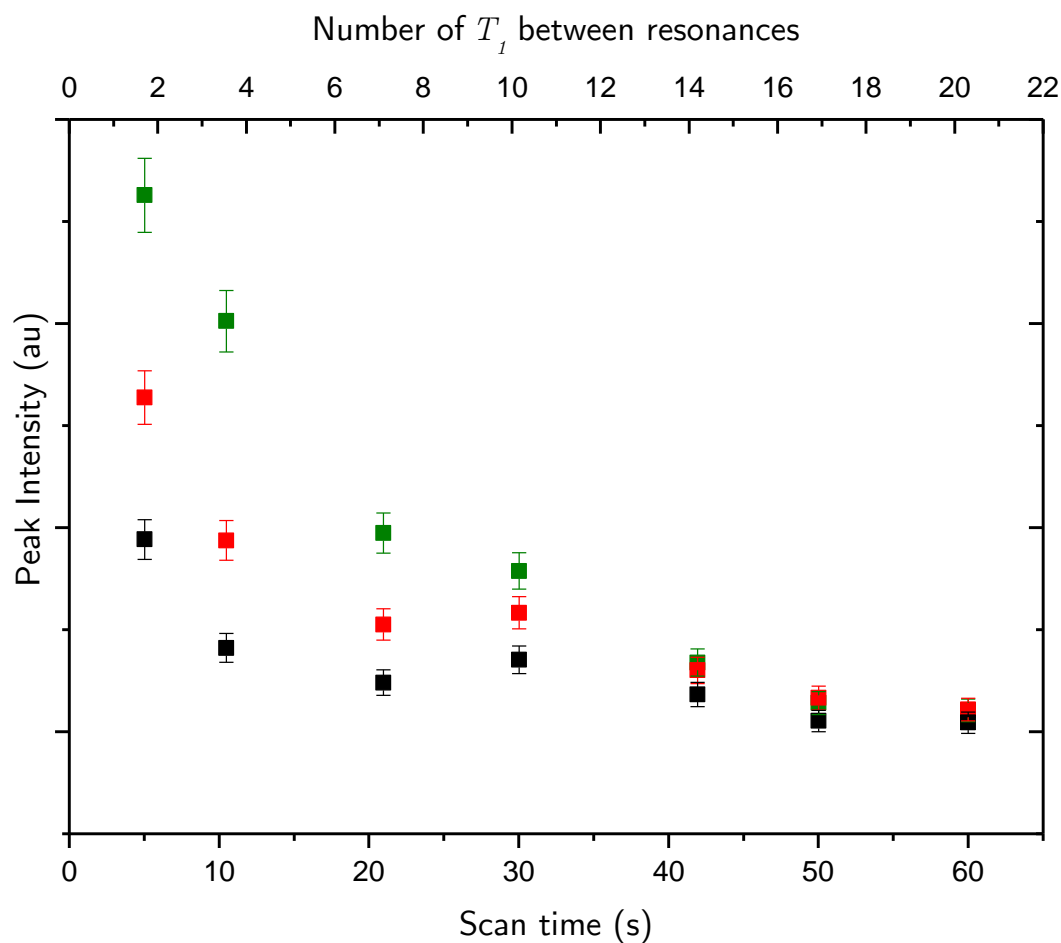
Figure 5-6 The intensities of the EPR transitions at different sweep rates averaged for 25 scans. Black points are for $m_I=+1$, red point $m_I=0$, green $m_I=-1$. Recorded at 100 K on sample 097320P-A, all parameter optimised for peak signal.
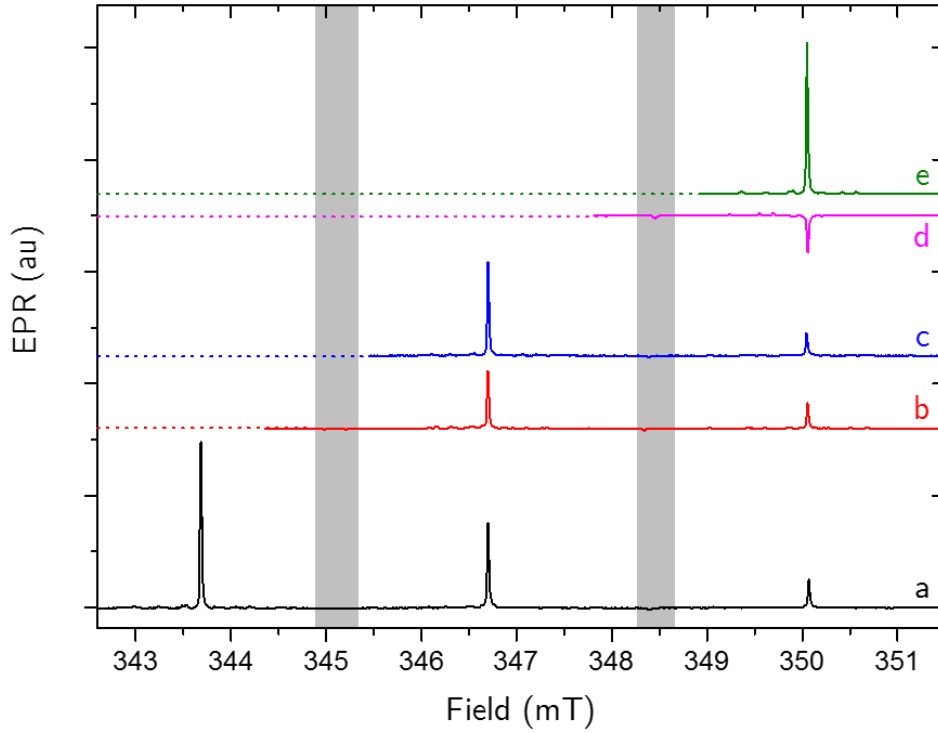
Figure 5-7 RP-EPR$^{(FM)}$ on 097320P-A for a single scan performed at 90 K with 1.9 mT/s scan rate with varying starting position; scans are offset for clarity. The starting point of each scan is indicated by the start of the solid line. The grey bars show the position of the "forbidden" transition. Fields have been corrected for magnet hysteresis.

To investigate the effect, the *"forbidden"* transition had on the N_S^0 spectrum measurement were taken from different starting fields, the results of which can be seen in Figure 5-7. When the spectrum is started such that an *"allowed"* transition is met first (Figure 5-7 a, c & e) this transition response has the expected intensity of the assumed thermal population. When the *"forbidden"* transitions are passed through first (Figure 5-7 b & d), the first *"allowed"* transition is found to be weaker or in the case of the $m_I = -1$ line is actually slightly inverted. These results show that it is the *"forbidden"* transitions that are causing the change for thermal equilibrium.

The distorted intensities of the N_S^0 spectrum at low temperatures are likely to be related to the reduced number of T_1 relaxation times between transitions. The requirement for ~14 T_1 between EPR *"allowed"* resonances to give a normal spectrum indicates that the distortions are not due to the magnetisation failing to return to equilibrium between transitions. The time between the EPR *"forbidden"* and *"allowed"* transitions is however only a few T_1 at 100 K indicating it is the *"forbidden"* transitions that are causing the distortion.

Transition	Field (mT) at 9.72 GHz	Probability
$\left\|-\frac{1}{2},+1\right\rangle \rightarrow \left\|+\frac{1}{2},+1\right\rangle$	343.4	1
$\left\|-\frac{1}{2},+1\right\rangle \rightarrow \left\|+\frac{1}{2},0\right\rangle$	345.4	0.0028
$\left\|-\frac{1}{2},0\right\rangle \rightarrow \left\|+\frac{1}{2},+1\right\rangle$	345.2	0.0027
$\left\|-\frac{1}{2},0\right\rangle \rightarrow \left\|+\frac{1}{2},0\right\rangle$	346.7	1
$\left\|-\frac{1}{2},0\right\rangle \rightarrow \left\|+\frac{1}{2},-1\right\rangle$	348.4	0.0045
$\left\|-\frac{1}{2},-1\right\rangle \rightarrow \left\|+\frac{1}{2},0\right\rangle$	348.5	0.0044
$\left\|-\frac{1}{2},-1\right\rangle \rightarrow \left\|+\frac{1}{2},-1\right\rangle$	350.1	1

Table 5-4   Table of the transition probabilities for transition for N_S^0 with B_0 aligned along [001] calculated in EasySpin [30]. *Transitions for double nuclear spin flips are omitted.*

The results presented show the relatively high microwave power used for RP-EPR$^{\text{(FM)}}$ is driving the *"forbidden"* transition in a process analogous to solid effect DNP. In solid effect DNP a *"forbidden"* transition is excited by high power microwaves in order to enhance the nuclear populations. This polarisation begins to decay once the *"forbidden"* transition is no longer on resonance and therefore the effect would normally have decayed away and could only be seen if the relaxation time is long. At 120 K decay of the polarisation is sufficiently long that we can measure the perturbed populations.

Although both the $m_I = 0$ and the $m_I = +1$ transitions were measured after a *"forbidden"* transition there was a greater change in population for the $m_I = +1$ line. This is consistent with calculated transition probabilities outlined in Table 5-4 which shows the $\left|-\frac{1}{2},0\right\rangle \rightarrow \left|+\frac{1}{2},-1\right\rangle$ and the $\left|-\frac{1}{2},-1\right\rangle \rightarrow \left|+\frac{1}{2},0\right\rangle$ transitions have twice the probability of the $\left|-\frac{1}{2},+1\right\rangle \rightarrow \left|+\frac{1}{2},0\right\rangle$ and the $\left|-\frac{1}{2},0\right\rangle \rightarrow \left|+\frac{1}{2},+1\right\rangle$ transition and consequently a stronger affect. These results show that it is the *"forbidden"* transitions that are causing the change from thermal equilibrium population of the nuclear spins.

5.2.3 Sweep rate

The rate at which RP-EPR$^{\text{(FM)}}$ experiments are conventionally undertaken within this laboratory is limited by the use of large sweepable electromagnets to control the B_0. Such systems have an "inertia" that needs to be overcome at the start of the scan which leads to a mismatch between the recorded and actual field. This limits the sweep rate at which
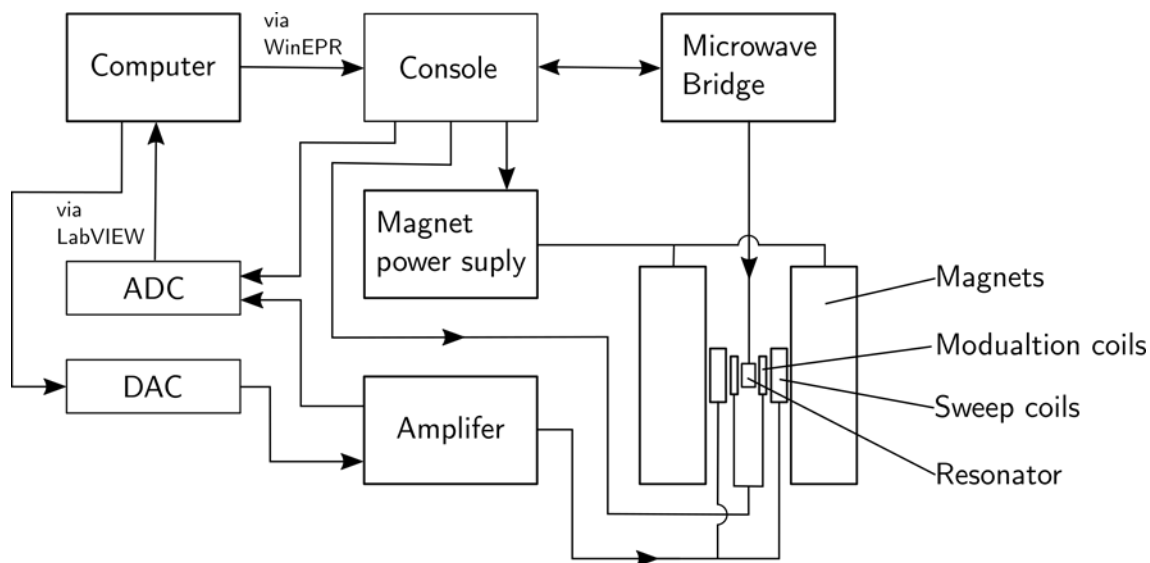
Figure 5-8 Schematic of the RP-EPR$^{(FM)}$ experimental equipment used for the increased sweep rates.

experiments can be reliably performed to 2 mT/s and even at this rate a 1 second delay is required before each scan to allow the magnets to stabilise and a buffer zone of 6 mT is required before resonances to allow accurate determination of field position. At faster rates this "corridor of uncertainty" comes to dominate the spectrum and cannot be easily corrected with post processing as the error is not reproducible between scans.

5.2.3.1   Experimental: sweep rate investigation

The problems associated with the large swappable magnets meant a different approach to field control had to implemented in order to investigate the influence of sweep rate on spin response. Making use of the existing large electromagnets present on the EMX systems to create a static field close to the total B_0 for the scan, ~348 mT for an X-band experiment, allows for the use of small coils to create the much smaller field required to sweep the spectrum. A schematic of the experimental setup can be seen in Figure 5-8. To make the experiment as portable as possible, much of the detection system from the existing EMX console was used including the modulation amplifier. However, the sweep coils and data recording were handled by software written in LabVIEW™. The maximum modulation frequency *"allowed"* by the Bruker modulation amplifier is 100 kHz and this was used for all results presented in this section. 100 kHz modulation limited the maximum sweep rate that could be used without causing distortions to the spectrum. The linewidth of a typical high purity sample is 0.02 mT and for
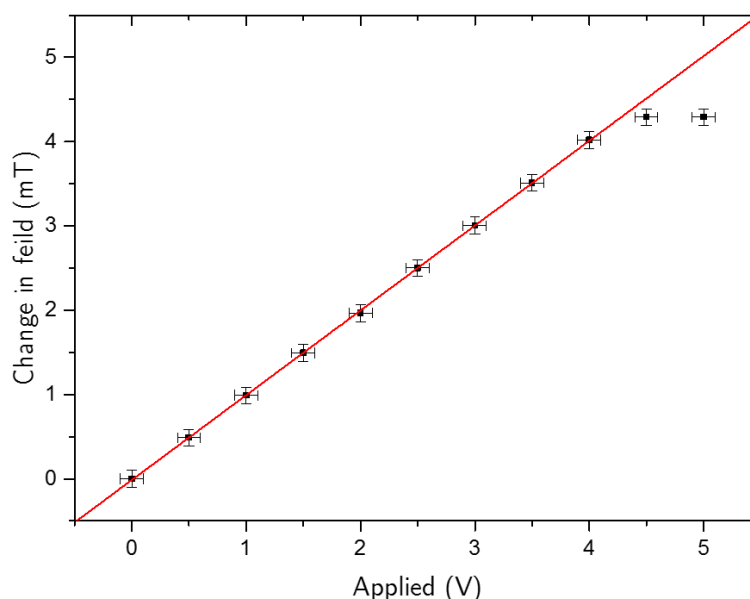
Figure 5-9 A typical calibration curve for the ER-4102ST RP coils. Linear fit (red line) is to 0 - 4 V region and has a gradient of 1.005(3) mT/V.

fitting at least 10 points are required in this width. To ensure a full modulation cycle at each field position a maximum sweep rate of 20 mT/s is possible but this was found to still provide spectral broadening and a maximum sweep rate of 100 mT/s was used.

LabVIEW™ software was used to generate a sawtooth wave function that was outputted through a NI 9263 digital to analogue converter. This signal was then amplified to create enough current to drive the sweep coils. In this way the sweep width was controlled by outputting 1-10 V amplitude wave functions and the sweep rate controlled by the frequency of the function. A variable delay of between 100-2000 ms was applied in between periods of the sawtooth to allow for any magnetic inertia, although for all but the fastest sweeps this was not strictly necessary. The amplified signal was split and was sent to the sweep coils and recorded for field position. To calibrate the field created by a given voltage, a constant voltage was applied to the coils and a conventional field swept SP-EPR spectrum was recorded, then the change in field position recorded; a typical example of this can be seen in Figure 5-9.

The demodulated analogue signal was taken from the console prior to amplification and along with the signal from the coil amplifier was digitised with a NI 9222; this unit gives simultaneous collection of data within an error of 2 µs in two channels [36]. To facilitate transfer between the digitiser and computer and avoid lag, the digitised data was buffered and then transferred at the end during the delay between scans. In this way sweep rates of up to 100 mT/s were achieved. All signal averaging and filtering was handled in the LabVIEW™ software which could output its spectrum as an ASCII file containing the field and EPR intensity. The software was also able to produce a sliced scan to enable the evolution of a system over time to be studied.

Temperature (K)	Sweep (mT)	Sweep Rate (mT/s)	Time Constant (ms)	Acquisition time (s)	Power (µW)	Modulation Amplitude (mT)	Phase (°)
292	20	1.5-100	0.16	300	Optimised	0.002	90

Table 5-5 Experimental parameters for the investigation into sweep rates

5.2.3.2   Results of sweep rate investigation

The sweep coils and amplifier were capable of generating a maximum sweep width of 8 mT (± 4 mT around the static B_o) without any appreciable heating. It was found that peak signal was achieved with the lowest possible modulation amplitude (2 µT) and at a 90° demodulation phase. The microwave power that provided peak EPR signal was found to vary with sweep rate (Table 5-6)

The results for the increased sweep rates at room temperature can be seen in Figure 5-10. All data was collected with a 500 ms delay between scans to allow the magnetic system to stabilise and at parameters optimised for peak signal. A sweep width of 3 mT was used to avoid potential distortion from *"forbidden"* transitions. Data was collected for the same total acquisition time at each rate. The SNR was found to increase logarithmically with increased sweep rate and at 100 mT/s a factor of 4.2 increase in SNR ratio was achieved. The increase in SNR cannot be accounted for purely by increased number of scans which are taken in the acquisition time. Whilst there is a slight improvement in noise from the increased number of scans, this is not the primary gain as is demonstrated in Figure 5-11 which shows the results
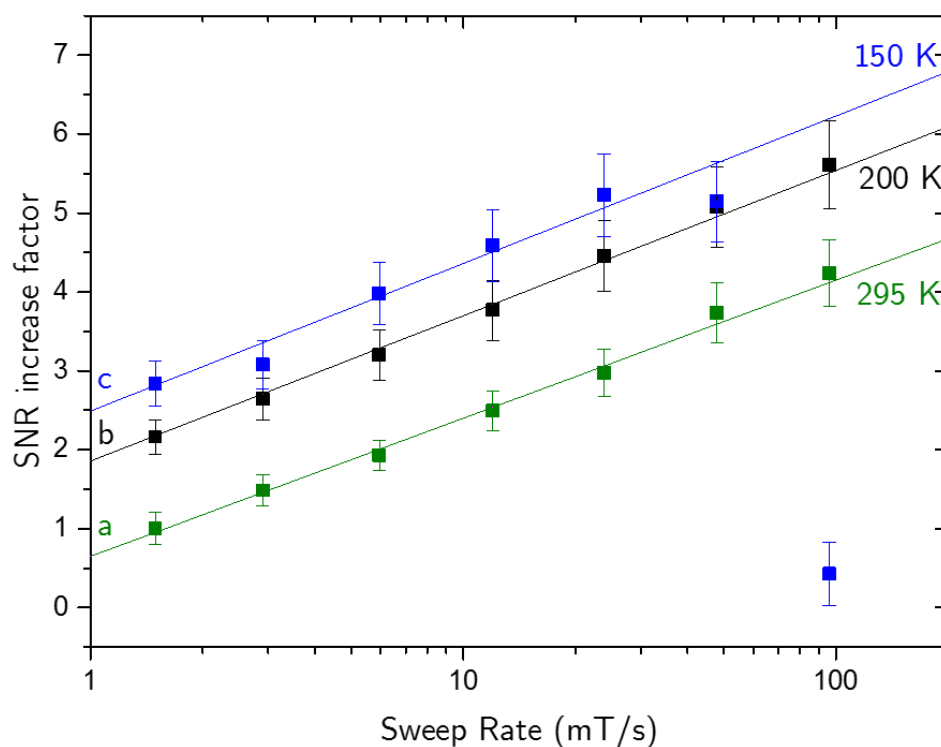
Figure 5-10 The SNR found for the same acquisition time at different sweep rates. All other parameters the same. Solid lines are semi-logarithmic fits
a, 295 K (green) gradient of fit 1.75(6)
b, 200 K (black) gradient of fit 1.83(5)
c, 150 K (blue) gradient of fit 1.8(1) (final two points omitted from fit)

for 50 scans at different sweep rates. This result shows an increasing SNR for the same number of scans, indicating that there is a greater EPR response to increased sweep rate.

Sweep rate (mT/s)	Microwave power for peak signal (mW)	Number of scans in 300 s
1.5	0.158 (31 dB)	120
2.9	0.158 (31 dB)	195
6.0	0.251 (29 dB)	300
12	0.316 (28 dB)	400
24	0.499 (27 dB)	480
50	0.592 (26 dB)	535
100	0.632 (25 dB)	566

Table 5-6 Typical powers for peak signal of room temperature rapid scan experiments with ESR 900 in place

It has been demonstrated in section §5.2.1.1 that there are potential gains to be had from reducing the temperature at which the experiment is conducted therefore an experiment was conducted to see if the benefits of increased sweep rate and lower temperature could be combined. A Bruker ER 4102ST cavity was used with an Oxford instruments ESR900 cryostat and as with the room temperature measurements all data was collected with a 500 ms delay between scans to allow the magnetic system to stabilise and at parameters optimised for peak signal.

Figure 5-10b shows at 200 K the same logarithmic increase in SNR as for room temperature experiments, the gradients for the two semi logarithmic fits found to be 1.78(6) and 1.83(5) for 295 K and 200 K respectively. In addition to the increase for sweep we also see an approximate 2-fold increase in signal compared to the room temperature measurement for the same sweep rate. A factor of 5.6 increase in SNR was found using 100 mT/s sweep rate at 200 K, this translates into a thirty-fold reduction in time for the same SNR; in the laboratory this could reduce a weekend to a little over 2 hours. A quantitative detection limit for N_S^0 in a 50 mg sample is now 0.01 ppb.

Reduction in temperature to 150 K does not provide an overall increase in SNR, Figure 5-10c. As sweep rate is increased there is initially the same logarithmic trend (gradient 1.87(7)), but for sweep rates above 30 mT/s the SNR is reduced. The decrease in signal can be explained by the lengthening of T_1, (200 ms at 150 K).
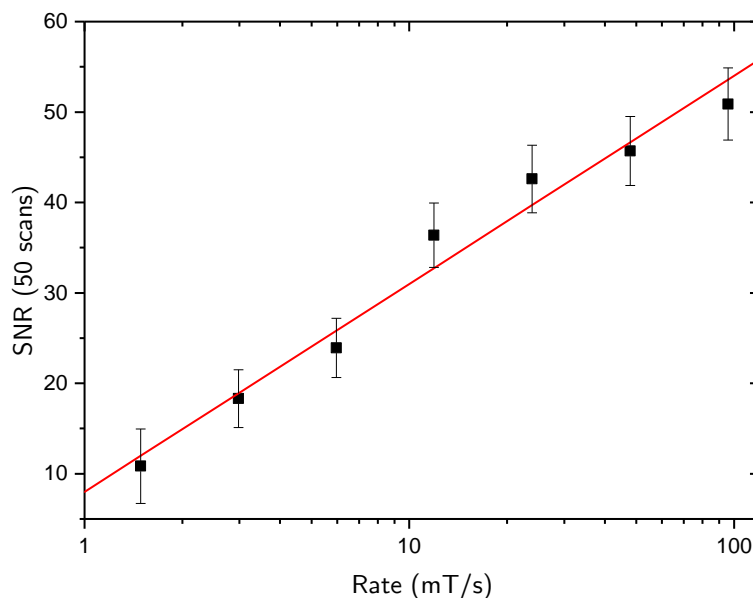
Figure 5-11   SNR ratio found at different sweep rates at room temperature. All spectra were taken for 50 acquisitions with the same conversion time (0.16 ms) with all parameters optimised.

5.2.4   Discussion

When a spin packet is traversed rapidly the net migration of the spin packet does not relax whilst the packet is on resonance. A significant component of magnetisation is created in the xy-plane which precesses analogous to the FID response in a pulsed experiment. In direct detected EPR a stretched FID is often the recorded signal as the field moves off resonance and the frequency of precision lowered. Faster sweep rates cause this stretching to be more pronounced and lead to a broadening of the EPR line. In this work there is no such broadening witnessed even at 100 mT/s. This is due to the absence of wiggles in the recorded spectra for two reasons. Firstly, when using field modulated RP-EPR the wiggles of the FID distortion can be suppressed by the detector filter bandwidth. Secondly, the wiggles of the FID will not be seen at all if the sweep rate is not sufficiently rapid such that (5.2) is not valid [37].

$$(5.2) \qquad \left(|\gamma| \left(\frac{dB_0}{dt} \right) \right)^{1/2} T_2 \geq 1$$

Even at the maximum sweep rate investigated (5.2) is never satisfied and no line broadening would be seen.

Increased sweep rates require an increase in microwave power to remain at peak signal intensity. For a constant microwave power, the total energy transferred to the spin system is decreased with increased sweep rate. Sweeping at a faster rate at peak power gives an increase in SNR for the same number of scans consistent with previous reports in direct detected RP-EPR [22]. Since the noise is the same, the increase in SNR is due to a larger response per spin; analogous to an increased turning angle in a pulsed experiment.

However, there is a limit to the gain which can be made through this since time must be left between scans to allow the spin system to return to equilibrium. At 150 K for sweep rates above 30 mT/s even the 500 ms delay between scans was not sufficient for the system to have fully relaxed. As such repeat scans produce less intensity than the initial scan. It was found that it was possible to regain the intensity by increasing the delay between scans but this has a massive impact on the number of scans that can be taken in the same acquisition time. Increasing the delay to 1 second effectively halves the number of scans that can be acquired in the same length of time since the delay was much longer than the time scanning.

Since the gains in SNR are due to the relative increase in sweep rate compared the relaxation times the peak conditions are balancing act of finding the optimum conditions. The maximum gains from increased sweep rate whilst using commercial modulation equipment are limited by the maximum sweep rate governed by the maximum modulation frequency. The maximum achievable sweep rate of 100 mT/s gives a factor of 4.2 improvent in SNR but this can be improved upon by reducing the temperature and increasing the relaxation times. At 200 K it was found that the increase in relaxation times was sufficient to improve SNR but not so much that it caused problems associated with distortions caused by the *"forbidden"* transition.

5.3 Large samples

For quantitative EPR to work effectively the modulation field, microwave field, and static magnetic field need to be homogenous over the sample, and other parameters such as Q and the filling factor need to be consistent between the sample under consideration and the reference sample. For many diamond samples this is true, or the sample has been prepared
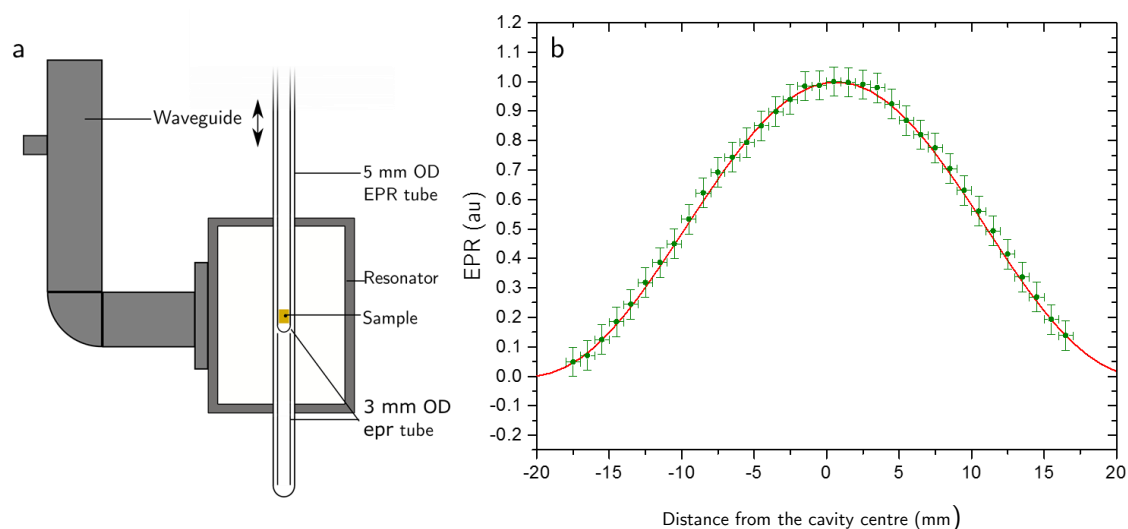
Figure 5-12 a, Experimental setup used to characterise a cavity. A 50 mm length of 3 mm od EPR tube was placed inside a 5 mm tube. The sample was placed in 3mm od sample tube which in turn was placed inside the 5 mm tube. This entire construction was moved vertically.
b, Characterisation of the HS cavity using a point-like sample. Fit is from the Bruker characterisation and is a 9th order polynomial. Data taken by E. Nako and processed by the author.

such that it is small enough for this to be true. Large natural samples and specially cut gem stones provide a challenge to these assumptions as potentially do powder samples.

EPR is conventionally performed at 9.8 GHz, wavelength 30 mm. If the sample is larger than this it is highly unlikely that the fields within the resonator will be uniform across the samples. A further consideration is the static field homogeneity; Bruker state that they have a working sample volume of 10 mm x 22 mm x 10 mm with a homogeneity of 10^{-5} Mt at a field of 350 mT [38]. The modulation fields are also an issue. Typical modulation coils are 1-2 cm in diameter and will only provide a true homogenous field at the very centre of the coil. All of these factors will need to be taken into account if quantitative measurements are to be made without large errors.

It is now possible to buy a characterised spectrometer that is capable of quantitative measurements without the need for a reference [39]. Such spectrometers rely on characterisation of how the spin response varies spatially within the cavity and also make the assumption that the sample is symmetric around the vertical axis; this assumption is reasonable to tubes of sample but may break down for samples where the filling factor is more complicated.

5.3.1 Cavity characterisation

To characterise cavity response along the vertical axis a 2 mg diamond was used and moved up and down within the cavity and the response at the same experimental settings was recorded. To avoid the movement in position of the sample holder changing the dielectric losses of the resonator, a sample holder was used that always had the same amount of quartz in the cavity no matter the position of the sample was used (Figure 5-12a). Using this method, it is impossible to deconvolve which factor, B_0, B_{mod} or $B_{\mu w}$, is changing but it does show the change in response at different points in the cavity. Figure 5-12b shows the characterisation of the HS cavity; the cavity has a flat response working area in the centre of the cavity of approximately 6 mm. The drop off in response away from this area is the primary problem in quantifying large samples.

5.3.2 Diamond powder

To investigate the errors associated with powder samples some Element 6 SDB1000 series grit, which has a high nitrogen content, was used. A number of small, <5 mg samples were measured to ascertain the concentration of N_s^0 and consistency of concentration across the batch, 290(10) ppm. After the expected concentration had been measured, increasing masses of sample were tested. To reduce the effects of the sample tube on the resonator the two tube process as outlined in section §5.3.1, was used but with varying lengths of tube below the sample and care was taken to ensure the centre of the sample was in the middle of the resonator. The results in Figure 5-13 show the apparent concentrations when different amounts of grit were compared to the near point sample: Syn93-04.

When correction for the length of the sample is not taken into account the apparent concentration matches the expected value up until the sample is 5mm long, at which point the apparent concentrations begin to drop. As the sample length approaches 10 mm the apparent concentration begins to be consistently underestimated although it is still within error bars. Once the sample length is greater than 20 mm the concentration is underestimated by over 25%, an unacceptable level of error.
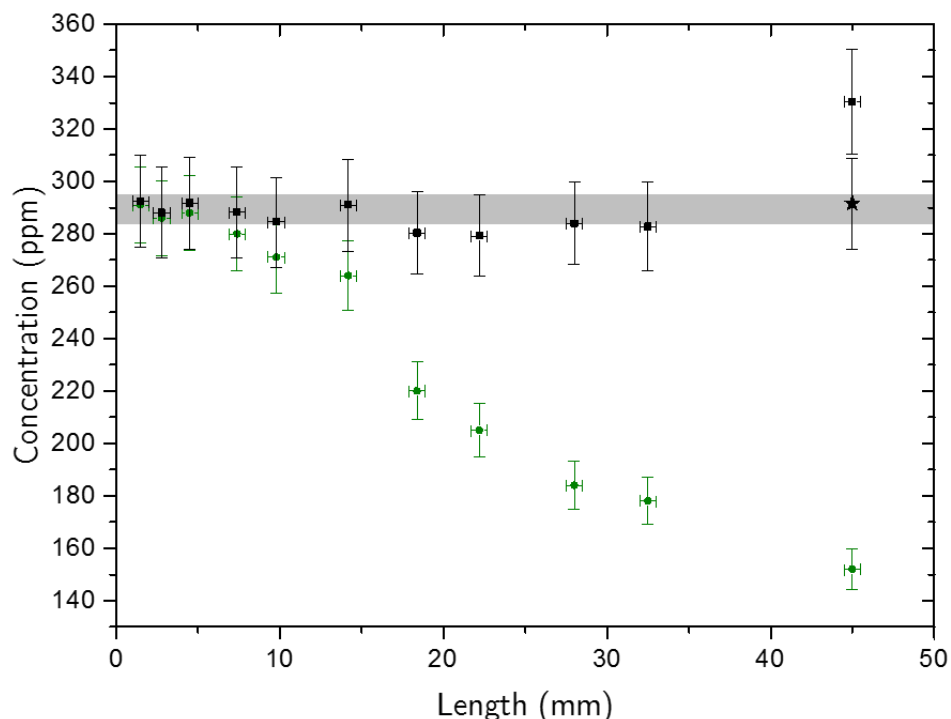
Figure 5-13 The measured concentration of N_S^0 for varying length of diamond grit (average concentration 290(10) ppm) in an EPR sample tube. The green data points are the measured concentrations without corrections. The black data points are corrected for changes in Q and the cavity response. The 45 mm data point also had to be corrected for the maximum working length of the HS cavity (40 mm) this point is shown as a star.

During the experiment the quality factor of the cavity was seen to drop from 5200 for the small sample to 4800 for some of the longer samples. This loss accounts for around 8% of the loss of signal of the affected samples. However, the dominating source of error is from changes to filling factor. Once the sample has left the central working part of the cavity the response of additional spins is no longer linear. This change in response can be estimated from the cavity characterisation above which is fitted to a 9th order polynomial and then the response of the sample can be corrected. The results of applying both of these correcting factors are seen in Figure 5-13. All the lengths now show a good agreement with the expected concentration except for the 45 mm sample where the correction returned an overestimate of concentration. If this sample was treated as being a 40 mm sample, the quoted working length of the HS cavity, the concentration agrees within error.
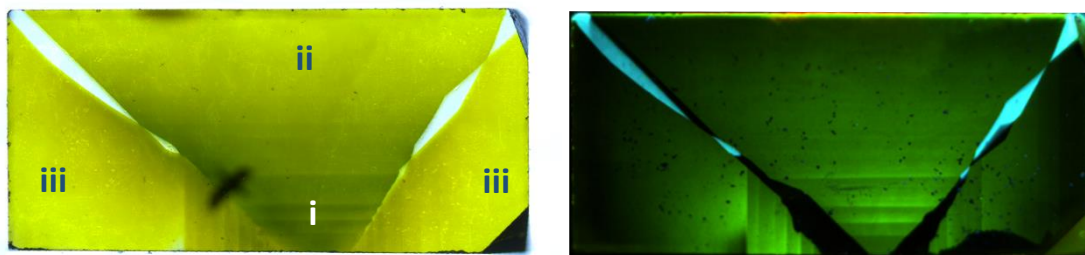
Figure 5-14 Photograph (left) and DiamondView ™ image (right) of Sample V showing the different growth sectors. Point where IR measurements were made are indicated (i, ii, iii).

5.4 High nitrogen concentration

Whilst quantifying a suite of high nitrogen high inhomogeneity HPHT grown diamond plates it was noted that for the very highest concentration samples there was an underestimate of the nitrogen expected from growth conditions [40]. The samples in question were highly sectored and as such, the best estimate for concentrations is often found from line width since it is not clear how large the different growth sectors contributing to the signal are [41]. Even after this approach was taken there was still an underestimation of nitrogen concentration. However, what was observed was a large broad feature which could be fitted to a single Gaussian line ~5 mT FWHM at g=2.0024. This feature was also found in other HPHT suites that were studied. An example of such a sectored diamond can be seen in Figure 5-14. The results presented here are from Sample V, one of a suite of ten Type IB samples that all exhibited this behaviour.

FT-IR measurements were made at the three points indicated in Figure 5-14 using a 0.5 mm aperture and the following N_S^0 concentrations were found: FT-IR(i) = 630(50) ppm, FT-IR(ii) = 300(30) ppm and FT-IR(iii) = 400(40) ppm (no significant concentration of A-centre was detected).

The EPR spectrum of the sample was taken well below any microwave power saturation to avoid the associated line broadening. Using the line widths of the EPR data to estimate the concentration of the two significant N_S^0 sectors, (P1a & P1b) P1a = 290(30) ppm and P1b = 420(50) ppm. EPR does not allow the position or size of these sectors to be assigned. Even after the subtraction of the Gaussian line, wobbles are seen in the residual of the EPR spectrum and may be evidence of some structure with the broad feature but could also be
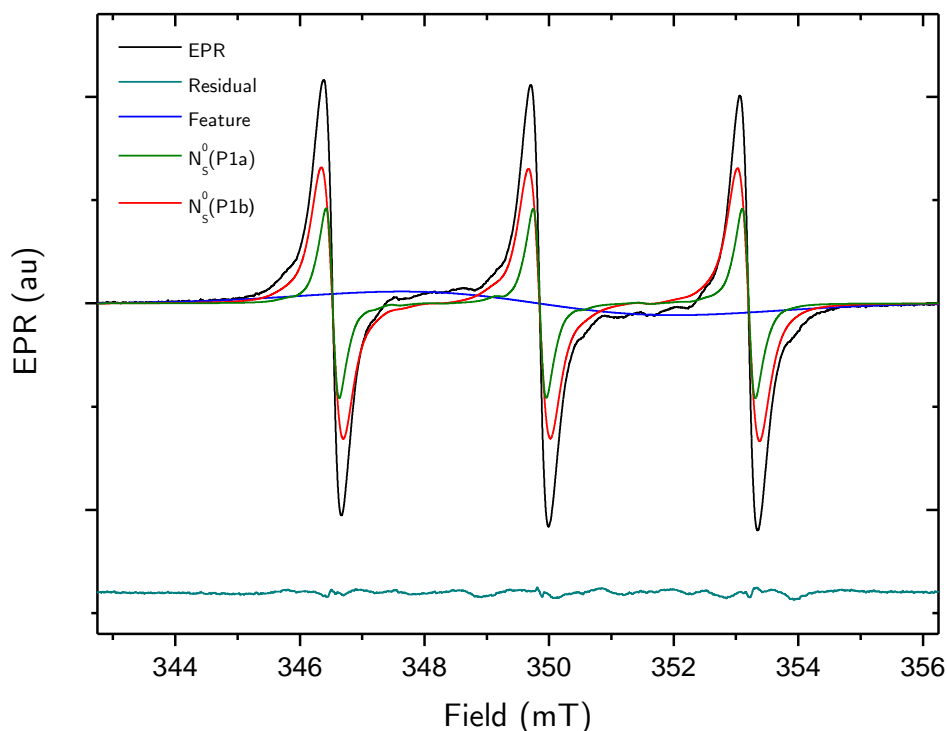
Figure 5-15 EPR spectrum of Sample V fitted to two N_S^0 simulations (line widths a=0.46 G and b=0.23 G) and a single broad feature.

from other unrelated defects present in relatively low concentrations. The total double integrated EPR intensity total was used to calculate the N_S^0 concentration averaged over the total sample 480(50) ppm. Within errors the concentration from FT-IR(ii) agrees with that from P1a and concentration from FT-IR(iii) agrees with and P1b it is possible that the EPR feature is from high concentration N_S^0 as measured in FT-IR(i).

FT-I(iii) and P1b have the same concentration and are possibly from the same sector. The photograph of the sample was to estimate the two triangular sectors of the sample that give the 400(40) ppm concentration in the FT-IR data. These areas are indicated in Figure 5-14 and account for ∼40% of the sample. An N_S^0 concentration of 410(40) ppb, was found if 40% of the total mass was applied to the integrated intensity of P1b, showing that the EPR P1b and FT-IT (iii) were indeed both from this sector.

The absence of a distinct boundary between sectors means that the two remaining concentrations cannot be accounted for in the same way. However, using the reverse process

outlined above the 630(50) ppm sector accounts for ~35% and the P1a 290(30) ppm sector the remaining ~25%.

It is believed that the broad feature in the EPR can be explained by interactions between distinct N_S^0 centres. The simulation of the spacing between nitrogen atoms in a sector with a high concentration of N_S^0 (600 ppm) shows that 90% are within 10 lattice spacing, compared to 72% for a 400 ppm sector and 5% for a 10 ppm sector [42]. Coupling between pairs of N_S has been witnessed in EPR. N_S^0 can interact with a next nearest neighbour N_S^+, forming the N1 defect and N_S^0 pairs can also interact at a greater distance to form the NOC1-3 family of defects [43,44]. It is believed that there are no electron traps in the high concentration sectors since there is no observable N_S^+, therefore, all the nitrogen is in the neutral charge state and N1 is unlikely. The NOC family of EPR defects gives a recognisable EPR spectrum so are also not responsible for the broad feature.

Two unpaired electrons that are sufficiently close to interact but where the interaction is so weak that they cannot be thought of in the same terms as a S=1 system. In this situation there is opportunity for electron spin exchange between two N_S^0 defects [45]. At high exchange rates the three hyperfine lines will coalesce into a single broad transition. The rate of electron exchange for a given molecule is proportional to the concentration of radicals.

The small number of samples tested means it is impossible to confirm that exchange coupling between paramagnetic centres leads to the broad feature found in the EPR spectrum. However, the inability for EPR to account for all the nitrogen reported in FT-IR means that care must be taken during the quantification of N_S^0 by use of EPR at X-band for these high concentration Type IB samples.

5.5 Conclusion

This chapter has aimed to increase the understanding of some of the problems associated with quantitative EPR. Despite the increased errors for misaligned samples the error in RP-EPR[(FM)]

is still comparable to that found for SP-EPR meaning that there is no penalty when alignment is not perfect. This represents a massive potential improvement in throughput of samples since aligning samples with very low concentration can be arduous and at times impossible unless growth faces are known. This reduction in random error is largely from the improved fitting offered by narrow line widths and increased SNR normally recorded in RP-EPR$^{(FM)}$. High SNR and a high quality of fit to simulation are key to useful quantitative measurements.

RP-EPR$^{(FM)}$ performed at low temperature and increased sweep rate have been performed. In §5.2.3.2 a factor of 5.6 improvement in SNR was possible at 200 K at a 100 mT/s sweep rate compared to the previous conditions. This is a potential 32-fold reduction in the acquisition time for the same SNR achieved under current experimental condition. A sample that currently requires a weekend scan (68 hours) for sufficient SNR to be achieved can now be measured in approximately 2 hours. A factor of 4.2 in SNR for the same acquisition time was found by increasing the sweep rate to 100 mT/s at room temperature. A factor of 17 reductions in acquisition time. This increase is attributed to a greater tipping angle of the magnetisation from the faster scan.

Low temperature RP-EPR$^{(FM)}$ offered a factor of 3.7 increase in SNR for the same acquisition time using 2 mT/s sweep rates (Figure 5-4). That this improvement is not only from the increased Boltzmann populations is demonstrated and the additional increase is attributed to a greater tipping angle from the lengthened relaxation times of N_S^0. At temperatures below 150 K the intensities of the N_S^0 EPR spectrum become distorted as a result of driving the "*forbidden*" transition and insufficient time between resonances for equilibrium populations to be restored.

It has been shown that care must be taken when using samples that are large compared to the working area of the cavity to access the increased SNR from an increased filling factor. It has been shown in Figure 5-12 that the changing response of the cavity at different points can alter the intensity of the recorded spectra and this must be taken into account when comparing to a reference. High concentration of nitrogen also poses a problem when assaying N_S^0.

Comparisons to FT-IR measurement of the same samples showed a discrepancy in the concentrations of N_S^0. A broad feature which is tentatively assigned to interaction between near neighbour N_S^0 is thought to stop some N_S^0 contributing to the EPR spectrum leading to an underestimation of total concentration.

5.6 References

[1]   H. Godfried, WO 2004.0464271 (2004).

[2]   D. Raabe and T. Liu, Appl. Phys. Lett. 94, 5 (2009).

[3]   R. Samlenski, C. Haug, R. Brenn, C. Wild, R. Locher, and P. Koidl, Appl. Phys. Lett. 67, 2798 (1995).

[4]   J. E. Field, *The Properties of Natural and Synthetic Diamond* (Academic Press, London, 1992).

[5]   R. Berman, P. R. W. Hudson, and M. Martinez, J. Phys. C Solid State Phys. 8, L430 (1975).

[6]   B. Ramsay, F. Schoofs, R. Bodkin, and A. P. Jardine, in *Diam. Conf.* (Warwick, 2015).

[7]   K. Ohno, F. Joseph Heremans, L. C. Bassett, B. A. Myers, D. M. Toyli, A. C. Bleszynski Jayich, C. J. Palmstrom, and D. D. Awschalom, Appl. Phys. Lett. 101, (2012).

[8]   A. T. Collins, Phys. B Condens. Matter 185, 284 (1993).

[9]   F. De Weerdt and A. T. Collins, Diam. Relat. Mater. 17, 171 (2008).

[10]   B. L. Cann, Magnetic Resonance Studies of Point Defects in Diamond - PhD Thesis, University of Warwick, 2005.

[11]   F. Jelezko and J. Wrachtrup, J. Phys. Condens. Matter 16, R1089 (2004).

[12]   Element   six, http://www.e6.com/wps/wcm/connect/E6_Content_EN/Home/Materials+and+prod ucts/Single+crystal+synthetic+diamond/CVD+synthetic+diamond   accessed: 31/5/2016 (n.d.).

[13]   Element   6, http://www.e6.com/wps/wcm/connect/E6_Content_EN/Home/Materials+and+prod ucts/Single+crystal+synthetic+diamond/HPHT+large+single+crystal+synthetic+dia mond accessed: 31/5/2016 (n.d.).

[14]   V. N. Mochalin, O. Shenderova, D. Ho, and Y. Gogotsi, Nat. Nanotechnol. 7, 11 (2012).

[15]   U. F. S. D'Haenens-Johansson, A. Katrusha, K. Soe moe, P. Johnson, and W. Wang, GEMS Gemol. Fall, 260 (2015).

[16]   R. S. Alger, *Electron Paramagnetic Resonance: Techniques and Applications.*, First (Wiley & Sons Inc, New York, 1968).

[17]   G. R. Eaton, S. S. Eaton, D. P. Barr, and R. T. Weber, *Quantitative EPR*, 1st ed. (Springer, New York, 2010).

[18]   Weil and J. R. Bolton, *Electron Paramagnetic Resonance*, 2nd ed. (Wiley & Sons Inc, New York, 2007).

[19]   Bruker, *Elexsys E500 User's Manual* (Bruker Instruments, Inc., 2001).

[20]   R.   P.   Mason, Https://www.niehs.nih.gov/research/resources/epresr/sensitivity/index.cfm accedded: 2016 (n.d.).

[21]   D. G. Mitchell, M. Tseitlin, R. W. Quine, V. Meyer, M. E. Newton, A. Schnegg, B. George, S. S. Eaton, and G. R. Eaton, Mol. Phys. 111, 2664 (2013).

[22]   J. W. Stoner, D. Szymanski, S. S. Eaton, R. W. Quine, G. A. Rinard, and G. R. Eaton, J. Magn. Reson. 170, 127 (2004).

[23]   A. W. Kittell, T. G. Camenisch, J. J. Ratke, J. W. Sidabras, and J. S. Hyde, J. Magn.

Reson. 211, 228 (2011).

[24] A. W. Kittell, E. J. Hustedt, and J. S. Hyde, J. Magn. Reson. 221, 51 (2012).

[25] T. Czechowski, W. Chlewicki, M. Baranowski, K. Jurga, P. Szczepanik, P. Szulc, P. Kedzia, M. Szostak, P. Malinowski, S. Wosinski, W. Prukala, and J. Jurga, J. Magn. Reson. 243, 1 (2014).

[26] J. R. Biller, M. Tseitlin, R. W. Quine, G. a Rinard, H. a Weismiller, H. Elajaili, G. M. Rosen, J. P. Y. Kao, S. S. Eaton, and G. R. Eaton, J. Magn. Reson. 242, 162 (2014).

[27] J. A. van Wyk, E. C. Reynhardt, G. L. High, and I. Kiflawi, J. Phys. D. Appl. Phys. 30, 1790 (1997).

[28] M. W. Doherty, V. V. Struzhkin, D. A. Simpson, L. P. McGuinness, Y. Meng, A. Stacey, T. J. Karle, R. J. Hemley, N. B. Manson, L. C. L. Hollenberg, and S. Prawer, Phys. Rev. Lett. 112, 47601 (2014).

[29] A. M. Edmonds, Magnetic Resonance Studies of Point Defects in Single Crystal Diamond - PhD Thesis, University of Warwick, 2008.

[30] A. S. Stefan Stoll, J. Magn. Reson. 178, 42 (2006).

[31] M. W. Dale, Colour Centres on Demand in Diamond - PhD Thesis, University of Warwick, 2015.

[32] P. P. Sorokin, G. J. Lasher, and I. L. Gelles, 1546, (1959).

[33] C. Ammerlaan and E. Burgemeister, Phys. Rev. Lett. 47, 954 (1981).

[34] E. C. Reynhardt, G. L. High, and J. A. van Wyk, J. Chem. Phys. 109, 8471 (1998).

[35] A. C. Wright, H. K. Song, and F. W. Wehrli, Magn. Reson. Med. 43, 163 (2000).

[36] National Instruments, *NI 9222 Datasheet* (2012).

[37] B. A. Jacobsohn and R. K. Wangsness, Phys. Rev. 73, 942 (1948).

[38] Bruker BioSPin, in *52nd Rocky Mt. Conf. Magn. Resoance* (2010).

[39] B. Biospin and S. C. Procedure, (2010).

[40] R. Bodkin, (2015).

[41] J. A. vanWyk, E. C. Reynhardt, G. L. High, and I. Kiflawi, J. Phys. D-Applied Phys. 30, 1790 (1997).

[42] A. T. Collins, J. Phys. Condens. Matter 14, 3743 (2002).

[43] V. Nadolinny, A. Yelisseyev, J. Baker, D. Twitchen, M. Newton, A. Hofstaetter, and B. Feigelson, Phys. Rev. B 60, 5392 (1999).

[44] A. Cox, M. E. Newton, and J. M. Baker, J. Phys. Condens. Matter 4, 8119 (1992).

[45] J. E. Wertz, *Electron Spin Resonance : Elementary Theory and Practical Applications* (McGraw-Hill, New York, 1972).

Chapter 6

6 Relaxation of N_S^0

6.1 Background

Substitutional nitrogen is the most common defect found in synthetic diamond and in the neutral charge state, N_S^0, is EPR active. Its prevalence makes understanding its properties and the potential effects on other defects in the lattice of great importance.

6.1.1 Reorientation of N_S^0

The elongated anti bonding orbit that accommodates the unpaired electron in N_S^0 reduces the defect symmetry to C_{3v}, therefore, there exist four possible defect orientations for the defect within the diamond lattice: $[111]$, $[\bar{1}\bar{1}1]$, $[1\bar{1}\bar{1}]$ & $[\bar{1}1\bar{1}]$ (Figure 6-1). When free from external or internal strain the energy of all orientations is degenerate and equal populations will be found in all four orientations. This however, is a dynamic equilibrium with each defect free to move between the four possible orientations; the mechanism for the reorientation depends on the temperature of the system. In the high temperature, or dynamic, regime, the electron has sufficient energy to "hop" over the potential barrier rotating between the four orientations. At temperatures greater than 600 K this manifests itself as motional averaging of the N_S^0 hyperfine lines in the recorded EPR spectrum and at 1200 K the reorientation rate is sufficient that the average position of all hyperfine resonances are observed as a single isotropic line. An Arrhenius plot made in this regime revealed an activation energy for this "hopping" reorientation of 0.76 eV [1].

The defect continues to reorientate at low temperatures but the rate of reorientation deviates substantially from the expected Arrhenius behaviour seen in the high temperature regime. This low temperature, or static, regime reorientation was investigated by Ammerlaan [2]. Uniaxial stress was applied to lift the degeneracy between orientations and thus create a
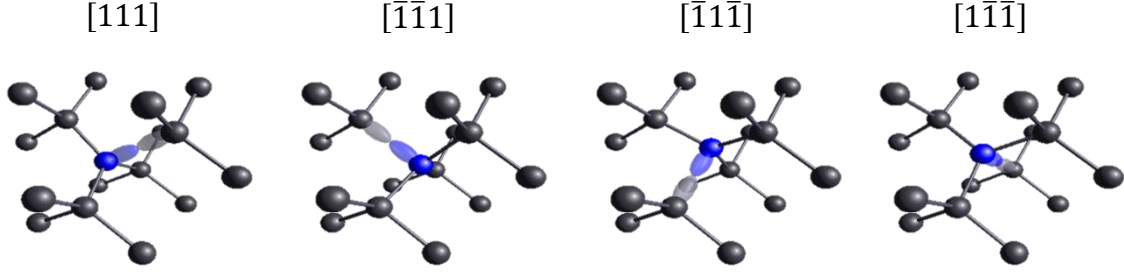
Figure 6-1   The four unique orientations of N_S^0.

preferential population in the non-stressed orientations. Pressure was applied at room temperature and preferential populations were created before the sample was brought to cryogenic temperatures where the pressure was released and the reorientation of the defect could be measured. The rates observed from 80 - 200 K were much greater than expected from the Arrhenius relationship and a model whereby the electron tunnelled between orientations was proposed [2]. One dimensional quasi-classical modelling (WKB) showed that a good prediction for the reorientation rates could be found if tunnelling between excited vibrational states was considered, although, the precise frequencies calculated were dependent on the shape of well used [2].

6.1.2 Spin lattice relaxation

Spin lattice relaxation T_1 is governed by interactions where the electron spin states lose energy to the surrounding lattice. Lattice is a historic term from early work conducted on crystals and can be replaced by *"local environment"* where appropriate [3]. These relaxation processes can be placed into three groups according to the nature of the phonon interaction: the direct process, Raman processes, and higher order process such as the Orbach process [4]. The temperature dependence of the relaxation rate $\left(\frac{1}{T_1}\right)$ can be fitted to (6.1) where A_{Direct}, A_{Raman} and A_{Orbach} are coefficient of the interaction:

(6.1)
$$\frac{1}{T_1} = \underbrace{A_{Direct}\,T}_{Direct} + \underbrace{A_{Raman}\,T^n}_{Raman} + \underbrace{A_{Orbach}\exp\left(\frac{-\Delta E}{k_B T}\right)}_{Orbach}\,.$$

The direct process occurs when there is an exact match in the transition energy and phonon energy [5]. This enables the direct transfer of energy between the phonon bath and the spin

system. In systems where the temperature is much lower than the Debye temperature (2300 K in diamond) the increase in relaxation rate due to the Direct process will be linear with temperature $\frac{1}{T_1} = A_{direct}T$ [6].

The Raman process involves two phonons of different energies that interact with the spin. A spin flip occurs if the difference in the phonon energies is equal to the spin transition energy. It can be visualised as the first low energy phonon exciting the spin to a virtual state and then a second phonon (higher energy phonon) being immediately released. The temperature dependence for the relaxation rate for different Raman processes vary as T^n where $n = 3,5,7$; depending on the spin levels involved [7]. The strength of Raman interactions is governed by the quality of the coupling between the lattice and the relevant part of the phonon bath, A_{Raman}. This process is more likely than the direct process below the Debye temperature due to the increased number of phonon pairs that can satisfy the energy requirement.

The Orbach process is possible when an excited state of the spin system, ΔE above the ground state, is accessible by phonon energies. In this process the spin is excited from the ground state to the excited state by absorbing a phonon of energy ΔE and then is able to decay, releasing a second phonon of energy $\neq \Delta E$ and therefore returning to a different spin ground state. This process is not especially efficient in two level systems [8].

For N_S^0 '*spin-orbit phonon-induced tunnelling*' has been proposed as a method of relaxation [9]. In this process, an electron tunnelling between two N-C bond orientations does not tunnel to the same spin due to local strains distorting the energy levels in one of the defect orientations relative to the others (Figure 6-2). The rate for this relaxation was expected to be related to the temperature by [9]:

$$(6.2) \qquad \frac{1}{T_1} = AT + BT^5$$
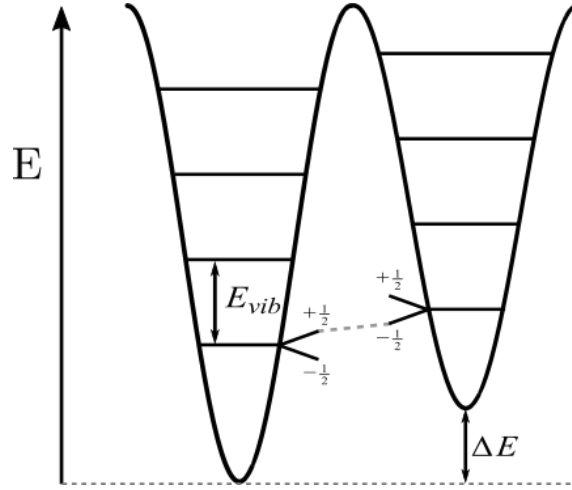
Figure 6-2 Schematic representation of two of the four potential barriers for N_S^0 with a local strain causing ΔE change in energy barrier. The dashed line demonstrates the non-spin conserving reorientation between orientations. E_{vib} is the energy between vibrational states. Adapted from [9].

The temperature dependence of N_S^0 has previously been shown to be in agreement with this dependence. This does could not unambiguously confirm '*spin-orbit phonon-induced tunnelling*' since a combination of Raman and the direct process would follow the same relationship [9]. Similar quantum tunnelling has previously been suggested as a relaxation mechanism for Ethanol glasses and also for an *"off centre"* lithium in CaO:Li crystal that can create localised tunnelling [10,11]. Both of these reports considered T_1 to be inversely proportional to temperature.

Relaxation processes can also be investigated by their field/frequency dependence. The relaxation rate due the direct process has been shown to vary as $B_o{}^2$ (even number of electrons) or $B_0{}^4$ (odd number of electrons) [6]. The relationship between the Raman process and field depends on the nature of the Raman process involved. The first order Raman relaxation rate is proportional to $B_o{}^2$ [6] but other Raman processes are predicted to be linearly dependent on the static magnetic field [7] or field independent [4]. The Orbach process will also be independent of field apart from potentially the altering of the energy gap between the ground and excited state [4]. The T_1 of N_S^0 diamond has been reported as being independent of field at room temperature between 350 mT and 3360 mT but the presence of other defects in the samples studied meant it was likely that the observed spin-lattice relaxation was dominated by cross relaxation [12].

6.1.3 Measurement of T_2

The relaxation time constant T_2 is a measure of the dephasing time for the magnetisation of resonant spins in the x,y-plane. Dephasing is predominantly caused by interactions with non-resonant spins, nuclear or electron, that are present in the local environment. These interactions decrease the amount of time that the magnetisation remains in phase. An echo decay experiment ($\pi/2–(\tau+\delta\tau)$-π-$\tau+\delta\tau$-echo) measures the contribution from all of these relaxation processes and the echo intensity, I_{echo}, will decay according to:

(6.3) $$I_{echo}\left(2\tau\right) \propto \exp\left(\frac{-2\tau}{T_m}\right)^{x}$$

where T_m is the phase memory and x is a phenomenological fitting parameter dependent on the dephasing mechanism [13]. It is the electron-electron interactions that are of interest to this work, specifically spectral and instantaneous diffusion where $x=1$.

To discuss these additional relaxation phenomena, it is conventional to group all the electron spins into two groups: those that are directly measured, A spins, and the remainder, B spins. The interactions between these groups of spins describe the different relaxation mechanisms that attenuate the echo intensity. Spectral diffusion is a term for interactions between the A and B spins, of the same or very close resonant frequency to the A spins, during the evolutionary periods that lead to an A spin no longer contributing to the echo. Such interactions are random in nature. They occur as a result of spin-lattice interactions of the B spin changing the field at an A spin or through mutual spin flip-flops of A and B spins. Instantaneous diffusion is the result of any interactions during the refocusing microwave pulse (π). If there is a sufficiently high concentration of spins it is possible for the A spin to be dipolar coupled to a neighbouring B spin at the same resonant frequency. In this case the microwave pulse flips both spins, however the change in spin state of the B spin leads to a small change in field at the A spin and a corresponding change in the A spin's resonant frequency causing it to no longer contribute to the echo. The change of field at A will occur

"instantly" and is referred to as instantaneous diffusion. Taking these process into account the echo intensity (6.3) can be better defined (assuming $x = 1$) as:

$$(6.4) \qquad I_{echo}(2\tau) \propto \exp\left(\frac{-2\tau}{T_m}\right), \qquad \frac{1}{T_m} = \frac{1}{T_2} + \frac{1}{T_{SD}} + \frac{1}{T_{ID}}$$

where T_{SD} and T_{ID} are the time constants associated with spectral and instantaneous diffusion respectively. In this work it is assumed that spectral diffusion can be ignored: $\frac{1}{T_2} \approx \frac{1}{T_2} + \frac{1}{T_{ID}}$.

The large B_1 used in pulsed experiments means it is likely that instantaneous diffusion is a substantial contributing factor on T_m when measured by a simple echo decay experiment. The rate of instantaneous diffusion can be defined as equation (6.5a) and its attenuation on echo intensity is given by equation (6.5b) [3]:

$$(6.5) \qquad \text{a,} \quad I_{echo}(2\tau) \propto \exp\left(\frac{-2\tau}{T_m}\right), \qquad \text{b,} \quad \frac{1}{T_m} = \frac{1}{T_2} + \gamma_e \left\langle B_{dip} \right\rangle \sin^2\left(\frac{\theta_2}{2}\right)$$

with θ_2 the turning angle of the refocusing pulse, T_2 is the relaxation in the absence of instantaneous diffusion and $\left\langle B_{dip} \right\rangle$ the average of all dipolar interactions.

6.2 Experimental

6.2.1 Uniaxial stress

To investigate the effect of uniaxial stress on N_S^0 a number of samples were prepared covering a range of concentrations, growth conditions and isotopic enrichments; these are detailed in Table 6-1. All the samples were approximately the same size (1 mm x 1 mm x 2 mm). The samples were polished such that no crack or chips were visible under $\times 10$ magnification. The accuracy of the face plane orientation was found to be $\pm 1°$; measured with Laue X-ray diffraction. This preparation was required to reduce the risk of fracture or cleavage of the

samples whilst under uniaxial stress. All experiments were conducted using the purpose-built EPR probe detailed elsewhere in this thesis §4.5.

Sample	Faces	$\left[N_S^0 \right]$(ppm)	Notes
Syn93-391	$\langle 111 \rangle \langle 110 \rangle \langle 11\bar{2} \rangle$	41 (4)	HPHT – natural isotopic abundances
0373821-A(ii)	$\langle 110 \rangle \langle 1\bar{1}0 \rangle \langle 001 \rangle$	7.9 (5)	CVD – (NVH^- present)
Syn339-B(i)	$\langle 110 \rangle \langle 1\bar{1}0 \rangle \langle 001 \rangle$	115 (10)	HPHT – 99% ^{15}N
Syn339-C(i)	$\langle 111 \rangle \langle 110 \rangle \langle 11\bar{2} \rangle$	90 (10)	HPHT – 99% ^{15}N (NV present)

Table 6-1 List of samples used for uniaxial stress investigation.

SP-EPR experiments were conducted on either the Bruker EMX or E580 spectrometers, and relaxation measurements were made on the Bruker E580. During pulsed experiments pulse lengths of 26 ns and 52 ns were used for the $\pi/2$ and π pulses respectively. These pulses excite approximately 1.3 mT and 0.7 mT of the spectrum creating a response predominantly from individual N_S^0 resonances.

6.2.2 Relaxation

Spin lattice measurements were made using the saturation recovery sequence §3.1.9. Spin-spin relaxation was investigated as outlined in §6.2.3. All measurements were made on the Bruker E580 spectrometer equipped with the MD-5 or MD-4 resonator for X-Band and Q-Band work respectively. Cryogenic temperatures were achieved with an Oxford Instruments CF935-O cryostat controlled via a calibrated ITC. At all temperatures sufficient time was left for the temperature of the sample and probe to settle before measurements were made; at least 45 minutes. The sample was aligned with B_0 along the [001] crystal direction for all measurements using a single axis Rexolite™ mount.

6.2.3 T_2 measurements

It can be seen from equation (6.5) that it is possible to remove the effect of instantaneous diffusion by reducing the turning angle of the refocussing pulse, θ_2. Experimentally there are two ways to achieve this: either by reducing the power of the pulse, or by increasing the length of the pulse. In this work the former is preferred since changing the length of a pulse alters the bandwidth of the pulse and potentially the population of measured A spins.
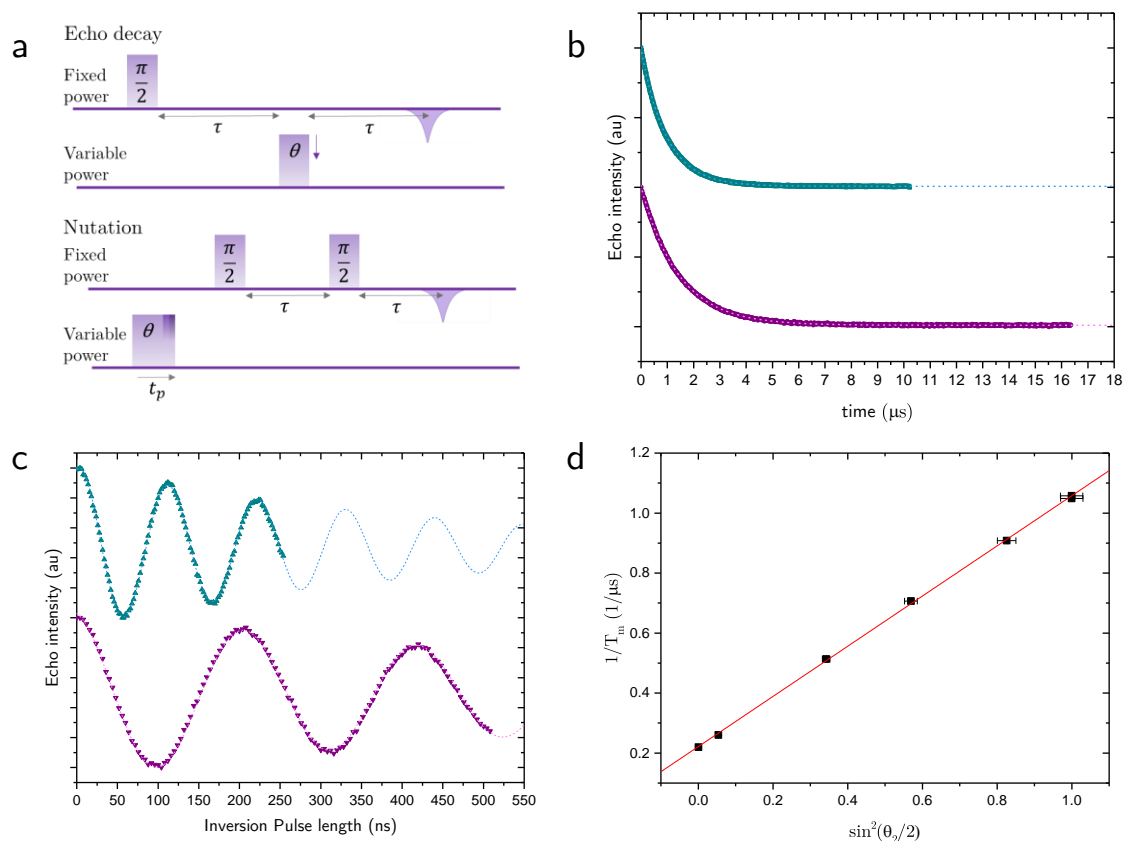
Figure 6-3 Experimental procedure for the determination of T_2.
A, Pulse sequences for echo decay and an echo detected nutation with variable power.
B, Echo decays of sample Syn93-391 at full power (top blue) and reduced power (lower purple) offset for clarity.
c, Nutations of sample Syn93-391 at full power (top blue) and reduced power (lower purple) offset for clarity.
d, Plot of $\frac{1}{T_m}$ against turning angle with intercept showing T_2.

It is possible using the Bruker E580 to control the power of individual channels and therefore create different pulse turning angles for two pulses of the same length. Pulse lengths were kept constant, an initial pulse 26 ns and a 52 ns refocusing pulse, so the same spectral width was excited. When using this approach, it is important to accurately determine the turning angle of the 52 ns refocussing pulse. The turning angle was measured with a modified version of the nutation experiment outlined in §4.3.1, this pulse sequence is shown pictorially in Figure 6-3a.

The initial inversion pulse was moved from the fixed power channel into the variable power channel, and the microwave phased to mimic the fixed power channel. The echo detection sequence was left in the fixed power channel. The inversion pulse was set to the desired power and then the echo measured for inversion pulses of increasing length. Typical examples of nutations at full and decreased power are shown in Figure 6-3c. After the tipping angle had been measured a modified echo decay sequence was performed with the refocusing pulse in the
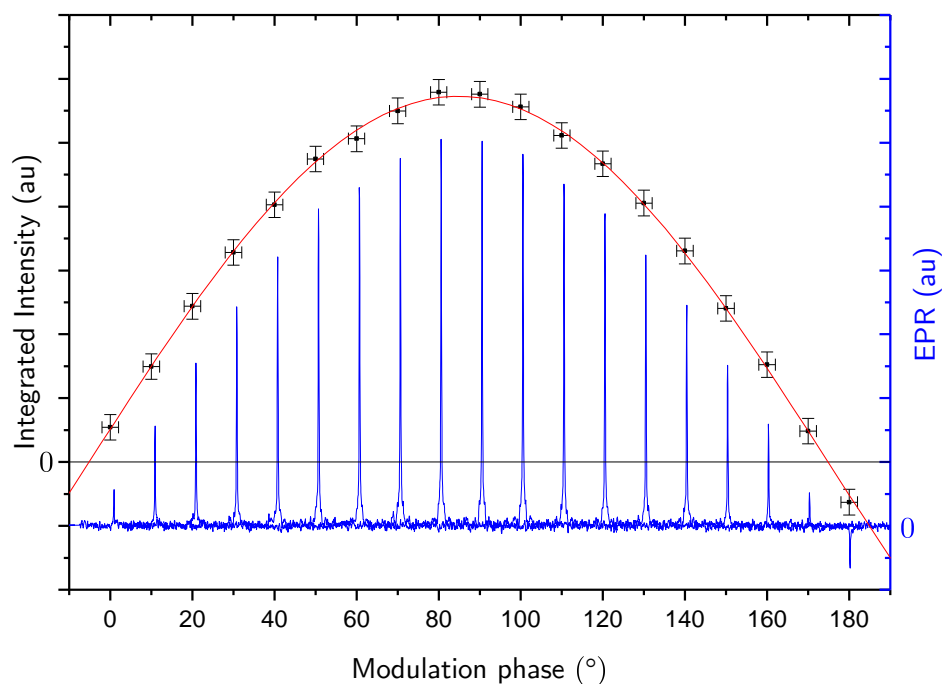
Figure 6-4   RP-EPR$^{(FM)}$ signal of N_S^0 recorded at different modulation phases at 100 kHz modulation frequency (blue lines) for 0743185-A. The fitted intensity is also shown (black data points), the fit to a sine function of 180° wavelength (red line) is also shown. All data taken with standard passaged conditions at room temperature at X-band.

variable power channel (Figure 6-3b). As the refocusing tipping angle was reduced, the decay time of the echo increased. Unfortunately, as the angle of the refocusing pulse is reduced so is the projection of the magnetisation in the xy-plane (detection plane), therefore, signal to noise is reduced. Equation (6.5) shows that a $\theta_2 = 0$ would remove all instantaneous diffusion. Although $\theta_2 = 0$ would fail to create an echo, a plot of $\frac{1}{T_m}$ against $\sin^2\left(\frac{\theta_2}{2}\right)$ can be extrapolated to $\theta_2 = 0$ to find T_2 (Figure 6-3d).

6.3 Results and analysis

6.3.1 Relaxation times from RP-EPR$^{(FM)}$

CW-EPR of electron paramagnetic systems gives a possible route to quantifying relaxation times. One route is via the measurement of microwave power saturation behaviour where the saturation factor is given by $S = 1 + \sqrt{\gamma_e^2 B_1^2 T_1 T_2}$. However, for accurate measurements detailed knowledge of B_1 is required, which may not be practically obtained in many circumstances.
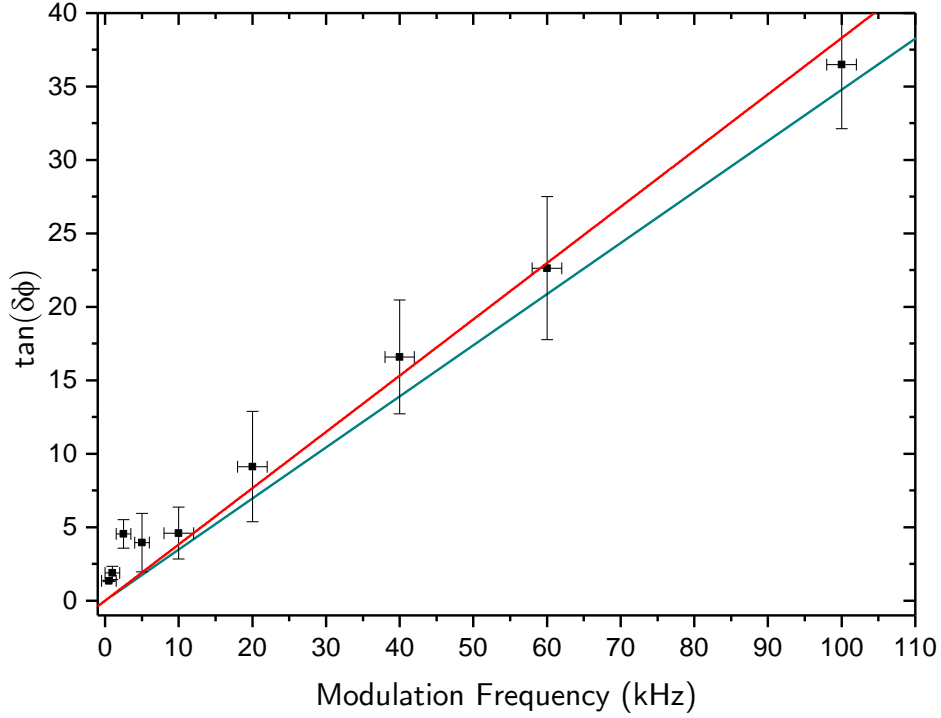
Figure 6-5 The tan of the modulation phase giving peak RP-EPR$^{(FM)}$ signal for N_S^0 against modulation frequency. Measurements made at room temperature on 0743185-A and conducted at X-Band. The solid cyan line is a simulation of the expected results to equation (6.6) using $T_1 = 2.2$ ms and $T_m = 55$ μs. The solid red line is a best fit with gradient 0.38(1) ms which predicts a $T_m = 65(5)$ μs for a $T_1 = 2.2$ ms

As discussed in §3.1.10, RP-EPR$^{(FM)}$ is a relaxation-related phenomenon and therefore it may be possible to extract information pertaining to relaxation times from the response. A method for this was proposed by Portis [14], using the relationship between the recorded phase of the peak signal and the modulation frequency, v_{mod}:

$$(6.6) \qquad \tan\left(\delta\phi\right) = v_{\mathrm{mod}}\sqrt{T_1 T_2} \quad .$$

This relationship can be inferred from the Bloch equation and has no dependence on B_1. Previous studies into the relationship between the phase shift and relaxation times [15,16] did not compare the results with conventionally measured relaxation times and consequently were unable to be certain that the correct relaxation times were recovered.

This relationship was tested with a CVD grown sample, 0743185-A, that had an N_S^0 concentration of 70(5) ppb. Measurements were made on the Bruker E580 spectrometer equipped with the SHQE resonator. The sample was mounted in a dual axis goniometer and

aligned with B_o along [001]. To establish the phase of the peak signal, the sample was measured under standard RP-EPR$^{(FM)}$ conditions except for the demodulation phase, which was stepped in 10° increments from 0-180°. The recorded spectra were then fitted and the integrated intensity for each demodulation phase was used to create a data set that could be fitted to a sine wave with fixed wavelength of 180° and the phase shift recorded (Figure 6-4). This process was then repeated at different modulation frequencies between 1 kHz and 100 kHz. To correct for any calibration issues the SP-EPR spectra of a single crystal of DPPH, was also recorded and processed in the same manner at each modulation frequency. This allowed the value taken for the phase shift, $\delta\phi$, for the RP-EPR$^{(FM)}$ from the expected SP-EPR signal to be accurately measured ($\delta\phi = \phi_{RP} - \phi_{SP}$).

The results (Figure 6-5) show that the $\delta\phi$ does indeed shift with modulation phase as predicted by equation (6.6). The relaxation times were measured using the saturation recovery and echo decay sequences and found to be $T_1 = 2.2(2)$ ms and $T_m = 55(5)$ µs. These values were used to simulate the expected value of $\delta\phi$ and show a good agreement to the experimental data. A linear fit to the data found a predicted $\sqrt{T_1 T_2} = 0.3(1)$ ms compared to the measured values of T_1 and T_m $\sqrt{T_1 T_m} = 0.35(2)$ ms showing reasonable agreement. Due to the low spin density in this sample T_{ID} and T_{SD} are negligible and therefore $T_m \sim T_2$. This assumption is reasonable since the best fit line predicts a $\sqrt{T_1 T_2} = 0.38(1)$ ms which would give a $T_2 = 65(5)$ µs.

6.3.2 Uniaxial stress of N$_S^0$

6.3.2.1 Reorientation

The application of uniaxial stress to an orientation of a defect changes the energy levels associated with it. Since the defects can reorient, this leads to a preferential population of the defects into the now energetically favourable configuration. An example where stress is applied in the [110] crystal direction is shown in Figure 6-6. In this arrangement the [111] and [$\bar{1}\bar{1}$1] elongated N-C bonds are compressed by a component of the applied uniaxial stress whilst the [1$\bar{1}\bar{1}$] and [$\bar{1}$1$\bar{1}$] have no component along the elongated N-C bond of N_S^0. Therefore, the
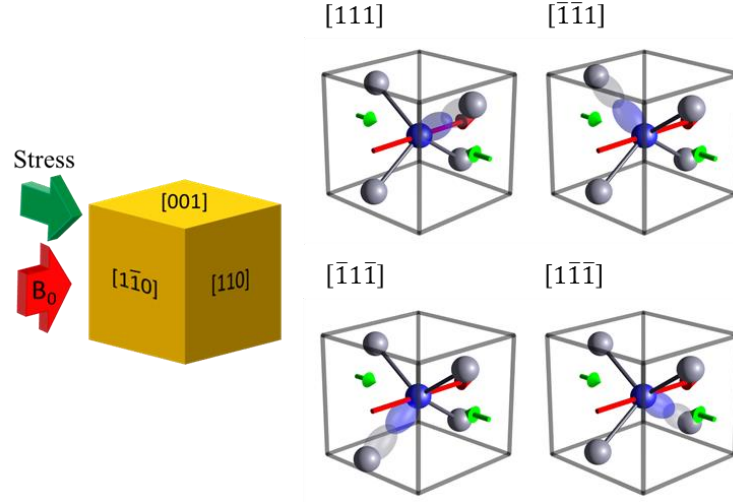
Figure 6-6 Diagram of the orientations for N_S^0 and how they interact with the static magnetic field along [$1\bar{1}0$] and the applied uniaxial stress along [110]. Grey boxes indicate the external shape of the sample with faces described on the yellow cube.

energetically favourable [$1\bar{1}\bar{1}$] and [$\bar{1}1\bar{1}$] orientations will become preferentially populated. In EPR each defect orientation can be addressed individually due to the hyperfine splitting. The magnitude of the hyperfine splitting is dependent on the angle between the defect magnetic moment and the applied field B_0. Since EPR signal is proportional to the population of defects in each orientation it is possible to monitor the populations of these individual defect orientations (Figure 6-7).

6.3.2.2 Energy

Compression along the [110] direction creates two pairs of degenerate orientations: the high energy "compressed" orientations and the low energy orientations. The probability, p_i, of a defect occupying one of these states is given by:

$$(6.7) \qquad p_i = \frac{g_i \exp\left(-\frac{E_i}{k_B T}\right)}{\sum\limits_{j=1-4} g_j \exp\left(-\frac{E_j}{k_B T}\right)}$$

where E_i is the energy level of orientation i and g_i the degeneracy of the energy level. With EPR it is possible to extract the relative populations of the "stressed" (P_1) and the "unstressed"
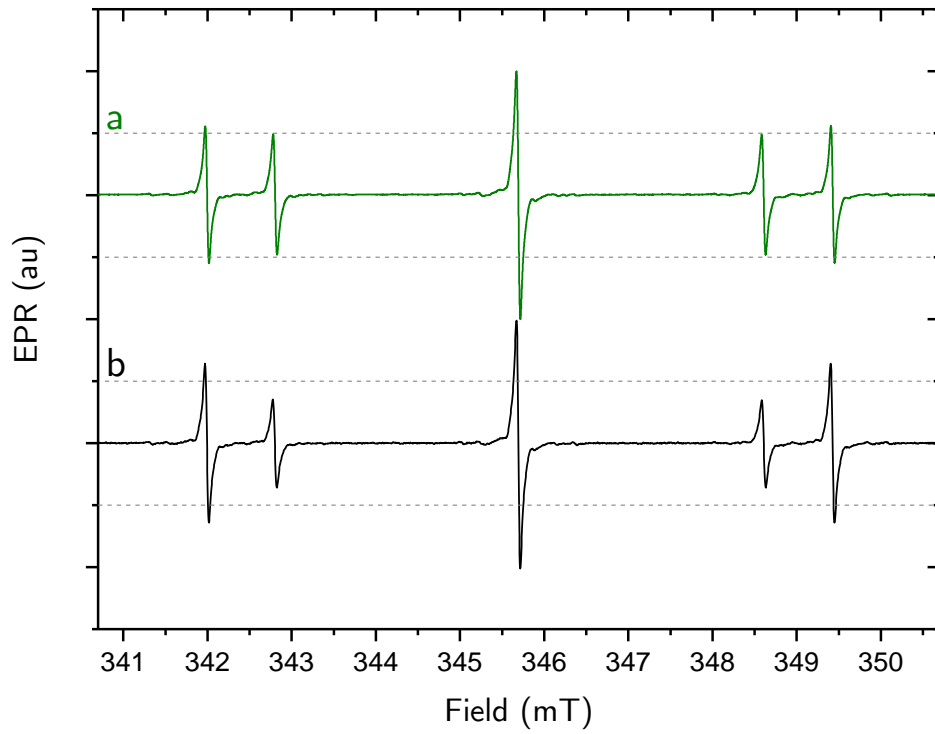
Figure 6-7 Sample Syn93-391 with applied stress along [110] *and* B_0 *along* [1$\bar{1}$0] *at room temperature. Grey dashed lines indicate expected intensity of the N_S^0 hyperfine lines.*
a, recorded with 0 GPa of applied uniaxial stress.
b, recorded with 1 GPa of applied uniaxial stress.

(P_2) orientations and therefore, the energy difference between them. By setting $E_0 = 0$ the difference in energy is expressed by:

(6.8)
$$\left(\frac{P_2}{P_1}\right) = \exp\left(-\frac{\Delta E}{k_B T}\right), \quad \text{where } \Delta E = \varepsilon\sigma$$

where σ is the applied stress in GPa and ε is a measure of the dependence of the energy on stress in meV/GPa.

An external reference spectrum was not necessary as only the relative difference in populations was required. This also meant changes in cavity Q seen as pressure was increased had no effect on the results. All spectra were taken at non-saturating microwave powers. The resonances in the recorded spectra were then fitted to individual lines to find their relative intensities. For the ^{15}N enriched samples a $^{14}N_S^0$ EPR spectrum was accounted for.
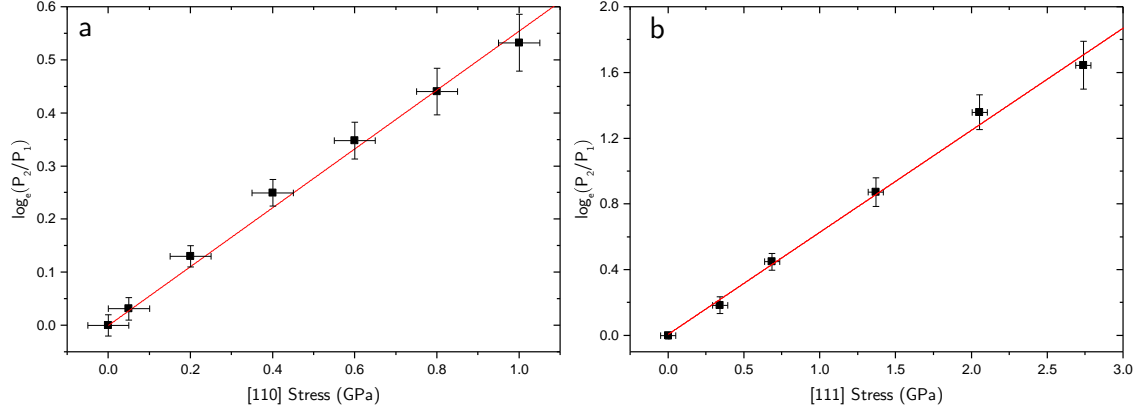
Figure 6-8 The ratio of intensities for the orientations that are depopulated (P_1) and the intensities of the remaining orientations (P_2).
a, Stress applied parallel to [110] and sample Syn93-391 at room temperature.
b, Stress applied parallel to [111] and sample Syn339-C(i) at room temperature.

Syn339-C(i) was stressed at room temperature along the [111] crystallographic direction up to a pressure of 2.7 GPa and the EPR spectrum recorded with B_o aligned along [110] crystallographic direction. Figure 6-8b shows the change population for the stressed orientation with pressure, with a minimum population of 25% of equilibrium at 2.7 GPa. A linear fit to the populations of the [111] orientations predicts that total depopulation would be expected at 3.2(2) GPa at 293 K assuming the process remained linear. The population differences were used to calculate the energy difference using equation (6.8) and a linear fit reveals an energy dependence of 17(1) meV/GPa at room temperature.

Samples Syn339-B(ii) and Syn93-391 were stressed along the [110] direction up to a maximum pressure of 0.7 GPa and 1.0 GPa respectively, at room temperature. Unfortunately, the maximum pressure attainable was limited by the larger areas of the faces, therefore, the maximum working pressure of the quartz in the stress probe was reached[*]. The results of Syn93-391 are shown in Figure 6-8a and a 25% reduction in population of the orientations under stress was observed at maximum pressure. A linear fit to the populations predicts that a stress of 3.8(2) GPa would be required to fully depopulate the stressed orientations. Sample Syn339-B(ii) showed excellent agreement with the value for total depopulation requiring 3.8(3) GPa of [110] stress. The energy dependence on stress was determined and values of

---

[*] Established through destructive testing!

13.3(3) meV/GPa and 13.0(3) meV/GPa were found for samples Syn339(b) and Syn93-391 respectively at room temperature.

Uniaxial stress has previously been employed by Liggens to determine the symmetry of the 1344 cm^{-1} (0.166 eV) local vibration mode and therefore confirm N_S^0 as its origin [17]. Liggens found a mismatch between the intensity of the stress induced transitions and the predicted intensities. This mismatch was modelled as originating from the reorientation of N_S^0 away from orientations under pressure. For [111] stress a change in energy of 22(5) meV/GPa was required to explain the intensities and lower factor of 11(2) meV/GPa for [110] stress [17]. These numbers show a good agreement with the values directly measured from Figure 6-8. Liggens reported that a stress of 3.7 GPa along [111] had effectively depopulated the defect orientation parallel to the stress [17]. A requirement of 3.7 GPa for total depopulation is in disagreement with the value of 3.2(2) GPa predicted in Figure 6-8 but the value in this work assumes that the depopulation remains linear. A linear depopulation rate is probably unrealistic; it is more realistic to expect the change in population to plateau as complete depopulation is approached.

6.3.2.3 T_m

The effect of stress on T_m was investigated for two samples 037821-A(ii) and Syn93-391 at room temperature. Both samples were aligned with B_0 along the [1$\bar{1}$0] crystal direction, and uniaxial stress of up to 1 GPa was applied in the [110] crystal direction. Under atmospheric conditions the recorded T_m can be seen in Table 6-2.

Transition	037821-A(ii) - T_m (µs)	Syn93-391 - T_m (µs)
$M_I = -1$ (orientations [1$\bar{1}\bar{1}$] and [$\bar{1}$11$\bar{1}$])	4.09(4)	1.78 (3)
$M_I = -1$ (orientations [111] and [$\bar{1}\bar{1}$1])	3.97(4)	1.81 (3)
$M_I = 0$ (all orientations)	1.73(5)	0.99 (4)
$M_I = +1$ (orientations [111] and [$\bar{1}\bar{1}$1])	3.87(4)	1.75 (3)
$M_I = +1$ (orientations [1$\bar{1}\bar{1}$] and [$\bar{1}$11$\bar{1}$])	3.91(4)	1.77 (3)

Table 6-2 T_m for samples under atmospheric conditions at 293 K with a 52 ns π pulse.
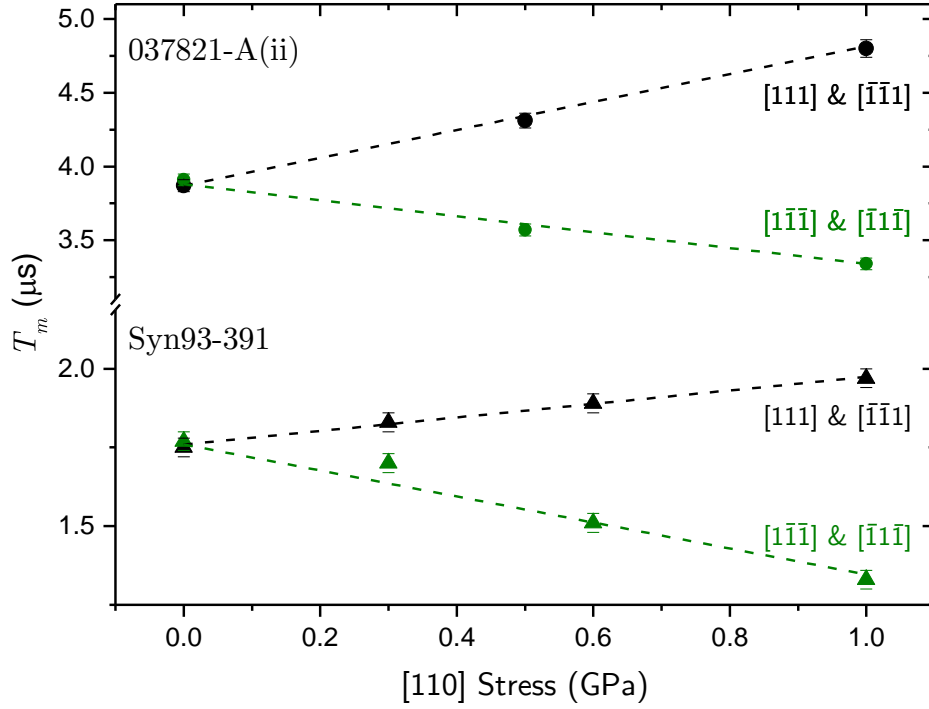
Figure 6-9 T_m for samples 037821-A(ii) (circles-top) and Syn93-391 (triangles bottom) with increased uniaxial stress parallel to [110] crystallographic direction recorded at X-band at room temperature. Orientations with a component of stress along the uniaxial stress direction are shown in green. Measured by echo decay with a 52 ns π pulse.
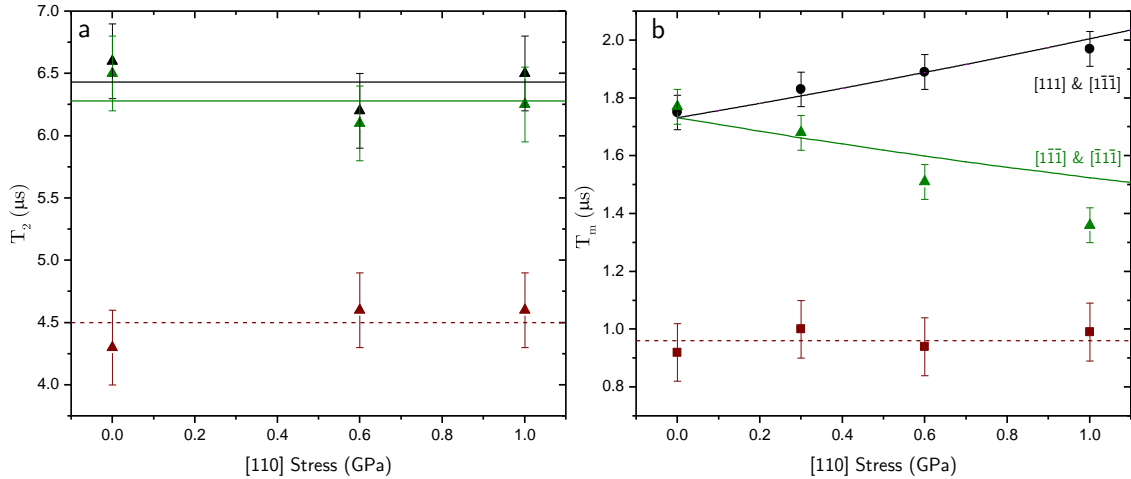
Figure 6-10 a, T_2 against uniaxial stress applied parallel to the [110] crystal direction at room temperature, for the $m_I = 0$ transition (red) dashed line indicates average T_2 for this transition. The $m_I = +1$ transition orientations under stress (black) and remaining orientations (green): solid lines are simulations discussed in the text.

b, T_m against uniaxial stress applied parallel to the [110] crystal direction at room temperature, for the $m_I = 0$ transition (red) all orientation dashed line indicates average T_m for this transition. The orientations under stress $m_I = +1$ transition (black) and remaining orientations (green); solid lines are simulations based on (6.11) with a ratio of $\frac{b}{b'} = 2.5$, all measurements made with a 52 ns π pulse.

As would be expected from its reduced concentration of N_S^0, the T_m relaxation times are longer in the 037821-A(ii) sample than the Syn93-391 for all transitions. The $M_I = 0$ echo decay showed a poor fit to a single exponential and has a shorter T_m relaxation time; this is attributed to cross relaxation with the NVH^- present in the sample. For both samples the $M_I = 0$ has a shorter relaxation than the $M_I = \pm 1$ transitions. There was no difference in T_m between orientations parallel ([111] and [$\bar{1}\bar{1}$1]) or orientations at an angle of 35.36° ([1$\bar{1}\bar{1}$] and [$\bar{1}$1$\bar{1}$]) to B_0.

As pressure was applied to the samples at room temperature the T_m of the $M_I = 0$ N_S^0 EPR transition remained the same within error bars for all pressures. In contrast the $M_I = +1$ transitions saw a definite change with pressure (Figure 6-10). For the orientations with a component along the elongated N-C bond ([111] and [$\bar{1}\bar{1}$1]) T_m was seen to lengthen with increased pressure in both samples. For the orientations with no component of the uniaxial stress along the elongated N-C bond ([1$\bar{1}\bar{1}$] and [$\bar{1}$1$\bar{1}$]) T_m was seen to shorten with increased pressure in both samples.

6.3.2.4 T_2

The T_2 of sample Syn93-391 was measured under no uniaxial pressure with B_0 aligned along the [1$\bar{1}$0] crystallographic direction, the results are shown in Table 6-3. All transitions saw an increase in the relaxation time constant as expected. Uniaxial pressure up to 1 GPa was applied along the [110] crystallographic direction: and T_2 recorded at each pressure. T_2 was not seen to change with increased pressure for any of the orientations or transitions (Figure 6-a).

The $M_I = 0$ transition saw no change with stress within error bars. For the $M_I = +1$ transitions no change was detected within error bars for either orientation under a component of uniaxial pressure ([111] and [$\bar{1}\bar{1}$1]), or orientations under no component of uniaxial pressure ([1$\bar{1}\bar{1}$] and [$\bar{1}$1$\bar{1}$])). In addition to this the measured T_2 for the two sets of orientations were

the same as each other, within error bars.

Transition	T_m (μs)	T_2 (μs)
$M_I = +1$ (orientations [$1\bar{1}\bar{1}$] and [$\bar{1}1\bar{1}$])	1.72(5)	4.6(3)
$M_I = +1$ (orientations [111] and [$\bar{1}\bar{1}1$])	1.75(5)	4.6(3)
$M_I = 0$ (all orientations)	0.92(5)	4.3(2)

Table 6-3 Tm measurements on Syn93-391 comparing T_m and T_2 at room temperature. All measurements made with a 52 ns π pulse.

6.3.2.5 Dipolar coupling

The energy of the dipolar interaction between two magnetic point dipoles with magnetic moments, μ_{e1} and μ_{e2}, in a large applied field (Figure 6-11a) can be expressed classically as:

$$(6.9) \qquad\qquad U_{dipolar} = \frac{\mu_0}{4\pi} \frac{3\cos^2\theta - 1}{r^3} \mu_{e_1 z} \mu_{e_2 z}$$

where r is the distance between dipoles and θ is the angle between the inter-dipole vector, **r**, and the applied magnetic field. When assessing the dipolar coupling between defects it is important to consider the range of spacing between pairs of defects. These distances can be placed into three groups: those very close together, those a long distance apart and all others. Those close to each other such that the wave functions can have some overlap, within approximately 10 lattice spacing [18], will couple strongly and form N_S^0 paired systems that may be $S = 0$ or $S = 1$, for example the NOC family of defects [19]. These coupled pairs will not contribute to the N_S^0 EPR spectrum and will have little impact on the T_m relaxation times. Therefore, it is reasonable for the purposes of this discussion for the interactions between these close coupled pairs to be ignored. For the second group of defects that are a long distance apart the relative orientation of the defects in the lattice will have a small effect on the coupling, since $r \gg R$. In addition, the coupling between distant defects will be weak due to the distance between them.
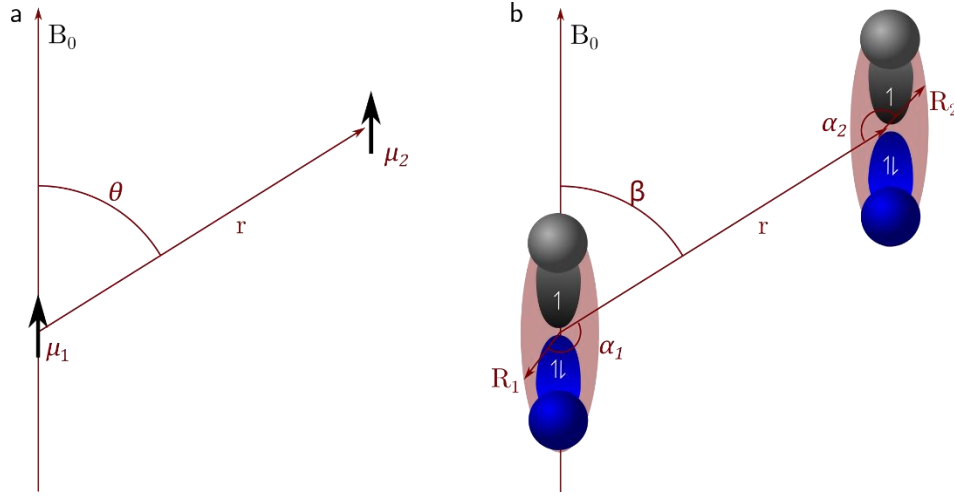
Figure 6-11 Diagram of the dipole-dipole interactions
a, two point dipoles aligned by a large magnetic field
b, Two N_S^0 aligned by the field and defect orientation; adapted from [24].

Calculating coupling is also complicated by the dipole associated with N_S^0, not being a point dipole. The unpaired electron's probability density is spread over the whole wavefunction of both defects (Figure 6-11b). The dipolar interaction is the average interaction between all points of both wavefunctions (all α and β) and as such the relative orientation of the defects must be taken into account. Considering a defect in the [111] orientation, it interacts most strongly with the other defects in the [111] orientation that are parallel (or anti parallel). The same [111] oriented defect will interact less strongly with defects in [1$\bar{1}\bar{1}$], [$\bar{1}\bar{1}$1] and [$\bar{1}$1$\bar{1}$] orientations that are at an angle of 109°. The effect of these interactions on T_m when all orientations are of even populations can be expressed as:

(6.10)
$$\frac{1}{T_{SD}} = \frac{1}{4}\langle b\rangle + \frac{3}{4}\langle b'\rangle$$

where $\langle b\rangle$ is the weighted average of all interaction between two defects in parallel orientations and $\langle b'\rangle$ the weighted average of interactions between two defects with a 109° angle of orientation. Equation (6.5) now becomes:

(6.11)
$$\frac{1}{T_m} = \frac{1}{T_2} + \left(p_1 b + p_2 b' + p_3 b' + p_4 b'\right)$$
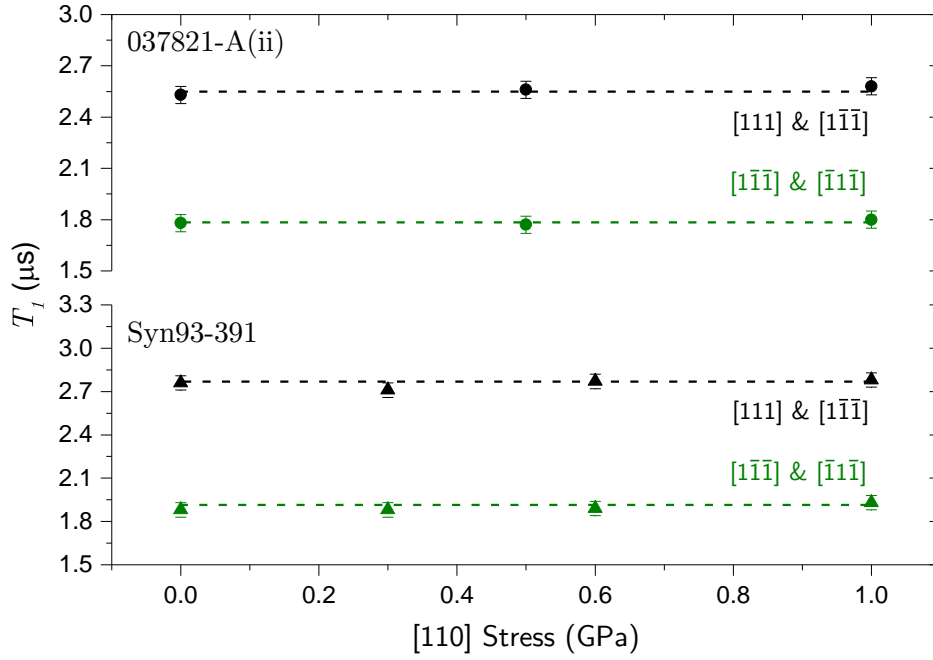
Figure 6-12 Variation in T_1 against stress parallel to the [110] crystal direction for two samples. Orientations under stress (black) and remaining orientations (green); dashed lines are the average T_1 for each transition. Measured by saturation recovery with a 52 ns π pulse.

where p_1 is the probability of a defect in the same orientation and p_2, p_3 and p_4 are the probability of it being in the remaining three orientations, defined such that $p_1 + p_2 + p_3 + p_4 = 1$.

Equation (6.11) can be used, along with the measured T_2 and change in energy due to stress, to simulate the expected change to T_m for each EPR transition under applied stress by varying the ratio between $\langle b \rangle$ and $\langle b' \rangle$. The results of this are shown in Figure 6- and show a reasonable agreement with the experimental results; the depopulated orientations are in good agreement to the simulations. For the orientations with increased aligned populations the experimental T_m reduces more rapidly with pressure than the simulation would suggest but the trend in change is correct, and an exact agreement was not expected given the crude nature of the assumptions made in the simulation.

6.3.2.6 T_1

Two samples, 037821-A(ii), Syn93-391, were selected for investigation for the effects of uniaxial stress on relaxation of N_S^0. The samples were aligned with B_0, along the [1$\bar{1}$0] crystal direction

and T_1 was measured under atmospheric conditions using saturation recovery with a picket fence of $\pi/2$ pulses where $n{=}12$ prior to echo detection.

Transition	037821-A(ii) - T_1 (ms)	Syn93-391 - T_1 (ms)
$M_I = -1$ (orientations $[1\bar{1}\bar{1}]$ and $[\bar{1}1\bar{1}]$)	1.77(3)	1.88 (2)
$M_I = -1$ (orientations $[111]$ and $[\bar{1}\bar{1}1]$)	2.54(3)	2.77 (2)
$M_I = 0$ (all orientations)	1.73(4)	2.11 (2)
$M_I = +1$ (orientations $[111]$ and $[\bar{1}\bar{1}1]$)	2.53(3)	2.76 (2)
$M_I = +1$ (orientations $[1\bar{1}\bar{1}]$ and $[\bar{1}1\bar{1}]$)	1.78(3)	1.88 (2)

Table 6-4   Table of the T1 times measured under atmospheric conditions at room temperature Measured by saturation recovery with a 52 ns π pulse.

The results for room temperature measurements are shown in Table 6-4. The T_1 times for the $M_I = 0$ transition where 18% shorter for the CVD grown sample 037821-A(ii) than the HPHT synthesised Syn93-391; this may be due to the presence of NVH^- in the CVD grown sample. The T_1 times for the $M_I = -1$ and $M_I = +1$ transitions both follow a similar pattern. The orientations parallel to B_0 ($[111]$ and $[\bar{1}\bar{1}1]$) showed the longest relaxation times in both samples and the CVD grown sample's times were shorter by 9%. The T_1 for orientations with B_0 at an angle of 35.26 ° ($[1\bar{1}\bar{1}]$ and $[\bar{1}1\bar{1}]$) have a reduced difference between samples but are much shorter ($\sim$30%) than the perpendicular orientations.

Uniaxial stress was applied in a $[110]$ crystal direction up to 1 GPa at 293 K and T_1 measured (Figure 6-12). The data recorded at all pressures showed a good fit to a single exponential decay with adjusted R^2 of 0.995 being typical. As pressure was increased, no change in the T_1 was observed for any transition, within the error bars of the experiment. Taking into account the errors bars on the measurements, the maximum increase of 0.04 ms and 0.05 ms is possible in the Syn93-391 and 037821-A(ii) samples, respectively.

6.3.3   Field dependence

Sample Syn93-07 with N_S^0 of 270(10) ppm was chosen for multi-frequency work. Syn93-07 is a single sectored HPHT sample grown with natural isotopic abundances; the sample was part
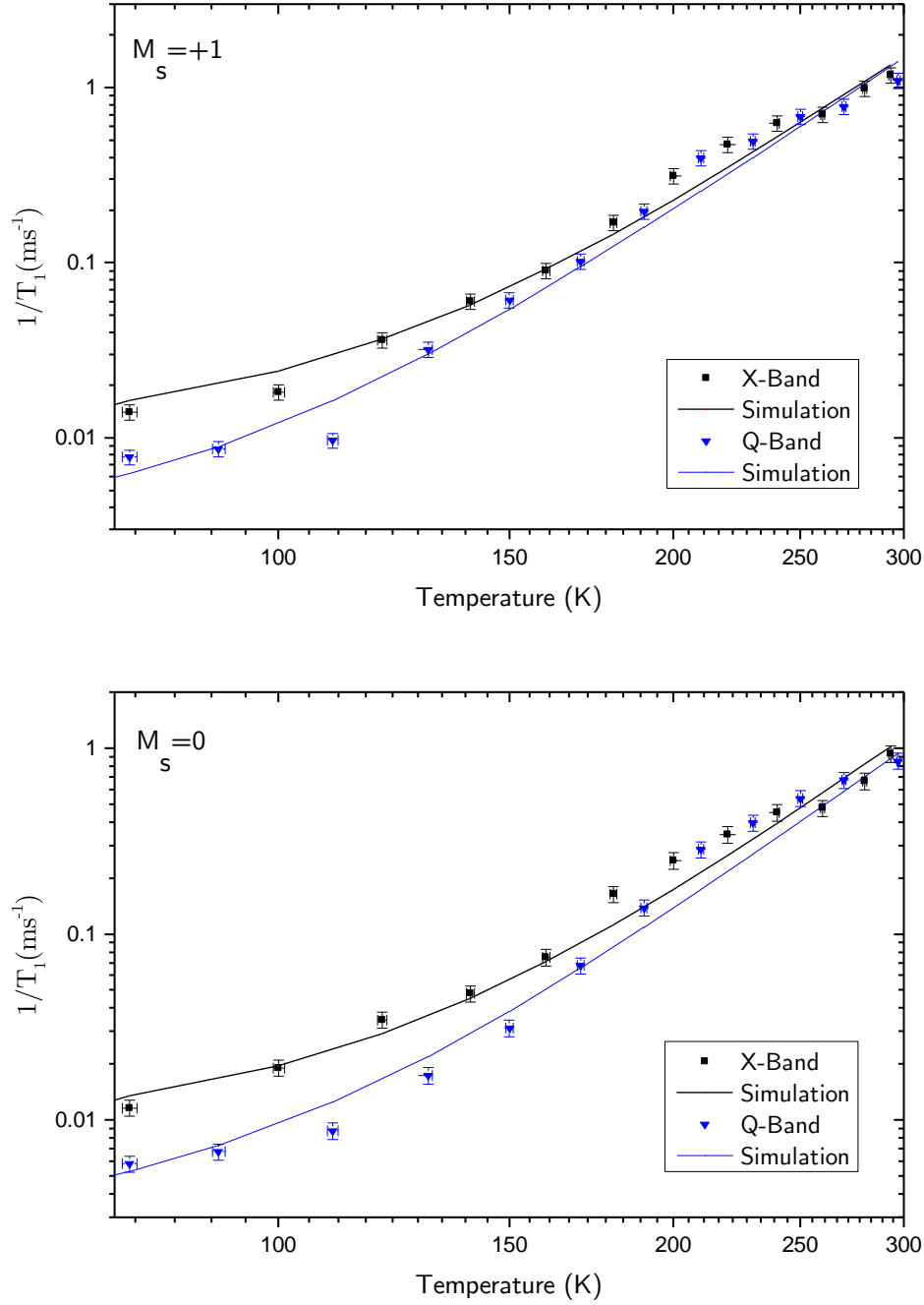
Figure 6-13 Temperature dependence of T_1 for Syn93-07 with B_0 aligned along the [001] crystallographic direction. Top for the $M_s=+1$ transition and bottom for the $M_s=0$ transition. Measured by saturation recovery with a 52 ns π pulse at X-band (black) and Q-band (blue). Fits are for equation (6.2) with values shown in Table 6-5.

of the same growth run as our highly characterised reference sample. Saturation recovery measurements were performed on both samples between 77 K to 297 K at both X-band, nominally 9.6 GHz, and Q-band, nominally 34.5 GHz. Measurement of T_m at both frequencies was found to be 180(10) ns at X-band and 185(10) ns at Q-band and was invariant with

temperature at both frequencies. At X-band T_2 was also invariant with temperature and found to be 402(5) ns at 293 K and 395(10) ns at 77 K.

Saturation recovery measurements failed to demonstrate a good fit to a single exponential at X-band with a very fast decaying signal present. Fitting to a bi-exponential revealed a short and long time constant. The component of the relaxation with a short time constant 2(1) µs was found to be invariant with temperature and alignment and was reproducible in this sample. Since the short time constant was invariant with temperature it will not be discussed further. The measured T_1 for the $M_I = 0$ and $M_I = +1$ transitions are shown Figure 6-13.

The best fit for the data was found using equation (6.2) as has previously been reported [9] (the values used for fitting are found in Table 6-5). It should be acknowledged that the quality of fits to this model are not perfect but it does allow comparison of the general trends. From these it can be seen that the B parameter remains approximately unchanged for all transitions at all fields, but the A parameter increases by approximately a factor of 3 to 3.5 times at room temperature; this value approximately correlates with the increase in field.

	X-band		Q-band	
	A $\left(T\,ms^{-1} \right)$	B $\left(T^{-5}ms^{-1} \right)$	A $\left(T\,ms^{-1} \right)$	B $\left(T^{-5}ms^{-1} \right)$
$M_I = 0$	$1.5(2) \times 10^{-4}$	$5.1(5) \times 10^{-13}$	$5.2(1) \times 10^{-5}$	$4.5(5) \times 10^{-13}$
$M_I = +1$	$1.8(2) \times 10^{-4}$	$4.5(5) \times 10^{-13}$	$6.0(2) \times 10^{-5}$	$5.0(5) \times 10^{-13}$

Table 6-5 Parameters used for fitting multi frequency relaxation measurements to (6.2).

6.4 Conclusions

In this chapter, it has been demonstrated that it is possible to extract relaxation times from the phase shift in RP-EPR[FM]. However, the value extracted is $\sqrt{T_1 T_2}$ and a family of combinations of T_1 and T_2 values could satisfy the relationship. For samples in the Redfield limit [20] where $T_2 = T_1$, this does not present such a problem. It may be possible to use this relationship to estimate T_2 since in diamond T_1 is independent of concentration. It must also be noted that this method can only be used for samples where it is possible to meet the RP-EPR[FM] condition.

The energy shift created by uniaxial stress on N_S^0 has been directly measured for the first time and shows excellent agreement with previous theoretical predictions and inferred measurements. In addition to this, spin relaxation measurements have been made under high uniaxial stress for the first time in diamond. It has been demonstrated that instantaneous diffusion during the π pulse is a strong factor in the T_m for N_S^0 where there is < 1 ppm concentration of the defect. The result for the spin-spin relaxation measurements under uniaxial stress show that it is possible to manipulate T_m for a given defect orientation. This is achieved by tuning the dipolar interactions between defects in different orientations and an empirical model shows a reasonable agreement with results. Further research into the tuning of T_m should focus on repeating the results in preferential orientations created by other methods.

The mechanism of '*spin-orbit phonon-induced tunnelling*' relied on there being vibrational levels at equivalent energy but different spin states due to local stresses on the lattice. At X-band frequencies the energy between spin states is ~0.04 meV by application of 1 GPa uniaxial stress in the [110] crystalline direction and a perturbation of 13.3(3) meV was created between two orientations. This would have removed any accidental equivalency between the excited vibration states of the orientation under stress and those not. Therefore, if '*spin-orbit phonon-induced tunnelling*' was the dominant mechanism an increase in T_1 would be expected once accidental degeneracies had been lifted. Since no change was observed it is concluded that reorientation could not play a factor.

The field dependence work showed that at room temperature T_1 is approximately independent of field, supporting previously reported results [12]. However, at temperatures below 150 K there is a dependence on field. This is inconsistent with the direct process or any of the common Raman processes being dominant at these temperatures [4]. The T^5 temperature dependence at high temperatures combined with the field independence is most likely the result of a multi-phonon Raman process, which may be field independent [21]. Further measurement at higher and lower fields and multiple temperatures would be required to confirm this behaviour.

There is potentially a wide range of experiments where the in situ uniaxial stress EPR probe could be of use. In diamond uniaxial stress could be employed in the investigation of NVH^- whose EPR spectrum is proposed to be the average of two motionally averaged configurations [22]. The perturbation of uniaxial stress may be able to freeze in one configuration confirming this model, the same approach could be used to investigate other motionally averaged defects such as N_2VH^0 [23]. The probe may also be used in the investigation of NV^0 where Jahn-Teller distortions prohibit the observation of the defect in EPR. Stopping the motion between configurations may allow observation of the ground state of this defect for the first time.

6.5 References

[1]   J. H. N. Loubser and W. P. Van Ryneveld, Br. J. Appl. Phys. 18, 1029 (1967).

[2]   C. Ammerlaan and E. Burgemeister, Phys. Rev. Lett. 47, 954 (1981).

[3]   K. M. Salikohov and Y. D. Tsvetkov, in *Time Domain Spin Reson.*, edited by L. Kevan, R. N. Schwartz, and . (John Wiley & Sons Ltd, 1980), p. 414.

[4]   S. S. Eaton and G. R. Eaton, Biol. Magn. Reson. 19, (2000).

[5]   V. Vleck, Phys. Rev. 59, (1941).

[6]   K. N. Shrivastava, Phys. Status Solidi 117, 437 (1983).

[7]   A. Abragam and B. Bleaney, *Electron Paramagnetic Resonance of Transition Ions*, Reprint Ed (Oxford University Press, 2012).

[8]   R. Orbach and M. Blume, Phys. Rev. Lett. 8, 478 (1962).

[9]   E. C. Reynhardt, G. L. High, and J. A. van Wyk, J. Chem. Phys. 109, 8471 (1998).

[10]   M. K. Bowman and L. Kevan, J. Phys. Chem. 81, 456 (1977).

[11]   J. Melorose, R. Perroy, and S. Careas, Phys. Rev. B 27, 5386 (1983).

[12]   C. J. Terblanche and E. C. Reynhardt, Chem. Phys. Lett. 322, 273 (2000).

[13]   S. S. Eaton and G. R. Eaton, J. Magn. Reson. Ser. A 102, 354 (1993).

[14]   A. M. Portis, Phys. Rev. 100, 1219 (1955).

[15]   C. Mailer and C. P. Taylor, Biochim. Biophys. Acta 322, 195 (1973).

[16]   I. . Campbell, J. Magn. Reson. 74, 155 (1987).

[17]   S. Liggens, Identification of Point Defects in Treated Single Crystal Diamond by Department of Physics, University of Warwick, 2010.

[18]   A. T. Collins, J. Phys. Condens. Matter 14, 3743 (2002).

[19]   V. Nadolinny, A. Yelisseyev, J. Baker, D. Twitchen, M. Newton, A. Hofstaetter, and B. Feigelson, Phys. Rev. B 60, 5392 (1999).

[20]   Redfeild, IBM J. (1957).

[21]   M. K. Bowman and L. Kevan, in *Time Domain Spin Reson.* (Wiley & Sons Inc, New York, 1979), pp. 68–105.

[22]   A. M. Edmonds, Magnetic Resonance Studies of Point Defects in Single Crystal Diamond - PhD Thesis, University of Warwick, 2008.

[23]   C. B. Hartland, A Study of Point Defects in CVD Diamond Using Electron Paramagnetic Resonance and Optical Spectroscopy - Phd. Thesis, 2014.

[24]   H. M. McConnell and J. Strathdee, Mol. Phys. 2, 129 (1959).

Chapter 7

7 *Optical spin polarisation of $^{15}N_3V$ and $^{15}N_s{}^0$ centres*

7.1 Introduction

There is currently a significant interest in systems which may be used in quantum information processing. Long coherence times, offered by the relatively spin free lattice, coupled with point defects that are single photon emitters make diamond an excellent base material for such devices. The NV^- centre was the first acknowledged single photon emitter in diamond [1,2]. The NV^- centre has great potential in quantum information because it can be initialised by optical spin polarisation creating a near 100% polarisation of the $m_s = 0$ level. It can then be manipulated through applied microwaves and then read out optically. As well as NV^- the SiV^- [3] centre was amongst a collection of single photon emitters to be identified in diamond [2–5]. Research has been conducted into the NV centre and it has potential in the sensing of electric and magnetic fields [6,7], temperature [8,9] and stress [10] measurements. The silicon-vacancy centre has potential in complementary fields such as quantum photonics [11,12].

For the most part these useful systems work in isolation of each other and magnetic coupling between defects has been limited to level anti-crossing at specific, usually low, fields [13–15] . If two defects could be shown to interact with each other at arbitrary fields, it would have great implications for the construction of large quantum arrays. A potential pair of interacting systems, N_S^0 and N_3V^0 , was tentatively proposed by Green [16].

The low polarisation of the nuclear spin makes NMR an inherently insensitive technique. Dynamic nuclear polarisation, DNP, transfers the greater polarisation of the electron to the nucleus and increases the sensitivity of NMR. DNP was initially proposed by Overhauser in 1953 and was demonstrated experimentally later that year [17,18]. Solid state DNP *in-situ* and at high field was not initially given much consideration due to predictions that it would be

Sample	Conditions (^{1}H detection frequency)	^{13}C T_{1N}	Ref
Kanda "Greenish" Synthetic	300 MHz, ^{13}C 99.9% Enriched	8 – 157 s	[27]
Kanda HPHT "Green" Synthetic	300 MHz, ^{13}C 99.9% Enriched	15.5 (8) s	[28]
DeBeers HPHT Type Ib	60 MHz and conscious wave DNP from 8 W 39.49 GHz microwaves	220 (20) s*	[29]
Type Ib Natural	80 MHz and continuous wave DNP from 80 mW 53.9 GHz microwaves	300 s*	[30]
HPHT Type Ib irradiated and annealing at 800 C	300 MHz and optical DNP	30 min*	[31]
Natural Type Ia	60 MHz and conscious wave DNP from 8 W 39.49 Ghz microwaves	<30 min*	[29]
Natural Type Ib	300 MHz	1-5 Hours	[32]
GE Synthetic High purity	300 MHz, ^{13}C 99% Enriched	5(1) Hours	[28]
Natural Type Ia	300 MHz	35 Hours	[32]
Natural**	270 MHz	~3.5 Days***	[33]

Table 7-1 Review of ^{13}C spin lattice relaxation in diamond all measurement made at room temperature(in part adapted from [27]).
**Indicates measurement is of decay after polarisation*
** *'The gem diamonds were borrowed from a local jewellery store' and presumed natural at time of paper (1984).*
*** *Precise measurement not made.*

inefficient at high field and reviews of early attempts can be found [19,20]. Techniques where polarisation was conducted out of field and transferred have been successful but polarisation is lost during transfer. Solid state DNP was reinvigorated by advances in gyrotron microwave generation first at 140 GHz (225 MHz ^1H detection) [21] and later 250 GHz (400 MHz ^1H detection) [22]. These advances enabled work in biopolymers [23,24] and beyond [25,26].

Studies on diamond with NMR are scarce due to the experimental difficulties presented; from the low spin density and small sample size coupled with long relaxation times. T_{1n} for ^{13}C vary widely, from a few seconds for ^{13}C isotopically enriched samples to an estimated 3.5 days summarised in Table 7-1. Relaxation has also been shown to have a small orientation dependence [27,34]. Nuclear hyperpolarisation was achieved in diamond by Zhou *et al* [30] by using continuous wave 53.9 GHz microwaves to drive forbidden transitions in N_S^0. Following this Hoch and Hill observed the ^{13}C satellite structure in diamond by application of polarising microwaves at low field before transferring the sample to high field for NMR detection [35].

Hyperpolarisation of nuclear spins can be achieved by optical pumping, through the creation of hyperpolarised electron populations [36]. Optically pumped DNP has garnered increased interest in diamond during the last ten years because of the ability to polarise the NV^- electron spin. The majority of schemes where this is employed are at low fields, ~ 50 mT [37–39], to take advantage of accidental level anti-crossings and are therefore very field dependent. Recent studies at high field [13,31] from the same group have found bulk ^{13}C polarisation and assumed NV^- as the source of polarisation due to its presence in the samples. These studies lack a plausible mechanism for transfer of the electron hyperpolarisation to the ^{13}C bulk matrix. The focus of this chapter is the investigation of the reported electron and nuclear polarisation of $^{15}N_s^0$ and $^{15}N_3V^0$. The relationship of the polarisation to temperature, optical energy and optical power are investigated as well as the possibility that this polarisation is transferred to the bulk ^{13}C matrix.

7.1.1 N_s^0

The reduced symmetry of N_S^0 creates a deep donor level found experimentally to be at 1.62-1.7 eV below the conduction band [40,41]; this agrees with the prediction from DFT [42,43]. In UV-Vis optical absorption measurements of samples containing N_S^0 there is a rising continuum starting at ~ 1.7 eV and finishing at the band edge at 5.5 eV with a vibrionic feature at 4.6 eV, which can be used to quantify nitrogen concentrations [44,45]. This continuum is the result of transitions between the deep donor level and the conduction band and transitions into the local electronic level of the unpaired electron from the valence band. N_s^0 has an optical feature in the one phonon region with a peak at 1130 cm^{-1} [46] and a feature at 1344 cm^{-1}; resulting from vibrational modes associated with the shortened N-C back bonds, this feature is isotope insensitive [47]. These features can be used to quantify nitrogen in diamond [48].

N_S^0 has been shown to be thermos and photochromic and can donate an electron to other defects such as NV^0, NHV^0 and V^0 [49,50]. The energy required to drive this change in charge state is less than the 1.7 eV required to excite an electron from N_S^0 to the conduction band,

for NHV^0 the energy required is 0.6-1.2 eV [49]. If instead an electron is thermally/optically excited from the valence band to a defect and N_S^0 subsequently donates an electron to the valence band or captures a hole.

7.1.2 Charge transfer of N_3V

Photochromic behaviour of N_3V^0 has been reported though optical measurements of N3 [51]. In this report a 514 nm laser was used to excite the sample whilst UV-Vis measurements were performed and a large long-lived increase in N_3V^0 was seen and found to be insensitive to temperature. This was proposed to be charge transfer between the N_3V^0 and a local electron trap, T:

$$(7.1) \qquad N_3V^- + T^+ \xrightarrow{\quad h\nu \quad} N_3V^0 + T^0.$$

From the history of the sample it is possible to assume that the trap, T, would be N_S^0, but measurements of either charge state of N_S were conducted. This behaviour was later investigated in ^{15}N diamond through EPR, where measurements of N_3V^0 and N_S^0 could be made simultaneously [16]. Under broadband excitation from a Xe arc lamp, no change was observed in the spectrum at room temperature. However, at low temperature both defects were seen to be spin polarised.

7.1.3 Electron structure of N_3V^0

The vacancy cage model established by Colson and Kearsely [52] has proved highly successful in understanding numerous defects in diamond and related materials [52–55]. The vacancy cage model assumes that the lowest energy state arises from the orbitals of the radicals around a vacancy. For a defect with C$_{3v}$ symmetry such as N_3V^0 the molecular orbitals can be described thus:

$$\text{(7.2)} \qquad \begin{array}{l} a_{1C} \left\{ \phi_{C1} \right. \\[2ex] e \left\{ \begin{array}{l} \frac{1}{\sqrt{6}} \left(2\phi_{N1} - \phi_{N2} - \phi_{N3} \right) \\[1ex] \frac{1}{\sqrt{2}} \left(\phi_{N2} - \phi_{N3} \right) \end{array} \right. \\[3ex] a_{1N} \left\{ \frac{1}{\sqrt{3}} \left(\phi_{N1} + \phi_{N2} + \phi_{N3} \right) \right. \end{array}$$

where the subscripts C and N indicate the predominant nucleus for the orbital. The P2 EPR spectrum and N3 optical signal are proposed to originate from the neutral N_3V^0 and have the many electron states:

$$\text{(7.3)} \qquad \begin{array}{l} a_{1N}^2 e^4 a_{1c}^1 \rightarrow \, ^2A_1 \\[1ex] a_{1N}^2 e^3 a_{1c}^2 \rightarrow \, ^2E \quad . \\[1ex] a_{1N}^1 e^4 a_{1c}^2 \rightarrow \, ^2A_1 \end{array}$$

The N3 ZPL was assigned to $^2A_1 \leftrightarrow \, ^2E$ by use of uniaxial stress [56].

This model for the N_3V^0 using only sp^3 orbitals does not prove to be satisfactory when considering the possibly related transitions N2 and N4. Additionally the luminescence lifetimes of N3 were found to increase above 400 K [57]. To explain this, a model was put forward with the N2 transition being vibronic and by assigning a $^2A_2$ symmetry to the N2 excited state, (Figure 7-1a). This could be used to explain the extended photoluminescence lifetimes at high temperatures; phonon induced decay was possible between the excited N3 ^2E state and an excited state of N2 if a small Jahn-Tellor distortion was present. This model still failed to explain the N4 transition.

The application of polarised DFT calculations to N_3V^0 demonstrated that it may be a counter example to the sp^3 only model [58]. Simulations suggested that orbitals outside the vacancy cage should be taken into account even for ground state energies. The authors proposed that these additional orbitals would give rise to a high energy level, a_1^*. This model shown schematically in Figure 7-1b potentially explains all reported phenomena of the N_3V^0 centre. The broad, low intensity N2 and N4 features arise from transitions to the a_1^* level but the
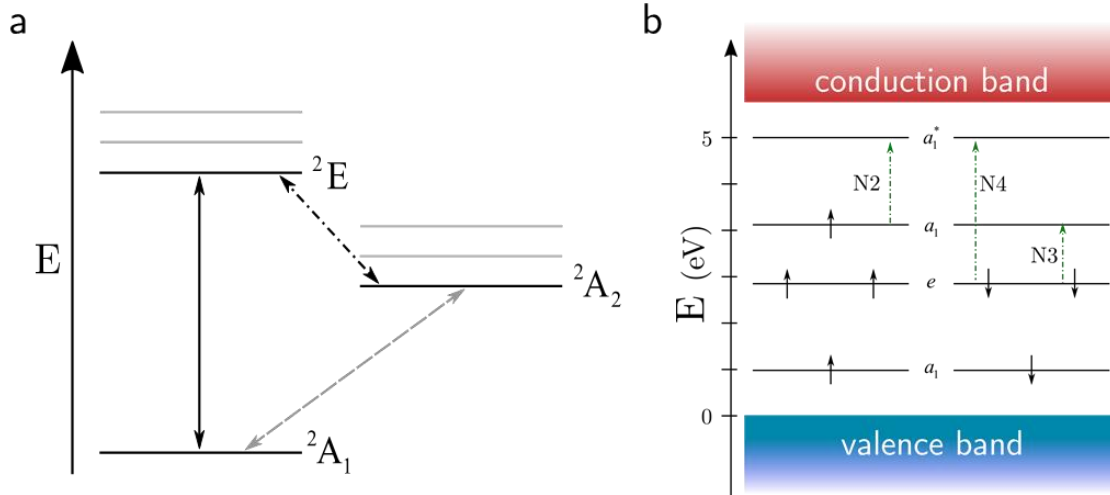
Figure 7-1 Energy level structure of N_3V:
a, the Thomaz and Davies Model [57], sold line is a spin and symmetry allowed transition, grey dashed line
is symmetry forbidden and dot dash line a vibrational transition.
b, the Jones Model [58] with optical transitions marked.

dipole strength of such transitions would be small due to the limited overlap of wave functions. This model also allows for the increased luminescence time at high temperatures, predicting transitions from the excited N3 ^2E state to the delocalised $^2A_1^*$ state.

7.2 Sample history

The work of this study will focus on Syn339-5 which contains significant amounts of both $^{15}N_S^0$ and $^{15}N_3V^0$. The sample was grown via HPHT, under controlled environmental conditions; isotopically enriched nitrogen gas was used in the process [59]. The highest purity enriched gas available for nitrogen is 98% ^{15}N [60], this translates to approximately a 95% ^{15}N enriched sample. Syn339-5 had an initial average concentration 105(2) ppm $^{15}N_S^0$ determined by FT-IR measurements [16].

The sample was initially cut along the crystal axis into an approximate cube of mass 6 mg. The distribution of nitrogen through the sample is significantly heterogeneous and different sectors are visible to the eye (Figure 7-2).

Figure 7-2 Photograph of Syn339-5 used for study showing different sectors.

To produce the $^{15}N_3V^0$, the sample was neutron irradiated with a dose of 5×10^{15} n cm^{-2} at a maximum temperature of 200 °C [61]. After irradiation the sample was annealed at 1500 °C in a non-oxidising atmosphere for 15 hours. Finally, the sample was annealed for 1 hour at 1900 °C under HPHT conditions. The post treatment defect concentrations can be seen in Table 7-2. The absence of a suitable $^{15}N_S^0$ B-centre reference precludes perfect fitting of FT-IR measurements, resulting in large errors. A 15 ppm ^{14}N B-centre was used as a substitute since it is qualitatively similar and improved fitting. The heterogeneous distribution of nitrogen makes calculations of defect concentrations exceedingly unreliable from EPR and average concentration across the sample and higher concentrations are likely (Table 7-2). Using the EPR line width to estimate concentrations for the $^{15}N_S^0$ showed two sectors with 60(10) ppm and 25(10) ppm respectively; indicating there are significantly lower concentrations in other sectors of the sample. Low concentration of H3 (NVN^0), H2 (NVN^-), NV^- and NV^0 were also present in photoluminescence measurements.

Technique	EPR			FT-IR		
defect	$^{15}N_S^0$	$^{14}N_S^0$	$^{15}N_3V^0$	$^{15}N_S^+$	^{15}A-Centres	^{15}B-Centres
Concentration (ppm)	21(2)	0.7(5)	1.6(2)	5(1)	40(10)	~15

Table 7-2 Concentrations of defects in Syn339-5.

7.3 Experimental detail

7.3.1 Optically excited magnetic resonance

The source of optical illumination for all optically excited magnetic resonance experiments was Laser diodes mounted in a Thor Labs temperature controlled laser diode mount (LTC100-A); the laser diodes used are detailed in the Appendix. Laser diodes were used as
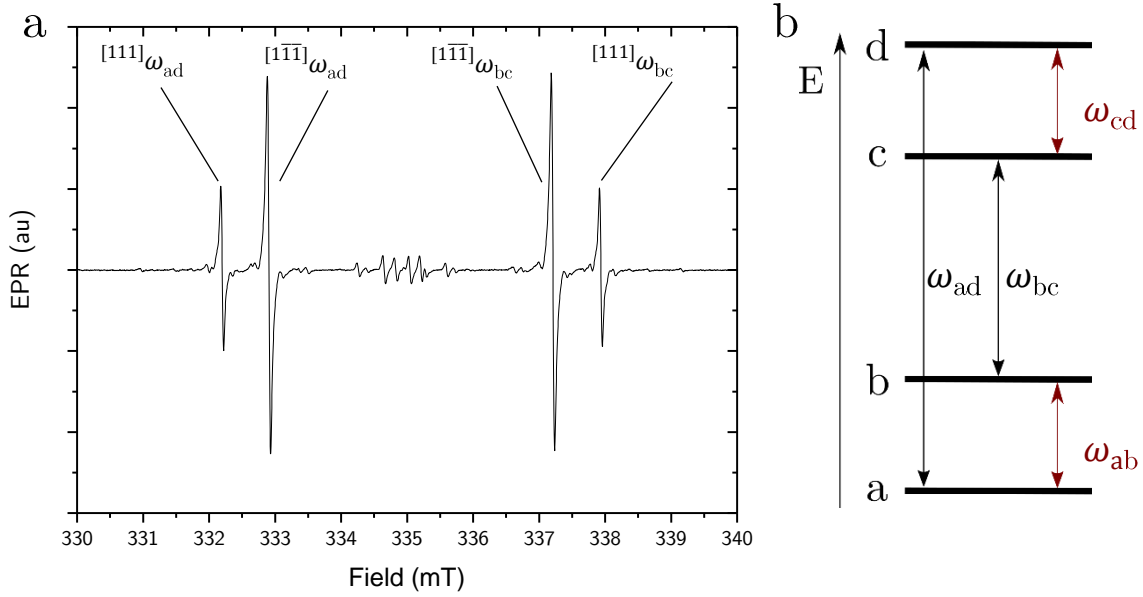
Figure 7-3   a, Example of an EPR spectrum for Syn339-5. Recorded at non-saturating powers with B_0 aligned along the [111] crystallographic direction. The transitions are marked with the naming conventions used in this work.
b, schematic of the energy level diagram for $^{15}N_S^0$ with EPR (black) and NMR (red) transitions shown.

they provide a cost-effective way of accessing single energy light sources at variable powers. The light from the laser diode was first collimated before being focused directly onto a 1 mm diameter optical fibre. The fibre used was a 0.5 N.A. high hydroxyl fibre designed to transmit light over the 200–1200 nm range [62]. Both ends of the fibre were polished to an optical finish. The measurement of optical power was performed using a digital optical power meter at the end of the fibre directly before the sample. In this way the optical properties of the fibre and coupling were not a source of error in the optical power measurement.

Due to the long relaxation times of both N_S^0 and N_3V^0, measurements were conducted using a Bruker EMX spectrometer equipped with a 90 dB bridge and a 4119 HS cavity. Cryogenic temperatures were achieved by use of either a Bruker VT unit, or an Oxford Instruments ESR900 continuous flow cryostat. The sweep width of each experiment was such that the whole spectrum was collected and the results were fitted to simulations. All data was taken with the optical fibre in place, as this was found to have an effect on the Q of the resonator. The sample was mounted in a custom-made sample mount with a chamber for the sample and a hollow shaft to allow access for an optical fibre; this design removed the need for glue at the

interface of the optical fibre and the sample. The sample has a [110] surface that accommodated measurements with B_0 aligned along the [001], [110] and [111] crystallographic directions.

An example EPR spectrum with B_0 parallel to the [111] crystal direction is shown in Figure 7-3a. With EPR it is possible to individually address not only different energy level transitions but also different orientations of a defect. An EPR line for a transition between energy levels x and y of defect orientation $[ijk]$ will be referred to as:

$$\text{(7.4)} \qquad\qquad\qquad {}^{[ijk]}\omega_{xy} \,.$$

The transitions are labelled in Figure 7-3. It also possible to use the Hamiltonian parameters to calculate the eigenstates of the system and these are shown in Table 7-3. The energy levels associated with the [111] orientations are pure eigenstates of the spin system, but the $[1\bar{1}\bar{1}]$ orientations have mixed eigenstates.

Level	Eigenstate [111]	Eigenstate $[1\bar{1}\bar{1}]$
d	$\varphi_d = \left\vert +\frac{1}{2}, -\frac{1}{2} \right\rangle$	$\varphi_d = -0.18\left\vert -\frac{1}{2}, -\frac{1}{2} \right\rangle + 0.47\left\vert -\frac{1}{2}, +\frac{1}{2} \right\rangle + 0.25\left\vert +\frac{1}{2}, +\frac{1}{2} \right\rangle - 0.10\left\vert +\frac{1}{2}, -\frac{1}{2} \right\rangle$
c	$\varphi_c = \left\vert +\frac{1}{2}, +\frac{1}{2} \right\rangle$	$\varphi_c = 0.47\left\vert -\frac{1}{2}, -\frac{1}{2} \right\rangle + 0.18\left\vert -\frac{1}{2}, +\frac{1}{2} \right\rangle + 0.10\left\vert +\frac{1}{2}, +\frac{1}{2} \right\rangle + 0.25\left\vert +\frac{1}{2}, -\frac{1}{2} \right\rangle$
b	$\varphi_b = \left\vert -\frac{1}{2}, +\frac{1}{2} \right\rangle$	$\varphi_b = -0.25\left\vert -\frac{1}{2}, -\frac{1}{2} \right\rangle - 0.10\left\vert -\frac{1}{2}, +\frac{1}{2} \right\rangle + 0.18\left\vert +\frac{1}{2}, +\frac{1}{2} \right\rangle + 0.47\left\vert +\frac{1}{2}, -\frac{1}{2} \right\rangle$
a	$\varphi_a = \left\vert -\frac{1}{2}, -\frac{1}{2} \right\rangle$	$\varphi_a = 0.01\left\vert -\frac{1}{2}, -\frac{1}{2} \right\rangle - 0.25\left\vert -\frac{1}{2}, +\frac{1}{2} \right\rangle + 0.47\left\vert +\frac{1}{2}, +\frac{1}{2} \right\rangle - 0.18\left\vert +\frac{1}{2}, -\frac{1}{2} \right\rangle$

Table 7-3 Eigenstates for two different orientations of $^{15}N_S^0$ with B_0 aligned along [111].

Optically excited NMR measurements were made using a 300 MHz NMR spectrometer at a nominal field of 7.04 T and a variable temperature static probe. The sample was mounted onto a quartz tube and then glued into a 4.5 mm NMR rotor with a direction arrow marked on it. Once the sample was mounted in the rotor the EPR spectrum of N_S^0 was used to ensure the sample was mounted so that the mark was aligned along the [111] crystal direction. This mark was then used to align the sample with the NMR B_0 along [111] crystal direction. As with EPR no glue was placed at the interface between the sample and the optical fibre. Due to restrictions in available space and the bend radius of the optical fibre a 200 um 0.25 NA fibre,
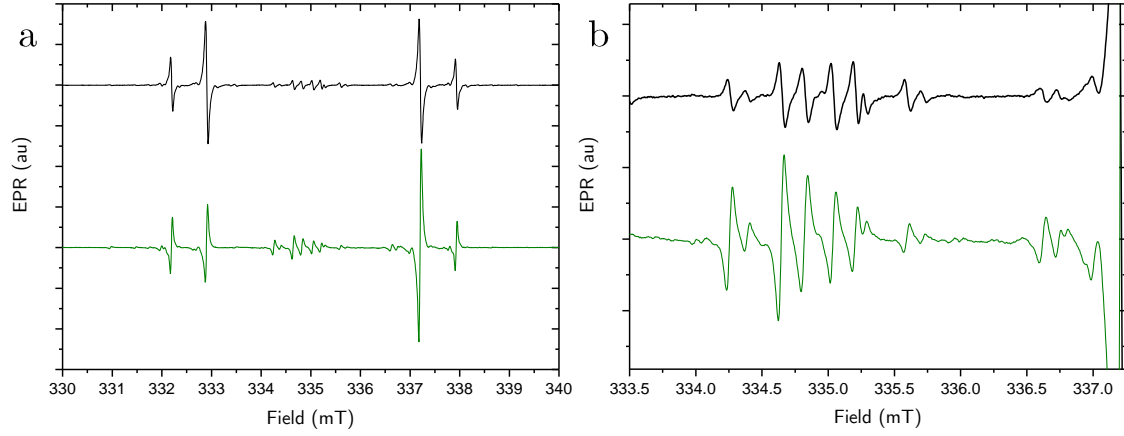
Figure 7-4   Example spectra of Syn339-5, recorded at non saturating powers with B_0 aligned along the [111] crystallographic direction at 50 K. Black spectra (top) are collected in the dark and green spectra (bottom) are collected with 80 mW optical excitation at 532 nm
a, shows the full spectrum
b, a zoom in of the N_3V^0 spectrum.

designed to transmit light of wavelengths between 250-1200 nm, was used [63]. The Illuminated spectrum is inverted compared to the dark spectrum indicating that the resonances are now in emission rather than the absorption typically measured in EPR.

7.3.2 Optically excited FT-IR

FT-IR spectra were collected with the Perkin Elmer Spectrum GX spectrometer. Cryogenic temperatures where achieved with a home-built finger cryostat. The cryostat has optical access on three sides to allow illumination of the sample at low temperature. The light source was the same laser diode assembly as described in §7.3.1 without the optical fibre; instead the laser light was coupled directly onto the sample.

7.4 EPR measurements of spin population

To investigate the optical spin polarisation of the $^{15}N_s^0$ and $^{15}N_3V$ EPR spectra were collected such that the EPR transitions were not power saturated. Polarisation factor, ε, was calculated using a dark spectrum (taken on the same day as the illuminated spectrum to minimise any changes in spectrometer response) and is defined as:

$$(7.5) \qquad \varepsilon = \frac{I_{pol} - I_{dark}}{I_{dark}} \ .$$

Due to the different response of each transition to optical illumination each line was individually fitted and the ε calculated for that transition and alignment. An example of the polarised spectrum can be seen in Figure 7-4.

7.4.1 Relaxation

Previous reports into the relaxation of N_3V^0 have been hampered by the spectral overlapping with the $m_I = 0$ transition of $^{14}N_S^0$ that is absent from the $^{15}N_S^0$ spectrum [64–66]. In an effort to establish the limiting factor on the polarisation build up, both spin-spin and longitudinal relaxation were investigated. Spin-spin relaxation was only investigated in the basic case via echo decay and was found to be temperature independent for both defects; T_m for $N_s^0 = 0.93(3)$ µs and $N_3V = 4.3(1)$ µs were measured.

To investigate the spin-lattice relaxation behaviour, saturation recovery experiments were performed on both N_3V and N_s^0. The results of these experiments, with magnetic field aligned along [001], are presented in Figure 7-5. The measurements were made in the absence of optical illumination in order to access the intrinsic behaviour of the defects. Room temperature T_1 relaxation times of $^{15}N_s^0 = 2.1(3)$ ms and $^{15}N_3V = 9.3(2)$ ms were measured. The best fit for N_s^0 and N_3V^0 was found for a model which included the direct process and a second term attributed to a Raman process [67]:

$$(7.6) \qquad \frac{1}{T_1} = A\,T + B\,T^5$$

where A and B are constants. The fits for the experimental data have been used to find a predicted T_1 of $^{15}N_S^0$ at 50 K ~ 2 s.
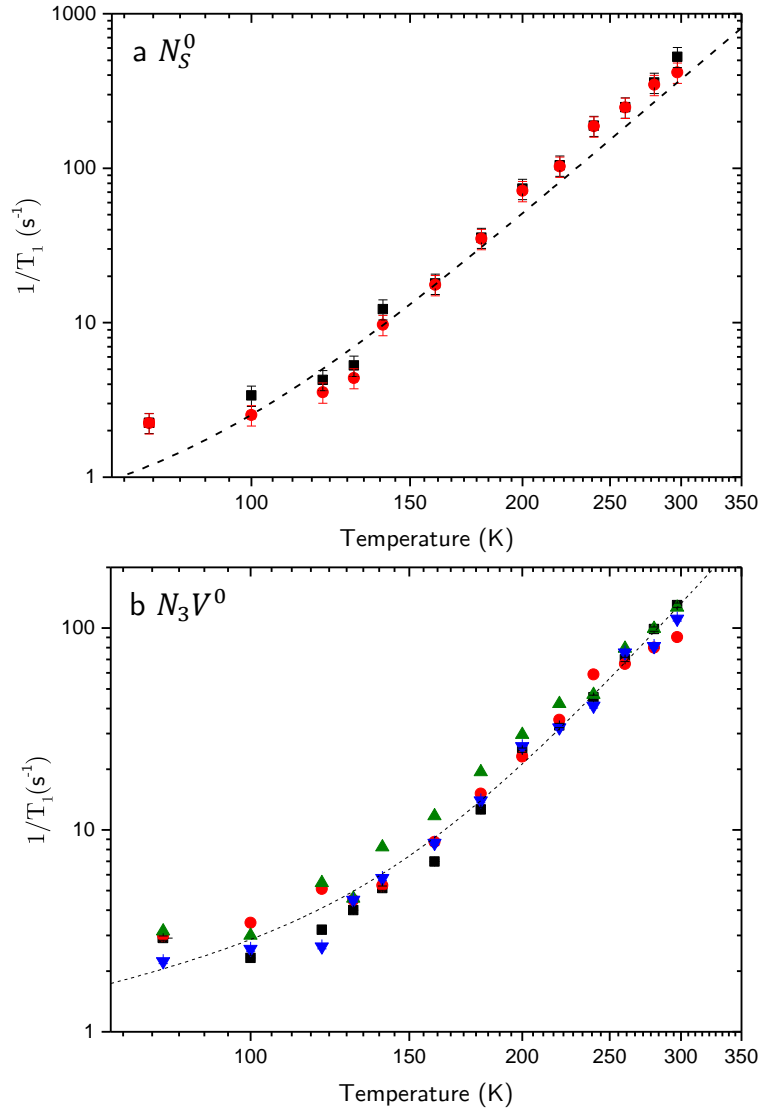
Figure 7-5 The temperature dependence for a, $^{15}N_S^0$ and b, $^{15}N_3V^0$ at x band with fits to equation (7.6) where:

a, A=0.011(5) $K^{-1}s^{-1}$ and B=1.5(2)×10^{-11} $K^{-5}s^{-1}$

b, A=0.023(2) $K^{-1}s^{-1}$ and B=5.2(2)×10$^{-11}K^{-5}s^{-1}$.

All data collected with the samples aligned with B_0 along the [001] crystallographic direction using saturation recovery.

7.4.2 Microwave power

At cryogenic temperatures both $^{15}N_S^0$ and $^{15}N_3V^0$ have long relaxation times and working in a region free from microwave power saturation is difficult. Microwave power sweeps at 50 K of $^{15}N_S^0$ were conducted and fit to the saturation equation (4.6) and can be seen in Figure 7-6. The microwaves power sweeps indicate that the highest power that can be thought of in the linear response regime is 0.8 nW (84 dB); the same is true of $^{15}N_3V^0$ confirmed by the similar

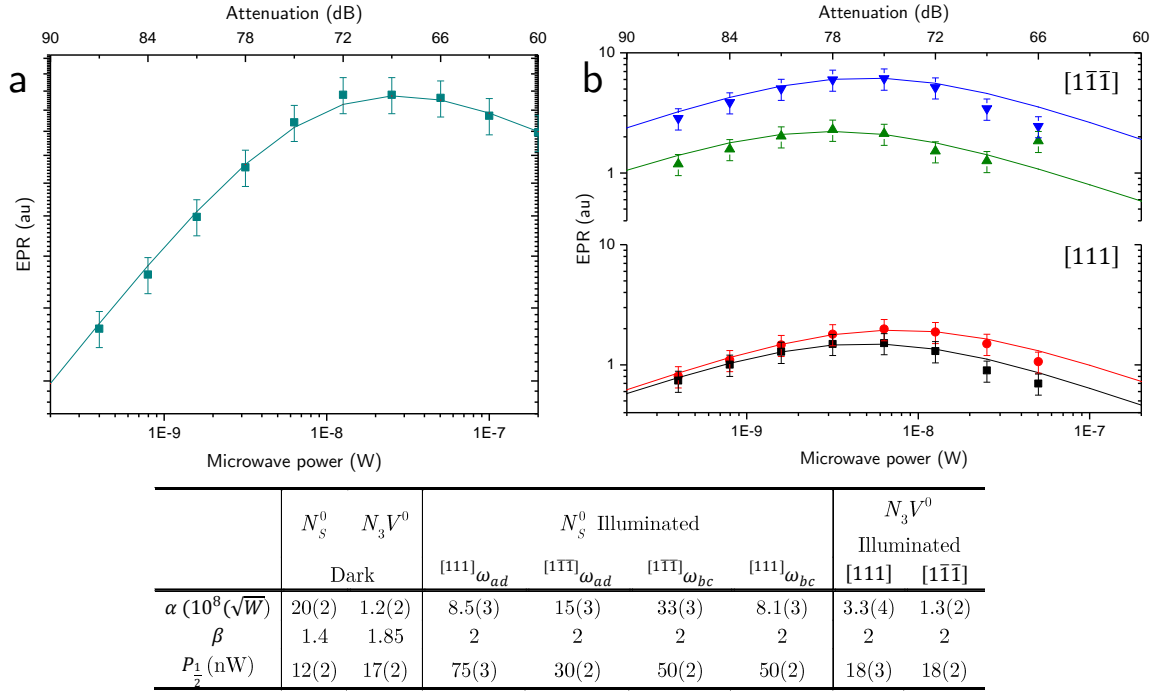|	N_S^0	N_3V^0		N_S^0 Illuminated			N_3V^0 Illuminated	
		Dark	$^{[111]}\omega_{ad}$	$^{[1\bar{1}\bar{1}]}\omega_{ad}$	$^{[1\bar{1}\bar{1}]}\omega_{bc}$	$^{[111]}\omega_{bc}$	[111]	[1$\bar{1}\bar{1}$]
α $(10^8(\sqrt{W})$	20(2)	1.2(2)	8.5(3)	15(3)	33(3)	8.1(3)	3.3(4)	1.3(2)
β	1.4	1.85	2	2	2	2	2	2
$P_{\frac{1}{2}}$ (nW)	12(2)	17(2)	75(3)	30(2)	50(2)	50(2)	18(3)	18(2)

Figure 7-6 Power saturation curves of $^{15}N_S^0$ recoded with B_0 aligned along the [111] crystallographic direction at 50 K, fits are to the saturation curve equation (4.7) with parameter outlined in the table.
a, the whole spectrum in the dark,
b, separate transitions under optical excitation from 80 mW at 532 nm $^{[111]}\omega_{ad}$ (red circles) $^{[111]}\omega_{bc}$ (black squares) $^{[1\bar{1}\bar{1}]}\omega_{ad}$ (green up triangles) and $^{[1\bar{1}\bar{1}]}\omega_{bc}$ (blue down triangles).

$P_{1/2}$. Both $^{15}N_S^0$ and $^{15}N_3V^0$ required a β value above 1, 1.4 and 1.8 respectively; the value for $^{15}N_3V^0$ is especially high and the signal sharply drops away after saturation.

Once illuminated with 80 mW of 532 nm light, the microwave power saturation behaviour was different for the two defects. The data for $^{15}N_3V^0$ was fitted to very similar parameters across all transitions and examples for a [111] and a [1$\bar{1}\bar{1}$] orientation are shown in Figure 7-6. The $P_{1/2}$ remains unchanged from the dark spectrum but β has increased to 2. All $^{15}N_S^0$ transitions showed a slight increase in $P_{1/2}$ and all required $\beta = 2$. However, the changes in saturation behaviour are small and the illuminated spectra must still be taken at 0.8 nW (84 dB) to avoid microwave power saturation.

7.4.3 Optical energy

In previous work by Green [16] the optical energy required to perform spin polarisation was investigated by use of a 1 kW arc lamp light source and optical filters. The use of longpass
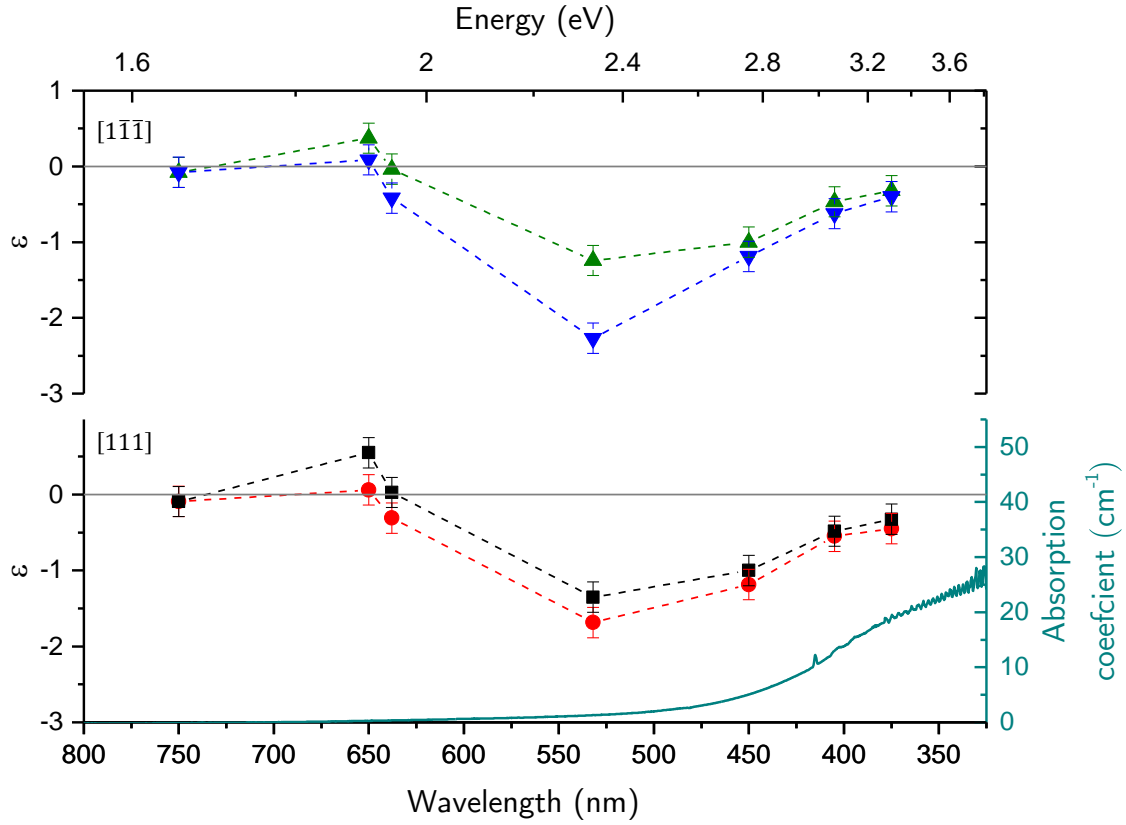
Figure 7-7 The excitation energy dependence of polarisation factor ε for $^{15}N_S^0$ recorded with B_0 aligned along the [111] crystallographic direction at 80 K. 80(3) mW of excitation used at each energy. Bottom $^{[111]}\omega_{ad}$ (red circles), $^{[111]}\omega_{bc}$ (black squares). Top $^{[1\bar{1}\bar{1}]}\omega_{ad}$ (green up triangles) and $^{[1\bar{1}\bar{1}]}\omega_{bc}$ (blue down triangles). The absorption spectrum for Syn339-5 recorded at 80 K is also shown for reference in cyan with the [111] data.

glass filters for energy selection may have led to unintended reduction in optical power, which in turn could have led to changes in spin polarisation.

The experimental procedure outlined in §7.3 allowed different optical excitation energies to be employed whilst keeping the optical power interacting with the sample fixed. The polarisation factor achieved at each energy is shown Figure 7-7. The results shown were recorded at 80(2) K and with the diamond aligned with B_0 parallel to the [111] crystal direction. Where possible 80 mW of optical power was used; the exception is the data collected at 3.30 eV (375 nm) where the available laser diodes limited power at the sample to 50(2) mW. In contrast to previous reports a sharp threshold around 2.2-2.6 eV was not found. There was some level of electron and nuclear polarisation found at all energies greater than 1.90 eV (605 nm) and the maximum polarisation factor was found at 2.38 eV (520 nm) for all lines.

There are differences in the polarisation factor for different transitions and orientations but there are broad trends in common between all lines. As excitation energy is decreased from 3.3 eV to 2.38 eV the magnitude of ε increases from 0 to 3 for $^{[1\bar{1}\bar{1}]}\omega_{bc}$. For lower energies than 2.38 eV the magnitude of polarisation decreases again. There is a greater magnitude of polarisation for the $[1\bar{1}\bar{1}]$ transitions than the $[111]$ transitions indicating that there is an angular dependence to the polarisation. There are differences in polarisation between transitions of like orientations indicating nuclear polarisation as well as electron. This is most pronounced at 2.38 eV where for $^{[1\bar{1}\bar{1}]}\omega_{bc}$ $\varepsilon = -2.3(2)$ whereas for $^{[1\bar{1}\bar{1}]}\omega_{ad}$ $\varepsilon = -1.2(2)$. In the $[111]$ orientations the difference is the opposite way round with the $^{[111]}\omega_{ad}$ have the greater polarisation; $\varepsilon = -1.7(2)$ compared to $\varepsilon = -1.3(2)$ for the $^{[111]}\omega_{bc}$, indicating there is also an angular dependence on the nuclear polarisation.

To ensure that the data taken at 1.90 eV (650 nm) was not in the window of the NV^- absorption spectrum which begins at 1.94 eV (637 nm) an additional 650 nm glass longpass filter was placed between the 650 nm laser and the optical fibre. This filter gave maximum 0.1% transmission of wavelengths less than 1.94 eV (637 nm).

7.4.4 Optical power

To analyse the response of spin polarisation to optical power, a 1000 mW 520 nm laser diode was used to excite the sample. This laser was able to produce a maximum power of 690(2) mW measured at the sample. The results of this experiment, with the sample aligned with $[111]$ crystal direction aligned along B_0 at 50 K, are shown in Figure 7-; all data was taken at non-saturating microwave powers and all EPR parameters were kept constant.

The spin polarisation of $^{15}N_S^0$ does not follow a simple linear response to optical power as has been previously reported for other defects in diamond [68]. Considering the $[111]$ orientation, the polarisation builds up to a maximum A of $\varepsilon = 2.6(2)$ at 200 mW, at higher optical powers the polarisation decreases with increased optical power. The $[1\bar{1}\bar{1}]$ orientated transitions show an increase in polarisation at optical powers up to 200 mW, but the magnitude of this
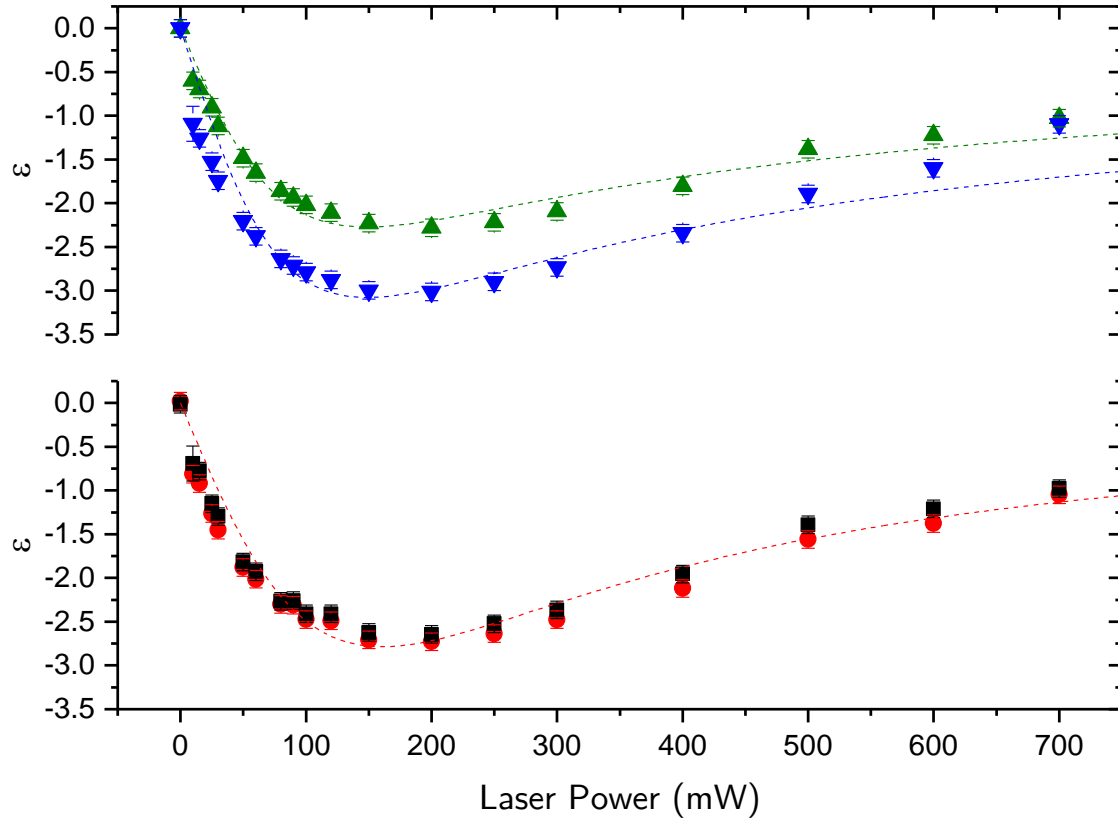
Figure 7-8 Polarisation dependence on optical power for $^{15}N_S^0$ recorded with B_0 aligned along the [111] crystallographic direction at 50 K, using 520 nm excitation. Fits are to a modified power saturation curve with $P_{1/2} = 168(5)$ mW for $^{[111]}\omega_{ad}$ (red circles), $^{[111]}\omega_{bc}$ (black squares). $P_{1/2} = 118(5)$ mW, top $^{[1\bar{1}1]}\omega_{bc}$ (green up triangles) and $P_{1/2} = 116(5)$ mW $^{[1\bar{1}1]}\omega_{ad}$ (blue down triangles).
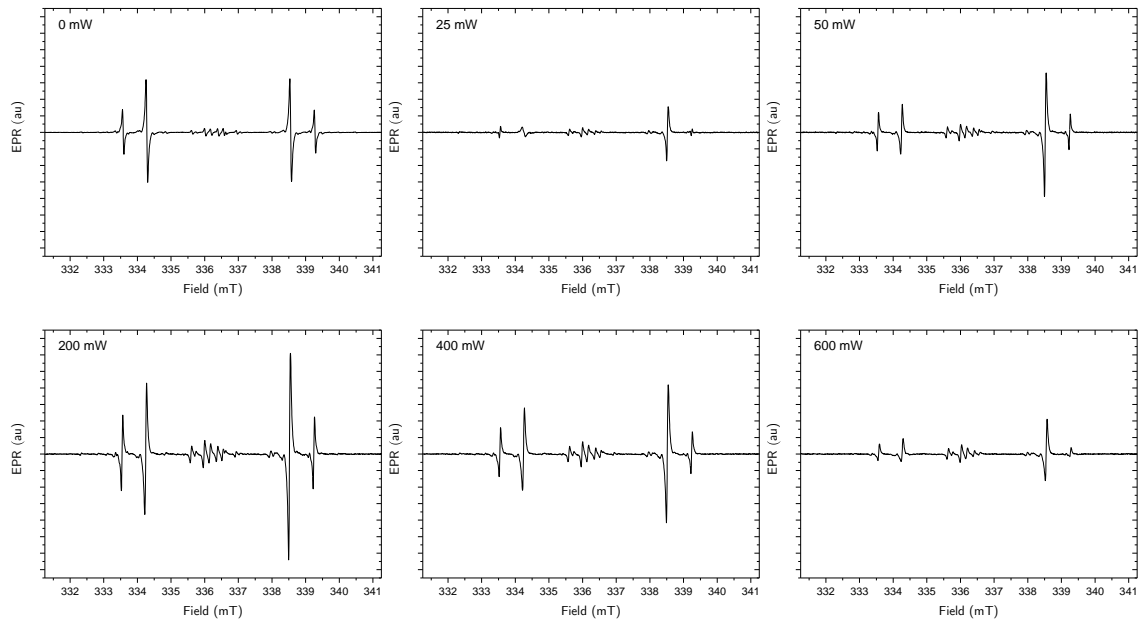
Figure 7-9 Spectra of Syn339-5 with increasing optical power for 520 nm excitation, at 50 K

polarisation is different; for the $^{[1\overline{1}\overline{1}]}\omega_{bc}$ transition $\varepsilon=3.0(1)$; with $\varepsilon=2.2(1)$ for $^{[1\overline{1}\overline{1}]}\omega_{ac}$. As with the [111] orientation the polarisation factor reduces at higher powers.

As the optical power increases the $^{[1\overline{1}\overline{1}]}\omega_{bc}$ transition is the first to respond and becomes inverted at low powers ($<25\,\text{mW}$) whereas the other three transitions do not invert until ~50 mW of optical power (Figure 7-). Once peak polarisation is built up (~150 mW) the shape of the spectrum remains the same, as the optical power is increased; however, each transition decreases in magnitude uniformly. The same trends are seen in $^{15}\text{N}_3\text{V}^0$ but the onset of the decreasing intensity is at a higher power (~300 mW) and the decrease is less pronounced.

7.4.5 Temperature dependence

Whilst the sample is under optical excitation (80 mW, 520 nm) the spin populations are not in equilibrium and no longer governed by Boltzmann statistics. As such, the signal intensity will not follow a Currie law dependence. There is potential for changes to the non-equilibrium population as the rates governing the new populations change with temperature. The T_1 of both $^{15}\text{N}_S^0$ and $^{15}\text{N}_3\text{V}$ are both highly temperature dependant, increasing as the temperature is lowered. As the rate of spin lattice relaxation opposing the polarisation reduces it is expected that that the spin polarisation will increase.

The results of variable temperatures measurements are shown in Figure 7-10. For experiments performed above 150 K there was negligible electron spin polarisation although a small amount of nuclear polarisation persisted at temperatures up to 200 K. Below 150 K there was significant polarisation on all transitions. The overall trends on all $^{15}\text{N}_s^0$ transitions were the same; the magnitude of the polarisation increased towards 50 K and at temperatures below 50 K the polarisation factor began to reduce. A different amount of polarisation was found for the $^{[1\overline{1}\overline{1}]}\omega_{bc}$ transition compared to the $^{[1\overline{1}\overline{1}]}\omega_{ad}$ at all temperatures below 100 K. The largest difference was found at 50 K where the polarisation of $^{[1\overline{1}\overline{1}]}\omega_{ad}$ is 50% of the polarisation of $^{[1\overline{1}\overline{1}]}\omega_{bc}$.
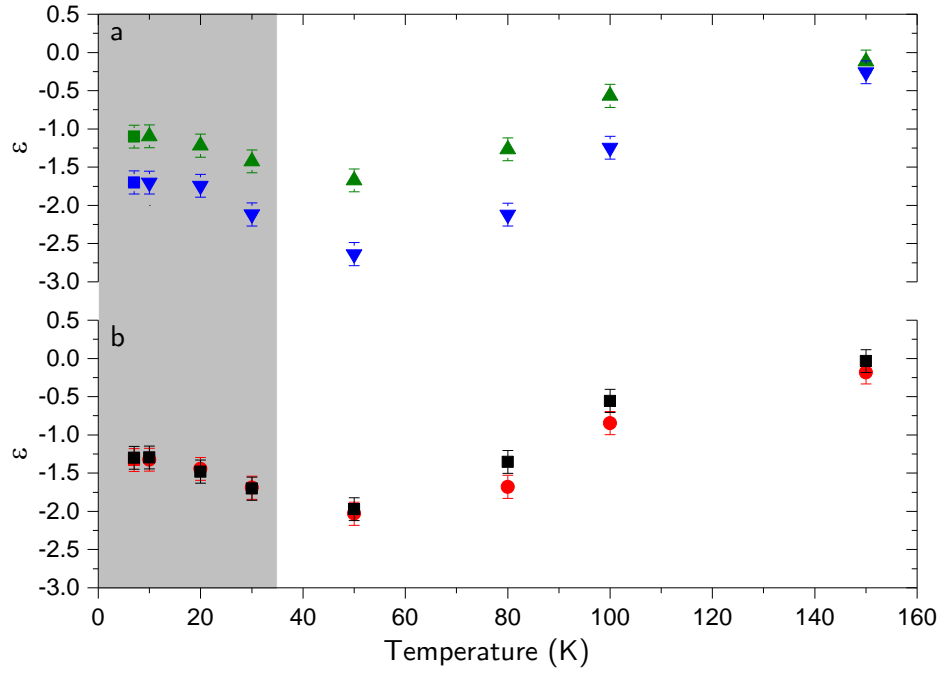
Figure 7-10   Temperature dependence of polarisation for $^{15}N_S^0$ recorded with B_0 aligned along the [111] crystallographic direction using 80 mW 520 nm excitation. Bottom $^{[111]}\omega_{ad}$ (red circles), $^{[111]}\omega_{bc}$ (black squares), top $^{[1\bar{1}1]}\omega_{bc}$ (green up triangles) and $^{[1\bar{1}1]}\omega_{ad}$ (blue down triangles). Measurements taken in the grey area were inhibited by microwave power saturation of both the dark and illuminated spectra.

At very low temperatures it was not possible to measure either the dark or illuminated spectrum without microwave power saturation. Where the increased spin lattice relaxation made the collection of an unsaturated dark spectrum impossible the expected dark intensity can be corrected for using an unsaturated spectrum from higher temperatures. However, it was also not possible to collect an unsaturated polarised spectrum at very low temperatures even with a 90 dB bridge. It is impossible to correct for this accurately and as such the data points below 40 K may not a true reflection of polarisation.

7.4.6   Polarisation rates

It is often the case with diamonds that long relaxation times mean it is impossible to collect unsaturated spectra at low temperatures. This is not usually the case for polarised samples where the limiting factor for relaxation is no longer T_1 but is now effective relaxation T_{eff} which is given by:

(7.7)
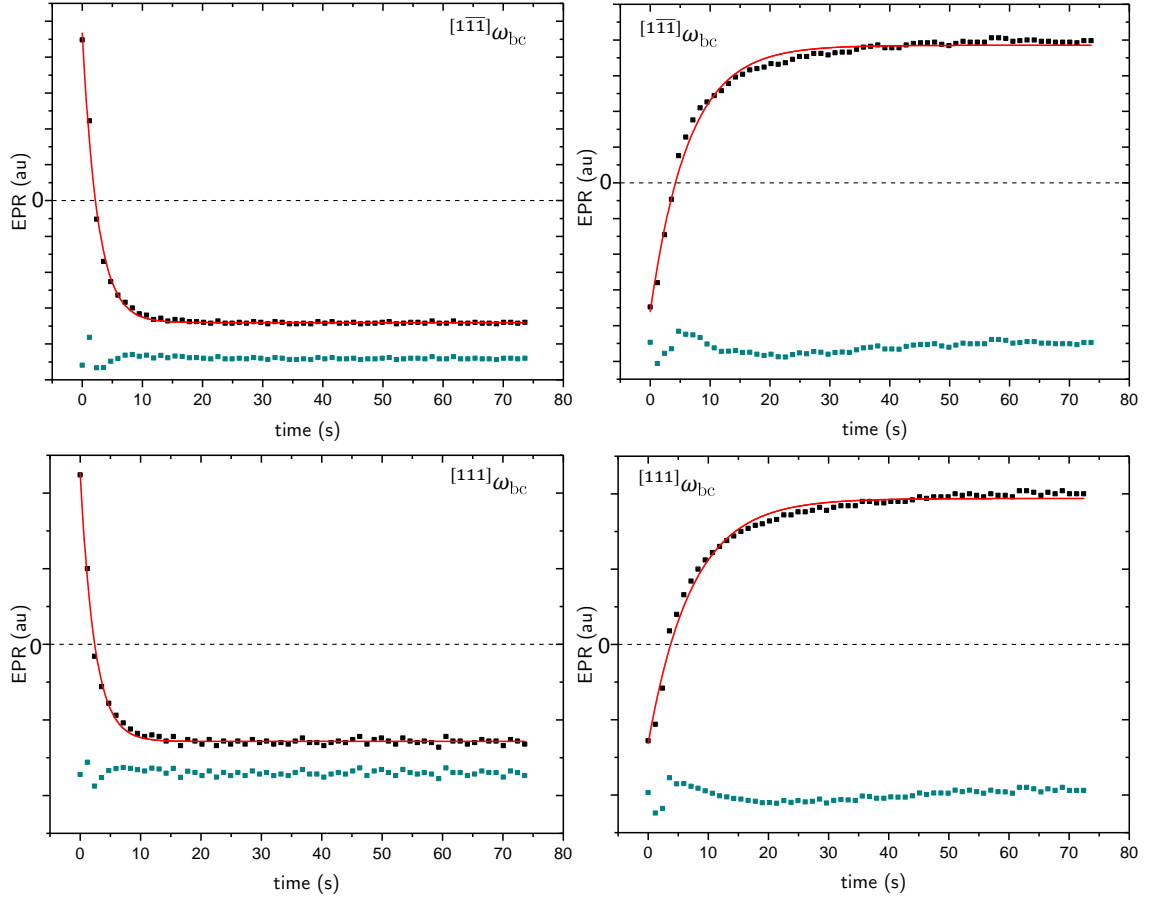$$\frac{1}{T_{eff}} = \frac{1}{T_1} + \frac{1}{T_{pol}}$$

Figure 7-11 Polarisation build and decay for $^{[1\bar{1}\bar{1}]}\omega_{bd}$ bottom and $^{[111]}\omega_{bc}$ top. Fits are exponential with the time constants discussed in the text. All data recorded at 50 K at non-saturating microwave powers. Left column, light turned on at t =0. Right column, light turned off at t=0.

where $\frac{1}{T_{pol}}$ is the polarisation rate. T_{eff} is by its nature shorter than T_1 since the optical polarisation effectively resets the system; for NV^- and SiV^0 optical polarisation reduces T_{eff} to below 10 ms [69]. The low temperature study in §7.4.5 indicates that the polarisation rate is slow for this system. The rate is sufficiently slow to allow its measurement from SP-EPR. Experiments were conducted by field sweeping across a single line as fast as possible without causing distortions due to passage and measuring the intensity of the line as the laser was suddenly switched on, to observe build up, and switched suddenly off to observe decay. The whole line was recorded rather than a time trace on the fixed field, as the laser light caused a change in the dielectric properties of the cavity, causing slight changing in position of the line. Typical results are shown in Figure 7-11 and full results in Table 7-4 .

Transition	T_1 (s)			T_{eff} (s)			T_{pol} (s)		
	10 K	50 K	80 K	10 K	50 K	80 K	10 K	50 K	80 K
$[111]\omega_{ad}$	6.3(2)	5.8(1)		2.46(3)	2.10(5)		4.0(2)	3.3(2)	
$[1\bar{1}1]\omega_{ad}$	6.1(1)	5.9(2)		2.52(5)	1.76(5)		4.3(2)	2.7(2)	
$[1\bar{1}\bar{1}]\omega_{bc}$	6.3(2)	5.3(2)	0.9(1)	2.51(5)	1.72(5)	0.75(3)	4.2(2)	2.6(2)	4.5(2)
$[111]\omega_{bc}$	7.2(2)	6.0(3)	0.9(1)	2.36(5)	1.78(7)	0.76(3)	3.5(2)	2.5(2)	4.8(2)

Table 7-4 Time constants for polarisation build up and decay.

The results show that the polarisation time constant is increasing as temperature is lowered. The average increase in T_{pol} for the four transitions as the temperature is reduced from 50 K to 10 K is 0.6(2) s. The polarisation build up was found to show a good agreement with a single exponential.

The picture is less clear for the decay of polarisation to equilibrium populations. It was expected that these measurements would also fit to a single exponential with a time constant of T_1, analogous to an inversion recovery pulsed experiment. The relatively large errors on these measurements are the result of a relatively poor fit to a single exponential.

7.4.7   Long lived nuclear polarisation

It was noted during experiments that the intensities of the EPR lines did not immediately return to the equilibrium values (Figure 7-12a). To study this behaviour, the individual spectrum was collected repeatedly starting immediately after the light was turned off for 7 hours. The SNR was too low on the $^{15}N_3V^0$ to draw meaningful conclusions but was sufficient to observe the behaviour of the $^{15}N_S^0$. The results in Figure 7-12a were taken at 50 K after illumination with 100 mW of 520 nm for a period of 20 minutes and were recorded with non-saturating microwave powers. The total intensity of the $^{15}N_S^0$ spectrum was initially found to be increased 8% from the expected value, corresponding to a 1.6 ppm increase. This increased population decreased back to equilibrium value over 7 hours of the experiment (Figure 7-12b). Before processing, the change in the relative intensity of individual resonances from the total change in population was accounted for.
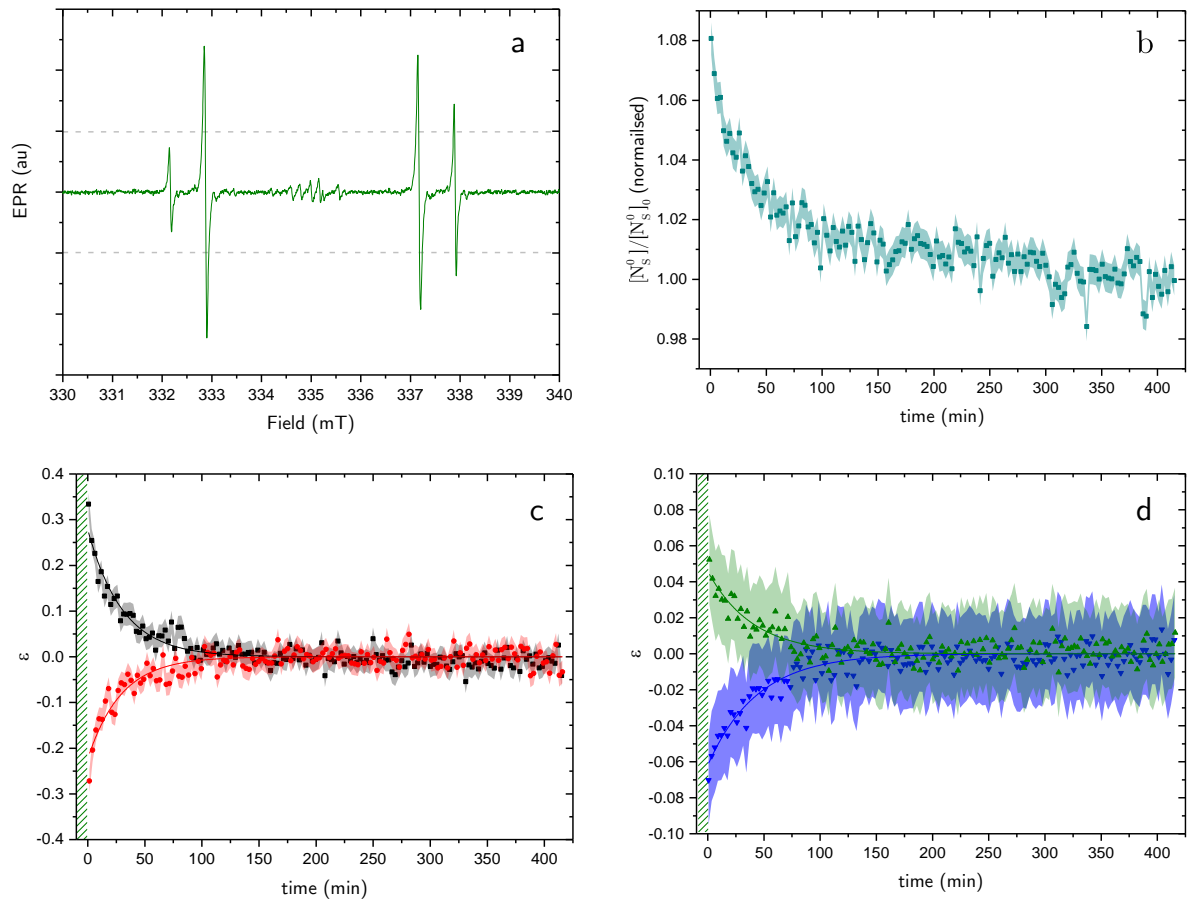
Figure 7-12 Long lived nuclear polarisation at 50 K.
a, Spectrum immediately after laser is switched off; grey lines indicate expected intensity of $^{15}N_S^0$ in the [111] orientations.
b,the change of concentration for $^{15}N_S^0$ normalised to the equilibrium population.
c, Return to equilibrium of [111] orientations. Fits are exponential decay with time constant of 29(2) min $^{[111]}\omega_{ad}$ (red circles), and 30(2) min $^{[111]}\omega_{bc}$ (black squares)
d, Return to equilibrium of $[1\bar{1}\bar{1}]$ orientations. Fits are exponential decay with time constant of 43(3) min $^{[1\bar{1}\bar{1}]}\omega_{ad}$ (green up triangles) and 39(3) min $^{[1\bar{1}\bar{1}]}\omega_{bc}$ (blue down triangles).

The behaviour was different between the different orientations, considering defects in [111] orientations, $^{[111]}\omega_{ad}$ and $^{[111]}\omega_{bc}$, where the polarisation was most pronounced. These transitions were found to have an initial polarisation of $\varepsilon = 0.35(2)$ and $\varepsilon = -0.28(2)$ for $^{[111]}\omega_{bc}$ and $^{[111]}\omega_{ad}$ respectively. The relaxation time constants for these transitions were found to be identical within errors, 29(2) min and 30(2) min respectively (Figure 7-12c). These rates are much longer than those found in the electron decay outlined in §7.4.6 and such long time scales are more likely to be associated with nuclear relaxation processes than electron relaxation. As outlined in Figure 3-3 (DNP Schematic) there are two routes for relaxation from

nuclear polarisation to Boltzmann populations: longitudinal nuclear relaxation T_{1n}, or classically *"forbidden"* double spin flips.

Whilst it is experimentally difficult to measure the rates of *"forbidden"* transitions, an estimation can be made from the ratio of transition probabilities. The probability of each *"forbidden"* transition is greatly reduced in ^{15}N material, due to the lack of a quadrupole interaction. Simulations conducted with EasySpin [70] show the *"forbidden"* transitions of N_S^0 for all orientations have the same probability, approximately a factor 2.5×10^{-6} of the allowed transition. For this reason, it is likely that the measured value is a reflection of $^{15N}T_{1n}$ for the substitutional nitrogen in the N_S^0 paramagnetic centre.

 The defects in the $[1\bar{1}\bar{1}]$ also showed deviation from the equilibrium populations but at reduced initial levels $\varepsilon = -0.07(2)$ for $^{[1\bar{1}\bar{1}]}\omega_{ad}$ and $\varepsilon = 0.06(2)$ for $^{[1\bar{1}\bar{1}]}\omega_{bc}$. The polarisation decay for these two transitions has a time constant of $44(3)$ minutes and $40(4)$ minutes respectively (Figure 7-12d). The line shape of the $^{[1\bar{1}\bar{1}]}\omega_{bc}$ transition was asymmetric initially after polarisation was stopped, and this asymmetry persisted for the 7 hours of the experiment. This distortion only ceased after the field sweeps were stopped for a period of time; in the first scan after this, a symmetric line shape was recorded.

7.5 Nuclear polarisation

Nuclear magnetic resonance, NMR, studies where carried out on the sample to ascertain if the polarisation of the ^{13}C visible in EPR had transferred out to the bulk spin bath. Initial investigations under no optical illumination indicated that the $^{13C}T_{1n}$ was long, in line with those reported for similar samples [32,33]. Unfortunately, the small size of the sample made precise measurement of the $^{13C}T_{1n}$ unrealistic. As such, the dark measurements to find the thermal polarisation were taken after the maximum reasonable magnetisation time, 86 hours, this scan can be seen in black in Figure 7-13. The peak was found at a chemical shift of $33(1)$ ppm at 297 K consistent with the previous reports [29,71].
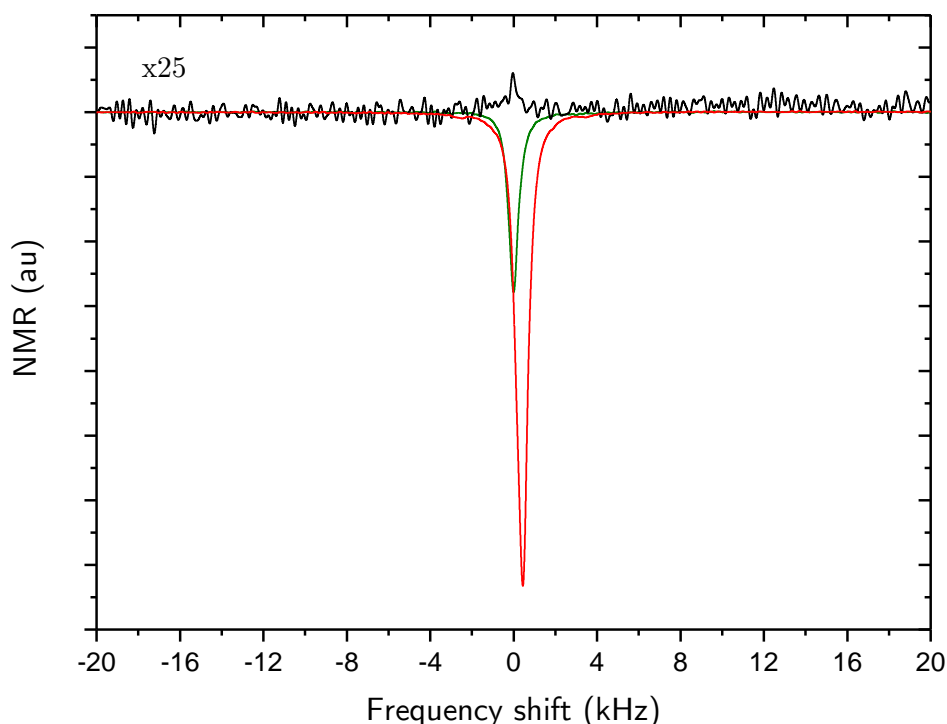
Figure 7-13 Single shot NMR experiment at 7.04 T of Syn339-5.
Black, 86 hours of polarisation in the dark at room temperature for clarity the spectrum has been multiplied by 25.
Green, 15 hours of polarisation under 300 mW of 520 nm optical excitation at room temperature,
Red, 15 hours of polarisation under 300 mW of 520 nm optical excitation at 240 K.

After the equilibrium population had been established, the sample was illuminated with 300 mW of light at 520 nm. The optical power was measured at the end of the fibre where it interfaces with the sample. To avoid any heating of the sample nitrogen gas was flowed over the sample and a temperature controller was used to keep the temperature stable at 293 K. Due to the reduced magnetisation time, see §7.5.1, it was not necessary to have a delay before acquisition and the polarised signal was collect after 10 T_{poln} of optical excitation. The peak was found at 34.5(5) ppm and was found to be inverted relative to the dark signal. The data was fitted to a Gaussian line and a $\varepsilon = $ -180(20) was found.

Using cooled nitrogen gas, it was possible to maintain a stable temperature of 240 K and the above experiment was repeated. Once the effect of the increased thermal population for the dark spectrum is taken into account a $\varepsilon = $ -480(30) is reported. On the polarised spectrum it is now possible to resolve two side peaks that have been attributed to next nearest neighbour interaction when aligned along [111] [35].
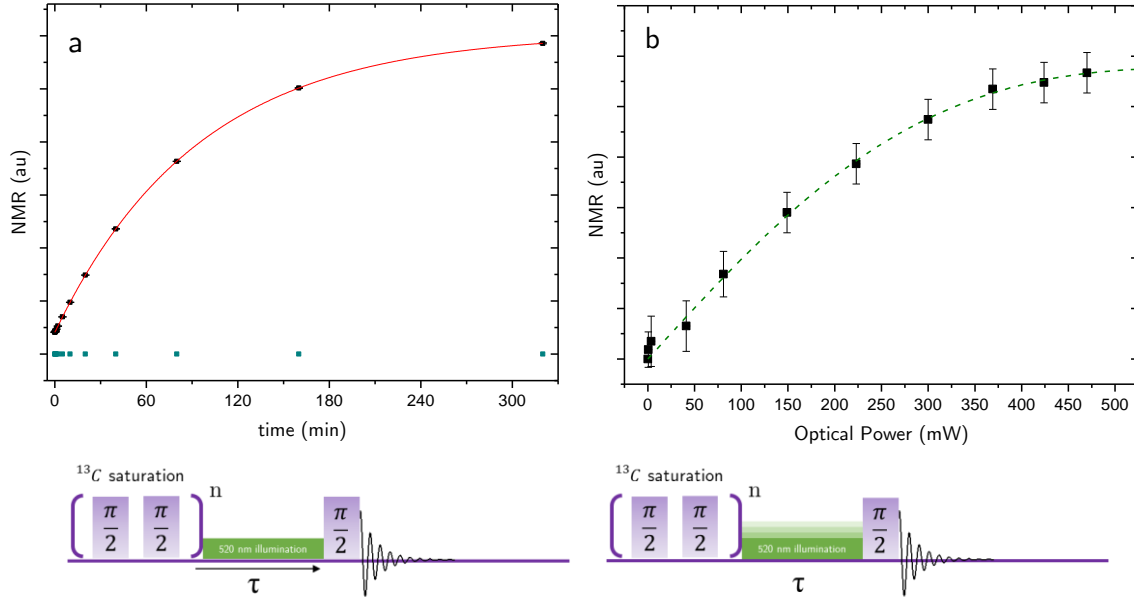
Figure 7-14 Polarisation of ^{13}C in NMR at 7.04T at room temperature with B_0 aligned along the [111] crystal direction with 520nm optical excitation. Pulse sequence is shown under data.
a, Build-up of polarisation over time with 300 mW optical power. Fit (red line) is an exponential with $T_{poln} = 94(1)$ min.
b, Build-up of polarisation for increasing optical power. Fit (green dashed line) is a power saturation curve with $P_{1/2} = 550\ (30)$ W.

7.5.1 Polarisation rates

The polarisation of the bulk ^{13}C has a rate $^{13C}T_{poln}$ associated with the build-up of the polarisation. This rate will be dependent on a number of other potentially competing different mechanisms: with electron polarisation build up, transfer between electron and nucleus, spin diffusion through the bulk lattice increasing polarisation and the $^{13C}T_{1n}$ restoring thermal equilibrium. To measure $^{13C}T_{poln}$ the pulse sequence in Figure 7-14a was used. The thermal polarisation of the sample was eliminated by a string of $\pi/2$ pulses before being illuminated for increasing periods of time with 520 nm light at 300 mW (measured at the sample). After this FID detection was carried out with a further $\pi/2$ pulse.

The build-up of polarisation followed an exponential rise with a time constant $^{13C}T_{poln} = 94(1)$ min (Figure 7-14a). This is considerably shorter than expected for the $^{13C}T_{1n}$ of the system, and therefore, the polarisation mechanism is the dominating process in magnetisation build up. The decay rate after illumination could not be accurately measured.

The polarisation measured an hour after illumination ended was found to be at 85% of its illuminated polarisation value.

NMR measurement of the ^{13}C nuclear population in diamond is not practical because of the low spin density and long relaxation time (Table 7-1). The optically pumped NMR demonstrated, potentially allows these measurements to be made. The increase in magnetisation of a factor of 180 creates the same level of SNR that would take over 190 days to measure in a thermally polarised samples (Figure 7-13). Additional gains are found for optically pumped NMR from a factor of 20 reduction in experiment repetition time (Figure 7-14), assuming a $^{13C}T_{1n}$ of ~30 hours [32].

7.5.2 Optical power

To investigate the effects of optical power on the bulk polarisation the pulse sequence outline in Figure 7-14b was used. The heating of the sample from the laser was overcome by use of ITC controlled flow of nitrogen gas to maintain a fixed 290(2) K throughout the experiment. At each power the polarisation was allowed to build up for 10 minutes after the saturation sequence. The results of this can be seen in Figure 7-14b and show that the polarisation is linear with increasing laser power until approximately 300 mW. For optical powers above 300 mW, there are only small increases in polarisation indicating that the polarisation mechanism is not optically limited on this timescale. The proposed mechanism for the polarisation of the bulk ^{13}C population is spectral diffusion and it is likely that in these experiments this is the limiting factor of the polarisation built up.

7.6 IR measurements

Both N_S^0 and N_S^+ can be quantified by the optical absorption in the one phonon region, IR is therefore an excellent choice to monitor potential charge transfer of the N_S^0 as proposed in §7.4.4. For the 520 nm laser the same pattern in behaviour was seen at room temperature and at 115 K, the lowest available temperature. Under 100 mW illumination there has been a change in the charge balance of $^{15}N_S$, an increase in $^{15}N_S^0$ by 1.1(1) ppm is matched by a
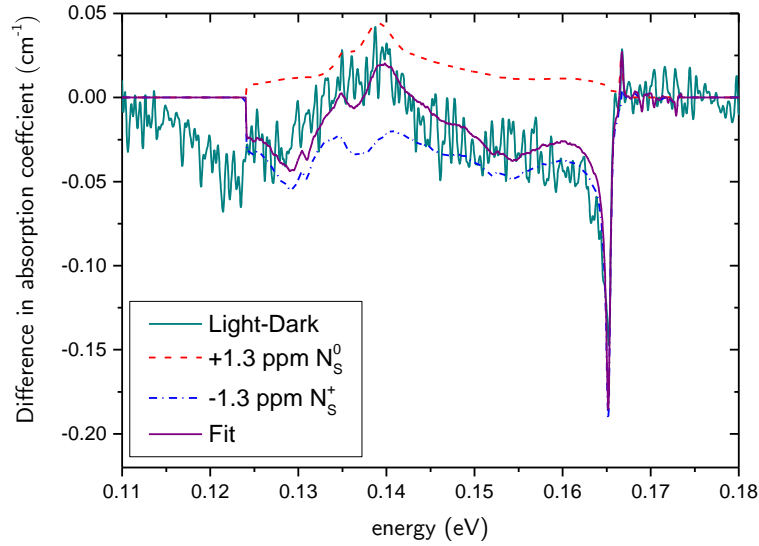
Figure 7-15 Example of change in charge state of N_S during with 100 mW of 520 nm optical excitation at 115 K. Solid line (cyan) residual of optically excited spectrum minus dark spectrum, total fit (solid purple line) is combination of 1.3 ppm of $^{15}N_S^0$ (red dashed line) and -1.3 ppm $^{15}N_S^+$ (blue dashed line).

decrease in $^{15}N_S^+$ by 1.1(1) ppm (Figure 7-15). With greater power it shows an increase in charge transfer, 400 mW showed a change of $\pm$ 1.3(1) ppm in the respective $^{15}N_S$ populations. Excitation with reduced optical energy (650 nm) showed comparable behaviour. Charge transfer is happening from an unknown source, X, being ionised to create $^{15}N_S^0$:

$$(7.8) \qquad\qquad ^{15}N_s^{\ +} + X^- \xrightarrow{\ \ h\nu\ \ } {}^{15}N_s^{\ 0} + X^0 \ .$$
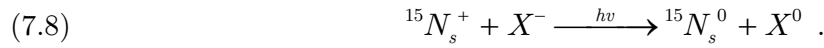
7.7 Summary of additional samples

In efforts to establish which defects were involved in the polarisation observed, samples other than Syn339-5 were tested in the same experimental setup. These included samples from the same growth run as Syn339-5 and a natural diamond; details of these samples can be seen in Table 7-5.

Sample	History	Defect Concentration (ppm)				
		$N_S^{0/+}$	NV$^-$	N_3V^0	A	B
Syn339-5	As in §7.2	26	<0.01	1.6	40	3
Syn339-B(i)	Irradiated	115	-	-	-	-
Syn339-B(ii)	Irradiated and annealed to 1000 °C	120	10	-	-	-
Syn331	Isotopically enriched 15% ^{14}N	6	-	-	-	-
	85% ^{15}N	32				
N6-1A	Natural	2	-	30	-	-

Table 7-5 Details of other samples tested for spin polarisation.

EPR under optical illumination was performed with B_0 paralleled to the [111] crystal direction on all the samples. Syn331 and Syn339-B(i) showed no difference between the illuminated and dark spectrum. Interpretation of N6-1A was hampered by the sample's long relaxation times. It was impossible to acquire unsaturated spectra at low temperatures, especially for N_S^0. The saturated N_3V spectrum did show small changes in intensity, and the N_S^0 was reported as saturating less. It is however difficult to draw conclusions from this data. RP-EPR$^{(FM)}$ measurements were made of N6-1A at 80 K to attempt to negate the microwave power saturation effects. Whilst the passage conditions for such experiments are complicated to say the least qualitative conclusions may be drawn. For Syn339-5 and sample N6-1A the N_S^0 RP-EPR$^{(FM)}$ signal was seen to reduce in intensity under illumination.

Finally, Syn339-b(ii) was the only sample to show any significant change under illumination (Figure 7-16). Figure 7-16 shows the expected large spin polarisation of the NV^- centre, of more significance to this work though are the changes to the N_S^0 centre. A large increase in signal is seen, this could be evidence of a positive polarisation, but could equally be evidence of charge transfer between defects. Such behaviour is reported for N_S^0 [49] and is most likely:

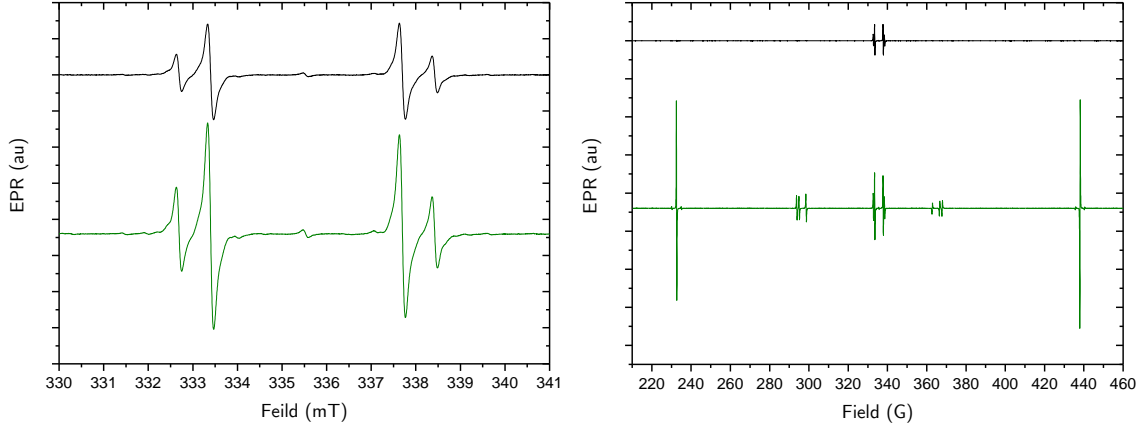$$(7.9) \qquad N_S^+ + NV^- \xrightleftharpoons{hv} N_S^0 + NV^0 .$$

Figure 7-16 Syn339-B(ii) measured in non-microwave saturating condition at 80 K. Top in the dark (black), Bottom under 150 mW 520 nm optical excitation (green).

A change in intensities between $^{[1\bar{1}\bar{1}]}\omega_{ad}$ and $^{[1\bar{1}\bar{1}]}\omega_{bc}$ is evidence of nuclear polarisation of the N_S^0 . This polarisation is much weaker than found in Syn339-5 but Syn339-B(ii) remains the only other sample to show such a response.

Measurements of the bulk ^{13}C populations under optical excitation were made of Syn339-B(ii) and N6-1A at 7.04 T. Syn339-B(ii) showed no optically induced polarisation at room temperature after 15 hours of illumination. The ^{13}C NMR lines shape of N6-1A was distorted under optical pumping, but the cause of this distortion was not established.

7.8 Discussion

The rates observed for the polarisation of $^{15}N_S^0$ and $^{15}N_3V^0$ in Figure 7-11 are slow, $T_{pol} \sim 3$ s. It is for this reason that the electron spin polarisation is not witnessed at room temperature, where any polarisation is prohibited from building up by the T_1 of both defects. The measurements of the decay of polarisation showed a poor fit for a single exponential, indicating that two processes were involved in the return of the Boltzmann population. One of these processes is certainly spin lattice relaxation, T_1, the second is most likely either spectral diffusion to off resonance lines or impact of the charge transfer of N_S^0 evident from the optically illuminated FT-IR measurements (Figure 7-15). The latter however, is not likely to have a large impact on the time scales of the polarisation decay experiments; approximately 2 minutes.

At temperatures below 150 K the T_1 of the defect is sufficiently long to allow the build-up of spin polarisation and as temperature is lowered further a greater polarisation can be built up (Figure 7-5). Unfortunately, the long relaxation times prohibit measurement of non-microwave power saturated spectra below 50 K.

The longer nuclear relaxation times allow the build-up of significant polarisation of the bulk ^{13}C population at 7.04 T. The T_1 time for $^{15}N_S^0$ and $^{15}N_3V^0$ are approximately invariant with field at room temperature [64]. It is therefore, not expected that there has been any build-up of electron polarisation at 7.04 T. The ^{13}C hyperpolarisation is a result of transfer of the Boltzmann electron spin population to the nuclear spin, which would give a maximum achievable polarisation factor of $\varepsilon=2618$, making the polarisation seen approximately 7% efficient. It is impossible to determine from the results if the polarisation comes from a small area of highly polarised spin or from a larger diffuse spin polarisation.

The reduction in polarisation factor witnessed at high optical powers ($>$300 mW in Figure 7-9) is interpreted as optical heating of the sample during the experiment, reducing the effectiveness of the polarisation. In EPR it is impossible to differentiate between a change in signal intensity due to a change in population of paramagnetic centres, or a change in spin polarisation of the paramagnetic centres. Therefore, single photon or multi photon processes resulting in charge transfer of the defects cannot be ruled out. Unfortunately, experimental constraints made it impossible to monitor the population of $^{15}N_S^0$ whilst under such high optical powers.

The data from the IR experiments reveal that during 200 mW, 520 nm optical excitation there is a 1.3 ppm increase in $^{15}N_S^0$ population at 110 K (Figure 7-15). This is supported by the data from the EPR at 50 K where an increase of 1.6 ppm $^{15}N_S^0$ is reported immediately after the optical excitation was removed (Figure 7-12). This is suggestive that a change in the charge state of the one or both defects may well be at the heart of the polarisation.

The energy dependence of the polarisation is also suggestive of a two defect process (Figure 7-7). Optically induced spin polarisation is witnessed for all energies greater than 1.9 eV with no sharp threshold. If the spin polarisation was due to an internal transition in either the $^{15}N_S^0$ or $^{15}N_3V^0$ systems a sharp threshold may have been expected. The absorption spectrum of

$^{15}N_S^0$ is a ramp from 1.9 eV so it is possible that this is the source of the polarisation. However, there are many possible transitions energies $^{15}N_S^0$ and $^{15}N_3V^0$ therefore a sharp threshold would not be expected if this was the source of polarisation.

7.8.1 Spin-correlated radical pairs

Spin polarisation requires a process that is on some level susceptible to spin and treats one spin state preferentially. Any mechanism for the polarisation must be able to work within the constraints of the experimental evidence. It is reasonable to assume that the origin of the polarisation is the same at 340 mT and 7.04 T. Therefore any mechanism responsible for the spin polarisation of both defects must be field independent. The process must be able to operate across a large range of energies and is therefore unlikely to originate from a discrete gap to gap transition within a single defect. It must also allow separate build-up of electron and nuclear hyper-polarisation and create polarisation simultaneously in both N_S^0 and N_3V^0 both of which are S=1/2 systems.

The polarisation of the bulk ^{13}C matrix in the absence of microwave excitation rules out Overhauser, solid effect and cross effect as the mechanism for the nuclear polarisation. There are theoretical models for spin polarisation in solids for S=1 systems where intersystem crossing allows preferential population to build up in the S=0 or the S=±1 manifolds [14,72,73]. Such mechanisms cannot be responsible for the polarisation seen in $^{15}N_S^0$ and $^{15}N_3V^0$ that are both S=1/2 defects.

One potential mechanism that satisfies these conditions is that of spin-correlated radical pairs. Radical pairs have been used to explain polarisation in avian navigation [74] and photochemical reactions [75,76] but can also be applied to solid state systems [77,78]. Spin-correlated radical pairs provide a mechanism for the generation of both nuclear and electron polarisation respectively [79] when the double matching condition (7.10) is met [78].

$$(7.10) \qquad 2\left|\Delta\omega_S\right| = 2\left|\omega_I\right| = \left|A\right|.$$
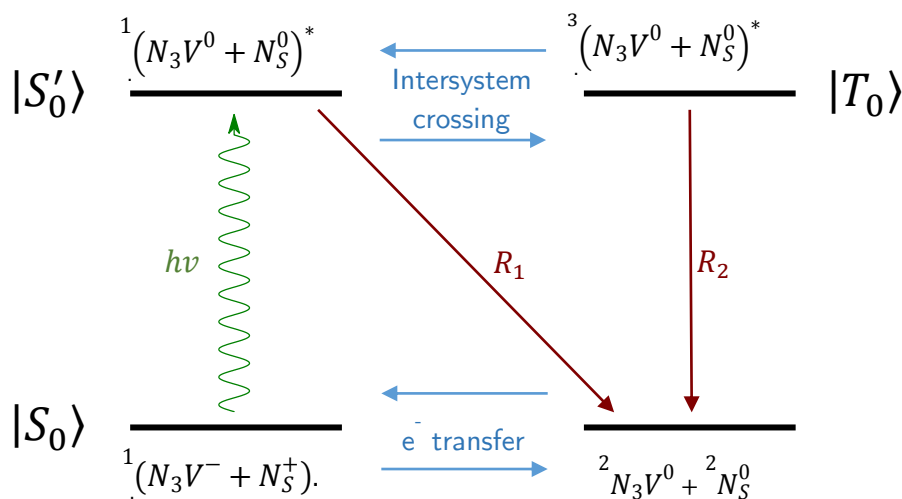
Figure 7-17 Potential model for the spin polarisation build up from spin-correlated radical pairs.

Such a mechanism could explain the behaviour observed in N_3V^0 and N_S^0: one possible route is shown in Figure 7-17. This path begins with N_S^0 - N_3V^0 pairs that are spatially close enough to be loosely coupled. There is electron exchange between these two systems, either once light is applied or as part of a dynamic thermal equilibrium. The absorbed photon energy excites the coupled pair to a coupled excited singlet state that can undergo intersystem crossing to an excited triplet state. Decay to the non-coupled EPR active ground state is possible from either singlet or triplet excited state, but the rate of the decay through each path must be different for polarization to build up.

For spin-correlated radical pairs to be a likely mechanism, the two centres must be near enough to interact. Statistical modelling of average distances for 20 ppm N_S^0 concentration shows that ~9% will be within 10 lattice spacings (~15 Å) [80]. The spatial extent of the orbit has previously been estimated as ~10 Å [16] in agreement with calculations of hydrogenised orbitals in diamond [81]. Given that the EPR line widths suggest concentrations are higher than this in some sectors, and that the N_3V^0 will be in those high concentration sectors, orbital overlap between some population of the two defects is likely.

The three spin mixing in spin-correlated radical pairs requires an anisotropic component to either the hyperfine, g interactions or dipolar coupling. The Hamiltonian parameters for N_3V^0 and N_S^0 in Table 7-6 show that anisotropy is present in the hyperfine parameters of both
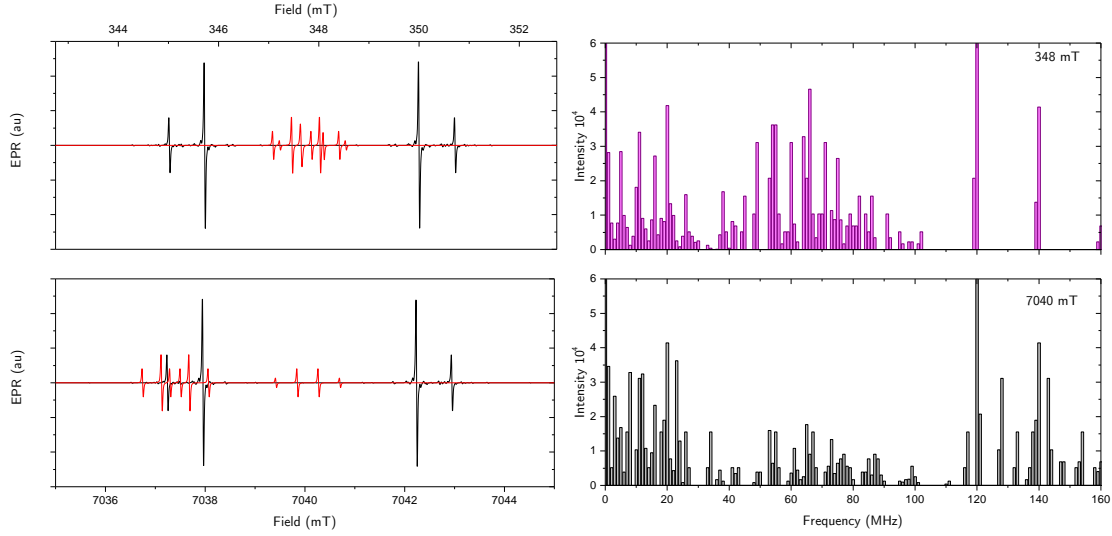
Figure 7-18 Simulations of the EPR spectrum (left) and $\Delta\omega_S$ (right) at 9.75 GHz (top) and 200 GHz (bottom) showing $^{15}N_S^0$ (black) and $^{15}N_3V^0$ (red).

systems as well as the electron Zeeman parameters of the N_3V^0. The nuclear Larmor frequencies for ^{13}C are 3.6 MHz and 75 MHz at 340 mT and 7.04 T respectively, and 1.46 MHz and 30 MHz for ^{15}N. Comparison of these values with the hyperfine parameters show that the Larmor frequency of ^{13}C is within the range of the available hyperfine coupling constant. All $\Delta\omega_S$ for the N_3V^0 and N_S^0 spectrum have been calculated at 348 mT and 7.04 T (Figure 7-18). The plot in Figure 7-18 does not take into account additional transitions caused by near neighbour ^{13}C. That there is a wide range of frequency differences present means that is likely that $2|\Delta\omega_S| = |A|$ will be at least approximately met at both 348 mT and 7.04 T.

		$^{15}N_3V^0$		$^{15}N_S^0$	
g	$g_\parallel$	2.002 52(2)			
	$g_\parallel$	2.002 36(5)	g_{iso}	2.002 4	
	$\theta_{[110]\to[001]}$ (°)	35.26			
A (MHz)	A_1	10.54(5)	$A_\parallel$	-159.730(7)	
	A_2	10.62(5)	$A_\perp$	-113.838(6)	
	A_2	15.77(5)			
	$\theta_{[110]\to[001]}$ (°)	157.8(2)	$\theta_{[110]\to[001]}$ (°)	54.74	

Table 7-6 Hamiltonian parameters for $^{15}N_S^0$ and $^{15}N_3V^0$ from [16,82].

7.9 Conclusions and further work

Both electron and nuclear polarisation has been demonstrated for $^{15}N_S^0$ and $^{15}N_3V^0$. The spin polarisation can be generated with a large range of optical energies. This is suggestive of the absorption coming from $^{15}N_S^0$ or from transitions between levels of N_3V^0 and $^{15}N_S^0$. Unlike polarisation of other defects in diamond (NV^-, SiV^0), the time constants associated with the polarisation are long, of the order of seconds.

Nuclear spin polarisation of the bulk ^{13}C matrix has been demonstrated via optically pumped NMR. The build-up of such polarisation is slow and most likely through spin diffusion away from the polarised paramagnetic centres. It is believed that this polarisation is transferred from the electron polarisation via the solid effect or thermal mixing, rather than being generated at the nucleus. When polarised the magnetisation build up is no longer limited by $^{13C}T_{1n}$ but is now limited by the much shorter $^{13C}T_{poln}$. The increases in SNR and reduction in shot repetition time demonstrated with optically pumped NMR allow ^{13}C that would be impractical in no polarised samples. The polarisation seen is of a similar order to that seen in diamonds from Overhauser techniques [35], but without the need for microwave excitation creating a simpler experimental setup.

The temperature dependence of the spin lattice relaxation times of $^{15}N_3V^0$ have been recorded for the first time in the absence of cross relaxation to the central line of the $^{14}N_S^0$ EPR spectrum. This temperature dependence is consistent with that expected from the direct process and a Raman process. The temperature dependence of both $^{15}N_3V^0$ and $^{15}N_S^0$ coupled with the directly measured polarisation time offers insight into the lack of observed polarisation at room temperature.

The spin-correlated radical pairs mechanism is proposed as the most likely route for the creation of the polarisation. It is relatively insensitive to field, allowing production of polarisation in two distinct defects. The mechanism would explain both the electron and nuclear polarisation, the simultaneous polarisation of two separate spin systems and even allow

polarisation at multiple fields. The exact route to this polarisation has not been determined but a route where $^1\left(N_3V^- + N_S^+\right) \xrightarrow{hv} {}^1\left(N_S^0 + N_3V^0\right)^*$ is not inconsistent with experimental evidence.

Further research into the behaviour of the N_3V^0 under optical excitation could be performed using the optical absorption measurements and would aid the determination of the route to polarisation by demonstrating charge transfer of the $^{15}N_3V$ system as well as the $^{15}N_S$. ELDOR measurements may also unambiguously confirm the coupling between N_S^0 and N_3V^0 assuming the coupling is in the ground state. Polarisation of the electron population has only been detected at X-band microwave frequencies and work performed at higher frequency (Q-band or W-band) would eliminate the possibility of accidentally degenerate transitions as the source of the electron polarisation. With the available data it was impossible to determine if the ^{13}C matrix polarisation represents a small population at high polarisation or the whole population weakly polarised with the increased signal. The reduced experimental times for the polarised systems mean it may be possible to conduct MRI measurements with sufficient resolution to aid in the spatial assignments of the signal within the sample.

7.10 References

[1] A. Beveratos, R. Brouri, T. Gacoin, A. Villing, J.-P. Poizat, and P. Grangier, Phys. Rev. Lett. 89, 187901 (2002).

[2] F. Jelezko, I. Popa, A. Gruber, C. Tietz, J. Wrachtrup, A. Nizovtsev, and S. Kilin, Appl. Phys. Lett. 81, 2160 (2002).

[3] C. Wang, C. Kurtsiefer, H. Weinfurter, and B. Burchard, J. Phys. B At. Mol. Opt. Phys. 39, 37 (2006).

[4] E. Wu, J. R. Rabeau, G. Roger, F. Treussart, H. Zeng, P. Grangier, S. Prawer, and J. F. Roch, New J. Phys. 9, (2007).

[5] I. Aharonovich, C. Zhou, A. Stacey, J. Orwa, S. Castelletto, D. Simpson, A. D. Greentree, F. Treussart, J. F. Roch, and S. Prawer, Phys. Rev. B - Condens. Matter Mater. Phys. 79, 1 (2009).

[6] L. Rondin, J. P. Tetienne, T. Hingant, J. F. Roch, P. Maletinsky, and V. Jacques, Rep Prog Phys 77, 56503 (2014).

[7] V. M. Acosta, E. Bauch, M. P. Ledbetter, C. Santori, K. M. C. Fu, P. E. Barclay, R. G. Beausoleil, H. Linget, J. F. Roch, F. Treussart, S. Chemerisov, W. Gawlik, and D. Budker, Phys. Rev. B - Condens. Matter Mater. Phys. 80, 1 (2009).

[8] T. Plakhotnik, M. W. Doherty, J. H. Cole, R. Chapman, and N. B. Manson, Nano Lett. 14, 4989 (2014).

[9] P. Neumann, I. Jakobi, F. Dolde, C. Burk, R. Reuter, G. Waldherr, J. Honert, T. Wolf, A. Brunner, J. H. Shim, D. Suter, H. Sumiya, J. Isoya, and J. Wrachtrup, Nano Lett. 13, 2738 (2013).

[10] M. W. Doherty, V. V. Struzhkin, D. A. Simpson, L. P. McGuinness, Y. Meng, A. Stacey, T. J. Karle, R. J. Hemley, N. B. Manson, L. C. L. Hollenberg, and S. Prawer, Phys. Rev. Lett. 112, 47601 (2014).

[11] L. J. Rogers, K. D. Jahnke, M. H. Metsch, J. M. Binder, T. Teraji, H. Sumiya, J. Isoya, M. D. Lukin, P. Hemmer, and F. Jelezko, Phys. Rev. Lett. 113, 1 (2014).

[12] E. Neu, D. Steinmetz, J. Riedrich-Muller, S. Gsell, M. Fischer, M. Schreck, and C. Becher, New J. Phys. 13, (2011).

[13] J. P. King, P. J. Coles, and J. A. Reimer, Phys. Rev. B 81, 73201 (2010).

[14] G. A. Alvarez, C. O. Bretschneider, R. Fischer, P. London, H. Kanda, S. Onoda, J. Isoya, D. Gershoni, and L. Frydman, Nat Commun 6, 8456 (2015).

[15] H. Wang, C. S. Shin, Seltzer, C. E. Avalos, A. Pines, and V. S. Bajaj, Nat. Commun. (2014).

[16] B. Green, Optical and Magnetic Resonance Studies of Point Defects in Single Crystal Diamond - PhD Thesis, Unviersity of Warwcik, 2013.

[17] A. W. Overhauser, Phys. Rev. 92, 411 (1953).

[18] T. R. Carver and C. P. Slichter, Phys. Rev. 92, 212 (1953).

[19] T. K. Y. Tam, Overhauser Dynamic Nuclear Polarisation Studies in Solution-State at 3.4T, Uiversity of Warwick, 2013.

[20] R. A. Wind, M. J. Duijvestijn, C. van der Lugt, A. Manenschijn, and J. Vriend, *Applications of Dynamic Nuclear Polarization in 13C NMR in Solids,* (1985).

[21] S. Un, T. Prisner, R. T. Weber, M. J. Seaman, K. W. Fishbein, A. E. McDermott, D.

J. Singel, R. G. Griffin, S. Una, T. Prisnera, R. T. Webera, M. J. Seamana, K. W. Fishbeina, A. E. McDermotta, D. J. Singelb, and R. G. Griffina, Chem. Phys. Lett. 189, 54 (1992).

[22] B. V.S. Bajaja, C.T. Farrara, M.K. Hornsteinb, I. Mastovskyb, J. Viereggb, 1, J. Bryanta and and R. G. G. Elénaa, 2, K.E. Kreischerb, 3, R.J. Temkinb, J. Magn. Reson. 2, 85 (2001).

[23] C. Song, K. N. Hu, C. G. Joo, T. M. Swager, and R. G. Griffin, J. Am. Chem. Soc. 128, 11385 (2006).

[24] † Melanie Rosay, † Jonathan C. Lansing, § Kristin C. Haddad, § William W. Bachovchin, ‖ Judith Herzfeld, †,‡ and Richard J. Temkin, and † Robert G. Griffin*, (2003).

[25] A. J. Rossini, A. Zagdoun, F. Hegner, M. Schwarzwälder, D. Gajan, C. Copéret, A. Lesage, and L. Emsley, (2012).

[26] K. J. Pike, T. F. Kemp, H. Takahashi, R. Day, A. P. Howes, E. V. Kryukov, J. F. MacDonald, A. E. C. Collis, D. R. Bolton, R. J. Wylde, M. Orwick, K. Kosuga, A. J. Clark, T. Idehara, A. Watts, G. M. Smith, M. E. Newton, R. Dupree, and M. E. Smith, J. Magn. Reson. 215, 1 (2012).

[27] E. Shabanova, K. Schaumburg, and J. P. F. Sellschop, J. Magn. Reson. 130, 8 (1998).

[28] K. Schaumburg, E. Shabanova, J. P. F. Sellschop, and T. Anthony, Solid State Commun. 91, 735 (1994).

[29] M. J. Duijvestijn, C. van der Lugt, J. Smidt, R. a. Wind, K. W. Zilm, and D. C. Staplin, Chem. Phys. Lett. 102, 25 (1983).

[30] J. Zhou, L. Li, H. Hu, B. Yang, Z. Dan, J. Qiu, J. Guo, F. Chen, and C. Ye, Solid State Nucl. Magn. Reson. 3, 339 (1994).

[31] E. Scott, M. Drake, and J. A. Reimer, J. Magn. Reson. 264, 154 (2016).

[32] C. J. Terblanche, E. C. Reynhardt, and J. A. van Wyk, Solid State Nucl. Magn. Reson. 20, 1 (2001).

[33] P. Mark Henrichs, M. L. Cofield, R. H. Young, and J. Michael Hewitt, J. Magn. Reson. 58, 85 (1984).

[34] K. Schaumburg, E. Shabanova, and J. P. F. Sellschop, J. Magn. Reson. Ser. A 112, 176 (1995).

[35] G. J. Hill, J. Wu, and M. J. R. Hoch, Hyperfine Interact. 120–121, 81 (1999).

[36] R. Tycko* and J. A. Reimer, (1996).

[37] R. Fischer, A. Jarmola, P. Kehayias, and D. Budker, Phys. Rev. B 87, 125207 (2013).

[38] V. Jacques, P. Neumann, J. Beck, M. Markham, D. Twitchen, J. Meijer, F. Kaiser, G. Balasubramanian, F. Jelezko, and J. Wrachtrup, Phys. Rev. Lett. 102, 57403 (2009).

[39] H. J. Wang, C. S. Shin, C. E. Avalos, S. J. Seltzer, D. Budker, A. Pines, and V. S. Bajaj, Nat Commun 4, 1940 (2013).

[40] R. G. Farrer, Solid State Commun. 7, 685 (1969).

[41] B. B. Li, M. C. Tosin, A. C. Peterlevitz, and V. Baranauskas, Appl. Phys. Lett. 73, 812 (1998).

[42] E. B. Lombardi, A. Mainwood, K. Osuch, and E. C. Reynhardt, J. Phys. Condens. Matter 15, 3135 (2003).

[43] A. Mainwood, 49, 7934 (1994).

[44]   D. J. Twitchen, P. M. Martineau, G. A. Scarsbrook, B. S. C. Dorn, and A. M. Cooper, WO03052177A1 (2003).

[45]   H. B. Dyer, F. A. Raal, L. Du Preez, and J. H. N. Loubser, Philos. Mag. 11, 763 (1965).

[46]   A. T. Collins, Phys. B Condens. Matter 185, 284 (1993).

[47]   R. Ulbricht, S. T. Van Der Post, J. P. Goss, P. R. Briddon, R. Jones, R. U. A. Khan, and M. Bonn, Phys. Rev. B - Condens. Matter Mater. Phys. 84, 1 (2011).

[48]   G. S. Woods, G. C. Purser, A. S. S. Mtimkulu, and A. T. Collins, J. Phys. Chem. Solids 51, 1191 (1990).

[49]   R. U. A. Khan, P. M. Martineau, B. L. Cann, M. E. Newton, and D. J. Twitchen, J. Phys. Condens. Matter 21, 364214 (2009).

[50]   B. L. Cann, Magnetic Resonance Studies of Point Defects in Diamond - PhD Thesis, University of Warwick, 2005.

[51]   Y. Mita, H. Kanehara, Y. Nisida, and M. Okada, Philos. Mag. Lett. 76, 93 (1997).

[52]   C. A. Coulson and M. J. Kearsley, Proc. R. Soc. Lond. A. Math. Phys. Sci. 241, 433 (1975).

[53]   J. Goss, R. Jones, S. Breuer, P. Briddon, and S. Öberg, Phys. Rev. Lett. 77, 3041 (1996).

[54]   M. Lannoo and J. Bourgoin, *Point Defects in Semiconductors I: Theoretical Aspects*, 1st ed. (Springer, 1981).

[55]   F. Larkins and A. Stoneham, 112 (1970).

[56]   P. A. Crowther and P. J. Dean, J. Phys. Chem. Solids 28, 1115 (1967).

[57]   M. F. Thomaz and G. Davies, Proc. R. Soc. A Math. Phys. Eng. Sci. 362, 405 (1978).

[58]   R. Jones, J. P. Goss, P. R. Briddon, and S. Oberg, Phys. Rev. B 56, R1654 (1997).

[59]   B. L. Green, M. W. Dale, M. E. Newton, and D. Fisher, Phys. Rev. B 92, 165204 (2015).

[60]   BOC, (2016).

[61]   S. Liggins, Identification of Point Defects in Treated Single Crystal Diamond - PhD Thesis, University of Warwick, 2010.

[62]   Thorlabs, 6647 (2015).

[63]   Thorlabs, 0 (2015).

[64]   C. J. Terblanche and E. C. Reynhardt, Chem. Phys. Lett. 322, 273 (2000).

[65]   C. J. Terblanche, E. C. Reynhardt, S. A. Rakitianski, and J. A. Van Wyk, Solid State Nucl. Magn. Reson. 19, 107 (2001).

[66]   J. A. vanWyk, E. C. Reynhardt, G. L. High, and I. Kiflawi, J. Phys. D-Applied Phys. 30, 1790 (1997).

[67]   E. C. Reynhardt, G. L. High, and J. A. van Wyk, J. Chem. Phys. 109, 8471 (1998).

[68]   U. F. S. D'Haenens-Johansson, A. M. Edmonds, B. L. Green, M. E. Newton, G. Davies, P. M. Martineau, R. U. A. Khan, and D. J. Twitchen, Phys. Rev. B 84, 245208 (2011).

[69]   U. F. S. D'Haenens-Johansson, Optical and Magnetic Resonance Studies of Point Defects in CVD Diamond, University of Warwick, 2011.

[70]   A. S. Stefan Stoll, J. Magn. Reson. 178, 42 (2006).

[71]   H. L. Retcofsky and R. A. Friedel, (2002).

[72]   P. Delaney, J. C. Greer, and J. A. Larsson, Nano Lett. 10, 610 (2010).

[73]   A. Gali, E. Janzén, P. Deák, G. Kresse, and E. Kaxiras, Phys. Rev. Lett. 103, 186404 (2009).

[74] C. T. Rodgers and P. J. Hore, Proc. Natl. Acad. Sci. U. S. A. 106, 353 (2009).

[75] M. T. Colvin, R. Carmieli, T. Miura, S. Richert, D. M. Gardner, A. L. Smeigh, S. M. Dyar, S. M. Conron, M. a. Ratner, and M. R. Wasielewski, J. Phys. Chem. A 117, 5314 (2013).

[76] G. Kothe, S. Weber, E. Ohmes, M. C. Thurnauer, and J. R. Norris, J. Phys. Chem. 98, 2706 (1994).

[77] G. Jeschke, J. Chem. Phys. 106, 10072 (1997).

[78] G. Jeschke, J. Am. Chem. Soc. 120, 4425 (1998).

[79] H. Van Willigen, P. R. Levstein, and M. H. Ebersoies, Chem Rev 93, 173 (1993).

[80] A. T. Collins and C.-H. Ly, J. Phys. Condens. Matter 14, L467 (2002).

[81] A. M. Stoneham, Mater. Sci. Eng. B 11, 211 (1992).

[82] A. Cox, M. E. Newton, and J. M. Baker, J. Phys. Condens. Matter 6, 551 (1994).

Chapter 8

8 The migration of R2

8.1 Introduction

Defects in diamond can be used for magnetometry and as a single photon source for quantum optics, and as such there is great interest in manipulating these defects to maximise the performance of such devices, for example preferentially orientating the defects. If there is no bias, defects will be found with equal probability in all symmetry equivalent defect orientations. When all possible orientations of a defect are not equally populated, either through growth conditions or external factors, the defect is said to be preferentially orientated. A good example of this is the NV^- centre which is of interest in many areas of sensing. NV^- has C_{3v} symmetry, and therefore has four possible equivalent orientations that under normal conditions have equal population. This potentially limits the number of centres that can be manipulated to a quarter of the total population. Preferential orientating a populating a single defect orientation would create an equivalent response from all of the centres and reduces the fluorescence background [1].

There have been successes in preferentially orientating NV^- during growth. Edmonds produced only two orientations of NV^- by CVD growth on a ⟨011⟩ substrate [2] and Lesik reported 97% of NV^- in a single orientation when growing on a ⟨111⟩ substrate [3]. There are, however, problems with this approach to creating preferential orientation. Both methods are based on CVD growth and concentrations of NV^- are limited to those produced during growth. CVD grown diamond is highly strained and less suitable for optical applications. In addition, diamond grown on a ⟨111⟩ substrate is prone to twinning [4], subsequently only thin layers of material can be produced.

An alternative approach is to engineer the defects into already grown material. Defects can be created by irradiation or implantation and subsequent annealing, allowing control of
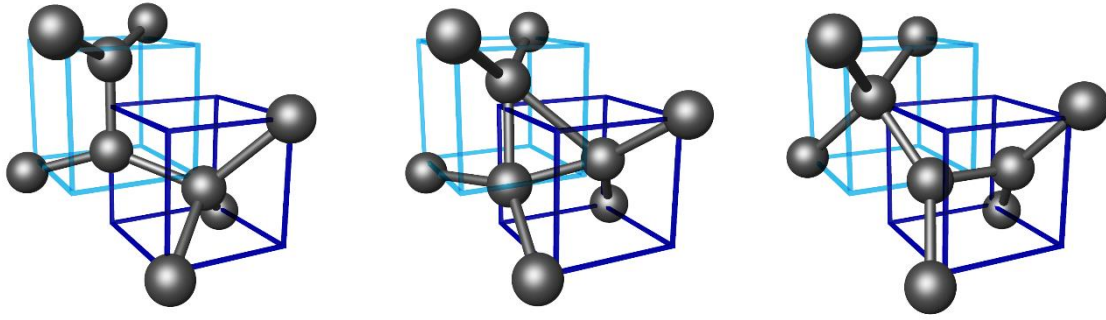
Figure 8-1 Model for the migration of R2 by reorientation; the blue boxes represent different lattice site for the defect. Left the initial position with the R2 align [001]. Central the intermediate triangular structure found at the midpoint of migration. Right the R2 is now aligned along [010]. Adapted from [9] by M.W. Dale.

concentrations, and to some extent location, removing the need to rely on doping during growth. *Ab inito* calculations suggest that it would be possible to create a preferentially oriented population by performing annealing under very high compressive strain, ~10 GPa [5], although this has yet to be experimentally explored for NV^-.

The focus of this chapter is a defect created by irradiation damage, the ⟨001⟩-split interstitial, R2. The understanding of how defects migrate through the material during annealing is an important step towards engineering preferentially aligned defects. There is additional interest in the migration of R2 through the lattice as it has previously been shown to have a significant role in the aggregation of nitrogen [6,7].

8.1.1 Migration of R2

R2 consists of two sp^2 bonded carbon atoms sharing an atomic site and is discussed in §2.2.1.2. With a D_{2d} point symmetry R2 has three distinct symmetry related defect orientations [001], [100] and [010]. The angular dependence of the zero-field splitting allows each defect orientation to be individually addressed in EPR and the relative populations of each defect orientation to be calculated.

The proposed model for migration of R2 is through the reorientation of the defect. One of the off-site carbon atoms moves towards a neighbouring on-site carbon and pushes that atom into an off-site position, effectively creating a new defect at a new orientation (eg. [001] → [010] or

[100]). This model for the migration of R2 is supported by *ab initio* calculations using local-density-functional pseudopotential theory and is predicted to have an energy barrier to diffusion $^{Th}E_A = 1.7 \, \text{eV}$ with an attempt frequency $^{Th}\nu = 4 \times 10^{13} \, \text{Hz}$ [8]. During migration a low energy intermediate structure is created, with all atoms four-fold coordinated (Figure 8-1). Recent work by Goss *et al* [9] on simulating the effect of the application of uniaxial compressive lattice strain in a [001] direction on the reorientation of R2 confirmed that inequivalent pathways for migration developed. The application of strain increases the energy barrier to reorientation for all defect orientations, with the greatest increase to the defect orientation under strain. The energy barrier for the defect orientation under 1% strain ($\sim 5 \, \text{GPa}$) is predicted to be $\sim 30\%$ greater than for an unstrained system, leading to reorientation into the strained defect orientation being greatly suppressed.

Initial experiments into preferentially orientating R2 by application of pressure were presented by Hunt [10]. A sample was annealed for 10 hours at 520 K under 0.6 GPa of uniaxial stress along the [001] direction. After this anneal, the population of the under stress [001] defect orientation was found to have reduced 30% and the other two defect orientations increased by 15% each, no R2 had been lost within errors. After a second identical anneal without uniaxial stress the populations returned to the equilibrium values and again no R2 was lost within errors.

A more detailed study on the effect of uniaxial stress on populations was conducted by Dale [11] with samples cooled during irradiation to room temperature. It was reported that irradiation under uniaxial stress did not increase the production of R2 and at the highest pressure (3 GPa) no preferential orientation was produced. In the same report uniaxial stress was shown to increase the production of R1 by a factor of two at 3 GPa; no preferential orientation was reported. It is inferred from this that the uniaxial stress reduced the interstitial-vacancy recombination rate. Preferential orientated population of the 3H defect was reported. This is consistent with reports of an excited state of the interstitial, I^*, that is present during irradiation [12]. I^* can migrate at low energies and remains mobile insensitive to applied stress until it returns to a ground state and is locked in position. It was also shown that annealing under uniaxial stress could produce preferential populations and that the degree

of preference increased with increasing applied stress. A maximum reported reduction of population for the defect orientation under stress was from 33.3% to 7(1)% at 2.0 GPa: a 2% population was predicted at 4.0 GPa.

8.2 Experimental

8.3.1 Sample history

The sample, 50013c, that is used in this study was cut from a Type IIa CVD grown synthetic diamond, with a starting concentration of 78(7) ppb of N_s^0. The sample was neutron irradiated with a total dose of 1×10^{18} n cm^{-2} of high energy neutrons. The energy of the radiation was sufficient to ensure a distribution of R2 throughout the 0.8 mm thick sample. After irradiation the sample was determined to have a concentration of 66(6) ppm R2 and was subsequently processed for experiments. The sample was laser cut into four plates 1.40 x 1.45 mm and polished to remove any sp^2 material from the cut edges. The top and bottom surfaces were also polished parallel to allow the application of uniaxial stress. Unfortunately, heating during part of this process annealed out the R2 in two of the plates and the remaining two reported a reduced R2 concentration of 55(5) ppm. Fortunately, this still gives a large signal in EPR. One of these plates, 50013c, was used for all the results present here.

8.3.2 Annealing under uniaxial stress

Annealing under uniaxial stress was achieved using custom equipment which has been fully characterised previously [11]. Uniaxial stress was applied with a probe originally designed for optical measurements, shown schematically in Figure 8-2.

High pressure was generated in a pressure vessel as described for the EPR stress probe detailed in §4.5. The pressure was transferred to the sample initially through a stainless steel rod, that terminated at a slug. The slug is a tight fit in the support tube and is primarily used to ensure the ram rod remains straight, as keeping the faces of the anvils parallel is critical to the success of the experiment. The slug interfaces with the first of the steel anvils, then a second steel anvil is mounted in the cap of the probe. The sample was mounted between two 10 μm thick
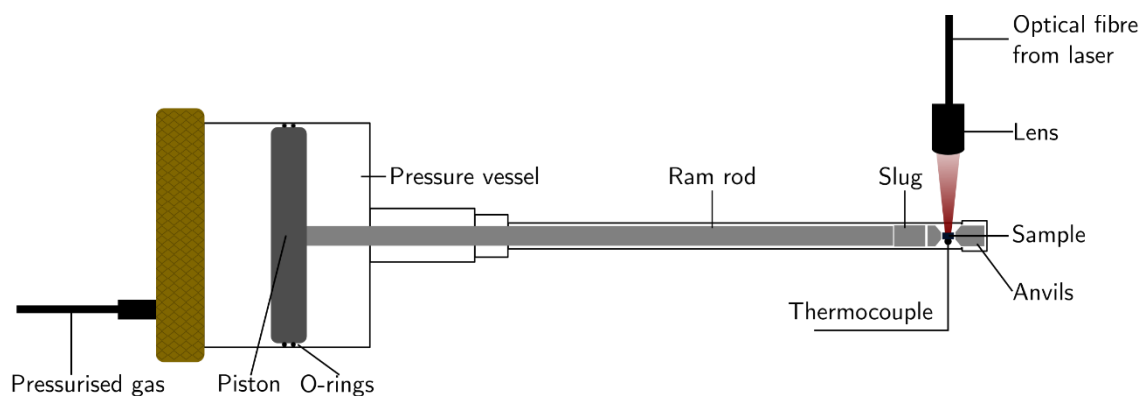
Figure 8-2   Schematic of the equipment used to perform uniaxial stressed anneals with key components labelled.

aluminium foil gaskets that were glued to the anvils with GE varnish. The steel anvils are polished to a mirror finish and they, along with the sample, were thoroughly cleaned before each measurement. Even small amounts of dust could lead to an uneven applied stress, resulting in fractures in the sample. After high temperature anneals each anvil was repolished before further use due to potential damage caused during the annealing.

Annealing of the sample was achieved using a 40 W, 938 nm, solid state CW laser diode from LIMO Lissotschenko Mikrooptik GmbH as a heat source. The laser was initially coupled into an optical fibre that terminated 55 mm in front of the sample mounted in the stress probe. A lens was used to focus the laser to a 1 mm spot at the sample. The temperature of the sample was monitored with a K-type thermocouple that was attached to the other side of the diamond with silicone thermal grease. The performance of this system has been discussed in detail previously [11]. The temperature of the diamond could be controlled using the variable power controller of the laser diode and was monitored for the length of the anneal. As the maximum temperature achieved in this work was 300 °C, the anneals could be carried out in atmospheric conditions without graphitisation of the diamond.

For each anneal under uniaxial stress the sample was mounted as described above and the pressure was slowly increased to 1 GPa. Once the uniaxial pressure was stable the sample was heated to a temperature of 300(2) °C. This typically took 15 minutes; this time was required for the probe to reach thermal equilibrium. The sample was maintained at temperature for
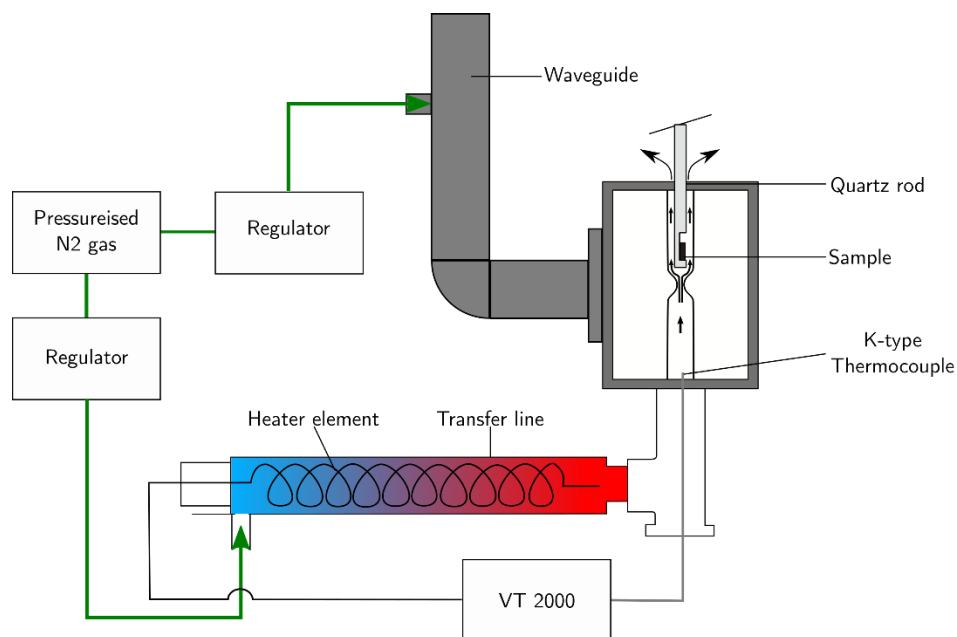
Figure 8-3 Schematic of the equipment used for high temperature EPR measurements with key components labelled.

1 hour before the laser was switched off and the sample was allowed to return to room temperature, before the pressure was slowly released.

8.3.3 High temperature EPR

The isothermal anneals were conducted using a Bruker VT2000 variable temperature unit equipped with the Type A heating element. A flow of nitrogen gas was passed over a long heating element inside a quartz transfer line below the resonator. The heated gas flowed up through the resonator inside a quartz insert (Figure 8-3). The sample is placed on a quartz rod with a ledge cut out, and placed inside the insert. In this unit temperature is monitored with a thermocouple in the gas flow just below the resonator and this is fed back to the unit. A Eurotherm PID temperature controller is employed to maintain a constant temperature.

It has been found that the actual temperature achieved at the sample varied by as much as 15 K compared to the set temperature, depending on the gas flow rate used. Even when extreme care was taken over gas flow rates, the set and sample temperatures were still inconsistent. To negate these errors a calibrated 0.3 mm K-type thermocouple was placed on a sample rod identical to the experiment mount, and placed inside the cavity at the same height as the sample. Unfortunately, the metallic nature of the thermocouple lead to a vastly

distorted EPR spectrum and it was therefore impractical to leave the thermocouple in place during the experiment. Instead temperature measurements were made before each isothermal anneal to ascertain the correct offset to achieve the desired temperatures. The cavity was then allowed to cool under the same gas flow before the sample was aligned. At the end of the isothermal anneal the sample was removed whilst still at high temperature and the thermocouple was immediately put in its place. This approach allowed the temperature to be measured under the exact experimental conditions. Great care was taken in positioning the thermocouple, both the height and orientation of the sample rod in the resonator had an effect on the flow of the gas and therefore the temperature of the sample. In this way the errors in temperature were reduced to ± 1 K; the majority of this error is associated with fluctuations in gas pressure over the many days of some of the experiments.

8.3 Results and analysis

8.3.1 Reorientation of the defect

To investigate the reorientation of the R2 defect through the diamond lattice, a preferential ordered population was first created by annealing under uniaxial stress. 50013c was stressed along the [001] direction at 1 GPa and heated to 573 K. A decrease in the population of the [001] orientation from 33.3% to ~19% was observed on each anneal (Figure 8-4) consistent with previous work [11]. It has been shown that temperatures above 573 K can cause significant annealing out of R2 [10–12], and 1 GPa was found to be a repeatable pressure; without significant risk to the diamond.

The orientation of R2 is fixed at room temperature and therefore a second anneal is required for reorientation to happen. The diamond was aligned in the spectrometer with the B_o field aligned along the [001] crystallographic direction before being brought up to temperature for isothermal annealing. Anneals were performed at temperatures between 520 K and 623 K. The spectra were collected such that the degenerate lines from the [010] & [100] oriented orientations and the depopulated [001] oriented line were recorded in the same scan. Due to the large number of scans collected the data was automatically fitted to two pseudo-modulated Voigt lines. The line widths of the simulations were constrained to less than 1% of the natural
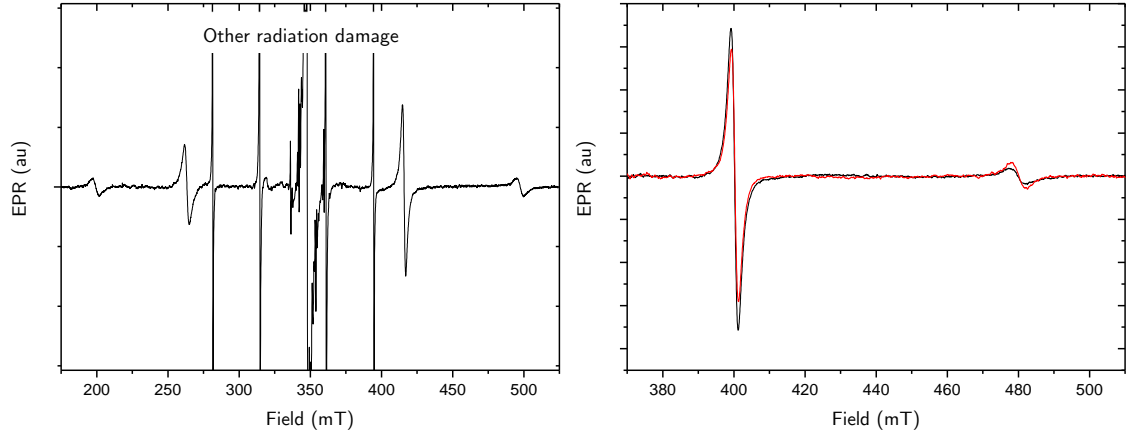
Figure 8-4 Examples of EPR spectra for 50013c.
Left, EPR Spectrum for R2 showing the assignment of sites with B_0 aligned along [001] crystallographic direction.
Right, first (black) and final (red) scan of isothermal anneal at 280 °C. The sample had undergone a one hour 573 K anneal at 1 GPa of uniaxial pressure prior to the initial spectrum. The final spectrum shown in red was recorded 80 hours after the initial spectrum.

line width. Before fitting, a cubic spline baseline had to be removed to correct for cavity background. The spline was created from five base points - two near the ends of the spectrum, one in the centre, and one near each line. Background removal and fitting in this consistent way removes inconsistency associated with manual fitting. The fitted data was then used to calculate the fractional population of the [001] defect orientation.

The R2 spectrum can be used to calculate the population in all three defect orientations using the relationship:

(8.1)
$$\mathrm{Pop}_{[001]} = \frac{R2_{outer}}{R2_{inner} + R2_{outer}}$$
$$\mathrm{Pop}_{[010]} + \mathrm{Pop}_{[100]} = \frac{R2_{inner}}{R2_{inner} + R2_{outer}}.$$

Under equilibrium conditions $\mathrm{Pop}_{[001]} = \mathrm{Pop}_{[010]} = \mathrm{Pop}_{[100]}$; there will be 33.3% of the total population in each defect orientation. During the isothermal anneals the total population was also monitored. A typical example can be seen in Figure 8-5a and shows that there is no loss in overall concentration. A standard deviation in the total concentration over the 80 hours for an anneal at 250 °C was 1.5%. These fluctuations will be due to slight fluctuations in experimental conditions over the course of the run and errors associated with fitting of the
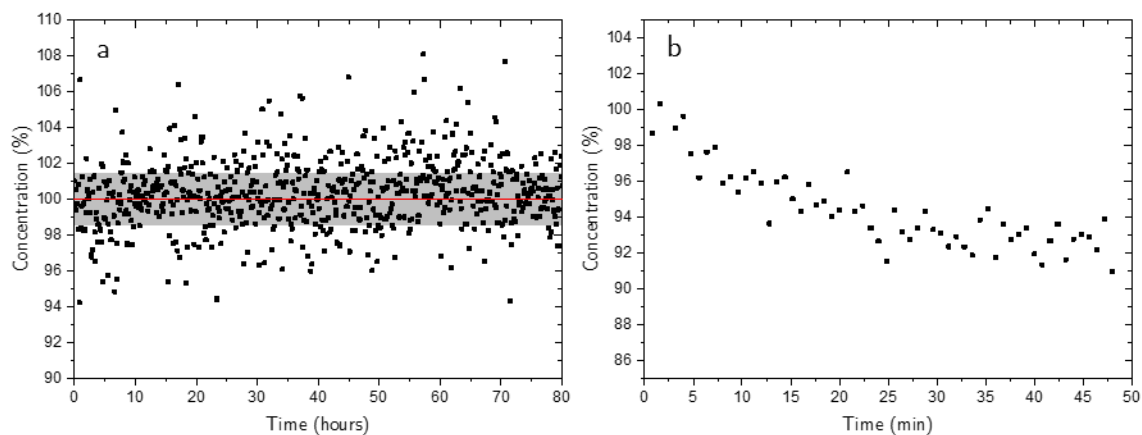
Figure 8-5 The total EPR intensities for the individual scans.
a, 280 °C anneal; solid red line is the average value with the shaded area 1 standard deviation.
b, 350 °C anneal reporting a loss of ~8% on intensity over the course of the anneal.

spectrum. However, these fluctuations will affect the entire recorded spectrum, therefore the ratio between the lines will still give a consistent measurement of relative populations. For the isothermal anneals above 320 °C a drop in total intensity was recorded. The different experimental times meant the loss of R2 was approximately 8% for both measurements made above 320 °C (Figure 8-5b)

The reorientation experiments were conducted at temperatures between 520-620 K. There is a practical lower temperature boundary for these measurements due to the decreasing reorientation rate at low temperature. At the lowest temperature presented here, 520 K, the time constant of reorientation was of the order of three days, and to measure a meaningful change in population would require multiples of this time. Maintaining spectrometer calibration and temperature for periods of time longer than this was impractical. The upper temperature limit is governed two fold, firstly by the annealing out of the defect which was already manifested at 590 K. The second problem was the ability to acquire data at the faster reorientation rates. The shortest achievable scan time for this measurement is 80 seconds and it is assumed that on this timescale the low and high field lines have experienced the same amount of reorientation. If the reorientation rates increased much further the validity of this assumption would break down.
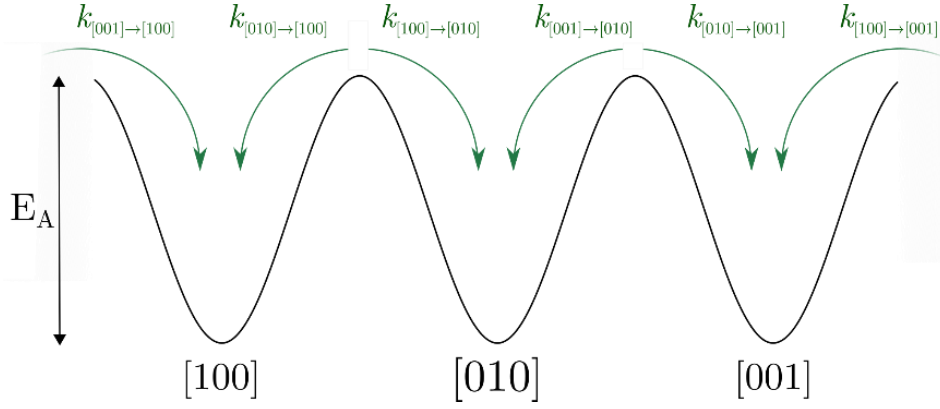
Figure 8-6 Simplified model of the energy wells for R2. showing the three orientations without applied stress.

8.3.2 Fitting

It is possible to model reorientation as a first order process using rate equations but it is important to consider all three defect orientations when this is performed. Under conditions of no external stress the energy between each defect orientation E_A is expected to be equal for all defect orientations and therefore it is possible for any defect orientation to reorientate into either of the other two, ie [001]→[010] and [001]→[100] etc. (Figure 8-6). A rate between any arbitrary two defect orientations, i and j, at temperature T can be defined as:

$$(8.2) \qquad k_{i \to j} = v \exp\left(\frac{E_{i \to j}}{k_B T}\right)$$

It is possible to model these process by the following simultaneous rate equations:

$$(8.3) \quad \begin{aligned}
\frac{d\left[\mathrm{Pop}_{[100]}\right]}{dt} &= k_{[010] \to [100]} \bullet \left[Pop_{[010]}\right] + k_{[001] \to [100]} \bullet \left[Pop_{[001]}\right] - k_{[100] \to [010]} \bullet \left[Pop_{[100]}\right] - k_{[100] \to [001]} \bullet \left[Pop_{[100]}\right] \\
\frac{d\left[\mathrm{Pop}_{[010]}\right]}{dt} &= k_{[100] \to [010]} \bullet \left[Pop_{[100]}\right] + k_{[001] \to [010]} \bullet \left[Pop_{[001]}\right] - k_{[010] \to [100]} \bullet \left[Pop_{[010]}\right] - k_{[010] \to [001]} \bullet \left[Pop_{[010]}\right] \\
\frac{d\left[\mathrm{Pop}_{[001]}\right]}{dt} &= k_{[100] \to [001]} \bullet \left[Pop_{[100]}\right] + k_{[010] \to [001]} \bullet \left[Pop_{[010]}\right] - k_{[001] \to [100]} \bullet \left[Pop_{[001]}\right] - k_{[001] \to [010]} \bullet \left[Pop_{[001]}\right]
\end{aligned}$$

For the isothermal anneals there is no stress and $E_{i \to j}$ is the same for all defect orientations, therefore the rate $k_{i \to j}$ will be the same for all defect orientations and as such were coupled to each other in the fitting algorithm. These equations were fitted to the data and an example is
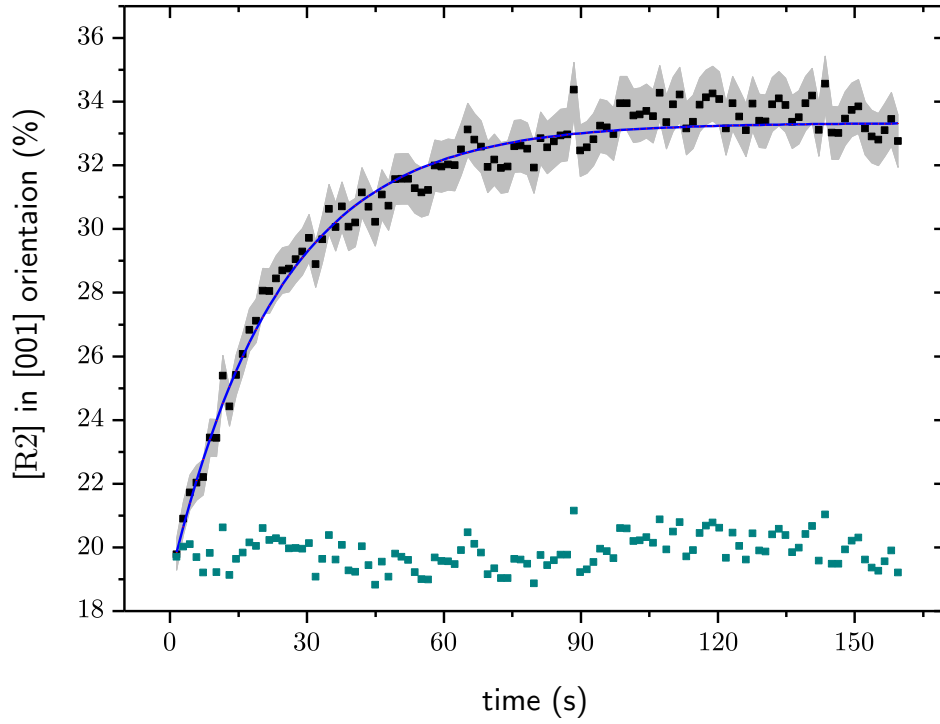
Figure 8-7 Example reorientation of the R2 defect during an isothermal anneal at 320 °C. Prior to the initial data point the sample was subject to a one hour anneal at 300 °C under 1 GPa of uniaxial pressure along [001] crystallographic direction. Data shown in black with associated error in the shading, blue line is fit to equations (8.3), residual (linearly offset) is shown in cyan.

shown in Figure 8-7. From this data it is clear that the reorientation is a first order process as expected. The rates of reorientation varied by three orders of magnitude over the temperature range tested, $k_{i \to j} = 1.3(1) \times 10^{-6}$ Hz at 523(1) K and $k_{i \to j} = 1.8(2) \times 10^{-3}$ Hz at 625(1) K.

The activation energy and attempt frequency were extracted from an Arrhenius plot. Equation (8.2) can be transformed to:

$$(8.4) \qquad \log_e \left(k_{i \to j} \right) = \log_e (v) - \frac{E_{i \to j}}{k_B} \frac{1}{T}$$

and by plotting $\log_e (k_{i \to j})$ against the reciprocal of temperature both the attempt frequency and E_A can be extracted. An Arrhenius plot of this data reveals an $E_A = 2.0(1)$ eV with an attempt frequency $v = 2(1) \times 10^{13}$ Hz (Figure 8-8).
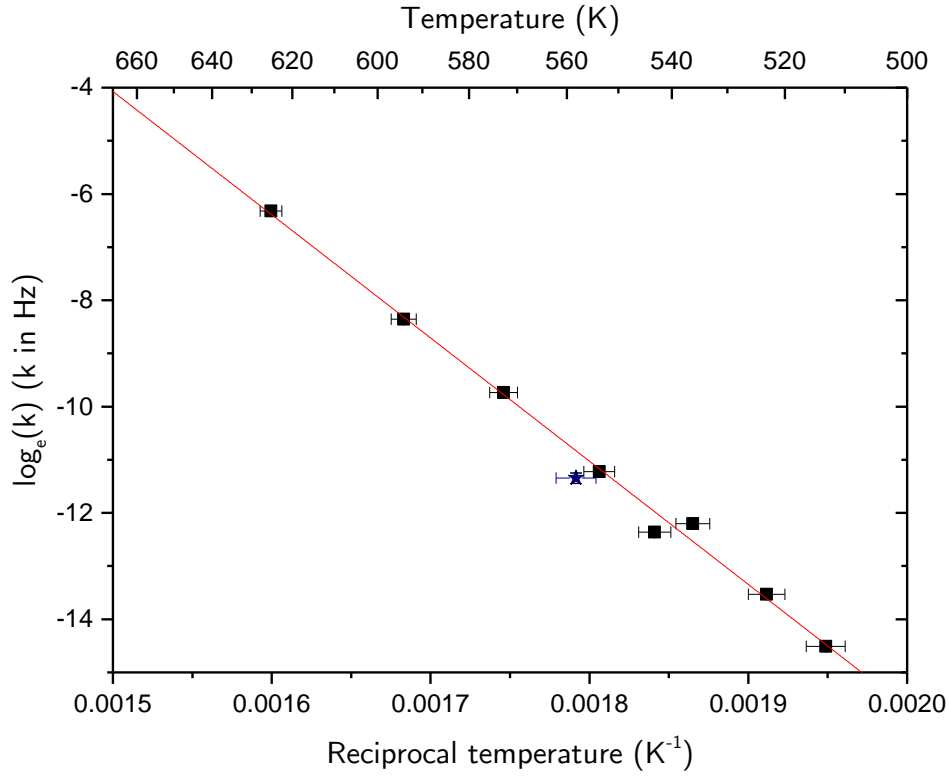
Figure 8-8 Arrhenius plot for the reorientation of the R2 defect. Solid line is linear fit to (8.4) with an attempt frequency of 2(1)×10¹³ Hz and an energy of 2.0(1) eV. The starred blue data point is from a previous study [14] is not included in the fit.

8.3.3 Isothermal anneal

Given that the activation energy determined is at odds with the accepted value an isothermal anneal was conducted on 50013c to investigate the annealing out of the R2 defect. Reference scans of Sample A were conducted at the start and the end of the anneal to allow quantitative changes to be calculated. The correction for the excited state population was performed as outlined by Hunt [10]. The results of this anneal conducted at 614(1) K can be seen in Figure 8-9. Fitting a single isothermal anneal does not allow extraction of either E_A or attempt frequency independently of each other and as such, a family of parameters could provide the best fit for the data.

The result of this anneal does not show a good fit to a first order process (Figure 8-9a) but does show a reasonable fit for a second order process (Figure 8-9b). The fit to the second order process assumes that there are similar populations of R2 and traps present at the start of the anneal. The loss of R2 has been shown to correlate with the loss of vacancies [12] and the
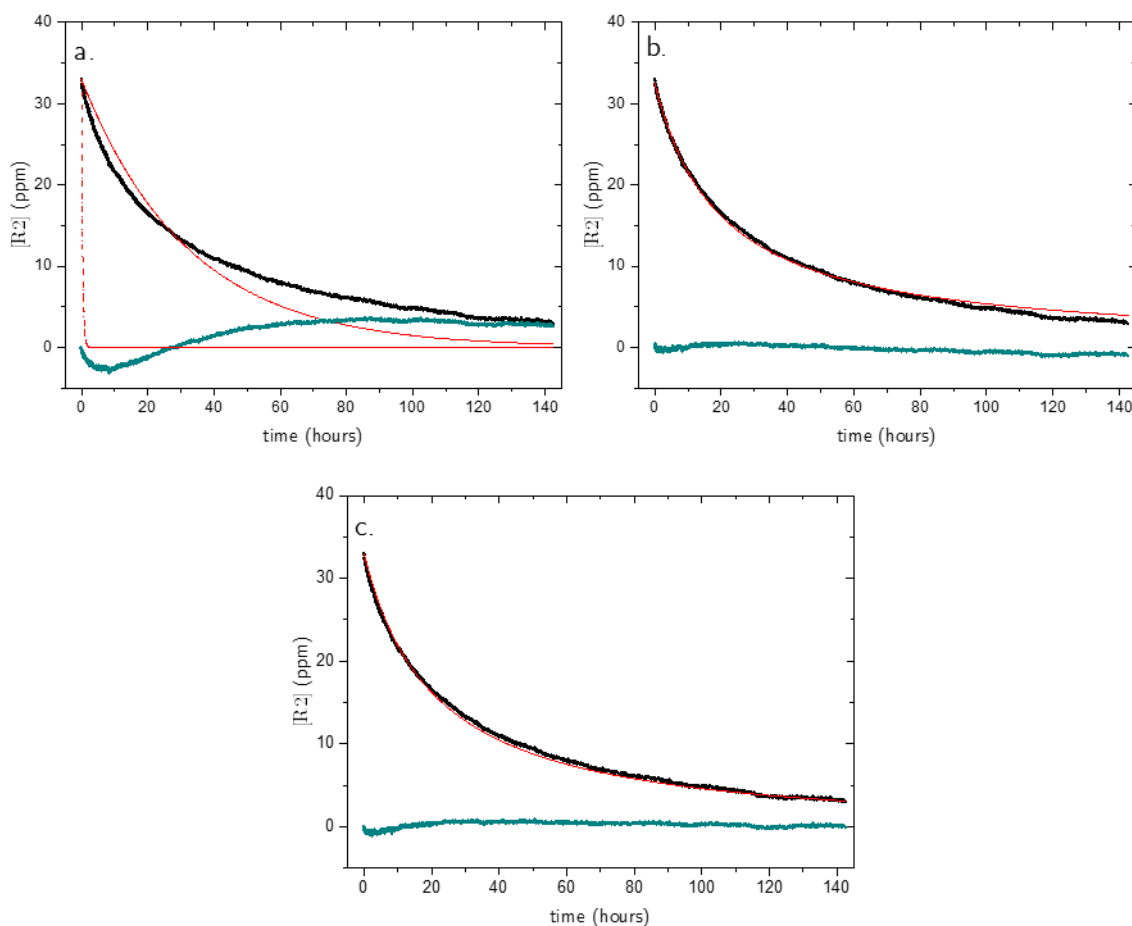
Figure 8-9 Isothermal anneal at 614 K with different order of rates simulations with $E_A=2\,eV$. Black points are the recorded concentration, red line the fit with values indicated below and the blue points are the residual.
a, first order $k_1=2.9(4)\times10^{13}\,Hz/ppm$.
b, second order $k_2=1.1(2)\times10^{10}\,Hz/ppm$.
c, mixed order $k_1=3(2)\times10^{10}\,Hz$ and $k_2=9(1)\times10^9\,Hz/ppm$.

predicted vacancy concentration after 1×10^{18} n cm^{-2} is 85(10) ppm [11]. The loss of R2 has also been shown to correlate to an increase in the di-interstitial related complex 3H defect. This recombination would lead to a reduction in the population of traps; this would therefore result in a second order process. The fit for second order process with an assumed $E_A = 2.0$ eV would have an attempt frequency of $k_2=1.1(2)\times10^{10}$ Hz/ppm.

Previous reports of isochronal anneals of R2 have used mixed order rates to fit the data. These are required when there are multiple routes to destruction. There may be routes to destruction which do not lead to a reduction in trap population such as recombination at boundaries or voids within the sample. These traps are effectively infinite compared to the R2 population and will therefore lead to a first order process. Assuming initial population of the one trap

that is infinite compared to [R2] and a second of order process such as R2 vacancy combination the change in the R2 population will be given by:

$$(8.5) \qquad \frac{d[R2]}{dt} = -k_{1^{st}}[R2] - k_{2^{nd}}[R2]^2$$

which has the solution:

$$(8.6) \qquad \frac{1}{[R2]} = \frac{\exp(k_{1^{st}}t)}{[R2]_0} + \frac{k_{2^{nd}}}{k_{1^{st}}}\left(\exp(k_{1^{st}}t) - 1\right) \ .$$

It follows that:

$$(8.7) \qquad [R2] = \frac{k_{1^{st}}[R2]_0}{k_{1^{st}}\exp(k_{1^{st}}t) + k_{2^{nd}}[R2]_0\left(\exp(k_{1^{st}}t) - 1\right)}$$

The fit shown in Figure 8-9c uses the rates of $k_{1^{st}} = 3(2)\times10^{10}$Hz and $k_{2^{nd}} = 9(1)\times10^9$Hz/ppm, with a fixed $E_A = 2.0$ eV. The mixed order process is a better fit than the second order process (adjusted R squared 0.999 from mixed rate compared to 0.997 for the second order fit), but the improvement is marginal.

8.3.4 Comparison with previous work

The E_A reported in §8.3.2 is different from the accepted values found from annealing out the defect. Experimental measurements have been made of the activation energy through annealing studies on the 1.859 eV optical transition; $E_A = 1.68(15)$ eV with an attempt frequency $\nu = 4 \times 10^{13}$ Hz [13] and $E_A = 1.6(2)$ eV with an attempt frequency $\nu = 1 \times 10^8$ Hz were reported [14]. In light of this it is interesting to revisit previous work.

Figure 8-10 shows previous results from Hunt [14] and Campbell [15] where isochronal anneals were used to ascertain an $E_A \sim 1.6$ eV. It is possible to simulate the expected results for second order processes using this activation energy (dashed lines in Figure 8-10) and the simulation
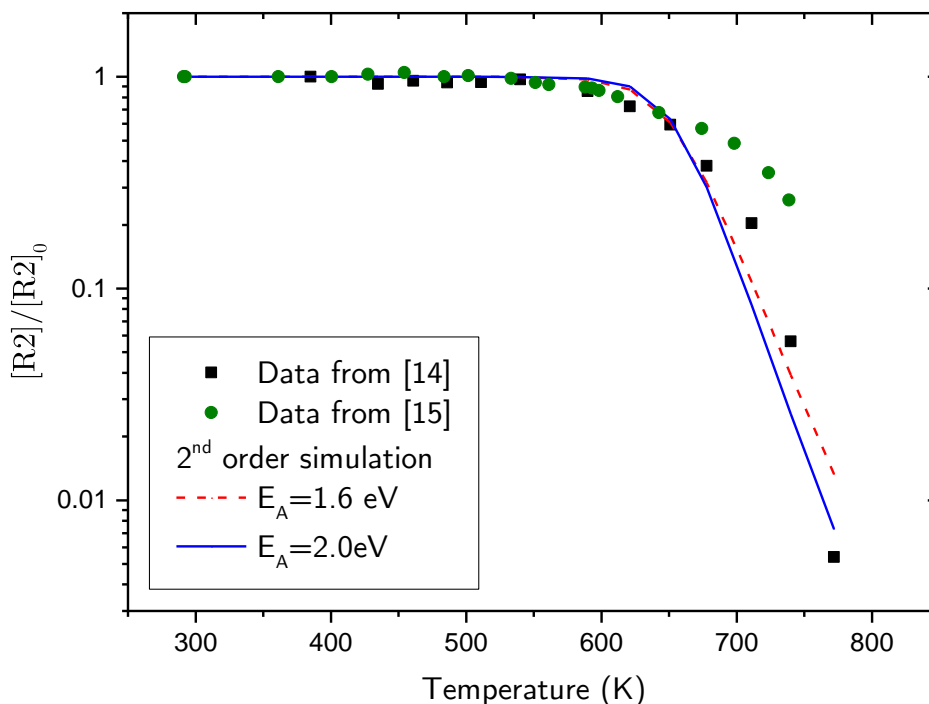
Figure 8-10 Data of Isochronal anneals conducted by Campbell (black squares) and Hunt (green circles). Second order rate equation simulations are shown with $E_A = 2$ eV, $k_2 = 1.0(2) \times 10^{10}$ Hz/ppm (solid blue line), and $E_A = 1.6$ eV $k_2 = 1.3(2) \times 10^{10}$ Hz/ppm (dashed red line).

shows a reasonable fit to the data. Simulations for a second order process were also made for the activation energy reported in this work ($E_A = 2.0$ eV). They show a very similar fit for the data the prefactor for the fit is $k_2 = 1.0(1) \times 10^{10}$ Hz/ppm in good agreement with the isothermal anneal. Both original authors reported simulations with a best fit for mixed rate processes but as discussed in §8.3.3 the physical meaning of such simulations is somewhat ambiguous.

8.4 Conclusion

Observation of the reorientation rates of R2 away from a previously preferentially orientated populated offers an unambiguous way of investigating migration of the defect. Previous reports on the migration of R2 have relied on the destruction of the defect to infer its migration. To the author's knowledge this approach of measuring migration has not been conducted in any other material and could easily be applied to paramagnetic centres in other crystalline materials.

The energy barrier associated with reorientation of R2 has been measured as $E_A = 2.0(1)$ eV with an attempt frequency $\nu = 2(1) \times 10^{13}$ Hz. This attempt frequency is consistent with the

Raman frequency for diamond. The reason for the large error in the attempt frequency is due to the relatively small temperature range measured. A small change in the gradient had a massive effect on the intercept.

The value for the migration energy and attempt frequency are higher than values previously reported. The energy for destruction is likely to be equal to or higher than the migration energy since the defect must diffuse through the lattice before interacting with another defect or boundary. Given that the isothermal data on defect destruction presented here and previous isochronal data do not follow simple first order processes, it is probable that the mechanism different starting materials, since both nitrogen and vacancies have been shown to affect the annealing of the defect. In this work the initial concentration of nitrogen was orders of magnitude below the concentration of R2 produced so it cannot have been the dominant factor in the process of destruction. As the sample was a CVD grown diamond it is likely to have dislocations that could operate as a sink for R2 but the poor fit for a first order process makes this unlikely.

It is interesting to note that from EPR data there is no way of knowing in which state the defect is migrating through the lattice. It is possible that the energy of migration is different for the excited state than it is for the ground state of the defect and determining this could be a goal for future work into the migration of R2. The process outlined in this chapter may be used in investigation of the migration of other defects in diamond and beyond.

8.5 References

[1] L. M. Pham, N. Bar-Gill, D. Le Sage, C. Belthangady, A. Stacey, M. Markham, D. J. Twitchen, M. D. Lukin, and R. L. Walsworth, Phys. Rev. B - Condens. Matter Mater. Phys. 86, 1 (2012).

[2] A. M. Edmonds, U. F. S. D'Haenens-Johansson, R. J. Cruddace, M. E. Newton, K.-M. C. Fu, C. Santori, R. G. Beausoleil, D. J. Twitchen, and M. L. Markham, Phys. Rev. B 86, 35201 (2012).

[3] M. Lesik, J. P. Tetienne, A. Tallaire, J. Achard, V. Mille, A. Gicquel, J. F. Roch, and V. Jacques, Appl. Phys. Lett. 104, 109 (2014).

[4] J. E. Butler and I. Oleynik, Philos. Trans. A. Math. Phys. Eng. Sci. 366, 295 (2008).

[5] T. Karin, S. Dunham, and K. M. Fu, Appl. Phys. Lett. 105, 2012 (2014).

[6] S. Liggins, M. E. Newton, J. P. Goss, P. R. Briddon, and D. Fisher, Phys. Rev. B - Condens. Matter Mater. Phys. 81, 1 (2010).

[7] R. Jones, J. P. Goss, H. Pinto, and D. W. Palmer, Diam. Relat. Mater. 53, 35 (2015).

[8] S. J. Breuer and P. R. Briddon, Phys. Rev. B 51, 6984 (1995).

[9] M. S. Al-Hadidi, C. Peaker, J. P. Goss, P. R. Briddon, M. J. Rayson, and A. B. Horsfall, in *67th Diam. Conf.* (Warwick, 2016).

[10] D. C. Hunt, D. J. Twitchen, M. E. Newton, J. M. Baker, T. R. Anthony, W. F. Banholzer, and S. S. Vagarali, Phys. Rev. B 61, 3863 (2000).

[11] M. W. Dale, Colour Centres on Demand in Diamond - PhD Thesis, University of Warwick, 2015.

[12] M. E. Newton, B. A. Campbell, D. J. Twitchen, J. M. Baker, and T. R. Anthony, Diam. Relat. Mater. 11, 618 (2002).

[13] L. Allers, A. T. Collins, and J. Hiscock, Diam. Relat. Mater. 7, 228 (1998).

[14] D. C. Hunt, A Study of Defect in Diamond - PhD Thesis, University of Oxford, 1999.

[15] B. A. Campbell, Point Defects in Diamonds - PhD Thesis, King's College London, 2002.

Chapter 9

9 Summary

This thesis has employed EPR along with NMR and FT-IR absorption spectroscopy in the study of point defects in diamond. RP-EPR$^{\text{(FM)}}$ has been successfully explored as a technique for improving the sensitivity of EPR. The errors associated with RP-EPR$^{\text{(FM)}}$ and SP-EPR have been considered and proposals made to mitigate these where possible. The spin-spin and spin-lattice relaxation of N_S^0 has been investigated using uniaxial stress as a perturbation. This has allowed insight into the mechanisms involved in the relaxation processes. Uniaxial stress during annealing has also been employed to create a preferentially orientated population of I_{001} which has allowed the migration of the defect through reorientation to be investigated. The polarisation of $^{15}N_3V^0$ and $^{15}N_S^0$ have also been investigated; these have led to a new understanding of the polarisation mechanism.

9.1 Quantification in diamond

The use of RP-EPR$^{\text{(FM)}}$ as a quantitative technique has been examined in this thesis. A random error of $\pm 2.5\%$ in determining N_S^0 concentration was found for measurements made with B_0 parallel to the [001] crystallographic direction. Measurements made away from the principal direction have an increased random error of $\pm 5\%$ due to the difficulty in fitting the hyperfine spectrum that no longer has a uniform intensity. SP-EPR quantitative measurements of N_S^0 made with aligned with B_0 parallel to the [001] crystallographic direction have previously been found to have a random error of $\pm 5\%$. The improvement is due to the increased quality of the fit of the simulation to the experiment. A typical RP-EPR$^{\text{(FM)}}$ spectrum of a 40 ppb sample will have greater SNR when compared to a typical SP-EPR spectrum for a 270 ppm sample. Low concentration samples also have narrow linewidths that provide increased confidence in alignment increasing the accuracy of the simulation. These two factors are the main reason for the increased accuracy in repeatability of RP-EPR$^{\text{(FM)}}$ compared to SP-EPR.

The effects of variable temperature and sweep rates on the RP-EPR$^{(FM)}$ signal have been explored. A factor of 5.6 improvement in SNR was reported at 200 K and a sweep rate of 100 mT/s compared to measurements made at room temperature with a 2 mT/s sweep rate. Further increases in sweep rate were not possible whilst using 100 kHz modulation frequency and not distorting the spectrum. Further reduction in temperature at the maximum sweep rate is not beneficial as the time between measurements of EPR transitions needs to be much greater than the T_1 for the spin system which increases at lower temperatures. This change in protocol represents nearly a factor of 32 reduction in acquisition time for the same SNR and therefore a massive increase in throughput for a busy lab. This also means that the limit in quantification of 1.6×10^{11} spins/mT in a 0.005 cm^3 sample (10 ppt).

Quantification of N_S^0 content of large samples has also been explored. Without any correction being applied, measurements of samples that exceed the uniform working area of the cavity in the z-direction provided an underestimate of the actual spin concentrations. Cavity characterisation coupled with awareness of the cavity Q_l have been employed to allow accurate quantification of N_S^0 of such samples. Further work is required for samples that exceed the cavity working area in the xy-plane but a similar approach should be beneficial.

A broad feature witnessed in the EPR of diamonds with high concentration of nitrogen has been used to explain the discrepancy between the apparent EPR quantification of N_S^0 and measurements made with FT-IR absorption spectroscopy. It is proposed that in sectors of the diamond where concentrations exceed 400 ppm that the near neighbour pairs have sufficient strong interactions to allow electron spin exchange. This has the effect of broadening the hyperfine EPR lines into a single feature. This work was conducted on a small set of samples and confirming that this is a universal problem should be the subject of future investigations. However, when assaying high concentration or highly sectored samples it is important to be aware of these potentially "lost" N_S^0 spins.

9.2 Relaxation of N_S^0

The relaxation of N_S^0 was investigated in chapter 6 of this work. The experimental parameters required for peak signal of field modulated RP-EPR$^{(FM)}$ were used to extract the $\sqrt{T_1 T_2}$ for N_S^0 in diamonds with concentrations <1 ppm. This is the first time that the effect of modulation frequency on the phase of the peak signal, as proposed by Porits [1], has been compared to directly measured relaxation times measured by pulsed EPR. A good agreement was found between the predicted relaxation times from RP-EPR$^{(FM)}$ and the measured relaxation times. Whilst this approach may only be used for paramagnetic centres that can be brought into RP-EPR$^{(FM)}$ it does provide a way of comparing the T_2 in different diamonds, since T_1 is independent of concentration [2].

The effect of uniaxial stress on N_S^0 was also investigated. By applying uniaxial stress along the principal crystalline directions *in situ* during EPR measurements it was possible to measure the changing populations of different orientations of the defect as a function of applied stress. The change in relative energies as a function of pressure was established. A dependence was found for the energy change because of applied stress of 13(3) meV/GPa for stress applied parallel to the [011] crystallographic direction and 17(1) meV/GPa for stress applied parallel to the [111] crystallographic direction. These results showed good agreement with predictions from uniaxial stressed FT-IR [3].

In situ uniaxial stress was also used as perturbation during investigations of the relaxation mechanisms of N_S^0. No change in T_1 was found for defects orientated such that a component of uniaxial stress was along the C_{3v} defect axis compared to those with the axis perpendicular to the stress. This result casts doubt on *"spin-orbit phonon-induced tunnelling"* [2] as the dominant relaxation mechanism. T_m was found to have a dependency on pressure. An increased T_m was found for defects orientated such that a component of uniaxial stress was along the C_{3v} defect axis. A reduction in T_m was found for defect orientations with the axis perpendicular to the stress. This tuning of T_m is shown to be due to the change in populations

of different defect orientations and the subsequent modification of the instantaneous spin diffusion.

The spin lattice relaxation times of N_S^0 have shown to be independent of field at room temperature but found to increase proportionally with field between 77-150 K. The temperature dependence shows an approximate fit to a $\frac{1}{T_1} = AT + BT^5$ relationship and it is A that changes with field. This is inconsistent with predictions for the direct process and is possibly due to a multi phonon Raman process. More data over a wider range of field would be required to establish the spin-lattice relaxation mechanism.

9.3 Polarisation of $^{15}N_S^0$ and $^{15}N_3V^0$

The optically induced spin polarisation of $^{15}N_S^0$ and $^{15}N_3V^0$ has been investigated. The use of monochromatic light sources has enabled the optical energy dependence to be examined and polarisation has been found at all energies greater than 1.9 eV. The maximum polarisation was found at 2.36 eV and no sharp threshold activation energy was found. The polarisation is observed at temperatures below 150 K, and increases in magnitude as temperature is lowered further. Measurements have been made of the polarisation build-up and decay and these indicate unsurprisingly that T_1 is the primary cause for the decay of polarisation. The polarisation build-up is relatively slow (2s at 50 K).

Nuclear polarisation of both the ^{15}N and ^{13}C populations was observed in the EPR spectrum of both $^{15}N_S^0$ and $^{15}N_3V^0$ and the polarisation of $^{15}N_S^0$ persisted after the excitation had been removed. EPR was used to monitor the return of this polarisation to equilibrium and a time constant of 40(3) min was measured; it is believed this is a measurement of the $^{15N}T_{1n}$. The nuclear spin polarisation of the bulk ^{13}C lattice has been measured using optically pumped NMR; polarisation factors of -180(10) at room temperature and -480(40) at 240 K are reported.

The two defects involved in the polarisation, $^{15}N_S^0$ and $^{15}N_3V^0$, are both S=1/2 and as such conventional inter-defect intersystem crossing polarisation mechanisms cannot be responsible

for the polarisation witnessed. Charge transfer of $^{15}N_S^0$ to $^{15}N_S^+$ has been witnessed through low temperature optically excited FT-IR.

A spin-correlated radical pairs mechanism has been previously used to explain avian navigation [4] and it is proposed as the mechanism for the spin polarisation here. In this process a coupled system of $\left(^{15}N_3V^- + {}^{15}N_S^+\right)^0$ can absorb a photon and move to an excited singlet state that then undergoes intersystem crossing to a triplet state. The rate of return to the ground state from the excited singlet and triplet states are different leading to a potential build-up of both electron and nuclear polarisation. As a potential mechanism, this appears to fit the experimental data acquired but more theoretical and experimental work is required to confirm the model.

9.4 Reorientation of the ⟨001⟩-split interstitial, R2

The final chapter in this thesis focused on the migration of the ⟨001⟩-split interstitial, known as R2 in EPR. The proposed method for the migration of the R2 involves the reorientation of the defect between different lattice orientations [5]. The methods employed in this thesis allowed this reorientation to be measured directly. By applying uniaxial stress parallel to the [001] crystallographic direction a difference was created in energy levels of the normally degenerate sites of the defect. Annealing under these conditions causes high energy orientation of the defect to be depopulated relative to the unperturbed sites. After the anneal these populations remain fixed in place until a second anneal is performed. This second anneal was carried out *in situ* in an EPR spectrometer. It is possible to address the three orientations of R2 independently with EPR and monitor the reorientation of the defect once the barrier had been removed. This process was repeated with increasing temperature of the second *in situ* anneal allowing an Arrhenius plot to be constructed and an activation energy and attempt frequency to be calculated, $E_A = 2.0(1)$ eV and $\nu = 2(1) \times 10^{13}$ Hz respectively.

The values for the attempt frequency and activation energy are higher than previously reported for the defect [6]. However, previous reports of the defect have measured the destruction of the defect during isochronal anneals and inferred the activation energy from an assumed

attempt frequency. Revisiting the previous data with the new activation energy has revealed a good agreement for the new activation energy to the data [7,8]. An isothermal anneal was conducted and the destruction of the defect monitored. As with previous isochronal annealing studies the reduction in R2 concentration did not show agreement to a first order process. There was reasonable agreement with a second order process, but it is likely that the route to destruction of R2 is more complicated than this.

The reorientation of the defect is at a higher energy than predicted by theory and this discrepancy may inspire future theoretical research. It should be noted that it is not possible to tell from EPR in which energy state the $\langle 001 \rangle$-split interstitial reorientates. Only the excited, $S=1$, R2 state is observed in EPR and it is possible that the defect does not migrate in this state. Further work is needed to establish the route to destruction of R2. It is likely that there are different routes to destruction in different samples and an investigation of a suite of samples with different starting materials is required to establish if there is a dominant path to destruction.

9.5 References

[1]   A. Portis, Phys. Rev. 91, 1071 (1953).

[2]   E. C. Reynhardt, G. L. High, and J. A. van Wyk, J. Chem. Phys. 109, 8471 (1998).

[3]   S. Liggens, Identification of Point Defects in Treated Single Crystal Diamond - PhD Thesis, University of Warwick, 2010.

[4]   C. T. Rodgers and P. J. Hore, Proc. Natl. Acad. Sci. U. S. A. 106, 353 (2009).

[5]   S. Breuer and P. Briddon, Phys. Rev. B 53, 7819 (1996).

[6]   D. C. Hunt, D. J. Twitchen, M. E. Newton, J. M. Baker, T. R. Anthony, W. F. Banholzer, and S. S. Vagarali, Phys. Rev. B 61, 3863 (2000).

[7]   D. C. Hunt, A Study of Defect in Diamond - PhD Thesis, University of Oxford, 1999.

[8]   B. A. Campbell, Point Defects in Diamonds - PhD Thesis, King's College London, 2002.

10 Appendix

10.1 Laser diodes

Wavelength (nm)	Optical power output (mW)	Case operating temperature (°C)	Part number	Supplier
375(5)	70	25	L375P70MLD	ThorLabs
405(5)	200	25	LD-405-200	Roithner LaserTechnik GmbH
450(10)	1600	25	LD-450-1600MG	Roithner LaserTechnik GmbH
520(10)	1000	25	NLD521000G	Roithner LaserTechnik GmbH
532(2)	80	25	GEM-FS	Laser Quantum
638(6)	500	25	ADL-63V0BTP	Roithner LaserTechnik GmbH
650(5)	200	25	RLT650-200G	Roithner LaserTechnik GmbH
780(5)	1000	25	RLT780-1000G	Roithner LaserTechnik GmbH

10.2 List of Samples

Sample	Growth method	Ns0 [ppm]	Other EPR defects	Chapters	Notes
Syn93-04	HPHT	270(20)		5/6/7/8	SP-EPR Referecen sample
0577207-C(ii)	CVD	0.040(4)		5/6/7/8	RP-EPR Reference Sample
097320P-A	CVD	0.50(5)		5	
Sample V	HPHT	>500		5	
SDB1000	HPHT	290 (20)		5	Diamond Powder
Syn93-391	HPHT	41 (4)		6	Stress Sample
0373821-A(ii)	CVD	7.9 (5)	NVH	6	
Syn339-B(i)	HPHT	115 (10)		6/7	Stress Sample 99% 15N enriched
Syn339-C(i)	HPHT	90 (10)	NV	6	Stress Sample 99% 15N enriched
0743185-A	CVD	0.070(5)		6/7	
Syn93-08	HPHT	270(20)		6	
Syn339-5	HPHT	21(5)	N3V	7	95% 15N enriched
Syn339-B(ii)	HPHT	120(10)	NV	7	95% 15N enriched Irradiated and annealed to 1000 °C
Syn331	HPHT	30 (5)		7	85% 15N enriched
N6-1A	Natural	2.0(2)	N3V	7	
50013c	CVD	0.078(8)	R2 R1	8	Neutron irradiated